UNIVERSITY OF SOUTHAMPTON

FACULTY OF MEDICINE

Human Development and Health

A Multi-parameter *In-vivo* Sensing Platform for Intra-uterine Environment Monitoring

by

Shilong Lu

Thesis for the degree of Doctor of Philosophy

July_2014

UNIVERSITY OF SOUTHAMPTON

ABSTRACT

FACULTY OF MEDICINE

Discipline (Human Development and Health)

Doctor of Philosophy

A MULTI-PARAMETER *IN-VIVO* SENSING PLATFORM FOR INTRO-UTEINE ENVIRONMENT MONITORING

by Shilong Lu

Human reproduction is a relatively inefficient process [1]. More than 30% of all conceptions do not advance beyond 20 weeks of gestation. 1 in 6 couples suffer from infertility, and in around 25% of couples no clear reason is identified. This may reflect the lack of pathophysiologic understanding and clinically relevant diagnostic approaches for interrogating uterine functions. Moreover, for those who require assisted conception, take home baby rates after artificial reproductive technologies (ART) have altered little in the last 5-10 years, again pointing to the lack of clinically relevant diagnostic approaches for interrogating uterine functions. If these clinical issues are to be addressed, a greater understanding of what contribute to infertility is required.

An interaction between the intra-uterine environment and reproductive health is likely, but very little is known about the biophysical characteristics of the uterus and how they alter through the menstrual cycle. Previous work has been undertaken on intra-uterine biophysical parameters, such as temperature, dissolved oxygen concentration (DOC) and pH, all of which are related to cell metabolism, embryonic development and other reproductive activities [2-6]. However the available data is mostly derived from snapshot technology and wired sensor probes, both of which do not enable real-time long-term *in-vivo* monitoring.

Within the constraints of the operating environment (the uterus), user comfort, safety and device life-time, this thesis proposed and developed a multi-parameter *in-vivo* platform for sensing critical biophysical parameters in the uterus (temperature, DOC and pH). This platform includes a miniaturised wireless and batteryless implantable sensor device incorporating temperature sensor, wearable receiver with various innovative antennas and well-developed software. The device achieves long-term capture of the intra-uterine environment information in real-time through direct implantation into the uterus. Two prototypes for miniaturised DOC and pH sensor were also researched and developed. First human trial is in progress after a series of animal tests. This work may push the *in-vivo*

sensing technologies forward and bring constructive contribution to intra-uterine information collection, human reproduction research and healthcare management.

Contents

Chapter 3 System design and development 33

Chapter 4 Design of implantable biosensors 99

List of Figures

List of Tables

Definitions and Abbreviations Used

ADC	Analogue-Digital Convertor
AEIROF	Anodically Electrodeposited Iridium Oxide Film
AI	Artificial Insemination
App	short for application software, more specific for mobile application
APTES	3-Aminopropyl Triethoxysilane
ART	Artificial Reproductive Technologies
ARRIVE	Animal Research: Reporting In Vivo Experiments
ASK-LSK	Amplitude Shift Keying-Load Shift Keying
ASIC	Application Specific Integrated Circuit
BDD	Boron Doped Diamond
BEST	Batteryless Endoluminal Sensing Telemeter
CE	Counter Electrode
CHB	Centre for Hybrid Biodevices
CT	X-ray computed tomography
CV	Cyclic Voltammetry
DAQ	Data Acquisition
DO	Dissolved Oxygen
DOC	Dissolved Oxygen Concentration
E-field	Electric Field
EP	European Pharmacopoeia
ETO	Ethylene Oxide
FDA	Food and Drug Administration
FSH	Follicle Stimulating Hormone
GERD	Gastroesophageal Reflux Disease
GI	Gastrointestinal
GIFT	Gamete Intra-Fallopian Transfer
GnRH	Gonadotropin Releasing Hormone
GPIO	General Purpose Input/output
GPTMS	3-Glycidoxypropyl Trimethoxysilane
GUI	Graphic User Interface

H-field	Magnetic Field
H&E	Haematoxylin and eosin
ICs	Integrated Circuits
ICSI	Intra-Cytoplasmic Sperm Injection
IMD	Implantable Medical Device
IROF	IrOx film
IrOx	Iridium Oxide
ISFET	Ion-sensitive Field Effect Transistors
ISM	Industrial, Scientific and Medical
IUCS	In-Utero Culture System
IUD	Intra-uterine Device
IVF	*In-vitro* Fertilization
LF	Low Frequency
LF RFID	Low Frequency Radio Frequency Identification
LH	Luteinising Hormone
LIAP	Lab-In-A-Pill
LoC	Laboratory-on-a-chip
LPM	Low Power Mode
MCU	Micro-programmed Control Unit
MDD	Medical Device Directive
MFB	Main Function Board
MG-PDMS	Medical Grade Polydimethylsiloxane
MHPC	Multi-harvesting Power Chip
MHRA	Medicines & Healthcare Products Regulatory Agency
MOSFET	Metal Oxide Semiconductor Field Effect Transistor
MUX	Multiplexer
NFC	Near Field Communication
NPIMR	Northwick Park Institute for Medical Research
NOC	National Oceanography Centre
NTC	Negative Temperature Coefficient
OCP	Open Circuit Potential
ODO	Optical Dissolved Oxygen
OPM	Oxygen Permeable Membrane
PaLFI	Passive Low Frequency Interface
PBS	Phosphate Buffered Saline
PCB	Printed Circuit Board
PCM	Proton Conductive Matrix
PDMS	Polydimethylsiloxane
PE	Polyethylene

PicMill	Picrosirius red plus Miller’s elastin
PID	Pelvic inflammatory Disease
PO_2	Partial Pressure of Oxygen
PRT	Platinum Resistance Thermometers
PSB	Power Supply Board
PSS/PL	Poly Styrene-sulphonate/poly L-lysine
Pt	Platinum
PTC	Positive Temperature Coefficient
PTFE	Polytetrafluoroethylene
PMMA	Polymethyl methacrylate
RE	Reference Electrode
REDOX	Reduction-Oxidation
RF	Radio Frequency
RFID	Radio Frequency Identification
RTV silicon	Room Temperature Vulcanizing silicon
RVn	Receiver Version n (n = 1 or 2)
QFN	Quad Flat-pack No-lead
SAR	Specific Absorption Rate
SCS	Spinal Cord Stimulation
SDVn	Sensor Device Version n (n = 1, 2, 3 or 4)
SHE	Standard Hydrogen Electrode
SoC	System-on-chip
SPI	Serial Peripheral Interface
S-SD	Stick-type Sensor Device
Tx	Transmission
T-SD	T-type Sensor Device
UART	Universal Asynchronous Receiver/Transmitter
USB	Universal Serial Bus
USP	United States Pharmacopeia
VLSI	Very Large Scale Integer
V-I	Voltage-Current
WE	Working Electrode
WHO	World Health Organisation
WPANs	Wireless Personal Area Networks
WSN	Wireless Sensor Networks

Academic Thesis: Declaration Of Authorship

I, ……Shilong Lu………………………………………………………………………………………

declare that this thesis and the work presented in it are my own and has been generated by me as the result of my own original research.

A Multi-parameter In-vivo Sensing Platform for Intra-uterine Environment Monitoring
……

I confirm that:

1. This work was done wholly or mainly while in candidature for a research degree at this University;
2. Where any part of this thesis has previously been submitted for a degree or any other qualification at this University or any other institution, this has been clearly stated;
3. Where I have consulted the published work of others, this is always clearly attributed;
4. Where I have quoted from the work of others, the source is always given. With the exception of such quotations, this thesis is entirely my own work;
5. I have acknowledged all main sources of help;
6. Where the thesis is based on work done by myself jointly with others, I have made clear exactly what was done by others and what I have contributed myself;
7. Either none of this work has been published before submission, or parts of this work have been published as: [please list references below]:

Signed: ……

Date: ……

Acknowledgements

First of all, I would like to thank my supervisors, Dr Tracey Newman, Prof Hywel Morgan, Dr Ying Cheong and Prof Nicholas Macklon. I greatly appreciate the opportunity they have given me to take part in this project. Their guidance, ideas and resources are essential to this project. They have also given me much help in my personal life. I thank Xi Huang. We know each other for a long and he has always been a great help. I would like to thank Katie Chamberlain, Gareth Lyle Jones, and Martin Arundell, they helped me a lot with the dissolved oxygen sensor design and sensor chips manufacture. My thanks also go to my colleagues in the same group, I am really happy to work with them. Especially, I want to thank my friends Chunxiao Hu, Yan Zhao, Mark, Marcel, Sumit, Prameen and Tianyi Jiang.

Finally and most importantly, I would like to thank all my family, in particular to my wife, Nan Li, who always trusts me and gives me great support and help. I also want to give my love to my little boy, Yishen.

Chapter 1

Introduction

1.1 Overview of research

Human reproduction is a relatively inefficient process, and more than 30% of conceptions do not advance beyond 20 weeks of gestation. This is primarily due to peri-implantation pregnancy loss and first-trimester miscarriage, even after assisted conception. 1 in 6 couples suffer from infertility, and in around 25% of these couples no clear reason is identified. This reflects the lack of pathophysiologic understanding and clinically relevant diagnostic approaches for interrogating uterine functions. The past decade has seen much interest in the emerging technologies, particularly artificial reproductive technologies (ART). Despite major advances in embryo culture and selection, take home baby rates after ART have altered little in the last 5-10 years, again pointing to endometrial function as an important factor determining fertility.

In the field of human reproductive research, there is growing recognition of the need to better understand the intra-uterine environment, such as the temperature, dissolved oxygen concentration (DOC) and pH, which are related to cell metabolism, embryonic development and other reproductive activities may affect uterine receptivity and successful pregnancy [2-6]. Research from multiple groups has demonstrated that the environment within the endometrial cavity not only affects the chance of implantation, but also the developmental health of the early embryo, and the resulting offspring [7]. If these clinical issues are to be addressed, a greater understanding of what contribute to uterine receptivity and pregnancy failure are required. However, data on the biophysical characteristics of this compartment is hindered by a lack of reliable, relevant measurement tools. Biophysical data from this understanding of the physiological mechanisms underlying reproduction and even the normal variation of fundamental biophysical parameters remain limited. There is an unmet need to develop a device designed as a diagnostic investigative tool capable of characterizing in real-time, long-term dynamic changes in a number of biophysical parameters likely to impact on the success of implantation. If this clinical tool is available, a better understanding of what contribute the infertility can be achieved and future novel interventions may be made to optimise the peri-implantation milieu encountered by the embryo, both in the context of ART and spontaneous conception.

This thesis proposed and developed a multi-parameter *in-vivo* sensing platform with the aim of achieving long-term, real-time intra-uterine environment information capture. Within the constraints of the operating environment (in the uterus), user comfort, safety and device lifetime, this platform was well-designed and optimised for directly implantation in the uterus to sense critical biophysical parameters (temperature, DOC and pH). It includes a miniaturised wireless and batteryless implantable sensor device incorporating miniaturised biosensors, wearable receiver with various innovative antennas and well-developed software.

1.2 Contribution and achievement

This thesis has developed a multi-parameter *in-vivo* sensing platform for the intra-uterine environment monitoring. The system prototype was developed, encapsulated and fully evaluated in lab, and first human trial is in progress after a series of animal tests. The key contributions and achievements of this project are listed below:

Contribution 1:

A multi-parameter *in-vivo* sensing platform was proposed and developed for enhanced medical diagnostics. This powerful tool achieves long-term real-time *in-vivo* biophysical parameters measurement which is hard to achieve by conventional snapshot technologies and cable sensors;

Achievements:

- A three-module structured system was proposed, and two core technologies were discussed and optimised for the intended *in-vivo* sensing platform including wireless energy transfer and wireless data communication.

- Four versions of sensor devices were developed and the latest one was adequate to work as a wireless and batteryless implantable sensor device to meet the size and energy limitation of the intra-uterine application.

- Two different versions of wearable receiver were developed and the latest version was portable, robust, and powerful to achieve long-term real-time monitoring. A two-board three-layer stacked structure and optimised multi-layer PCB layout results in a smaller receiver with less interference and better signal performance than previous version.

- Different software were developed for remote real-time monitoring, including two Java software designed for the single and multiple antenna receiver systems, an Android monitoring software for smart phones and an embedded software GUI which was running in the receiver. All software were designed with various Interfaces and good scalability for friendly user experience, easy debugging and future upgrade.

Contribution 2:

World's first miniaturised, wireless, batteryless, fully implantable sensor device was researched and developed for long-term real-time intra-uterine environment monitoring;

Achievements:

- The latest sensor device was adequate to work as a wireless and batteryless implantable sensor device to meet the size and energy limitation of the intra-uterine application.

- Two different shapes of sensor device prototypes were proposed, including T-type and stick-type sensor devices, which were size comparable with the currently widely used intra-uterine devices (IUDs). Different encapsulation solutions were developed for bench test, animal test and further human trial.

Contribution 3:

Well designed and optimised various antennas for implantable sensor device and wearable receiver were developed for different application scenarios. An innovative belt antenna achieves friendly user experience and good wireless signal performance;

Achievements:

- Different antenna prototypes were designed and developed for sensor device under the limitations from size and wireless performance. A homemade winding machine was made for the fabrication of antenna coils. The tube antenna (ϕ4.3 X 15.2, with ferrite core) was deemed as the optimal antenna to the sensor device which achieved a 23cm maximum working distance to a 20X20cm receiver antenna;

- Five different designs of receiver antenna were developed and a belt antenna was proved to be the most suitable antenna for pig tests and future human trial. Its novel design of an antenna coil connector and adjustable hooks made it easy to use as a normal belt and well fitted on the body;

- A multi-antenna receiver system was proposed for the applications where the position and orientation between the sensor device and receiver varies, such as rabbit intra-uterine environment monitoring. A multi-antenna receiver system (six antennas) was developed for the animal tests on rabbit and successfully achieved a two weeks *in-vivo* monitoring.

Contribution 4:

Two highly innovative, multi-layer structured, miniaturised, ultra-low power consumption, electrochemical sensors were proposed and developed based on lab-on-a-chip and MEMS technologies for *in-vivo* dissolved oxygen concentration (DOC) and pH measurement;

Achievements:

- An implantable temperature sensor was developed based on a NTC (negative temperature coefficient) thermistor due to its stability and accuracy and the sensor circuit was optimised for small size and low power consumption application. The final packaged sensor device reached an accuracy of ±0.03°C during two weeks continuously *in-vivo* measurement;

- After discussion of the principle and core technologies of dissolved oxygen (DO) sensor, a miniaturised electrochemical DO sensor (7mmX4mmX2mm) was designed and developed. Good linear relationship between the oxygen reduction current and the DOC of bulk solution were observed and the measurement error was confirmed in a range of ±7μM. The stability of built-in Ag/AgCl RE and the characteristics of medical grade OPM were also researched and discussed in this thesis;

- A miniaturised Iridium Oxide film (IROF) pH sensor was developed by using the anodical electrodeposition method (AEIROF) based on Yamanaka's recipe for the intended application. An auto-testing platform was developed for AEIROF pH sensor evaluation. The minimized AEIROF pH sensor presented a super-Nernstian response with a sensitivity of 76.33±2.58mV/pH and an accuracy of 0.04pH in the tests by standard pH buffers.

Contribution 5:

Initial animal tests have been undertaken, the implantable sensor device and *in-vivo* sensing platform were verified and tested on pig cadavers and rabbits. Two weeks long-term real-time intra-uterine monitoring was successfully achieved on rabbit. Valuable experience has been obtained for further animal tests and future human trials.

Achievement:

- Animal tests were undertaken on the pig cadaver and rabbit. The pig cadaver tests verified design of prototypes and wearable receiver deployment. A proposed clinical procedure for sensor device implantation and retrieval was demonstrated and confirmed, and valuable experience was obtained for future live pig tests and human trials;

- The rabbit tests achieved real-time long-term intra-uterine temperature monitoring up to two weeks. These tests not only demonstrated the implantation of sensor device in live animals, but also evaluated this *in-vivo* sensing platform performance, and obtained novel *in-vivo* data for rabbit intra-uterine environment research (incorporating temperature).

1.3 Document structure

This thesis describes the research and development of an innovative multi-parameter sensing platform for the intra-uterine environment monitoring. Firstly, it introduces the relevant background and motivation of intra-uterine environment monitoring, reviews the latest results and challenges of human reproductive research, and then compares the state of the art technologies for *in-vivo* biophysical parameters measurement. Next, it presents the design and development of the intended *in-vivo* sensing platform including the system architecture design, key technologies development and implantable biosensors fabrication. The thesis also includes the tests in the lab and animal tests. The structure of the thesis is listed as below:

Chapter 2 introduces the background and motivation of intra-uterine environment monitoring, human reproduction research results, the state of the art technologies, the research strategies and expected specifications of the intended intra-uterine sensing platform.

Chapter 3 describes the theories and core technologies of the wireless and batteryless *in-vivo* sensing platform, and presents the development of each component of the intended system, including miniaturised wireless and batteryless sensor device, wearable receiver and remote monitoring software.

Chapter 4 presents the theories and development of three different miniaturised, implantable biosensors for *in-vivo* temperature, DOC and pH measurement.

Chapter 5 describes the animal tests for the prototype system verification and evaluation on pig cadaver and rabbit.

Chapter 6 draws conclusion and makes recommendations for the future work.

1.4 Declaration

This thesis describes the research undertaken by the author while working within a collaborative research environment. This thesis reports the original work of the author except in the following sections:

1. The fabrication of microelectrodes and SU8 layer for the DO sensor and pH sensor were manufactured by Katie Chamberlain[1] and the fabrication of TMMF layer was manufactured by Shimul Saha[1] in the cleanroom, University of Southampton.
2. The animal tests were undertaken with the help from Aaron Southgate[2] at the Department of Surgical Research, NPIMR, including the surgeries for sensor device implantation and retrieval, and histology research after implantation tests.
3. The DO sensor was developed with the help and suggestions from Xi Huang[1], Martin Arundell[3], Gareth Lyle Jones[1], Sumit Kalsi[1] and Shimul Saha[1].
4. The mechanical fabrication of the antenna winding machine and the machining of the enclosure of the all-function receiver were carried out by the mechanical workshop of the University of Southampton.
5. The glass tubes for the antenna protection were manufactured by the glass workshop of the University of Southampton.

---

[1] Centre of Hybrid Biodevices, Faculty of Physical Sciences and Engineering, University of Southampton, UK

[2] Department of Surgical Research, Northwick Park Institute for Medical Research (NPIMR)

[3] Faculty of Natural & Environmental Sciences, University of Southampton, UK

Chapter 2

Background of intra-uterine environment *in-vivo* sensing

In the field of human reproductive research, there is growing recognition of the need to better understand the intra-uterine environment [8-10]. However, the understanding of the physiological mechanisms underlying reproduction and even the normal variation of fundamental intra-uterine biophysical parameters remain limited. Available data on the biophysical characteristics of this compartment is hindered by a lack of reliable, relevant measurement tools. This chapter presents the rationale for the development of an *in-vivo* sensing platform to measure temperature, dissolved oxygen concentration (DOC) and pH in the uterus. State of the art technologies in development or already developed for other *in-vivo* sensing platform are introduced to illustrate how the design was informed.

2.1 Motivation behind intra-uterine environment sensing

2.1.1 Human infertility

In humans, 1 in 6 couples experience clinical subfertility (failure to conceive after 1 year of unprotected intercourse). Empirically, infertility investigations are usually initiated when there has been failure to conceive after two years of frequent unprotected intercourse during the reproductive period [11]. The key factors considered to contribute to human infertility are varied as shown in Figure 2.1. In about 30% of cases, infertility originates in the male partner and the main problem is low semen quality. In another 30% of cases, infertility is associated with the female partner, such as the problems of ovulation failure and blockage of the fallopian tubes. Moreover, human infertility may be caused by the combined problems of the male and female partners in around 10% of cases, and they may include immunological and genetic causes. Other factors are also suspected to contribute to infertility, include environmental factors and lifestyle. These factors collectively may cause

5% of infertile cases. Although some cases identified as having probable underlying causes, there are about 25% of cases no clear reason is identified [11, 12]. Cumulatively therefore, more than half cases of infertility can be attributed to issues affecting the female reproductive tract (about 55%).

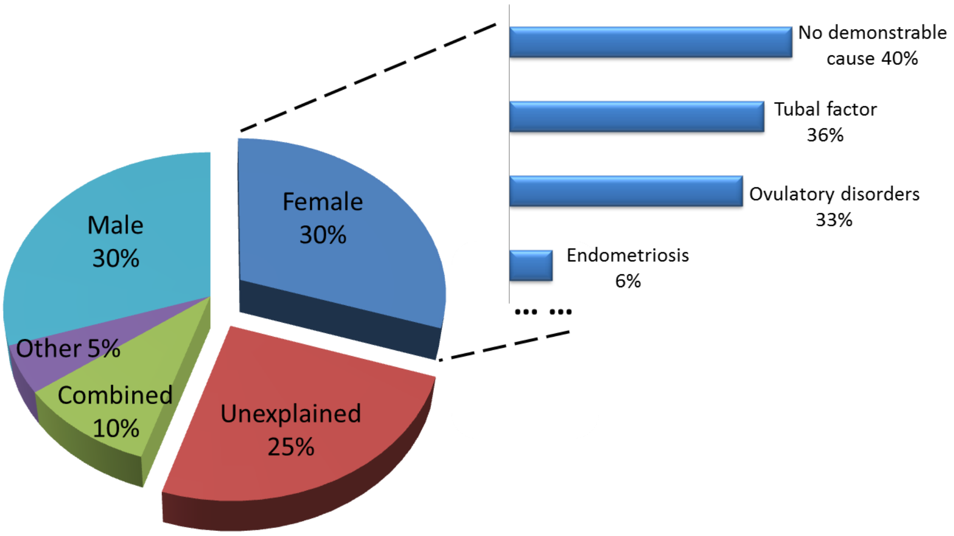

Figure 2.1 Causes of human infertility [11]. The causes of subfertility are from male partner (30%), female partner (30%), combined male and female (10%). Some other factors result in another 5% of infertile cases, such as environmental factors and life styles. In around 25% of cases no clear reason is identified. Female infertility of mixed aetiology accounts for over 55% of cases of infertility. Specific to female infertility, although tubal factor, ovulatory disorders and endometriosis have been reported as common causes of women reduced fertility, there are around 40% of cases which are associated with female partner no demonstrable cause is confirmed [12, 13].

For the infertile cases associated with female partner, a World Health Organisation (WHO) task force reported that the main causes included tubal factor, ovulatory disorders and endometriosis [12, 13]. Around 36%, 33% and 6% of infertile women are diagnosed as being affected by those pathologies respectively. However, there are about 40% of infertile women no demonstrable cause is confirmed. Specifically, research into female infertility [12, 14] has identified the following factors.

Firstly, ovulatory disorders may contribute to the abnormal ovulation which results in reduced fertility, such as oligo-ovulation or anovulation. Human ovulation occurs around the middle of menstrual cycle and is controlled by hypothalamic regulation of hormones secretion, such as luteinising hormone (LH) and follicle stimulating hormone (FSH) as shown in Figure 2.2. Eggs may not develop or be released properly if menstrual cycles and hormone secretion are irregular. For example, in polycystic ovarian syndrome, a typical cause of anovulation, eggs developed partially in the ovary. Hypothalamic anovulation is probably caused by abnormal releasing of gonadotropin releasing hormone (GnRH). However, the precise causes and quantitative analysis of polycystic ovarian syndrome and hypothalamic anovulation remain unknown. Menstrual evaluation is usually achieved by hormone measurements and ultrasonography which are both labour-intensive and inconvenient for continuous monitoring during menstrual cycle. The knowledge gained from conventional technologies for investigating the normal and abnormal menstrual cycle is limited and the detailed mechanisms of hormone control are not clear. Data collected in snapshots makes it hard to ascertain the normal and abnormal menstrual pattern and physiological mechanisms of ovulatory disorders.

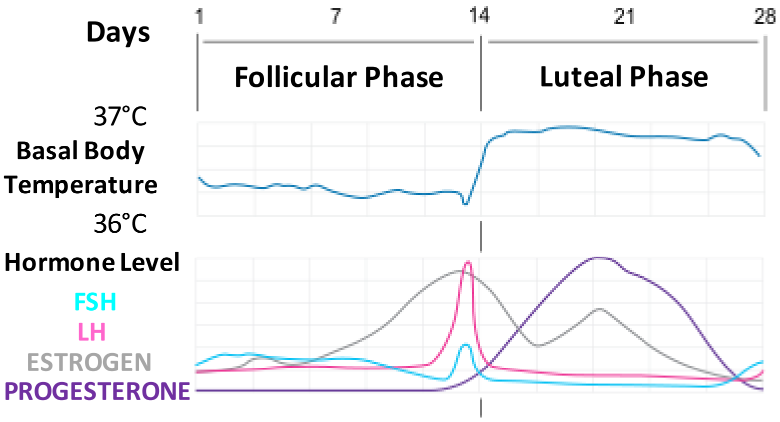

Figure 2.2 Diagram of the hormone level and basal body temperature changing over a menstrual cycle [15].

Secondly, infertility due to tubal pathologies is common. Total or partial obstruction of the fallopian tubes impedes the contact of the sperm and ovum, and reduces the opportunity of fertilization. Bilateral tubal occlusion, pelvic adhesions and acquired tubal abnormality are typical syndromes of tubal infertility which have proportions about 11%, 13% and 12% of female infertile cases [13]. Pelvic inflammatory disease (PID) is the main cause of tubal infertility and the risk of subsequent tubal infertility increases by at least 10% after each episode of infection [12].

Thirdly, endometriosis is often seen in women experiencing infertility and around 6% of infertile cases are attributed to endometriosis [13]. Endometriosis is a gynaecological condition in which the endometrial tissues are found outside the uterine cavity, in sites including the pelvic cavity, ovaries, fallopian tube, bladder, vagina and rectum. Endometriosis may compromise fertility by causing pelvic adhesions, distorted anatomy, tubal obstruction and ovulatory disorders. However the aetiology of endometriosis is still not well understood and the association between endometriosis and infertility remains unclear. Different theories have been presented to explain the cause of endometriosis, the most common theory being that it arises through retrograde menstruation. This infers that endometrial debris associated with menstruation flow backward through the fallopian tubes and attach to other sites, instead of being ejected from the body during a menstrual cycle.

The endometrial tissues embedded outside the uterus are under the influenced of hormones in a similar way to the uterus. This may result in the endometrial tissues appearing and flourishing outside the uterus. However, the precise mechanisms of ectopic endometrial tissues are more complicated and involve the processes of attachment, invasion into the mesothelium, and survival and proliferation during menstrual cycle. The pathophysiology of endometriosis is likely to be multifactorial and involve interplay between different factors, such as abnormal immune response and genetic predisposition. This makes the study of endometriosis and how it impacts on fertility complicated, and it remains poorly understood.

Implantation failure and miscarriage are amongst the most common complications of human reproduction. Implantation is a complex biological process during while the embryo attaches to the endometrium of the uterus. The interaction between embryo and the endometrium are highly orchestrated. In human pregnancy loss, an estimated 30% of cases fail prior to implantation (pre-implantation loss) and another 30% fail before 6 weeks gestation (early pregnancy loss) [16]. Little is known about the cause of implantation failure. The empirical understanding is that the insufficient secretion of progesterone makes the endometrium unreceptive to the embryo. Therefore, either implantation failure or early pregnancy loss happens due to the mismatch between endometrium and embryo. However, the factors which contribute to the endometrium receptivity and the mechanisms involved are still far from being fully understood. Miscarriage is the spontaneous pregnancy loss prior to the fetal viability. Recurrent miscarriage affects about 1-3% of couples [16] and is associated with chromosome abnormalities, anti-phospholipid antibodies and uterine cavity abnormalities. Although it is tempting to link the recurrent miscarriage to infertility, the principle of miscarriage and how the uterine cavity abnormalities precisely contribute to miscarriage are not clear.

Furthermore, Chromosome abnormalities may cause infertility in both men and women, although they are most common among men. Chromosomal abnormalities may cause congenital defects of reproductive system and result in infertility. For example, women with Turner’s syndrome (45XO) often have under developed ovaries.

Although decades of research work have been undertaken in infertility research, there is a significant knowledge gap in the understanding of human implantation and uterine receptivity contributed in part by the lack of a clinically relevant monitoring tool for interrogating human fertility in health and disease. In particular, what happens within the uterine cavity where the embryo implants remains a ‘black box’.

2.1.2 Approaches to explore the receptivity of uterus

The uterus is the site of embryo implantation, placentation, fetal growth and development prior to birth. The endometrium, the innermost layer of uterus, provides support to enable embryo implantation and further fetal growth and maturation [9]. The endometrium undergoes cyclical changes including endometrial functional layer growth, differentiation, desquamation and regeneration, and endometrial receptivity also alters during the menstrual cycle. The ‘window of implantation’ is known as a spatially and temporally restricted period when the endometrium becomes receptive to the embryo [7]. Limited knowledge is known about the characteristics of endometrial function variation and the mechanisms underlying the endometrial receptivity and which factors determine the ‘window of implantation’. Abnormalities of the endometrium may cause reproductive complications leading to pregnancy failure and infertility. Implantation failure and miscarriage are commonly caused by the aberrant interaction of embryo-endometrium interface. The receptivity of uterus is determined by the condition of endometrium. Therefore, research into the complex mechanisms controlling cyclical endometrial changes is crucial to not only better understand the ‘window of implantation’, but also to identify targets for treatments of reproductive complications. Advanced knowledge of endometrium will contribute to the improvement of human reproductive success.

Evaluation of endometrium health

Currently, ‘Omics’ high-throughput analyses are widely applied in human endometrial studies, including genomics, epigenomics, transcriptomics, proteomics and metabolomics [9]. However, the understanding of the complex endometrial physiology, endometrial disorders and fertility complications remains incomplete, inconsistent and with limited practical value. For instance, ‘Omics’ technologies require high-quality samples which are obtained by various steps of collection and storage. Inconsistent results may be caused by varying quality of sampling and it is unable to achieve real-time long-term continuous monitoring. Currently no clinical means of assessing endometrial receptivity exists, and only surrogate markers such as endometrial thickness or subendothelial blood flow can be measured using current clinical tools. They both have very poor sensitivity and specificity except when extreme abnormalities are identified [17]. The conventional approaches to evaluate endometrium clinically include performing an endometrial biopsy dilatation and curettage, Pipelle biopsy, hysteroscopy and transvaginal ultrasonography [17-19] as shown in Figure 2.3. Despite advantages of these approaches to obtain samples in the uterus directly and achieve visualization, they have complex protocols and the results from these approaches are always segmentary, fuzzy and limited.

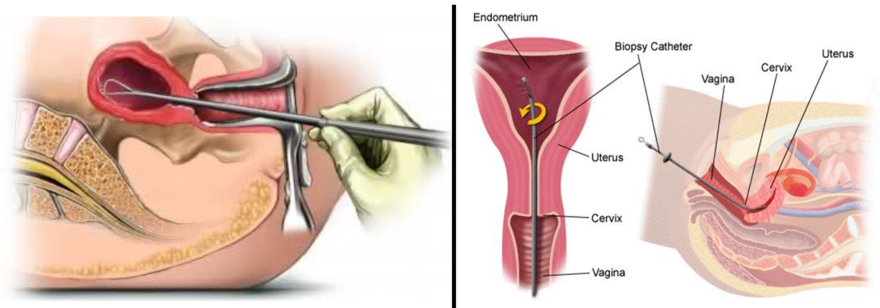

(a) Dilatation & curettage

(b) Pipelle biopsy

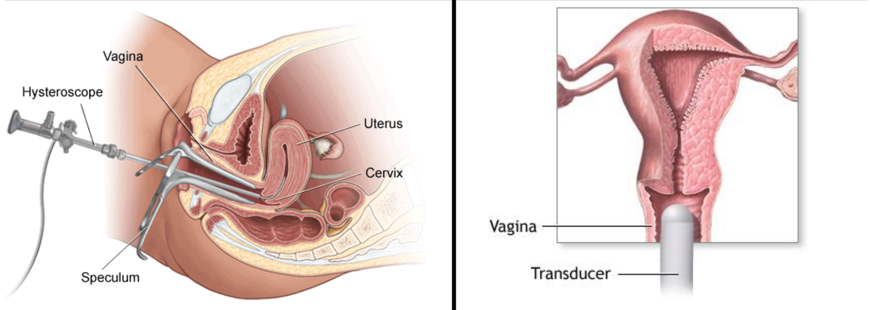

(c) Hysteroscopy

(d) Transvaginal ultrasonography

Figure 2.3 Conventional approaches for endometrium evaluation, including (a) dilatation and curettage; (b) Pipelle biopsy; (c) hysteroscopy; (d) transvaginal ultrasonography. Figures are taken from [18, 20].

The biophysical characters of intra-uterine environment are potential markers to ascertain the endometrium receptivity and for more precise monitoring, such as temperature, dissolved oxygen concentration and pH [3]. The measurements of these biophysical parameters are relatively simpler than the above approaches and can probably achieve long-term continuous monitoring. However, very little is known about the biophysical characteristics of the environment in the uterine cavity, such as the normal range of biophysical parameters and how they alter through the menstrual cycle. There is a clear need for a new means of evaluation of endometrial receptivity by interrogating a number of intra-uterine biophysical parameters.

Evaluation of intra-uterine environment

Research from multiple groups has demonstrated that the environment within the uterine cavity not only affects the chance of implantation, but also the developmental health of the early embryo, and the resulting offspring [7, 21]. An appropriate intra-uterine environment is controlled by oestrogen and progesterone secretion for embryo implantation. The typical hormone and basal body temperature periodically alter throughout the menstrual cycle as shown in Figure 2.2. The intra-uterine temperature abnormalities may result in pregnancy failure. For example, the temperature fluctuation at the early cleavage stages has been also demonstrated that it may decrease the subsequent development potential of embryos *in-vitro*. Human oocytes were reported with induced damage to the meiotic spindle after exposure to room temperature. Moreover, oxygen levels appear to be important in embryo culture and low oxygen environment around 5-8% recently having been shown to be optimal for in-vitro culture. Similar to acid-base balance, it had been shown that a transient exposure of zygotes and 2-cell mouse embryos to medium with elevated pH significantly reduced subsequent development to the blastocyst stage [22].

Although the intra-uterine environment has been believed to be crucial for human fertility, knowledge of the characteristics of the environment in uterus is limited. There is also a knowledge gap on endometrial abnormalities associated with implantation failure and human infertility. These reveal the difficulties to interrogate the environment in uterus and a lack of appropriate instrument to measure intra-uterine biophysical parameters. Without better and more efficient technologies, the approaches and treatments proposed to improve uterus receptivity have been persistently used for more than 60 years which is due to their empirical and clinically ineffective nature.

2.1.3 Causes of limited success rate of pregnancy under artificial reproductive technologies

For those who suffer from subfertility can in part be resolved by applying artificial reproductive technologies (ART). Typical techniques of ART include *in-vitro* fertilization (IVF), intra-cytoplasmic sperm injection (ICSI), gamete intra-fallopian transfer (GIFT) and artificial insemination (AI). For example, egg donation and IVF can be applied to achieve pregnancy for women with chromosome abnormal problems and ovulatory disorders. IVF or GIFT can be used to help couples who experienced tubal infertility to successful pregnancy. Generally, the number of IVF treatment cycles worldwide has reached approximate 1.5m per annum and this number is thought to be growing annually at the rate of between 7-10%. The average all-up cost per treatment cycle is £5,000 (including drugs) per patient [23-25]. Despite major advances in embryo culture and selection, take home baby rates after ART are still limited and have altered little in the last 5-10 years. Specifically, success rates of IVF treatment were lower than 35% and have altered less than 3% from 2006 to 2010. More details of success rates at different ages are shown in Figure 2.4.

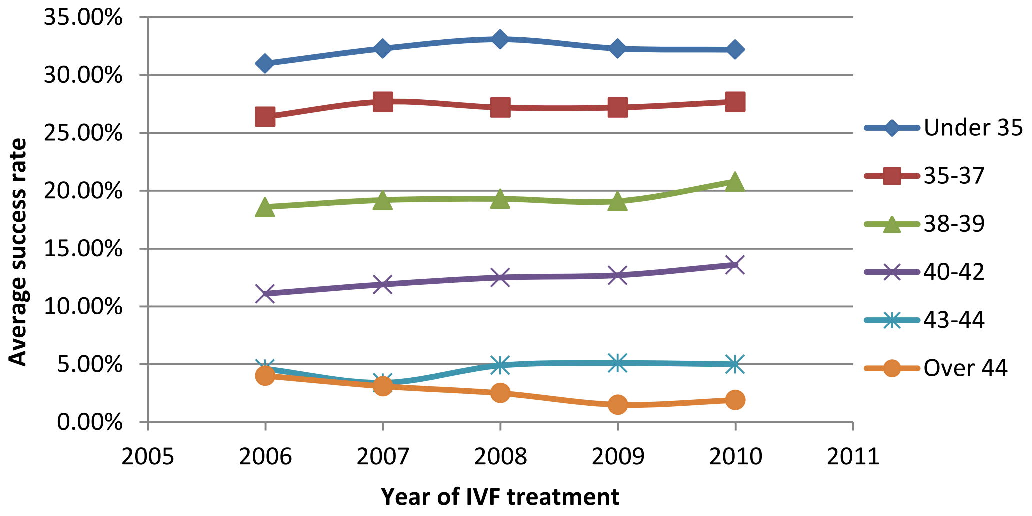

Figure 2.4 The average success rate of IVF treatment using own fresh eggs in the UK from 2006 to 2010 [26-28]. The success rate is depends on the age of the women undertaking treatment. Younger women have relatively higher success rate. Success rate altered less than 3% from 2006 to 2010.

The limited success of IVF may be caused from many aspects. One of the causes is inefficient *in-vitro* embryo development. The success of embryo development is not only dependent upon the composition of the culture medium but also affected by physical parameters of incubation environment, such as temperature, oxygen level and pH [21, 29-33]. Minimizing environment stress maintains cellular homeostasis which is a crucial component to optimise embryo development and resulting IVF success. Current culturing protocols are based on a very limited knowledge of the changes and fluxes within the normal uterine environment. The recommended settings for the embryo *in-vitro* culture system are very empirical and less detailed, and the optimal embryo culture procedure is hard to achieve [21, 34]. For example, human embryo is suggested to be cultured in a low oxygen environment (5-8%), and it is advisable to maintain a constant temperature of 37°C during all stages of culture. A pH, range of 7.2-7.4 is applicable. It is not possible precisely to determine the culture environment of human embryos without fully understanding the *in-vivo* embryo culture environment.

Another reason for limited IVF success rate may come from the prediction about the developmental potential of pre-implantation embryos and selection of embryos to be transferred. It is clinically carried out by pronuclear and embryo morphology evaluation. The results from observation are highly empirical and limited in efficiency. A possibility for more accurate prediction may be from the quantitative analysis of biophysical parameters. If the normal and abnormal biophysical characteristics during embryo development are identified, embryo evaluation and selection can be carried out more precisely by measuring the biophysical parameters.

Furthermore, embryo transfer is the final but crucial step in IVF. Before embryo transfer, 80% of cases can progress successfully in various steps, but only around 25% of transferred embryos will successfully implant [21, 35]. Besides poor embryo transfer technique, the reduced receptivity of human endometrium is another main cause of embryo transfer failures which is similar to the complications of implantation failure and miscarriage. Although, uterine receptivity is believed as crucial to determine the outcome of IVF treatment, there remains a significant knowledge gap about the mechanisms of receptivity changing and markers to evaluate the receptivity. Therefore, it provides huge scope for investigating intra-uterine environment that may characterise uterine receptivity and can be monitored as a marker of receptivity changing.

Considering the unsatisfactory IVF success rate and little alteration in the last 5-10 years, this may not only reflect the lack of better understanding of uterine receptivity, but also clinical approaches to collect critical data for further research. An unmet need can be seen to develop an investigative tool capable of characterising dynamic changes of intra-uterine biophysical parameters. If this clinical issue is to be addressed, a greater understanding of what constitutes the receptive endometrium can be achieved and IVF success rate can be possibly significantly improved. My project involves developing a novel implantable *in-vivo* sensing platform with capability of evaluating the intra-uterine environment to meet above demand.

2.2 Key intra-uterine environment factors: temperature, pH & DOC

Previous work has been undertaken in both the pregnant and non-pregnant uterus to evaluate the uterine environment by means of uterine fluid, amniotic fluid or fetal blood sampling and using sensor probes [2-6]. The aim of these studies was to identify biophysical parameters that would reflect the change of intra-uterine environment and endometrium receptivity. Temperature, DOC and pH are three most concerned characters because they maintain a homeostatic controlled balance of gases and acid-base which is vital to human life and reproduction [3]. They are likely to determine the receptivity of the intra-uterine environment to the implanting embryo.

2.2.1 Intra-uterine temperature

Maternal temperature is one of the vital signs routinely measured, and cyclic changes on the basal body temperature throughout the menstrual cycle have been observed in previous studies [36, 37] as shown in Figure 2.2. Lower temperature values presented during the first half of the cycle (with low hormones level), and higher temperature occurred at the second half of the cycle when the hormones increased to a high level [36, 37]. The rectal temperature showed a 0.4°C increasing during the luteal phase of menstrual cycle compared with the follicular phase [38]. Moreover, core temperature is believed varied during labour, or even pregnancy. Elevated core temperature during labour is associated with high possibility of intra-uterine infection and increased risk of neonatal infection. The variations of core temperature during normal and abnormal labours were described in [39]. The mean temperature was measured rectally during labour. It was increased from 37.1°C at the beginning to 37.4°C after 22 hours. At the beginning of labour, temperature was comparable between normal and abnormal labours, but abnormal labour group demonstrated a faster increase of temperature than the normal group. Furthermore, the effect of temperature fluctuation on spindle integrity and chromosomal organisation in the human oocyte were investigated [40]. Exposure of oocytes to room temperature caused disruption of the spindle and chromosomal dispersal. These effects became irreversible after 10min exposure.

The measurement of core temperature is normally invasive and therefore not friendly to the patient (patient cannot move around without wires attached). The non-invasive techniques for temperature measurement, such as infrared, have to use snap shot method which difficult to achieve long-term monitoring. Compared with skin temperature and core temperature from other parts of the body, such as rectal temperature, oral temperature and tympanic temperature, intra-uterine temperature is less influenced by environmental conditions and presents temperature variation in the uterus more directly and accurately. In previous work, intra-uterine temperature was measured by a pressure-temperature catheter and the relationship among intra-uterine temperature, oral temperature and tympanic temperature were determined [41]. The normal mean intra-uterine temperature was 37.3 °C±0.4 °C in a range of 34.7 °C to 40.7 °C of 97 patients, and the oral and tympanic temperatures were 36.7 °C±0.5 °C and 36.8 °C±0.5 °C, respectively. Intra-uterine temperature was observed to be slightly above that of oral and tympanic temperatures. Therefore, temperature data captured in the uterus directly is necessary and important for intra-uterine environment evaluation. However, less available data of intra-uterine temperature were achieved for menstrual cycles, and the variation during whole menstrual cycle was still unclear.

2.2.2 Intra-uterine dissolved oxygen concentration (DOC)

Dissolved oxygen concentration is another key indicator for intra-uterine environment evaluation. Research into cell metabolism-related molecules is important for the characterisation of cellular activity, and gives a useful method to analyse the physiological responses of the cells to extrinsic chemical or physical stimuli. Among the metabolism-related processes commonly assessed, the change in the amount of dissolved oxygen consumed by the cells is an important index for cellular respiration activity [42]. Therefore, metabolism state of endometrium and embryo quality may be evaluated from the intra-uterine DOC changes [43]. In recent years it has become clear that *in-vitro* embryo development is highly sensitive to oxygen saturation levels [21, 44]. It has been observed that human blastocysts cultured in a low oxygen environment (5%) have significantly more cells than those cultured in a high oxygen environment (20%). The conventional method is measuring partial pressure of oxygen (PO_2) in the amniotic fluid. A mean value for PO_2 in amniotic fluid was reported as 11.0mmHg in early pregnancy and 7.00mmHg in late pregnancy[45]. Other previous works presented the mean values for PO_2 in late pregnancy changed between 8.8mmHg and 27.6mmHg [5].

Other work has been undertaken to understand the relationship between dissolved oxygen level in follicular fluid and developmental potential of the human oocyte [46]. Because of the difficulties of measuring follicular fluid DO directly and the lack of quantitative description of oxygen levels in the follicle, mathematical modelling was used to estimate the possible magnitude and variability. The model predictions introduced the mean dissolved oxygen level in human follicular fluid during the late antral and pre-ovulatory phases are from 11 to 51mmHg. It provided a reference value for the DO information in the uterus, although the mathematical predictions cannot meet the requirement of *in-vivo* knowledge. This again reflects the lack of clinically diagnostic approaches for intra-uterine environment monitoring.

2.2.3 Intra-uterine acid-base balance (pH)

PH is an important indicator to understand the acid-base balance of intra-uterine environment. The variation of pH, as well as temperature and DOC in the uterus, were established under the effects of the hormonal secretions associated with ovulation [3]. Moreover, pH was believed to have influences on sperm mobility which is crucial for fertilization. However, current knowledge of pH changes was mostly obtained from the amniotic fluid sampling [4-6]. The mean amniotic fluid pH was presented as 7.07±0.08 in [4]. The different pH values were reported between 7.10 and 7.23 in early and between 6.98 and 7.11 in late pregnancy[5]. Slight differences were observed between pH values in cervix and uterus. The mean pH values were 7.11 in cervix and 7.12 in the uterus [3].

2.2.4 Current knowledge about intra-uterine biophysical parameters

Table 2.1 Typical value of intra-uterine biophysical parameters and empirical settings for in-vitro embryo culture, including temperature, DOC and pH.

	Temperature	**DOC**	**pH**
Typical values and range for intra-uterine biophysical parameters	37.3 °C±0.4 °C[41] 37.1°C to 37.4°C during labour [39]	11~51mmHg [46] 11.0mmHg(early pregnancy) 7.00mmHg(late pregnancy) [45] 8.8~27.6mmHg (late pregnancy) [5]	7.12 [3] 7.07±0.08 [4] 7.10~7.23(early pregnancy) 6.98~7.11(late pregnancy) [5]
Empirical values for embryo culture [21, 34, 47]	37°C	5%-20% (low oxygen culture)	7.2-7.4 7.3-7.4 (fertilization) 7.2-7.3 (cleavage stage) 7.3-7.4 (Blastocyst)

The typical values of intra-uterine biophysical parameters and empirical settings for embryo culture system are listed in Table 2.1, including temperature, DOC and pH. These results were very rough, fragmentary and inconsistent. There is no systemic description about variations of these parameters during menstrual cycle. Neither the normal range nor abnormalities was identified. For the embryo *in-vitro* culture, the recommended settings are very empirical and lack of details. Therefore, there is still a strong demand for clinical diagnostic approaches to gain more detailed information about intra-uterine environment.

Furthermore, the majority of experienced data came from sampling measurements, such as amniotic fluid and follicular fluid. There may be errors in some parameters after sampling, such as temperature, pH and DOC due to the way in which the sample is handled. Specifically, when the fluid sample is taken out of uterus and enters the atmospheric environment, the dissolved oxygen concentration may differ from what it was at time of collection. A previous work has been undertaken on the effects of IVF aspiration on temperature, DO levels, and pH of follicular fluid [48]. The results showed the temperature of follicular fluid dropped by 7.7 °C ± 1.3 °C upon aspiration this was attributed to evaporation of fluid, DO levels rose by 5 ± 2 vol.%, and the pH increased by 0.04 ± 0.01 due to contact with air. Therefore, *in-vivo* data which measured in the uterus are required for more accurate evaluation of intra-uterine environment.

2.3 State of the art technologies for *in-vivo* sensing platform

2.3.1 Typical human implantable medical devices (IMDs)

To obtain the internal information about intra-uterine temperature, DOC and pH, an *in-vivo* sensing platform is needed. The implantable devices are conventional methods for long-term *in-vivo* measurement. So far, various commercial implantable medical devices (IMDs) are widely used to sustain human life or improve quality of life. Typical IMDs includes cochlear implant, cardiac defibrillator, pacemaker, insulin pump and some others as shown in Figure 2.5. Most of IMDs can detect human biophysical parameters and apply specific treatments for medical purpose. For example, the implantable cardiac defibrillator can constantly monitor the rate and rhythm of heart and correct cardiac arrhythmia by delivering electrical impulses. Cochlear implants convert environment sound to electric impulses to an array of electrodes which stimuli the nerves of auditory nerve system. Endoscopic capsule records internal images while it passes through digestive track. These typical implantable medical devices are designed for specific scenarios and cannot use in the uterus.

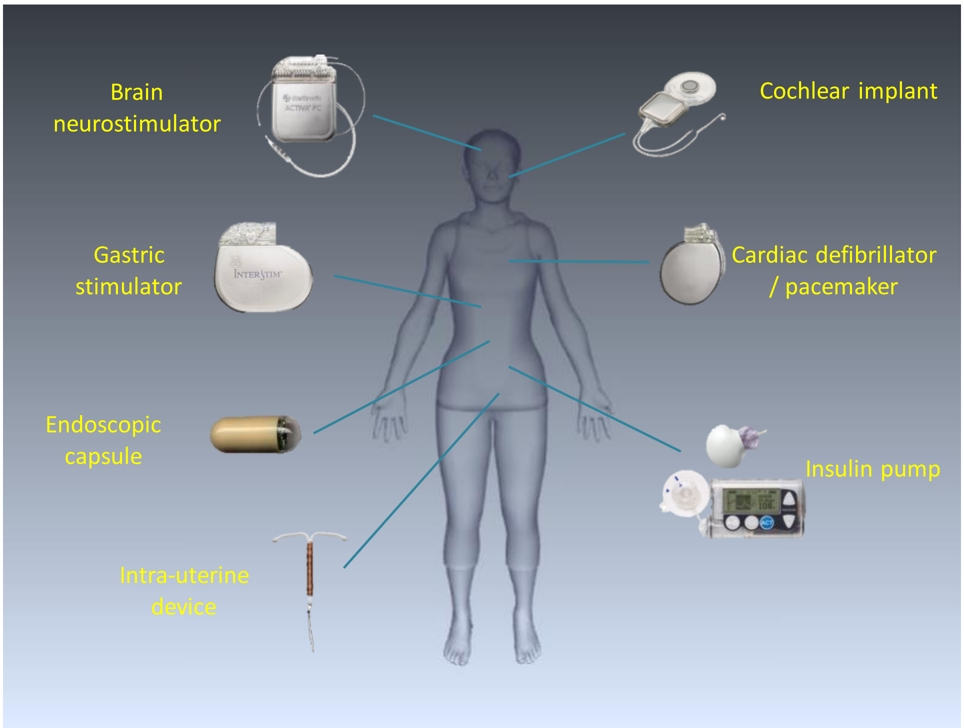

Figure 2.5 Typical implantable medical devices (IMDs) which are widely used on human to sustain human life or improve quality of life.

2.3.2 Typical intra-uterine devices (IUDs)

The most applied devices in the uterus are intra-uterine devices (IUDs) for contraception purpose. They are made of plastic containing either copper or levonorgestrel and work mainly by preventing sperm from surviving in your womb and reaching an egg. Some previous work has been undertaken to evaluate the influence of IUDs, including CuNovat, T380A, Nova T, on uterine artery blood flow [49-51]. From the results of pulsatility indices and resistive index by transvaginal colour Doppler, no significant differences were reported in the vessels sampled pre- and post-insertion inferring that the presence of an IUD does not interfere with the vascular resistance of the uterine arteries. However, there is no any electronic component in IUDs and they are not used for measurement purpose.

Another implantable device developed for intra-uterine application is in-utero culture system (IUCS) from Anecova [52, 53], as shown in Figure 2.6. It is designed to enable the fertilization and early embryo development to take place in the physiological environment of the maternal uterus instead of the laboratory incubator. This approach can eliminate the interferences from external culture environment and it keeps embryos in the original place for nutrients. Similarly, IUCS is not an electronic device and cannot obtain any information about intra-uterine environment.

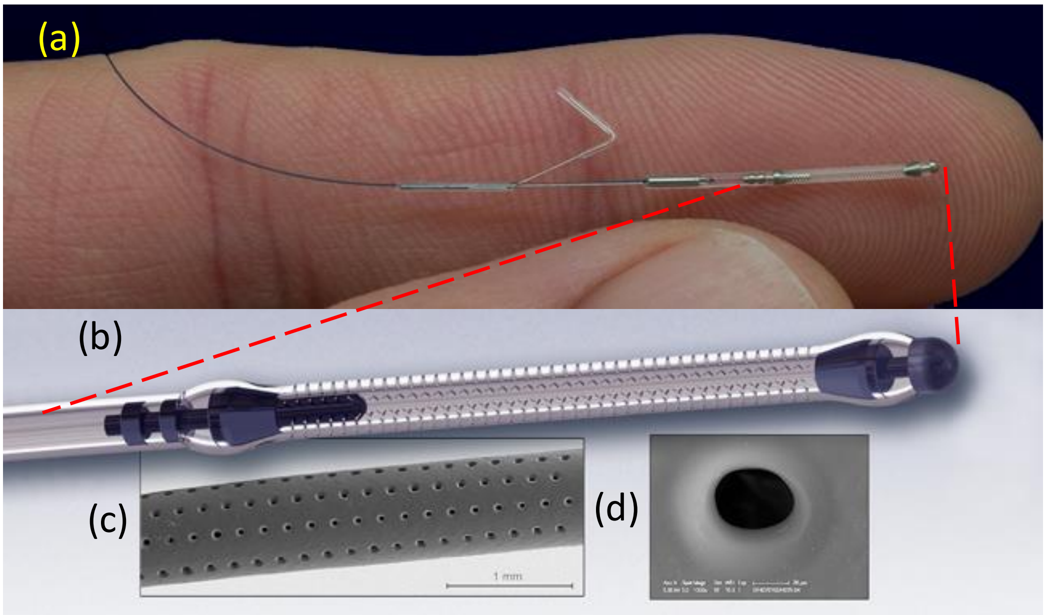

Figure 2.6 Diagram of Anecova device for in-utero culture: (a) size compared with human finger; (b) micro drilled silicon segment on the top of Anecova device; (c) scanning electron microscopy of the drilled silicon segment; (d) scanning electron microscopy of a laser-drilled hole [52, 53].

Some devices were developed for fertility information collection as shown in Figure 2.7. DuoFertility and OvuSense are two commercial devices available on the market for the fertility temperature measurement [54, 55]. They both have a wireless sensor and a receiver to record the temperature data. The sensor of DuoFertility sticks underneath human arm and continuously monitors the body temperature. It is not implantable and can't measure temperature in the uterus. OvuSense have a tampon shape sensor which can be inserted into vagina for internal temperature monitoring. However, similar to DuoFertility, it is also not fully implantable and its unfriendly user experience makes itself hard to achieve long-term monitoring. A pressure-temperature catheter was used to measure intra-uterine hydraulic pressure and temperature [41]. The sensor head on the catheter was connected to a monitor through a reusable connecting cable. A flexible and implantable sensor was developed for detecting deformation size and contraction frequency of human uterine musculature [56]. Three coils were embedded in an IUD frame and the deformation related coils inductance change can be used to evaluate the deformation of uterine cavity. This information was considered for the uterine contractility. Adequate uterine contractility is required to support gamete/embryo transportation through the fallopian tube and achieve embryo implantation successfully.

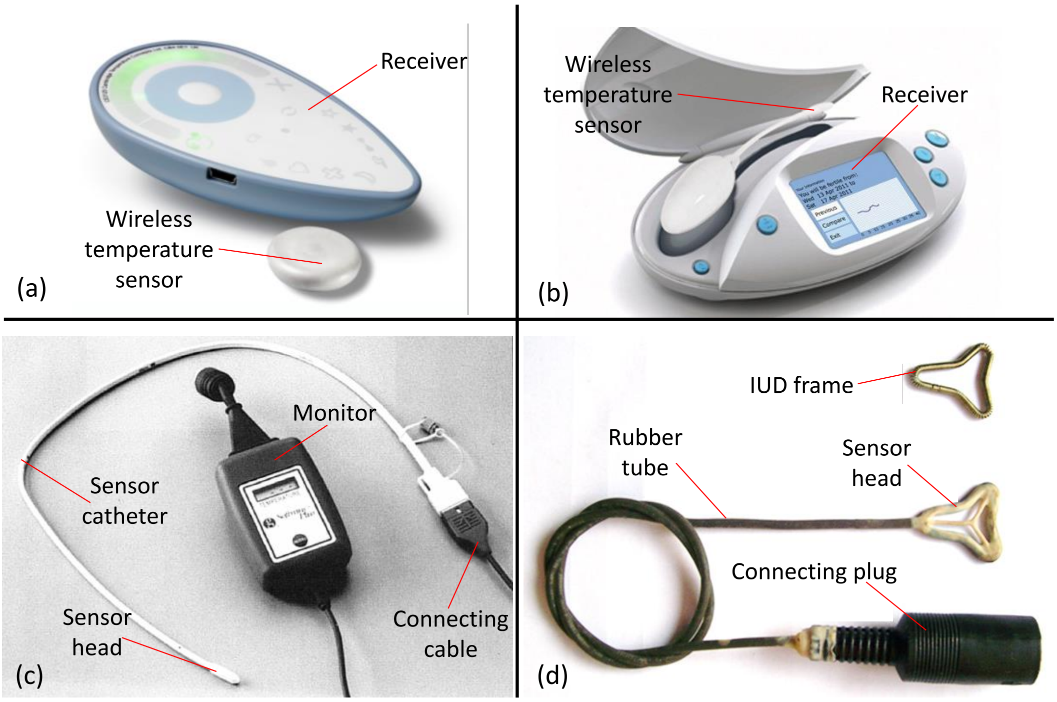

Figure 2.7 Examples of currently available devices for fertility information collection: (a) DuoFertility fertility temperature monitor has a wireless temperature sensor for body temperature sensing and a receiver [54]; (b) OvuSense fertility monitor includes a tampon shape wireless sensor and a receiver. It can measure the intra-vagina temperature [55]; (c) intra-uterine pressure-temperature catheter with pressure transducer and thermistor on the sensor head [41]; (d) sensor probe for detecting uterine musculature contraction. The sensing coils are fixed on the IUD frame and the outlet wires are wrapped in a soft rubber tube which is connected to a connecting plug [56].

These kinds of sensor probes had a sensor head which was connected to external monitor by cable. Although *in-vivo* sensing was achieved, their applicability was limited to short-term measurement due to the connecting cable and unsatisfactory size. Unfriendly user experience is another issue and interferences are unavoidable to user’s normal activities. Therefore, they are not suitable for our intended application of intra-uterine environment monitoring.

2.3.3 Typical endoscopic capsules

Some human IMDs should be considered as references of miniaturised wireless implantable devices for our intended *in-vivo* sensing platform. For instance, the endoscopic capsules were developed for gastrointestinal (GI) track monitoring and wireless capsule was designed for esophageal reflux testing.

Typical swallowable endoscopic capsule included M2A, Norika, SmartPill and a LIAP (Lab-in-a-pill) device. M2A was produced by the Given Imaging Ltd. to record internal images while traveling through the GI tract [57]. It was powered by embedded batteries and the data can be uploaded to an external wearable monitor. At the same time, the capsule’s position was determined by interrogating the wireless signal strength. Norika was developed by RF System Labs for endoscopy [58]. It consisted of a capsule, coil-embedded vest, external controller, and PC. The capsule didn’t include any battery and the energy was transferred from the vest wirelessly. In addition, Norika supported posture fine adjusting and two special tanks were added for drug release. SmartPill and LIAP device were both developed for the GI tract monitoring. Two micro-fabricated sensors were embedded on the LIAP device for temperature and pH [59]. SmartPill measured pH, pressure and temperature while transiting entire GI tract [60, 61]. Similar to M2A, they were powered by embedded batteries and can transmit data to an external receiver.

Bravo and BEST (Batteryless Endoluminal Sensing Telemeter) pH capsules can be implanted in the esophagus and the embedded pH sensors recorded internal pH change for the acidic esophageal reflux identifying. Bravo was powered by embedded battery and the recording time was up to 48 hours [62]. Beside pH, impedance was also measured by BEST for detecting of nonacidic reflux [63-65]. BEST was design as a batteryless device and wireless power supply was employed. The monitoring duration was no longer restricted by battery. The properties of these implantable capsules are shown in Table 2.2.

Table 2.2 Properties of different implantable capsules for human internal information sensing including M2A, Norika, SmartPill, LIAP device, Bravo and BEST [57-65].

	M2A	**Norika**	**SmartPill**	**LIAP**	**Bravo**	**BEST**
Dimensions	ϕ11mm X 26mm	ϕ 9mm X 23mm	Φ13mm X26mm	Φ12mm X36mm	26.7mmX6.3 mmX5.4mm	38mmX8mmX 4mm
Application	Endoscopy	Endoscopy	GI track monitoring	GI track monitoring	Esophageal reflux monitoring	Esophageal reflux monitoring
Sensors and accuracy	CMOS camera	CCD camera	Pressure (0-350mmHg), pH (1-9, ±0.5), temperature (20°C-40°C, ±1°C)	Temperature (0.25°C, resolution), pH (0.1, resolution)	pH (1-8)	impedance, pH
Implanted place	Travel through the GI track	Travel through the GI track	Travel through the GI track	Travel through the GI track	Esophagus	Esophagus
Power source	Battery	Wireless power supply	Battery	Battery	Battery	Wireless power supply
Life cycle	8 hours	Without limitation from battery	Several days transiting the GI track	<42 hours	48 hours	Without limitation from battery
Data link	Wireless	Wireless	Wireless	Wireless	Wireless	Wireless
Additional functions	Capsule position detection	Capsule posture adjusting	No	No	No	No
Shaded boxes describe features deemed to be critical for implantable devices.						

These capsules were all fully implantable and capable of *in-vivo* obtaining human internal information. Wireless communication technology made them get rid of connecting cables and real-time accessing was available. They minimised user’s discomfort during monitoring and most normal activities were unaffected. Battery was the conventional method for power supply and several days of recording time was achieved. However, their unsatisfactory size and battery required design limited their applicability to the intra-uterine scenario. For the implantation in the uterus, the intended device must meet the strict size limits. Compared with commercial intra-uterine devices (IUDs) widely used for contraception, above capsules were too big to be used in the uterus.

The designs based on battery have to face the limitation from battery size and lifetime. Besides, the potential risks from the toxic material of battery have to be considered. Although BEST didn’t need any battery and was relatively smaller than other devices, it was still at developing stage and no any human application was found. The electronics was special designed for impedance and pH measurement and data transmission based on relaxation oscillator circuits and load modulated technology. The analogue signal was transmitted by wireless link and its stability and anti-interference performance were very limited. Moreover, the device was hard to be optimised and upgraded due to its special designed circuits and lack of programmable components.

Although they cannot be used for intra-uterine environment sensing, the insights were provided on the structure design and encapsulation. As discussed above and in a survey of different wireless microsystems for biomedical capsule diagnosis [66], miniaturisation and encapsulation are required for medical devices development which to be fully implanted for *in-vivo* sensing. Wireless communication technologies are necessary for discarding of connecting cables. Especially, the digital wireless communication technologies are suggested because of its better stability and anti-interference performance. Wireless power supply, similar to Norika, is highly considered for a batteryless design to eliminate the risks and limitations from battery. Furthermore, various sub-system reference designs were discussed in [66], such as sensor front end, analogue-digital mixed circuit, power management unit and wireless communication solutions. Some of these technologies were widely used in various *in-vivo* sensing platforms.

2.3.4 Typical implantable devices for laboratory animal monitoring

Furthermore, some different types of implantable devices were developed as *in-vivo* sensing platforms for laboratory animal monitoring. They are very good references to this project and their technologies can be employed in the intended intra-uterine application.

KB1000 wireless rumen sensor (Kahne Ltd., New Zealand) is the best known and most widely used for continuous measuring rumen pH, temperature and pressure [67, 68]. The sensor was encapsulated in a winged capsule to enable a stable implantation position in the rumen. A 35-40 cm long nylon thread was attached for device collection. It used a battery and its weight was about 65-75g. This rumen sensor supports various livestock related researches, such as animal nutrition, animal health and behaviours. A commercial implantable programmable temperature transponder, IPTT-300, was developed to collect both identification and body temperature of laboratory animals [69]. Typical application was subcutaneous implantation of mice and rabbits, and the batteryless device needs a compatible reader for energy transfer and data collection wirelessly. Furthermore, two different versions of implantable blood pressure sensing platforms were developed successively [70, 71]. A miniature elastic cuff wrapped around a blood vessel and a flat sensing cuff were developed as blood pressure sensors to detect vessel expansion and contraction. To minimize device size, battery was not included and the device was powered wirelessly. CMOS IC was special designed for electronic circuits which decreased electronic components size to an area of 2.2mmX2.2mm. The properties of these *in-vivo* sensing platforms for laboratory animal monitoring are shown in Table 2.3.

Table 2.3 Properties of different *in-vivo* sensing platforms for laboratory animal monitoring [67-71].

	KB1000	**IPTT-300**	**Implantable blood pressure sensor**
Dimensions	Several centimetres	14mmX2mm	9mmX5mmX2mm
Application	Ruminal dynamics monitoring	Laboratory animal monitoring	Laboratory animal monitoring
Sensors and accuracy	pH (2-12,±0.02), temperature (-40°C -125°C, <0.8°C), Pressure (10-1100mbar, ±1.5mbar)	Temperature (32°C-43°C, ±0.5°C)	Blood pressure
Implanted place	Rumen	subcutaneous implantation	Attached on an aorta
Power source	Battery	Wireless power supply	Wireless power supply
Life cycle	Battery lifetime	Without limitation from battery	Without limitation from battery
Data link	Wireless	wireless	wireless
Additional functions	No	Animal identification	No
Shaded boxes describe features deemed to be critical for implantable devices			

These typical *in-vivo* sensing platform were all implantable and supported wireless communication. Wireless power supply solutions were more concerned, especially for small laboratory animals. Compared with KB1000, sizes of IPTT-300 and minimized blood pressure sensor were decreased a lot and they were available for mice subcutaneous implantation. However, the working distances were limited and their special designed circuits were hard to be upgraded and applied on other applications. The naked IC and MEMS structures enabled small size of implantable blood pressure sensor, but they required complex processes of fabrication, packaging and implantation. Nevertheless, their device structure and designs of wireless power supply and MEMS fabrication were very considerable for our intended intra-uterine *in-vivo* sensing platform.

2.4 Research targets and strategies

Based on the analysis about background of intra-uterine environment monitoring and state of the art technologies, an intra-uterine sensing platform is required for our intended application and five specific research targets and strategies are shown in Figure 2.8.

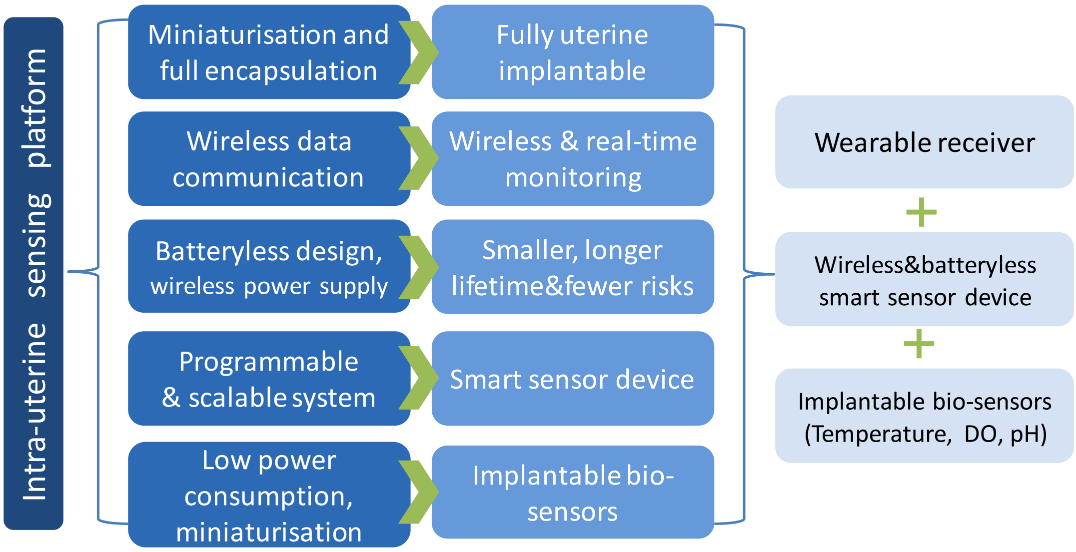

Figure 2.8 Research targets and strategies for the intended intra-uterine sensing platform. Five requirements should be considered for intended *in-vivo* sensing platform including miniaturisation and full encapsulation, wireless communication, batteryless design, system scalability and implantable biosensor development. Based on the analysis of background and current solutions, the intended *in-vivo* sensing platform for intra-uterine environment monitoring should include a wireless and batteryless sensor device, a wearable receiver and multiple biosensors for different parameters.

2.4.1 Miniaturisation and fully encapsulation of sensor device

Any device intended to be implanted in uterus must meet the strict size limits. The average dimensions of typical uterus are 87 mm x 50 mm x 41 mm overall, 73 mm x 43 mm x 32 mm for nulliparous women and 91 mm x 52 mm x 43 mm for multiparous women [72]. These assessments highlight the size constraints on a device intended for the use in uterus. Several commercial intra-uterine devices (IUDs) are manufactured for contraception and have used in humans for more than half century. They have achieved high rates of use with women with minimal discomfort or impact on daily quality of life [73]. Therefore, their dimensions guide the size of our intra-uterine sensor device. Simply, if our intended device is similar or smaller than these IUDs, it is likely to be suitable for the implantation in uterus.

IUDs for contraception come in various shapes, such as ‘T’ shape, double ‘S’ and anchor shape. Examples are shown in Figure 2.9, including TCu-380, Mirena, Lippes Loop and MLCu-250.

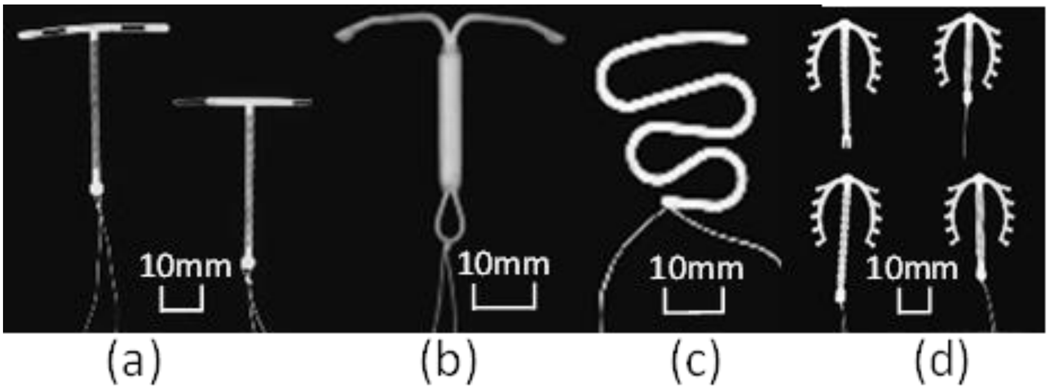

Figure 2.9 Examples of widely used intra-uterine devices for contraception:(a) TCu-380; (b) Mirena; (c) Lippes Loop; (d) MLCu-250.

These IUDs are all smaller than uterine cavity and their size are illustrated in Figure 2.10. Four widely used IUDs have similar dimensions. A much smaller device used for *in-utero* culture system (IUCS) from Anecova is shown in Figure 2.6. The device is a 1cm long micro-perforated hollow silicon elastomer tubing. Eight lines of 45 holes (ϕ 40μm) are designed to maintain embryos and allow exchange of nutrients, endometrial cells and other cellular and non-cellular components [52, 53]. The Anecova device is used for short time *in-utero* culture without any electronic component, its size is much smaller than the contraception devices. Considering the general contraception purpose IUDs are well accepted for intra-uterine application, therefore, the critical dimension of our intended implantable sensor device should not be greater than **36mm X 32mm**.

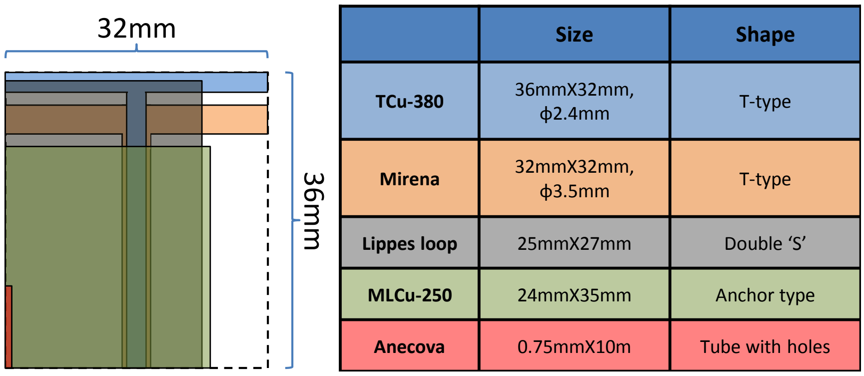

	Size	Shape
TCu-380	36mmX32mm, ϕ2.4mm	T-type
Mirena	32mmX32mm, ϕ3.5mm	T-type
Lippes loop	25mmX27mm	Double 'S'
MLCu-250	24mmX35mm	Anchor type
Anecova	0.75mmX10m	Tube with holes

Figure 2.10 Dimensions of the widely used IUDs including TCU-380, Mirena, Lippes loop, MLCu-250 and Anecova. Left coloured rectangles show the size comparison among this IUDs and their details can be found with same colour in right table.

Moreover, fully bench test, animal tests and human trials are all necessary and required for system verification and testing during the development. The intended sensor device should be robust and benign as possible to the environment when it is working. Obviously, encapsulation is required for both bench test and *in-vivo* tests. For example, some implantable devices used medical grade materials for structure and encapsulation to eliminate the potential risk from the electrical components [70, 71].

2.4.2 Wireless data communication

To obtain the internal information about intra-uterine temperature, DOC and pH, a fully implantable device is the optimal method for long-term *in-vivo* monitoring. Considering the requirement for fully implantation and friendly user experience, connecting cables for data communication cannot be used. Wireless data communication technology should be employed between the intended implantable device and external receiver for data collection. However, the limitations come from device size, energy and system functionality have to be concern during the system development. How to achieve a low power consumption, system scalability and circuit size balanced wireless data communication solution is a challenge.

2.4.3 Batteryless design

Considering limitations of battery size and lifetime, and the potential risks from battery's toxic materials, a batteryless design is highly recommended. Although a battery-based power supply is a conventional method for a portable device, currently the commercial batteries are still quite big compared with IUDs (the smallest commercial battery size is SR416, 4.8mm in diameter and 1.6mm in height). Moreover, batteries have limited lifetime and present some risks due to their toxic components. Therefore batteryless design is optimal and required for our intended intra-uterine sensing platform [74].

Wireless power supply technology is needed to get rid of the dependence of battery or power supply cable. Although there are some other source for energy harvest including solar, mechanical vibration and thermoelectrical energy, as discussed in [75] for self-powered strategies, they are all not suitable for implantable devices. Solar and thermoelectrical energy have very low efficiency due to the limited light intensity and temperature variation. Mechanical vibration needs complex structures to transfer to electoral energy which is unachievable to an implantable device. Therefore, wireless energy transfer technology is the optimal solution for our intended application.

2.4.4 Programmable and scalable system

As a multi-parameter *in-vivo* sensing platform which need support different types of biophysical sensors, flexible interfaces and system scalability are necessary. The use of microcontroller enables a programmable smart device with advantages on mixed signal processing, complex logical control, system development and future upgrade. The potential necessary interfaces and device components include multi-channel analogue and digital converter (ADC), general purpose input/output (GPIO) pins, serial communication units, RF unit and power management unit;

Due to the strict size limitation and limited energy supply, the sensor device development faces challenges from balancing the computing capability with sensor device size and power consumption. Some prototypes have powerful functionality but with an unacceptable size to our intended application. For example, a novel intra-body sensor has been developed to achieve continuous measurements of female intra-vaginal temperature [76, 77]. A temperature sensor and sensor device was embedded into a tampon-like container (60mm X 18mm) which can be used in the vagina, and the device supported wireless sensor networks based on ZigBee wireless communication protocol. A commercial device, OvuSense, is also available for the intra-vaginal temperature monitoring for the fertility purposes [78]. Although these devices can achieve *in-vivo* sensing and wireless communication, their sizes is too big for use in the uterus. Moreover, some another prototypes achieve a small size but they have to bear the limited functionality and less flexibility. BEST, A batteryless implantable sensor for oesophageal reflux monitoring, has a smaller size, 4mmX8mmX38mm [63, 64]. However this was specifically designed for pH and impedance measurement based on converting analogue signal to frequency shifts without any processing capacity and system scalability. Therefore, the intended intra-uterine sensor device is going to be a smart and scalable implantable device with reasonable size for intended intra-uterine application.

2.4.5 Miniaturisation and low power consumption of biosensors

As a part of sensor devices which will be implanted in the uterus, biosensors are required to be implantable which also should meet the strict size limitation and power consumption requirement.

The conventional sensor devices in clinical cannot applied for intra-uterine measurement due to their unsatisfactory size. The measurement based on sample collection cannot achieve real-time *in-vivo* sensing and the widely used sensor probes are too big to the intra-uterine application. For example, the probe of YSI ProODO handheld optical dissolved oxygen meter is 216mm x 83mm x 56mm [79] and the probe of HANNA INSTRUMENTS pH meter is 164mm x 76mm x 45mm [80]. Therefore miniaturisation of biosensors is required for our intended sensing platform. Moreover, because of the energy hunger situation of intra-uterine application, power consumption of biosensors becomes one of the most crucial properties which have to be considered. As mentioned in above sections, power cable or batteries are unavailable on the sensor device, energy has to be delivered by wireless link and stored on the board with limited size. Therefore, the energy can be used for measurement is very limited. Sensor device cannot afford too much energy for biosensors. It is a challenge to design biosensors with ultra-low power consumption and we have to consider this during whole system research and development.

2.4.6 Target specifications of intended multi-parameter *in-vivo* sensing platform

Once upper considerations are solved well, an intended miniaturised, wireless and batteryless *in-vivo* sensing platform for long-term real-time intra-uterine environment monitoring can be achieved. The expected properties are listed below and more details of system development will be discussed in the subsequent chapters.

Table 2.4 Target specifications of intended multi-parameter *in-vivo* sensing platform for intra-uterine environment monitoring

Multi-parameter *in-vivo* sensing platform	
Data link	Should support bidirectional wireless data communication
Portability	Sensor device should be fully implantable, receiver should be wearable
Working distance (between sensor device and receiver)	Depends on application scenarios, generally, should be no less than 10cm
Implantable sensor device	
Size	Size comparable to the commercial IUDs; Should be smaller than 36mm X 32mm
Weight	No clear reference. Should be light enough to stay in uterus
Shape	No specific requirement but should be similar to the IUDs
Power supply	Without power cable and battery
Power consumption	Should be optimised for batteryless design
Encapsulation	Need to be well packaged for lab testing, animal tests and human trial. The clinical requirements have to be considered
Waterproofness	Should be waterproof and can work in biological liquid environment for its lift time
Lifetime	Should be no less than one menstrual cycle (around 1 month)
Scalability	Should be programmable and scalable, support connectivity to multiple biosensors and easy to be upgraded

Wearable receiver	
Size	As a wearable device, receiver should be very portable and its size should be similar to commercial portable device, such as cell phone
Weight	Should be very portable and its weight should be similar to commercial portable device, such as cell phone
Power supply	Powered by rechargeable battery
Scalability	Should be programmable and scalable, easy to be upgraded
Biosensors	
Size	Should be compatible to the implantable sensor device
Power consumption	Should be optimised for batteryless design
Encapsulation	Need to be well packaged for continuously working in biological liquid environment for at least sensor device lifetime

Chapter 3

System design and development

In this chapter, a blueprint of intended multi-parameter *in-vivo* sensing platform for intra-uterine environment monitoring is introduced. This chapter introduces the design of the system structure, and core technologies employed for wireless energy transfer and data communication. Details of the implantable sensor device and wearable receiver development are discussed separately. A series of experiments for system performance evaluation are presented after the description of the monitoring software development.

3.1 Structure and core technologies of the sensing platform

3.1.1 Typical structure of sensing microsystems

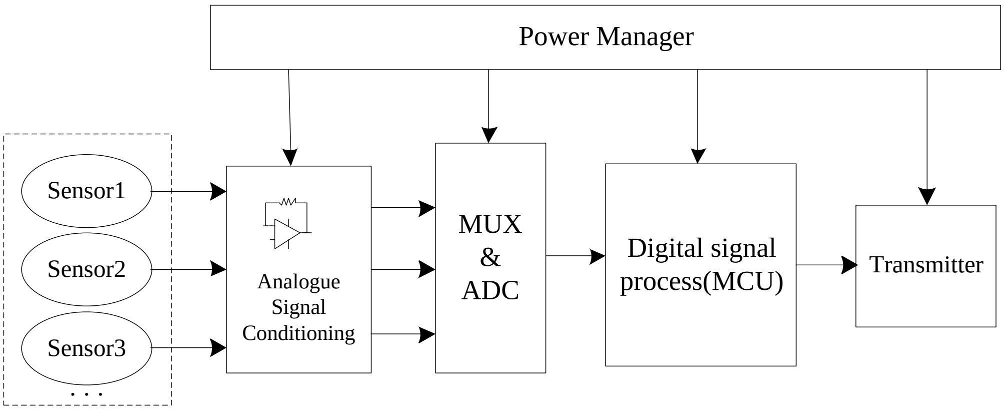

Figure 3.1 Block diagram of the typical microsystem structure. To achieves data capture, signal conditioning and processing, and wireless communication, a typical microsystem includes integrated sensors or a multi-sensor array, analogue signal conditioning circuit, analogue-digital converter (ADC) maybe including multiplexer (MUX), digital signal processor or micro-programmed control unit(MCU), wireless transmitter and power management units [81].

In line with the rationale for an *in-vivo* sensing platform outlined in chapter 2, there is considerable interest in the development of miniaturised, wireless and batteryless microsystems in biomedicine. Generally, microsystem technology is defined as an intelligent miniaturised system of sensing, processing and communicating components. A conventional microsystem includes an integrated sensor or multi-sensor array, analogue signal conditioning circuits, a digital signal processor or controller, a wireless transmitter and a power management unit for power consumption control, as illustrated in Figure 3.1 [66, 81].

Specifically, sensors convert physical parameters into electronic signals, and currently sensors can be fabricated on tiny silicon chips based on micro-fabrication technologies which are suitable for microsystems. Conditioning circuits are necessary within the system to improve the quality of the analogue signals from the sensors. Generally, high end conditioning performance requires more complex circuits. A simpler conditioning circuit results in limited performance that requires further data processing after analogue-digital conversion. Therefore, a balance between signal conditioning performance and circuit complexity has to be considered during system development. A multiplexer (MUX) may be employed for circuit hardware sharing, this has the advantage of reducing device size and power consumption. The processer undertakes logic control and digital signal processing. A micro-programmed control unit (MCU) is a widely used component for flexible functionality and good scalability. At the same time, compared with powerful processor, MCU enables power consumption to be minimized. The wireless transmitter and power manager are necessary for data transmission and power control. Integration of these units can facilitate device miniaturisation. For example, application-specific integrated circuits (ASIC) and one-chip solutions are already widely used for system integration.

In an *in-vivo* sensing system, there is a need to construct a system where the size, energy usage, encapsulation and cable usage are carefully considered. An optimal solution is a minimized implantable device able to achieve the required outcomes from the intended implantation site. For example, the Paratrend7 sensor (Diametrics Medical Inc., St Paul, MN, USA) is a monitoring system for *in-vivo* measurement of pH, oxygen partial pressure, carbon dioxide partial pressure and other parameters [2, 82]. A multi-sensor embedded sensing head is connected to a monitor by cable and the sensing head can be delivered to the measurement site for date collection. However, the usage of a cable immediately restricts the user experience and limits the opportunity for long-term measurements. Some fully implantable devices have been proposed, such as endoscopic capsule and endoluminal monitor which were discussed in section 2.3.3, and wireless technologies achieve data communication simultaneously. Most of them are powered by battery, but the battery size and limited lifetime has to be considered. Wireless energy transfer into devices offers a fundamental solution. A prototype of implantable spinal cord stimulation (SCS) system has been developed [83, 84] to treat chronic neuropathic pain. The SCS device was designed to generate electrical pulses to stimulate the somatosensory nerve fibres via a stimulating electrode array. It had a battery and in order to extend the battery's lifetime, a wireless energy transfer technology was employed to provide power to an internal battery after implantation surgery. The same inductive link in this system based on ASK-LSK (Amplitude Shift Keying-Load Shift Keying) was used for energy transfer and data transmission. This use of circuit sharing can effectively reduce the requirements on device size and power consumption, critical to implantable device design.

Consideration of the specific limitations of data capture from the intra-uterine environment and upper discussion on *in-vivo* sensing system design, it can be confirmed that a fully implantable device should support wireless energy transfer and wireless data communication. A three-module structured *in-vivo* sensing platform was proposed for the final application and the blueprint is shown in Figure 3.2. The first module is smart sensor which is a fully implantable sensor device embedded with multiple bio-physical sensors. The intention is a sensor device of comparable size to the widely used IUDs for contraception and it employs wireless energy transfer and wireless data communication technologies, dispensing with the need for a battery and cables. The wearable receiver is the second module as a medium between the sensor device and data analyser. It delivers energy to the sensor device and collects real-time information. The software module consists of a set of monitoring software running on a PC or smart terminal which is designed to be a friendly user interface for data processing and system configuration.

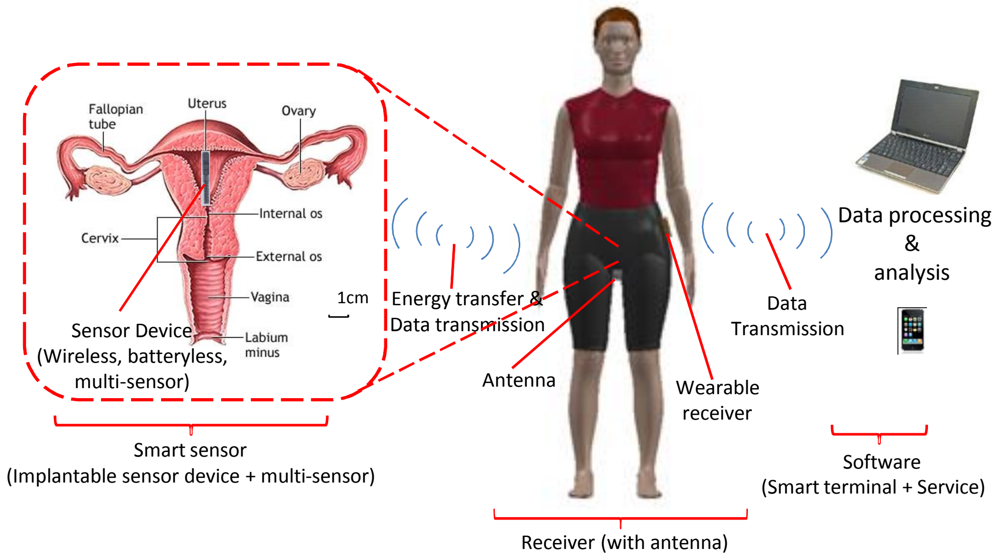

Figure 3.2 Blueprint of three-module structured multi-parameter *in-vivo* sensing platform for intended intra-uterine environment monitoring, including smart sensor, wearable receiver and monitoring software. Smart sensor module includes a fully implantable sensor device incorporating multiple embedded biosensors (intended for temperature, DOC and pH). It has a capacity for wireless power and wireless data transmission from a wearable receiver outside the body. Receiver works as medium between the implantable sensor device and software. The antenna of the receiver can be embedded into clothing and wired to the receiver. Software module is developed for *in-vivo* data uploading simultaneously to smart terminals or PC servers for post data processing and analysis.

In this three-module structured system, wireless energy transfer and data communication are two core technologies of system development. Their performance directly affects the usability of the intended system. An optimal design will not only result in better performance, smaller size, low power consumption and lower cost, but also improve end-user experience. These two core technologies will be described and discussed in the subsequent sections.

3.1.2 Development of the wireless energy transfer components

3.1.2.1 Background of technologies for wireless energy transfer

Review of wireless energy transfer technologies

Wireless energy transfer is the transmission of electrical energy from a power source to one or more electrical loads without artificial interconnecting conductors. It is ideal for applications where wired interconnections or batteries need to be avoided due to inconvenience, hazard or impracticality. For our intended application, the sensor device supporting wireless energy transfer enables facilitate implantation and eliminate the limited lifetime issue and potential toxic risks associated with batteries. Typically, electromagnetic induction and electromagnetic radiation are the most common forms of wireless power transmission [85].

Electromagnetic induction wireless transmission technology is used for near field energy transfer through the use of two coupled coils, primary and secondary coils. The electric current flowing through the primary coil creates a magnetic field that acts on the secondary coil producing an induced current within it. Tight coupling is needed for high energy harvest efficiency and long working distance. Increasing the distance between the coils results in the magnetic field extending beyond the secondary coil receiving area and leads to a loss of transmitted energy. A common use of electromagnetic induction is charging the batteries of portable devices, such as cell phones, electric toothbrushes, medical implants and electric vehicles. It is also used to power devices built without battery, such as RFID and contactless smartcards. Currently, the global standard for wireless energy transfer technology is not established, Qi and A4WP are two most possible candidates which are both based on the electromagnetic induction[86, 87]. Conversely, electromagnetic radiation is used in the far field scenarios. Power transmission via microwaves can be made more directional, allowing longer distance power beaming, with shorter wavelengths of electromagnetic radiation, typically in the microwave range. Application examples include power supply for long distance communication routers and spacecraft leaving orbit. It is ideal for high frequency, high power and long distance power supply. Compared with electromagnetic radiation, electromagnetic induction is more suitable for small size, low frequency, low power and near distance applications. A comparison of these typical wireless energy transfer technologies can be seen from Table 3.1.

Table 3.1 Comparison of electromagnetic induction and electromagnetic radiation wireless energy transfer technologies.

	Electromagnetic induction	**Electromagnetic radiation**
Energy form	Electromagnetic field	Microwaves or lasers
Working distance	Near field, less than meters	Far field, often multiple kilometre range
Signal frequency	Relatively low, MHz/KHz	High, >GHz
Typical application	Mobile phone battery charger, RFID	Spacecraft, long distance router
Advantage	Simple circuit, small size	Long range
Disadvantage	Short range, low power output	High power consumption, large size, directivity

Specific to our intended application, implantable sensor device requires small size, low power consumption and relatively short working distance, around 10cms. Obviously, electromagnetic induction technology is deemed more suitable. Moreover, energy loss due to tissue absorption of the wireless signals (the electromagnetic energy is transformed to other forms of energy by matter within the medium of tissues, for example, to heat) is dependent on the signal frequency. Signal at lower frequency has better propagation characteristics and results less tissue absorption. Therefore, the wireless energy transfer technology based on electromagnetic induction at low frequency is employed for our implantable sensor device.

Review of some wireless powered devices in literatures

An integrated platform was developed for energy and data transmission to a fully implantable medical device [88]. This design was based on inductive link and planar coils were fabricated for the inductive coupling. A maximum data rate of 180Kbps was achieved by using a 2MHz carrier and Hamming encoding was used to enhance data integrity. It also implemented an efficient Li-Ion battery charging circuit to achieve fast charge time and maintain battery health, including constant current charging and constant voltage charging.

However, the planar coils required large size and limited the working distance, and this platform was designed and optimised for the application with embedded battery which is not appropriate to our intended intra-uterine application.

A deep-seated implantable ultrasonic pulser-receiver was developed for size detection of thrombosis and renal artery after renal transplantation [89]. It was designed to be powered wirelessly by electromagnetic induction. A 30cm primary coil was wrapped around the body and was driven at a frequency of 5.7MHz to generate the magnetic field. A 2cm secondary coil was used on the implantable device which was positioned at the centre of the primary coil. Although the prototype demonstrated a wireless and batteryless device, it was hard to use in real situations. Its size was quite big, the circuit board of the implantable device was around 3cmX3.8cm, and the wireless energy transfer working distance was very limited, and was no more than 5cm.

A batteryless endoluminal sensing telemeter (BEST) was designed for esophageal reflux monitoring [63-65]. This implantable dual-sensor device can be used to measure pH and impedance for the diagnosis and monitoring of gastroesophageal reflux disease (GERD). It was wirelessly powered by an external device through electromagnetic field. The prototype device was 0.4cmX0.8cmX3.8 cm and the secondary coil was fixed around the circuit board. The resonant frequency was 1.3MHz to reduce absorption by tissue. The primary coil was 12cmX12cm, connected to the external device. The pH and impedance values were converted to frequencies loaded into carrier signal by relaxation oscillators and sent back to the external device. BEST achieved a prototype of implantable device without battery, however, it was still quite big and at the development stage, no human application has been found. The working distance was around 8cm which is deemed not suitable for our intended application. Although the authors considered tissue absorption and adopted a relatively low frequency carrier signal, there is still the possibility of employing a lower frequency signal to restrain tissue absorption and optimise wireless performance.

In order to achieve stable, sufficient energy delivery and decrease the influence of the capsule endoscopes orientation and position, a high efficiency wireless power transmission system was presented in [90]. It was based on electromagnetic induction, and consisted of a Helmholtz primary coil outside and multiple secondary coils inside the body (3 coils wound on a common ferrite core oriented toward different directions). The Helmholtz coil generated a uniform alternating magnetic field covering the whole of the GI tract, and the multiple secondary coils received energy regardless of the device’s position and orientation. However, this type of primary coil was too big and its power consumption was quite high that cannot meet our intended intra-uterine application requirements.

3.1.2.2 Circuit design for wireless energy transfer

As discussed above, the wireless energy transfer based on electromagnetic induction at low frequency was chosen for our system. The development of wireless energy transfer technology includes two coupled coils (primary and secondary coils) and their driving circuits. Overlaid on our system blueprint, the primary coil is the wearable receiver antenna. This is designed to emit the wireless signal. The secondary coil is the implantable sensor device antenna which will harvest energy to power the sensor device. Electric circuits are dedicated to drive both antennas. To accelerate the system development and achieve device miniaturisation, two passive low frequency interface (PaLFI) integrated circuits (ICs) were adopted which support energy transfer through generation of an electromagnetic field at a very low frequency (134.2 KHz). A diagram of the configuration of the wireless energy transfer circuit can be seen in Figure 3.3.

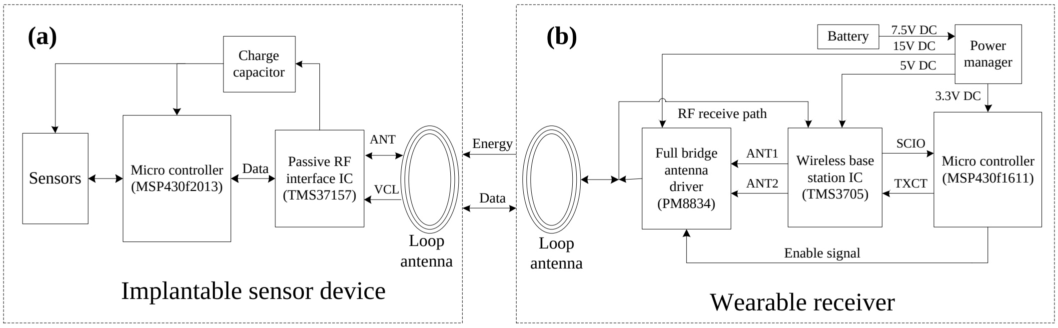

Figure 3.3 Configuration of wireless energy transfer circuits between the implantable sensor device (a) and wearable receiver (b): (a) PaLFI frontend circuit was designed on the sensor device to harvest energy and a ceramic capacitor was employed to provide energy to the MCU and sensors; (b) the wearable receiver had an optimised energy transfer RF circuit and a full bridge antenna driver was used to increase the output power. Power management was designed to provide multiple voltage outputs from the battery power supply.

TMS3705 (IC manufactured by Texas Instruments Inc.) was used to establish the energy transfer circuit of a wearable receiver. The core basic radio frequency (RF) frontend circuit and interface units are embedded into the TMS3705 so that only requires a few components to drive the receiver antenna for energy delivery and communication to an external MCU. This highly integrated solution has the advantage of saving circuit board space and minimizing power consumption. To increase the output power of the antenna, a high-speed dual metal oxide semiconductor field effect transistor (MOSFET), PM8834, was used in the TMS3705 driving circuit. The energy harvest circuit of the sensor device was based on TMS37157, a PaLFI frontend IC (manufactured by Texas Instruments Inc.), which is capable of supplying power to the external components, including the MCU and sensors. The TMS37157 also can be connected to an external MCU via a serial peripheral interface (SPI). The high integration and friendly interface of the TMS37157 made it suitable for our sensor device. A ceramic capacitor was employed as an energy reservoir rather than a battery. The capacitor is smaller, safer than battery and is the power source of the MCU and sensors.

3.1.2.3 Fabrication of the antennas for the sensor device and receiver

The performance of a wireless energy transfer based on electromagnetic induction is related to the effective electromagnetic induction area, the coupling between the primary and secondary coils, and the primary coil output power. Apart from increasing the primary coil output power as mentioned in the last section, the other way to improve energy transfer performance is through the optimisation of the antennas design. Two antennas of acceptable size, with tight coupling were required for our implantable sensor device and wearable receiver.

For the implantable sensor device, size is a key factor of the antenna as it needs to fit in the uterus. Obviously, a smaller antenna would be easier to use and more compatible with the intended application. However a smaller antenna leads to a smaller effective electromagnetic induction area which limits wireless energy transfer performance. Therefore, an antenna with as big an effective electromagnetic induction area as possible is required for the implantable sensor device.

Commercial antennas and some homemade antennas were developed and tested as shown in Figure 3.4. The best antenna assessed through testing was chosen for the sensor device. A commercial antenna was tested due to its applicable parameters (NEOSID MS32Ka, 2.53mH, 20.5 Ohm@200kHz, 11.6mmX3.5mmX2.5mm as shown in Figure 3.4a). Its size made it ideal for the sensor device and it was soldered on the printed circuit board (PCB) directly. The commercial antenna did not require any fabrication and would be suitable for a mass-produced device. However, on testing the small electromagnetic induction area resulted in limited energy transfer performance. Moreover, it was difficult to adjust antenna parameters to match the external circuits for error compensation which may arise after soldering and fabrication. Therefore the commercial antenna was deemed unsuitable for the sensor device.

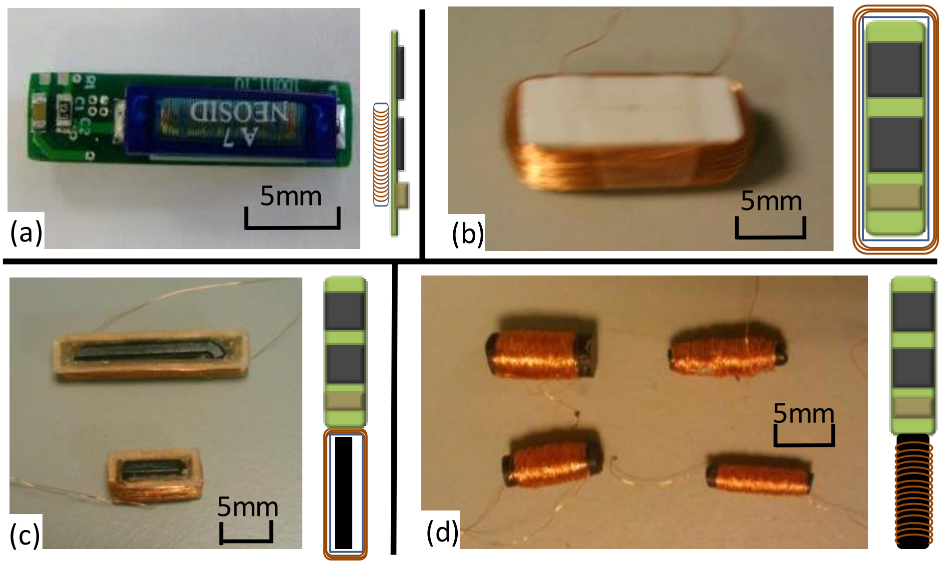

Figure 3.4 Different antennas developed for the sensor device (illustrated as green rectangular with two black squares and a brown rectangular): (a) a commercial antenna soldered on the printed circuit board; (b) rectangular loop antenna without a ferrite core. The sensor device can be fixed in the middle of this antenna, but antenna built in this way was too big for our application; (c) rectangular loop antenna was wound on a plastic frame with a ferrite core inside intended to be fixed at one end of sensor device; (d) tube antenna wound on a ferrite core.

Due to the limitations of the commercially available antennas, the homemade antennas were fabricated and tested for the sensor device. Compared with commercially available antennas, homemade antennas were more effective in prototype development. Antennas were developed with different shapes and sizes for the sensor device, including rectangular loop antennas (b and c, Figure 3.4) and tube antennas (d, Figure 3.4).

A rectangular loop antenna was developed with a relatively large area which could hook to the sensor device (b, Figure 3.4). It required a long length of varnished wire and needed to be relatively large (10mmX10mmX30mm) to establish the inductance needed and was therefore unacceptable for our intended intra-uterine application. A ferrite core has a much higher magnetic permeability than air and can be used to improve the antenna coupling and decrease antenna size. Some smaller rectangular loop antennas were made based on a ferrite core. The varnished wire was wound on a plastic rectangular frame and a hand-polished ferrite core was inserted into the frame. This decreased the overall size especially the height. For example, the two prototypes shown in Figure 3.4c were 5.3mmX6.3mmX12.7mm and 5.3mmX 5.7mmX27mm, respectively. However, due to the plastic frame, it was difficult to minimize the antenna to a satisfactory size, and the gap between varnished wire and ferrite core restricted the degree of coupling to the primary antenna.

Compared with upper mentioned three antennas, tube antenna can achieve a relatively small size and tight wound on the ferrite core because it doesn't need a coil frame.

Considering of fabrication complexity and the as small as possible size for the intended application, tube antenna with ferrite core is deemed as optimal antenna to the implantable sensor device. More details of four antenna prototypes' properties are listed in Table 3.2.

Table 3.2 Properties and comparison of four different sensor device antenna prototypes, including NEOSID commercial antenna, rectangular loop antenna without ferrite core, rectangular antenna with ferrite core and tube antenna with ferrite core.

	NEOSID antenna	**Rectangular loop antenna without ferrite core**	**Rectangular loop antenna with ferrite core**	**Tube antenna with ferrite core**
Dimensions	11.6mmX3.5mmX2.5mm	10mmX10mmX30mm	5.3mmX6.3mmX12.7mm or 5.3mmX 5.7mmX27mm	Vary from ϕ4.3mm X 15.2mm to ϕ2.7mm X 10.0mm
Features	Commercial antenna; Soldered on the sensor device PCB	The coil was wound on a frame without ferrite core; Sensor device PCB is fixed in the middle of this antenna	The coil was wound on a plastic frame with a ferrite core inside; Intended to be fixed at one end of sensor device	The coil was wound on a ferrite core directly
Advantages	Easy to use; Doesn't require further fabrication; Good reproducibility	Easy to make; Enable a smaller fabricated sensor device than others; Bigger induction area than tube antenna	Enable a smaller size than the rectangular antenna without ferrite core; Bigger induction area than tube antenna	No need coil frame; Smaller than rectangular antenna; The coil was wound quite tight on the ferrite core which results in good coupling performance
Disadvantages	Small electromagnetic induction area than others; Limited wireless performance; Difficult to adjust antenna parameters	Big size and hard to miniaturised to a satisfactory size	Complex structure; Hard to make; Big size and hard to miniaturised to a satisfactory size	Relatively small induction area

To achieve a smaller size, tube antennas were developed based on a ferrite rod (Fair-Rite) with different diameters onto which varnished wire was wound directly and tightly. To ensure tight wire winding, high reproducibility, and simple fabrication, a winding machine was used for wire winding as shown in Figure 3.5. This modified winding machine was based on a rolling tool purchased from Ebay online store. We made a customized spool rod for coil winding at different diameters. The spool rod had four parts inducing a middle spool set with 20mm length and different diameters, two support rods and a connection adapter to fit rod on the winding machine. A homemade tube antenna was made with a thin film wrapped on the middle spool with the varnished wire wound carefully onto it to form a multi-layer solenoid coil. Glue was applied to the coil surface and the coil removed from the machine. After insertion of the ferrite core, the key parameters of the antenna (including inductance, resistance @200KHz) were measured by PEAK Atlas LCR meter. After the fine trimming, the tube antennas were ready to use.

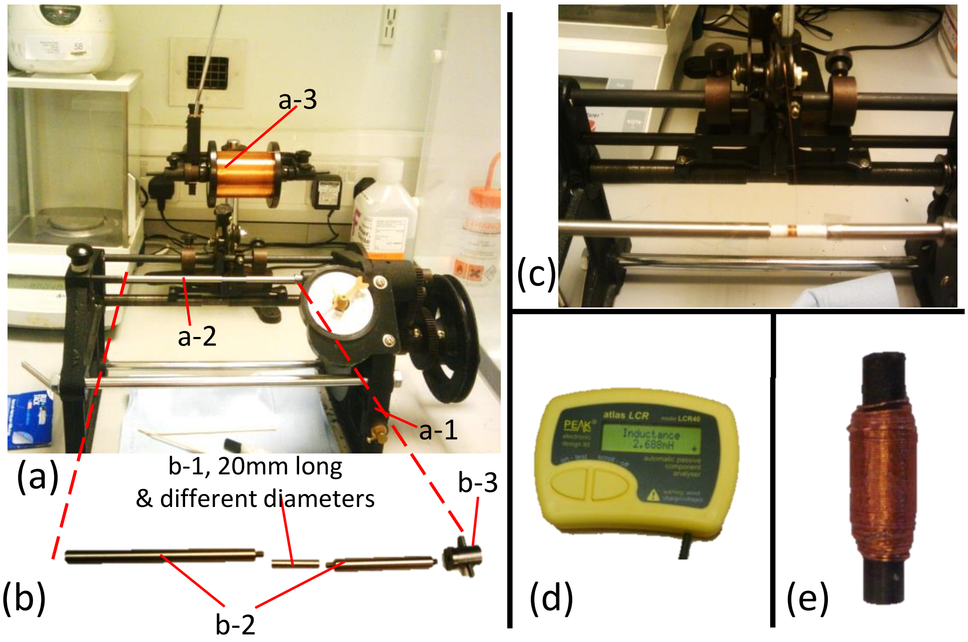

Figure 3.5 Winding machine for tube antenna fabrication: (a) The winding machine included a main machine (a-1), customized spool rod (a-2 and shown in (b)) and a wire holder (a-3); (b) the customized spool rod had four components including a middle spool set (b-1, 20mm long, with different diameters), two supporting rods (b-2) and a connection adapter (b-3); (c) a coil is winding on the machine; (d) PEAK Atlas LCR meter was used for antenna parameter measurement; (e) a completed tube antenna for sensor device.

Similar to the sensor device antenna, the antenna design for the wearable receiver is also important. Unlike the sensor device, the receiver antenna is more tolerant of dimensions and a larger antenna area leads to bigger working range. However, increasing the antenna size requires more power to drive the antenna. According to the scenario of a wearable device and human body size, the critical size of receiver antenna should not beyond an empirical value of 30cm. Compared with other types of antenna, a loop antenna without a ferrite core was used due to its big area, flat surface, small weight and the possibility of directly embedding it into clothing in future. A number of antennas were developed as shown in Figure 3.6.

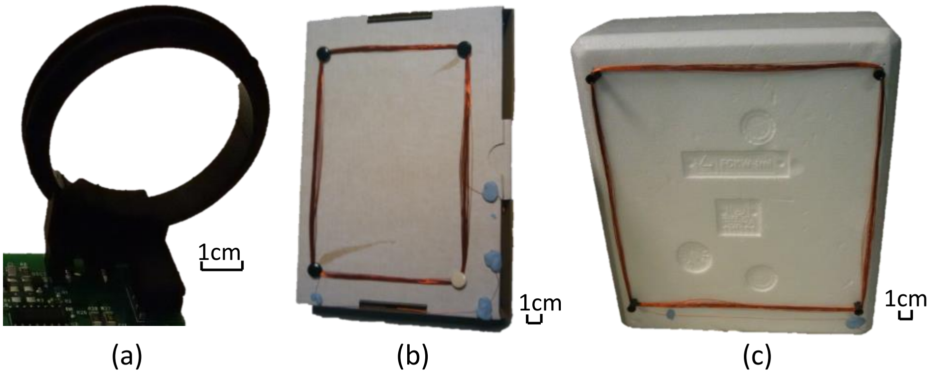

(a) (b) (c)

Figure 3.6 Antennas developed for a wearable receiver: (a) commercial ϕ3.5cm loop antenna was used for initial system development and debugging; (b) 15cm x 10cm rectangular antenna; (c) 20cm x 20cm rectangular antenna.

A commercial antenna (ϕ3.5cm, as shown in Figure 3.6a) was used for system development and basic function verification, this antenna is small with a limited working distance of around 5cm. Rectangular antennas were wound with different dimensions for the wearable receiver, including 15cmX10cm and 20cmX20cm. These antennas were all inspected with the PEAK LCR meter after fabrication.

3.1.2.4 Antenna testing

Wireless performance is a crucial feature that will determine whether our system can be deployed for the intended application. It is highly depended on the quality of antenna design. Once the antenna prototypes were built, they were tested and the optimal antenna designs for sensor device and receiver were determined.

A direct way to evaluate the performance of the antenna is to test its wireless working distance. Specific to our platform, the working distance can be identified as energy transfer distance or data communication distance. The energy transfer distance is the maximum distance at which the sensor device can harvest sufficient energy from the receiver. It is related to antenna design, receiver output power and sensor device power consumption. The data communication distance is the transmission range of wireless digital signal over which the information can be correctly identified. Generally, the energy transfer distance is shorter than the wireless data communication distance due to higher coil coupling requirement. Therefore, the energy transfer distance was chosen as a key indicator to express working distance for wireless performance evaluation.

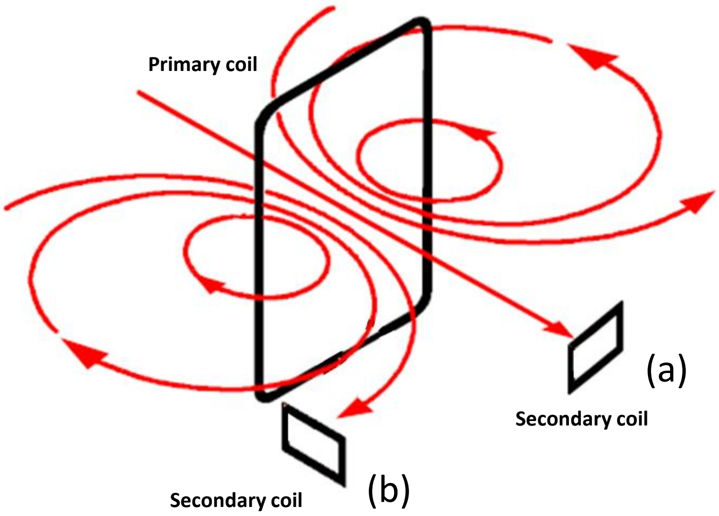

Figure 3.7 Typical magnetic field lines distribution of an rectangular antenna (primary coil) and two typical position of the secondary coil at the angle of 0° and 90° [91]: (a) the secondary coil is toward to the primary coil at an angle of 0°; (b) the secondary coil is on one side of the primary coil at an angle of 90°.

Considering the magnetic distribution of a loop antenna is not uniform (as shown in Figure 3.7) and the maximum working distance is strongly related to the relative position and orientation between sensor device and receiver, two typical positions were chosen for antenna testing as shown in Figure 3.7.

Under the same testing condition (using a sensor device with the NOESID antenna), receiver antenna prototypes were evaluated and compared on maximum working distance. The maximum working distance of three antenna prototypes at two different testing positions (illustrated by different colour) are shown in Figure 3.8. It was found that when the sensor device was aligned toward to the antenna of the receiver, i.e. when the cross section of sensor device antenna is parallel to receiver antenna, the result was better than at the other testing position. Moreover, the bigger antenna had better result than the smaller one and the 20cmX20cm antenna achieved best 14cm working distance. It was deemed sufficient for the following tests and the 20cmX20cm antenna was used to establish a baseline of the receiver antenna performance.

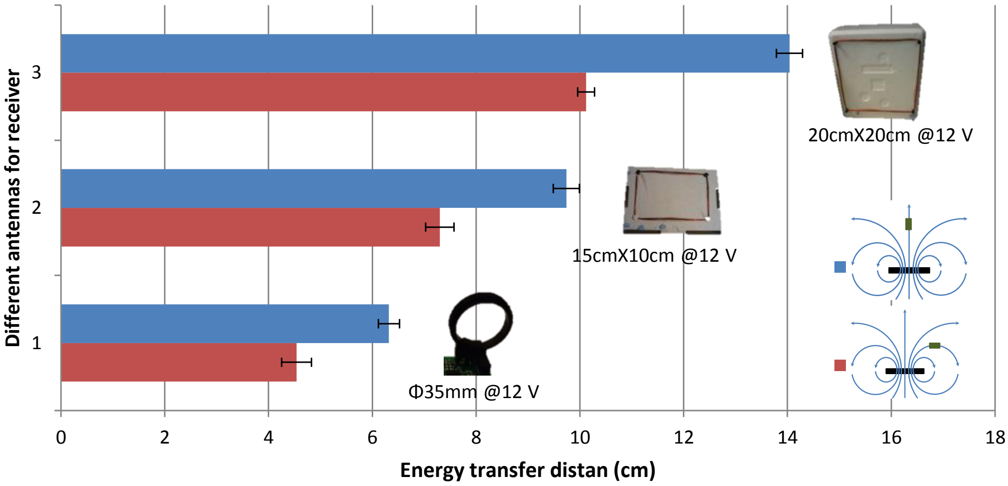

Figure 3.8 The working distance of three different antennas developed for receiver at two different testing positions. The working distance was measured 5 times at each position. Blue bars show the energy transfer distance when the sensor device was toward to the receiver antenna and red bars show the energy transfer distance at the testing position with 90° angle to receiver antenna. The black bars in the legend indicate receiver antenna and the green bars represent the sensor device.

After the evaluation of receiver antenna, based on the 20X20cm antenna, the antennas developed for sensor device were tested, including rectangular antennas with a ferrite core and tube antennas wound on different ferrite cores. The testing position was chosen where the sensor device antenna was toward to the receiver antenna with 0° angle. Similarly, the result of maximum working distance obtained from this position was used to evaluate the antenna performance. The properties of the antennas and their maximum working distances are shown in Table 3.3.

Table 3.3 The maximum working distance of different antenna prototypes developed for sensor device with different shapes and dimensions. The 20cmX20cm loop antenna of receiver was used as primary coil in this test.

Tube antenna with ferrite core					
Ferrite core size (mm)	**Wire (mm)**	**Size (mm)**	**L (mH)**	**R (Ohm)**	**Maximum working distance (cm)**
ϕ 4	0.05	ϕ4.7 X 10.0	2.39	47.6	16
ϕ 3	0.05	ϕ3.9 X 9.4	2.47	43.3	15
ϕ 3	0.1	ϕ4.3 X 15.2	2.45	12.7	23
ϕ 2	0.05	ϕ2.7 X 10.0	2.47	36.3	16
ϕ 2	0.1	ϕ3.8 X 11.2	2.59	13.1	20
Rectangular loop antenna with ferrite core					
Ferrite core size (mm)	**Wire (mm)**	**Size (mm)**	**L (mH)**	**R (Ohm)**	**Maximum working distance (cm)**
4.8 X 4.8 X 22.0	0.1	5.3X 5.7X27.0	2.42	46.4	23.5
4.8 X 4.8 X 10.0	0.1	5.3X6.3X12.7	2.54	35.2	20

Although the rectangular loop antennas with ferrite core had better result on maximum working distance than tube antennas, their size were relatively bigger and hard to minimize to a satisfactory size due to the plastic frame. The tube antennas are smaller and easy to make by using our home made winding machine. Three different ferrite cores and two different varnished wires were used to fabricate tube antennas. From the testing results in Table 3.3, the antenna with a bigger ferrite core and thicker wire had better results due to big ferrite core increased the induction area and the thick wire had less resistance giving a higher coil quality factor. However bigger ferrite core and thicker wire results in bigger antenna size. To achieve a small device size and considering the dimension limitation of sensor device PCB (4mm which will be), the tube antenna with ϕ3 mm ferrite core with 0.05mm wire was deemed as optimal configuration for the implantable sensor device.

3.1.3 Enabling real-time wireless data communication

Data transmission is a fundamental element of the microsystem. Wireless communication solutions are popular, as they eliminate the use of cables, are more comfortable, and are amenable to real-time monitoring. However, wireless systems have greater power consumption requirement and significantly greater levels of development and debugging than wired systems. Choice of the optimal technology can not only simplify design and shorten development cycle, but also make the system more portable and user friendly.

As shown in our blueprint in Figure 3.2, there are two wireless communication links, the low-level and high-level data communication links. The low-level link is the data communication between the implanted sensor device and wearable receiver, and the high-level link is between the wearable receiver and the data processing server (PC or smart terminals). So by comparing the currently mature wireless communication technologies, the most suitable solutions were determined and developed for our intended application.

There are numerous technologies for wireless communication which have been widely used in embedded systems. These include ZigBee, Bluetooth, Wifi, mobile telecommunications, and radio frequency identification (RFID). Because of their individual characteristics, they are suited to different scenarios and their general properties are shown in Table 3.4.

Table 3.4 Typical properties and comparison of wireless communication technologies, including ZigBee, Bluetooth, Wifi, Mobile telecommunication, NFC and LF RFID [92-98].

	ZigBee	**Bluetooth**	**Wifi**	**Mobile tele-communication**	**NFC**	**LF RFID**
Standards	IEEE 802.15.4	IEEE 802.15.1	IEEE 802.11	CDMA2000, WCDMA, LTE etc.	ISO 13157 etc.	ISO/IEC
Network Type	WPAN	WPAN	WLAN	WLAN	Point-to-point	Point-to-point
Range	10-100m	10-100m	35-100m	Depends on base station	< 0.2 m	~10cm
Data Rate	250 Kbit/s	varies with versions (typical 2.1Mbit/s, V2.0)	150 Mbit/s	22 Mbit/s	424 Kbit/s	8K bit/s
Power consumption	40 mA	varies with class (typical 45mA,V2.0)	100-300mA	High	< 15mA (read)	Lowest, <1mA
Frequency	2.4 GHz	2.4 GHz	2.4 GHz	850, 900 and 1,900 MHz	13.56 MHz	120–150 kHz, 13.56MHz
Compatibility	Low	High	High	Medium	Low	Low
Advantage	Small, low power consumption, simpler, less expensive	Well supported by smart terminals	High data rate, multi-connections, high compatibility	High data rate, long distance	Small, low power consumption, simpler, cheap	Small, low power consumption, cheap, no need battery, good propagation character
Dis-advantage	Low data rate, near distance	Relatively high power consumption	High power consumption	High power consumption	Short distance, low data rate, orientation dependent, low compatibility	Short distance, low date rate, orientation dependent
Typical application	Wireless sensor networks	Cell phone, wearable devices, headset	PC, PDA, wireless sharing	Cell phone, remote monitor	Cell phone, PDA	Smart ID

ZigBee is a specification for a set of high level communication protocols using small, low-power digital radios based on an IEEE 802.15.4 standard for wireless personal area networks (WPANs) [96]. It is intended to be simpler, less expensive and more application optimised than other WPANs, such as Bluetooth, it is already widely used in wireless sensor networks [99]. Bluetooth is a proprietary open wireless technology standard for exchanging data over short distances from fixed and mobile devices to create personal area networks with high levels of security [93]. Its high compatibility with the majority of smart terminal devices, such as cell phones, tablets, laptops, smart TVs and wearable devices, makes it very popular for embedded system development. The latest version is Bluetooth V4.0 which has been designed with lower power consumption and faster transmission speed than earlier versions. However, Bluetooth V2.0 is the most widely supported by Bluetooth modules for development. Wifi is a mechanism for wirelessly connecting electronic devices with high data rate and has a range of about 32 meters indoors and a greater range outdoors [92]. It is widely used in local network sharing and multi-media services due to its high compatibility and high data rate. Research and development are working to decrease its power consumption and to make it more suitable for smart terminals.

Mobile telecommunications are used for wide-area mobile phones and mobile telecommunication services [100]. There are four generations of mobile telecommunication technologies and many different protocols have been proposed to improve their performance. Their working ranges depend on the coverage of the base stations. As base stations coverage exists for almost all cities and countries, it has the largest range among the typical wireless communication technologies. However power consumption has to be considered and the possible health effects of electromagnetic radiation from mobile communications have been discussed for decades. Moreover, some technologies are used for data exchange based on existing RFID standards, such as near field communication (NFC) [94] and low frequency RFID (LF RFID) [95]. They are both proposed for near field, low transmission speed, small size and low power consumption applications. NFC has a relatively higher data rate and is already used in some mobile devices. Compared with NFC, LF RFID has lower power consumption, no need for any batteries. Additionally, the wireless signal frequency of LF RFID can be reduced to hundreds of KHz for better propagation characteristics.

A fully implantable device in the uterus and a wearable device for continuous monitoring need to have a minimal impact on the user’s normal activities and health. This creates criteria for wireless data communication technology selection. For the low-level data communication link between the sensor device and receiver, the power consumption is very limited; therefore the technology should have very low power consumption and work without any battery. Secondly, the device size is limited by the need to fit in the uterus. Thirdly, lower wireless signal frequency has better propagation characteristics and lower absorption by tissues. For the high-level data communication link between receiver and PC, the device should be small enough and light enough to be wearable for daily use. Low power consumption is also needed for continuous monitoring. Development of a system with high compatibility to commercial electronics can simplify system development and will be well supported by many smart terminals. The typical wireless data communication technologies were located in a Venn diagram for comparison, and the best solutions for our system were determined.

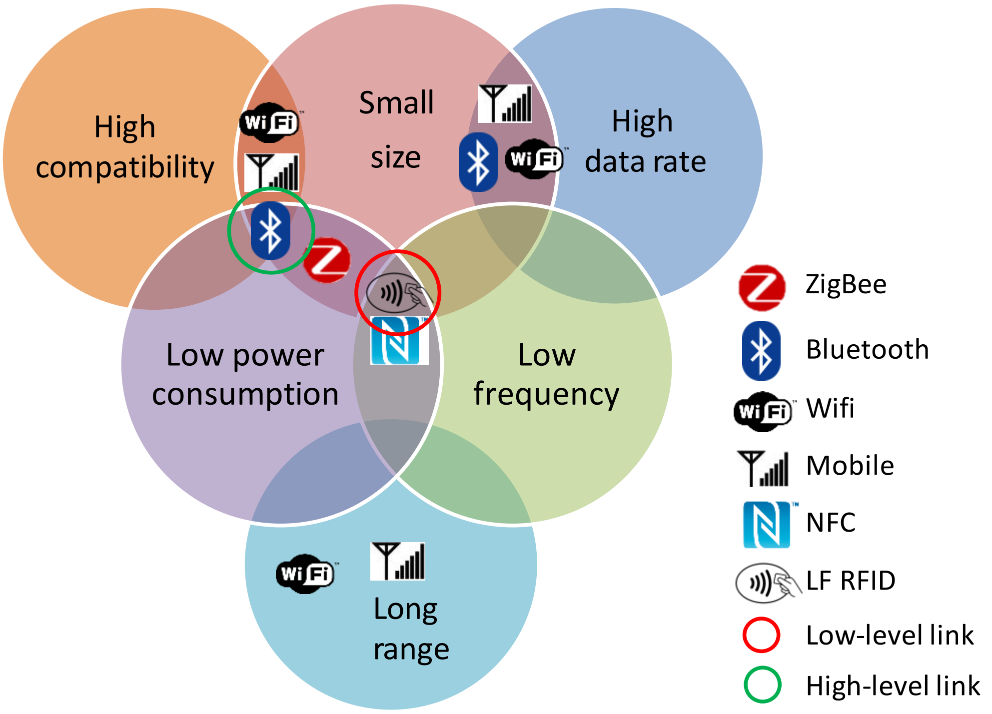

Figure 3.9 Venn diagram comparing of typical wireless data communication technologies. The LF RFID is the best solution for low-level link (between sensor device and receiver) due to its small size, low frequency and low power consumption, even no need any battery. Bluetooth is very suitable for the high-level link (between receiver and PC) because of its small size, low power consumption and high compatibility. It makes Bluetooth much easier to develop by using available Bluetooth modules.

From Figure 3.9, we see that the LF RFID covers the criteria for the low-level link. The advantages of LF RFID are its very low power consumption, and wireless energy transfer capability. The required hardware is relatively simple and can be minimized to an acceptable size for our intended application. Moreover, the circuit for wireless energy transfer can also serve as the wireless data communication as a LF RFID link, eliminating the needs for more circuits or board space for data communication. In the intended application, the *in-vivo* information and system configuration don’t require high data rate transmission and the LF RFID link can provide sufficient data bandwidth to meet the demand. The data communication range is usually further than the energy transfer distance meaning it is not the bottleneck of the effective working distance. Therefore, LF RFID technology was considered the best available solution and was used for the low-level link between the sensor device and receiver.

Bluetooth meets three criteria for the high-level link in Figure 3.9. Bluetooth has relatively low power consumption and can be easily minimized to work with battery powered portable devices. Bluetooth is widely used in numerous electronic systems and commercial products. Its high compatibility makes its development straightforward and able to interact with existing devices. For example, almost laptops, PCs and cell phones support Bluetooth, which eliminates the need for additional hardware developments to make our receiver compatible with them. Bluetooth was very considered suitable for the high-level link between our wearable receiver and the servers.

3.1.4 Summary of system design and core technologies development

Considering the specific requirements of our intra-uterine application, an optimised three-module structured system was proposed which includes a smart sensor, wearable receiver and software. The smart sensor is a wireless and batteryless implantable sensor device with the capacity for sensing multiple biophysical parameters (intended for temperature, DOC and pH). Wearable receiver works as medium between the implantable sensor device and software. The antenna of the receiver can be embedded into clothing for various scenarios and wired to the receiver. Software module is developed for *in-vivo* data uploading simultaneously to smart terminals or PC servers for post data processing and analysis.

Two core technologies were discussed and developed, including wireless energy transfer and wireless data communication. Electromagnetic induction technology was employed for wireless energy transfer and the antennas were specifically designed for sensor device and wearable receiver. **LF RFID** and **Bluetooth** were chosen for the two wireless links for data communication.

Once this three-module system structure is established and core technologies of basic functions are determined, more details of system development can be discussed. The development of implantable sensor device and wearable receiver are introduced in the subsequent sections.

3.2 Design of wireless and batteryless implantable sensor device

3.2.1 Electronic circuit design of the implantable sensor device

The sensor device is the pivotal component in this *in-vivo* sensing platform, and the aim of the electronic circuit design is to develop a robustly functioning implantable sensor device which meets the requirements shown in Figure 3.10. Firstly, to convert the actual biophysical quantities to digital information, the sensor device should include a complete signal link, including parameters for sensing, signal conditioning and digitization. Optimised size and power consumption make it available to the final application environment. Real-time, long-term *in-vivo* sensing requires the capability of remote access and reliable performance. Moreover, individual identity verification can provide flexible service for information management and user history tracking. Good scalability is also important for future upgrades for various applications.

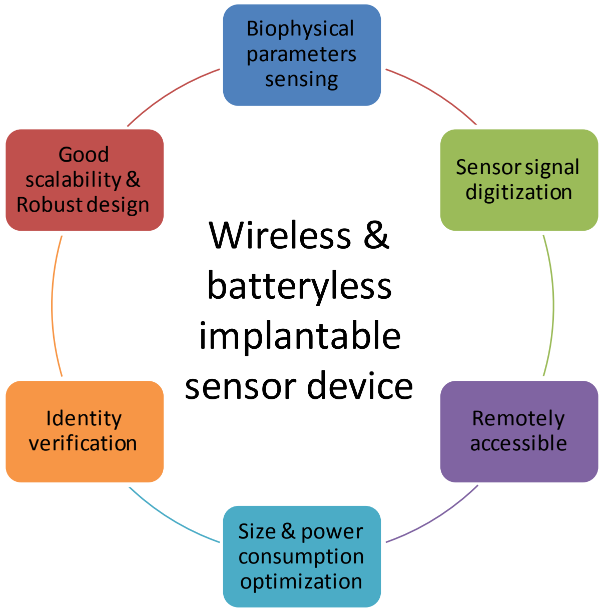

Figure 3.10 Essential requirements for circuit design of implantable sensor device, including biophysical sensors, analogue signal digitization, remotely accessible from outside of body, optimised size and power consumption, individual identity verification, robust enough for long-term *in-vivo* working and scalable for more potential sensors and more functions.

A well-developed implantable sensor device was designed to meet the required functionality and its structure is shown in Figure 3.11.

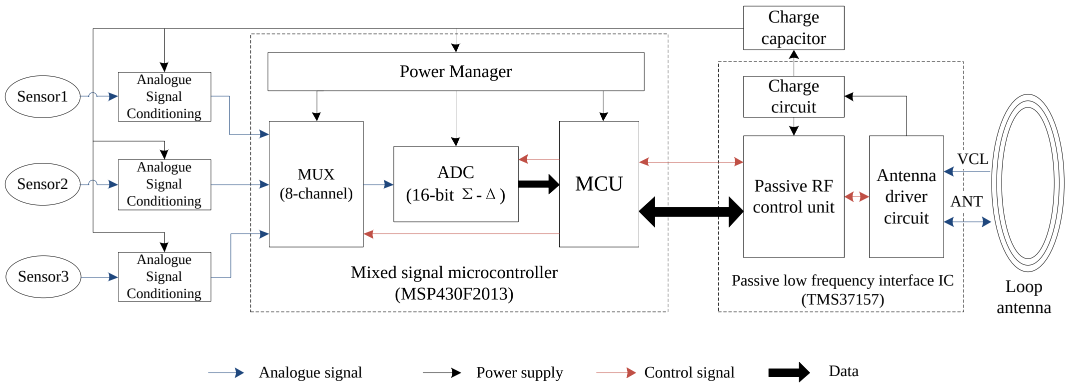

Figure 3.11 Main structure of sensor device, including sensors (temperature, DOC and pH in this case), signal processing units, MUC, ADC, MCU, power management unit and wireless unit. The wireless unit is based on a passive low frequency interface IC, TMS37157. Different signal flows were marked by different colour.

The information flow can be seen from left to right. There are sensor interfaces and individual signal conditioning circuits designed for temperature, dissolved oxygen concentration and pH measurement, although we incorporated the temperature sensor first in the prototype. A multiplexer (MUX) is necessary to reuse the common digitization circuit for energy and board space saving. The analogue signals from sensors are converted to digital data by an ADC after the multiplexer. An MCU reads the data from the ADC registers and uploads it through the wireless unit into receiver. The wireless unit includes a control unit, basic antenna circuit and antenna driver circuit.

In parallel, the energy flow is illustrated from right to left in Figure 3.11. The induced current in the antenna charges a ceramic charge capacitor to harvest energy. The capacitor works as an energy reservoir to provide energy to other components. A power manager is utilised to reduce the power consumption by setting idle modules to low power mode. An MCU is incorporated for its programmability and flexibility which makes the sensor device much smarter with capacity for primary data processing.

To reduce the number of discrete components and minimize the board size and power consumption, the MCU, ADC, MUX and power manager were integrated into a mixed signal microcontroller, MSP430F2013 (Texas Instruments Inc.). The wireless control unit, antenna driver circuit and charge circuit were integrated in a passive low frequency interface IC, TMS37157 (Texas Instruments Inc.), mentioned in section 3.1.2. The MCU supports flexible programming and JTAG debugging, significantly simplifying the development. An integrated 16-bit sigma-delta ADC with high impedance input buffer achieved accurate analogue signal digitization. An 8-channel MUX can switch the analogue signal from different sensors to ADC and its five external channels were considered sufficient for our application. One of the properties of the MSP430 serial microcontroller (Texas Instruments Inc.) is the ultralow power consumption; this can be reduced to 0.1µA (220µA @ active mode; 0.5 µA @ standby mode; 0.1 µA @ off mode). The TMS37157 provides a wireless energy harvesting interface and half duplex data transmission link over the same wireless link at a very low frequency (134.2 kHz). The data rate can reach 8 Kbits/s which is adequate for the transmission of multi-parameter *in-vivo* information and system configuration. In addition, its low resonant frequency confers better propagation characteristics and noise immunity to existing wireless communication systems at different frequency, such as Wi-Fi, mobile phones and Bluetooth.

For miniaturisation, the smallest available packages of these two core chips (MSP430F2013 and TMS37157) were chosen, and they are both plastic quad flat-pack no-lead (QFN) package, 4mm X 4mm X 1mm. Surface mounted packaging was used for all resistors, capacitors and other electronic components. The capacitor for energy storage was the biggest surface mounted package among the capacitors, as big as 3.2mm X 2.5mm X 2.5mm, but it was still smaller than the core chips. Overall, the size of the uterine cavity was considered in determining the critical dimension of all electronic components as 4mm.

3.2.1.1 Design of sensor device version 1 (SDV1)

Once the structure of the sensor device was decided together with the schematic of the circuit, we developed four different versions of the sensor devices. Sensor device version 1 (SDV1) was based on a development kit for circuit principle verification, embedded programming and debugging.

The basic wireless circuit of TMS37157 was developed together with a MSP430F2274 (Texas Instruments Inc.) as the MCU which was compatible to MSP430F2013 for embedded programming. More expansion pins were designed on the board for system development and debugging. An external temperature sensor (TSic506F, Innovative Sensor Technology) was used for temperature sensing with an accuracy of ±0.1°C to accelerate our development. This provided a digital interface to the MCU directly for temperature readings without the use of additional circuits. It was soldered on the backside of the PCB. Although SDV1 was about 33mm X 20mm which was too big for our intended application, it was very helpful for schematic verification and functionalities demonstration. The embedded software running in MCU was also developed on this prototype. The first version of sensor device is shown in Figure 3.12.

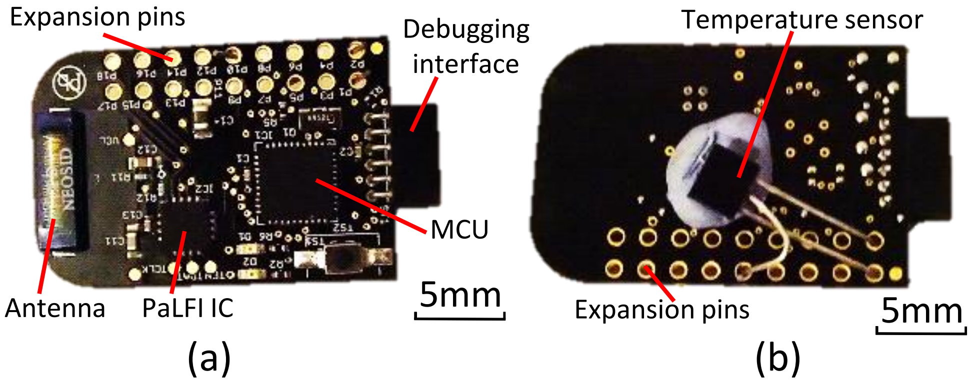

Figure 3.12 First version of sensor device (SDV1): (a) top view, the MCU, RF chip and antenna were soldered on the front surface and two rows of expansion pins were designed on the top side; (b) bottom view, an external temperature sensor is mounted on the back side for the temperature sensing.

From the SDV1, we demonstrated a very simple 2-3cm wireless powered temperature measurement. The working distance was limited due to the limited performance of commercial antenna and its unsatisfactory power consumption. Therefore, SDV1 was modified to optimise the size and power consumption. Specifically, optimisation was carried out by removing unnecessary functional units to simplify circuits, and by using alternative smaller components. For example, the unnecessary expansion interface was removed and the debugging interface was miniaturised to four tiny pads. The microcontroller was also optimised to MSP430F2013 (Texas Instruments Inc.) which is smaller while maintaining the required internal resources, and has lower power consumption. It is 4mm X 4mm and contains an embedded temperature sensor, so the external temperature sensor was eliminated for miniaturisation. Therefore, the sensor device version 2 (SDV2) was developed.

3.2.1.2 Design of sensor device version 2 (SDV2)

A four-layer new board was designed for smaller size, optimised PCB layout and signal link, and better wireless performance. It had increased grounding area, optimised the heat distribution, and improved the electromagnetic characteristics by incorporating two interlayers for power supply and grounding, and plenty of via holes between different layers. The schematic diagram and PCB design of SDV2 can be seen in appendix A (1, 2). A comparison image between the SDV2 and a 5 pence coin are shown in Figure 3.13.

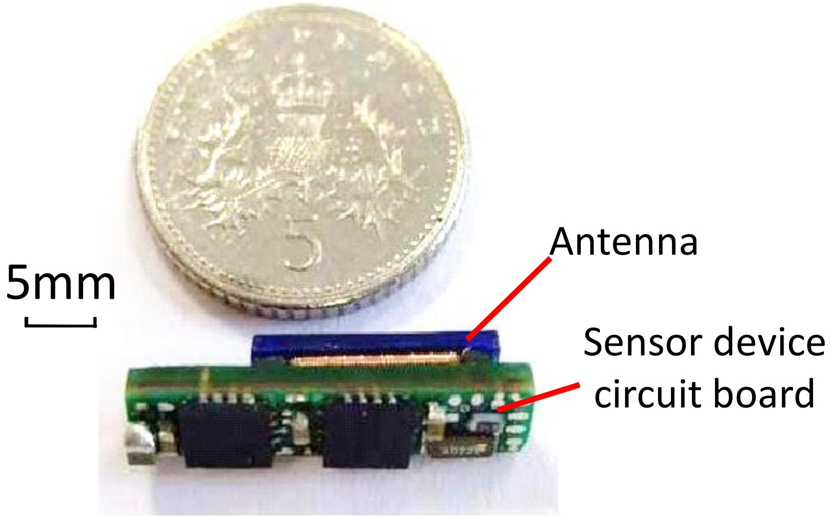

Figure 3.13 Second version of sensor device (SDV2). A fabricated device (4.88mmX5mmX18.4mm) compared with 5 pence coin, the commercial NEOSID antenna was soldered on the backside of SDV2.

SDV2 was much smaller than the SDV1, the dimensions were reduced to 4.88mmX5mmX18.4mm. A built-in temperature sensor of the MCU was used for temperature reading and a NEOSID commercial antenna was used. The built-in temperature sensor had a significant advantage by using the embedded sensor and circuits in the MCU without adding to the size. In principle, a built-in temperature sensor is connected to one of the ADC internal channels and the built-in voltage reference can drive the sensor and provide a reference to the ADC. The temperature reading can be obtained from the internal ADC directly, therefore there was no need to use any external components or wire connections. The resolution of the built-in temperature sensor is about 0.018°C, according to its 1.32mV/K temperature coefficient, 1.2V built-in voltage reference and 16-bit ADC.

From bench tests, all functions were verified including temperature sensing, wireless energy transfer, wireless data communication and individual identity verification. It was much smaller and had lower power consumption than SDV1. However, the commercial NEOSID antenna limited the wireless performance and the better performing antenna (tube antenna with ferrite core) was difficult to embed into the SDV2. Therefore, the SDV2 was upgraded to support tube antennas with a smaller size.

3.2.1.3 Design of sensor device version 3 (SDV3)

To fix the tube antenna onto the sensor device board, a middle connector was developed which will be discussed in section3.2.2. A spigot (2mm X 3mm) was placed at the left end of the sensor device version 3 (SDV3) board for connection to the middle connector. The schematic diagram and PCB design of SDV3 can be seen in appendix A (3, 4). A comparison image between SDV2 and SDV3 are shown in Figure 3.14.

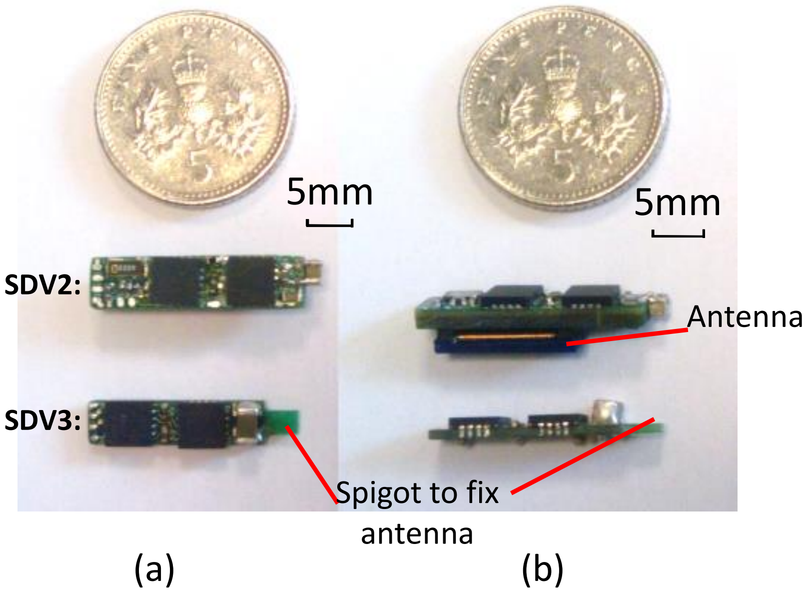

Figure 3.14 Third version of sensor device (SDV3): (a) top view of SDV2 and SDV3. The optimised SDV3 was smaller (around 4mm by 18.5mm) and a 3mm by 2mm spigot was designed at the left end to connect the tube antenna through a middle connector; (b) side view of SDV2 and SDV3. The size was decreased by simplifying the circuit, and PCB layout optimisation. The device boards were manufactured as thin as 0.8mm.

SDV3 was further miniaturised by replacing the external crystal circuit with an internal digitally controlled oscillator. Although the internal oscillator was not as accurate or stable as the external crystal oscillator circuit, it did meet the requirements for the sensor device which does not need very high frequency or an accurate clock. Considering the width of SDV2 is 4.88mm and the critical dimension of electronic components is 4mm (limited by the size of core chips), the width of the sensor device was reduced to 4mm, an 18% reduction in the size of the sensor device.

The plastic quad flat-pick package of core chips without leads requires bigger soldering footprint than the chip size for PCB assembly. This is to enable the chips to be soldered on the top of the board as shown in Figure 3.13b and mark 1 in the Figure 3.15. This led to a bigger width of SDV2 than chips, being 4.88mm. To overcome this limitation from soldering, specially designed half via holes were used on the PCB edges, meant the chips could be surface mounted on the vertical side (Mark 2, Figure 3.15). Therefore, the width of the sensor device further reduced to no more than 4mm.

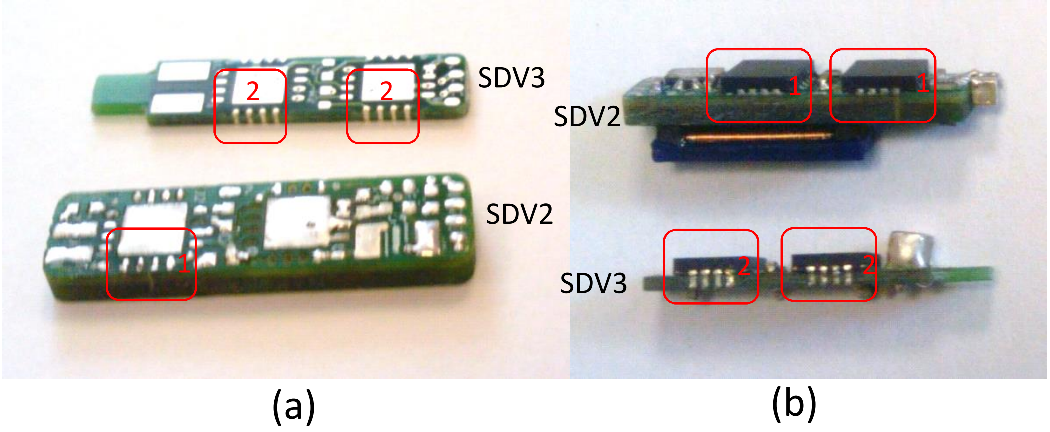

Figure 3.15 Comparison of the solder pads design between SDV2 and SDV3: (a) bare device boards of SDV2 and SDV3; (b) fabricated device boards. Mark 1 shows the soldering pads of SDV2 which on the top surface and the board is wider than the chips. Mark 2 identifies the solder pads of SDV3 on the vertical side of the board, and the chips can be soldered on the vertical side to decrease the board width. Therefore, the width of SDV3 was decreased to no more than 4mm from 4.88mm. The thickness of SDV3 was 0.8mm rather than 1.6mm of SDV2.

The height of the SDV2 board was 5mm, which was reduced in SDV3 by making the PCB thinner and removing the antenna from the backside. The thickness of bare board of SDV3 was decreased from 1.6mm to 0.8mm. Size comparisons between the two versions of sensor devices are shown in the Figure 3.14 and Figure 3.15. Overall, SDV3 bare board was measured as 4mmX 3.3mmX18.5mm. The critical dimensions, width and thickness, were already reduced to a similar size to the widely used IUDs. The minimum size possible has been achieved with the current chips; ASIC and bare chips will be used for the further size reduction.

3.2.1.4 Design of sensor device version 4 (SDV4)

The built-in temperature sensor in the MCU was also used in SDV3. Due to its limited performance (resolution and accuracy) in temperature sensing and relatively high power consumption, an external thermistor was employed in the fourth version of sensor device (SDV4). The built-in temperature sensor in SDV3 was designed with a large temperature sensing range which resulted in a limited temperature coefficient. Compared with normal range in human body temperature, its temperature range was too wide, and its resolution was limited. Optimisation of the built-in sensor performance would have been very difficult as the circuits were all embedded inside the MCU and not upgradable from outside. The packaging of the MCU also has a negative impact on the sensor response time. In addition, the power consumption of the temperature sensing was bigger than 910µA (190µA from built-in voltage reference and 720µA from ADC) which can be overcome by using external low power components. A discrete thermistor, 100K6A1B, was used in the SDV4 due to its small size, high sensitivity and good long-term stability. The diameter of the thermistor was 2.4mm, and small enough to be embedded into our sensor device, as shown in Figure 3.16a.

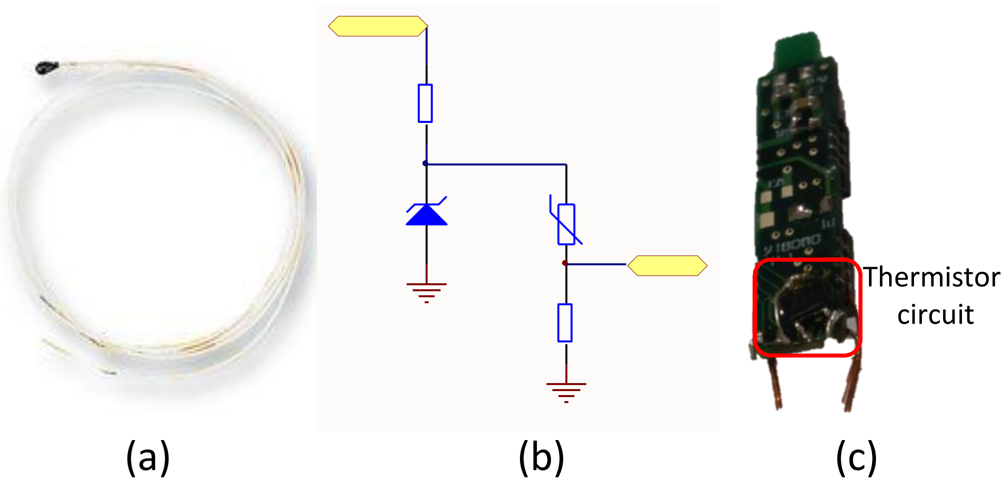

Figure 3.16 The thermistor in SDV4 and its circuit schematic, with the circuit soldered on the SDV3: (a) thermistor with long wire; (b) thermistor signal conversion circuit; (c) the thermistor circuit on the SDV3.

For the thermistor, a voltage divider circuit has been designed to convert the resistance change of thermistor to a voltage signal as shown in Figure 3.16b. Although a Wheatstone bridge is the conventional circuit for thermistor sensing due to its good immunity to common mode interference, our voltage divider requires fewer components and less board space and the common mode interference can be restrained by using a stable voltage reference to drive the thermistor. REF1112, a low power shunt reference with a low temperature coefficient (10ppm/°C, typically) and operating current (1μA, minimum) was used. Its low operating current contributed to lower power consumption of the sensor device. Although the actual working current was about 5μA, slightly bigger than 1μA, it was much smaller than SDV3 (190μA of internal voltage reference).

Considering the good scalability of SDV3 and to accelerate development, SDV4 was developed based on the circuit board of SDV3. The thermistor circuit was soldered on the backside of sensor device as shown in (C) in Figure 3.16.

After development and optimisation of SDV1-SDV4, a small, robust functioning, matured sensor device (SDV4) was developed and ready for encapsulation and testing. It met the requirements set out at the beginning of this section. The properties and comparison of four versions of sensor devices are shown in Table 3.5.

Table 3.5 The comparison of four different versions of sensor device.

	SDV1	**SDV2**	**SDV3**	**SDV4**
Size (mm)	33X20X5	18.4X4.9X5	18.5X4X 3.3	Slightly bigger than V3
Sensor	TSIC506F	Built-in sensor	Built-in sensor	External thermistor
Improvement	Good for circuit principle validation and debugging, first demonstration	Optimised PCB layout, better performance, smaller	Special designed for homemade antenna, smaller and thinner	Better external temperature sensor, lower power consumption, fast development
Disadvantage	Big size, limited performance	Less compatible to the homemade antenna	Limited performance of built-in sensor	Used same PCB with V3

3.2.2 Fabrication of the implantable sensor device

Two different shapes (T-type and stick-type) of sensor devices were designed and developed based on the latest sensor device circuit board, SDV4. To assemble the sensor device circuit board and homemade tube antenna together, a middle connector needed to be designed.

The T-type sensor device (T-SD) looks like a typical IUD with two arms, such as the Mirena and TCu-380. The arms are used to ensure a relatively stable position in the uterus and one of them was incorporated in the tube antenna. The orientation of antenna was horizontal to the ground, and was deemed suitable for a scenario where the receiver antenna was embedded in an upper garment. The middle connector of T-SD is as shown in

Figure 3.17. For fast prototyping, 3D printing technology was used to make the sensor device middle connectors. They were designed in SolidWorks (a 3D mechanical CAD program) and then printed by 3D printer (Objet Connex 350). The middle connector was fabricated using two materials with different hardness, including a hard light coloured material and a relatively soft dark material. The hard material was used to form the main body and two sockets for fitting the circuit board and tube antenna. The socket for the circuit board was at the bottom of the middle connector and the one for the antenna was incorporated into an arm. The soft material was used to form the arms, specifically one complete arm and the joint between two sockets as shown in Figure 3.17a. When the T-SD is delivered into the uterus, two arms can be bent opposite each other (as shown in Figure 3.17b), then recover to achieve a greater angle in the implantation site. Retrieval of the implanted sensor device is likely to be minimally traumatic as the arms can be squeezed together during sensor device retrieval. An assembled T-SD can be seen in Figure 3.17b.

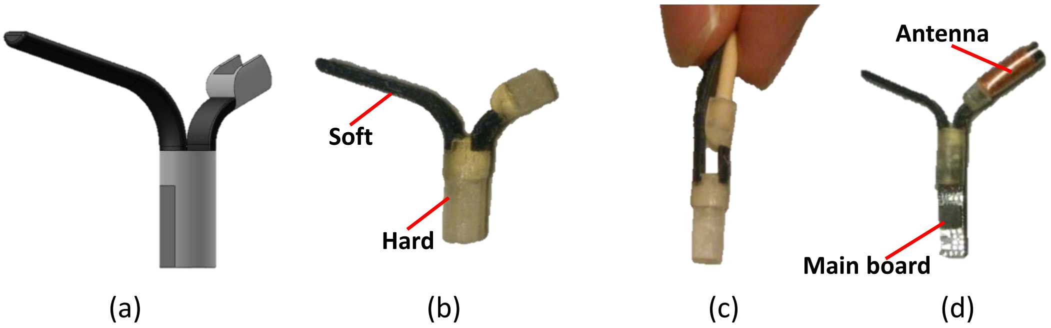

Figure 3.17 The middle connector and fabricated T-type sensor device (T-SD): (a) 3D model of the middle connector; (b) middle connector was made by two materials with different hardness, including hard material for main body and two accepters (light colour part) and soft material to form one arm and joint on the other arm (dark part); (c) two arms are bent together during delivery into the uterus and removing; (d) fabricated T-SD including main board, middle connector and antenna fixed on one arm.

Although the T-SD was designed to maintain a relatively stable position in the implantation site, the arm with the antenna was large and increased the width of two arms. Moreover, the flexible part of the middle connector increased the risk of breakage and possibly reduced reliability. To simplify the structure of the sensor device and enhance its reliability and robustness, a stick-type sensor device (S-SD) was designed and developed. The S-SD assembly and more details of the components are shown in Figure 3.18.

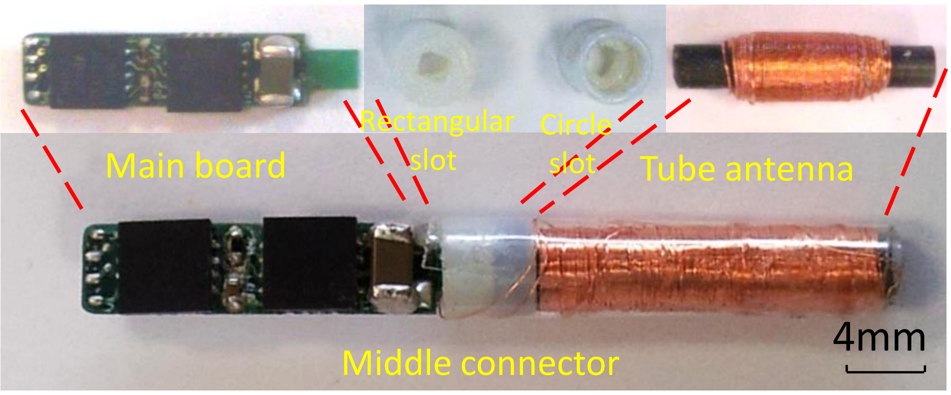

Figure 3.18 The connections of the stick-type sensor device (S-SD) and a fabricated sensor device. The middle connector had a rectangular slot and a circle slot at two ends to mount the main board and homemade tube antenna respectively.

Another middle connector was designed for the S-SD which had two sockets. A rectangular slot acted as a socket to fit the spigot of the sensor device circuit board and a circular slot was used to fit the tube antenna. The antenna was fixed on one end of the circuit board via this middle connector. This column middle connector was also designed and fabricated using 3D printing technology using a very hard material. A schematic illustrating the assembly of the stick-type can be seen in a 3D model in Figure 3.19a. An assembled S-SD was compared with typical IUDs (Mirena and TCu-380) in Figure 3.19. The sensor device orientation was vertical in the uterus making it optimal for use with a receiver having a belt antenna or an antenna embedded in the underwear (or disposable sanitary towel).

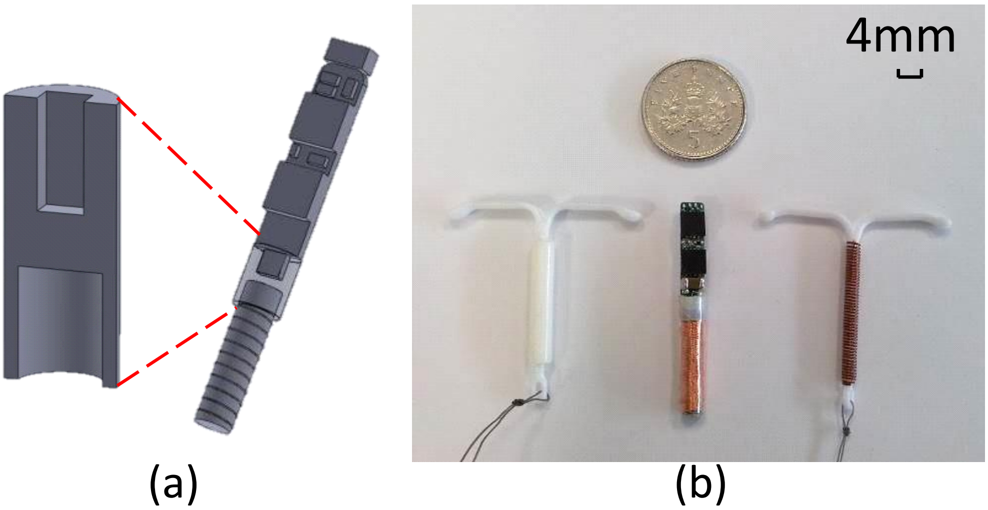

Figure 3.19 The 3D model of sensor device V3 and comparison with typical IUDs: (a) Assembly relationship of the S-SD. The middle connector has a circle and a square slot to mount the antenna and main board respectively. The left figure shows the cross section of the middle connector and the right one shows the internal connection of the middle connector; (b) size comparison with typical IUDs, including Mirena (left) and TCu-380 (right), and a five pence British coin.

Overall, two different types of sensor device were developed and both of them were size comparable to the typical IUDs. They were proposed for use with different receiver antennas. Compared with T-SD, the S-SD was smaller, more reliable and robust, which make it more suitable for the bench tests and animal tests.

3.2.3 Encapsulation of the implantable sensor device

Once the sensor device prototype was developed, necessary bench tests and animal tests were undertaken successively prior to future human trial. Suitable encapsulation was crucial and required for the safety of both the user and sealing of the sensor device.

3.2.3.1 Encapsulation for bench tests

Although the unpackaged sensor device achieved good results from testing in air on the bench, it was not enough for our intended intra-uterine application. As the uterus is an electrolyte rich environment and therefore the liquid inside is conductive which could result in electronic circuit shorting problems, sensor drift, and even device failure, waterproofness is crucial, and the device should be protected from water by proper encapsulation.

Conventional encapsulation methods include packaging in a capsule and coating a waterproof layer over the device. Due to size constraints, a waterproof layer coating was deemed more suitable. Epoxy has been widely used for encapsulation due to its stability and easy to use. PX804C from Robnor Resins Company is a non-toxic general purpose potting and encapsulating compound, and it was selected for its very low water absorption, 0.3% [4] after 30days at 20°C. It also exhibits a good surface finish, high electrical strength, excellent thermal conductivity, low exotherm and low cure shrinkage. For the full encapsulation of whole sensor device, two different packaging methods were discussed, including moulding packaging and dip packaging. Figure 3.20 and Figure 3.21 illustrate details of these two methods.

---

[4] %absorption = 100 * (B – A)/A. (A: Mass of oven-dry sample in air; B: Mass of surface saturated sample after a certain time immersing in water).

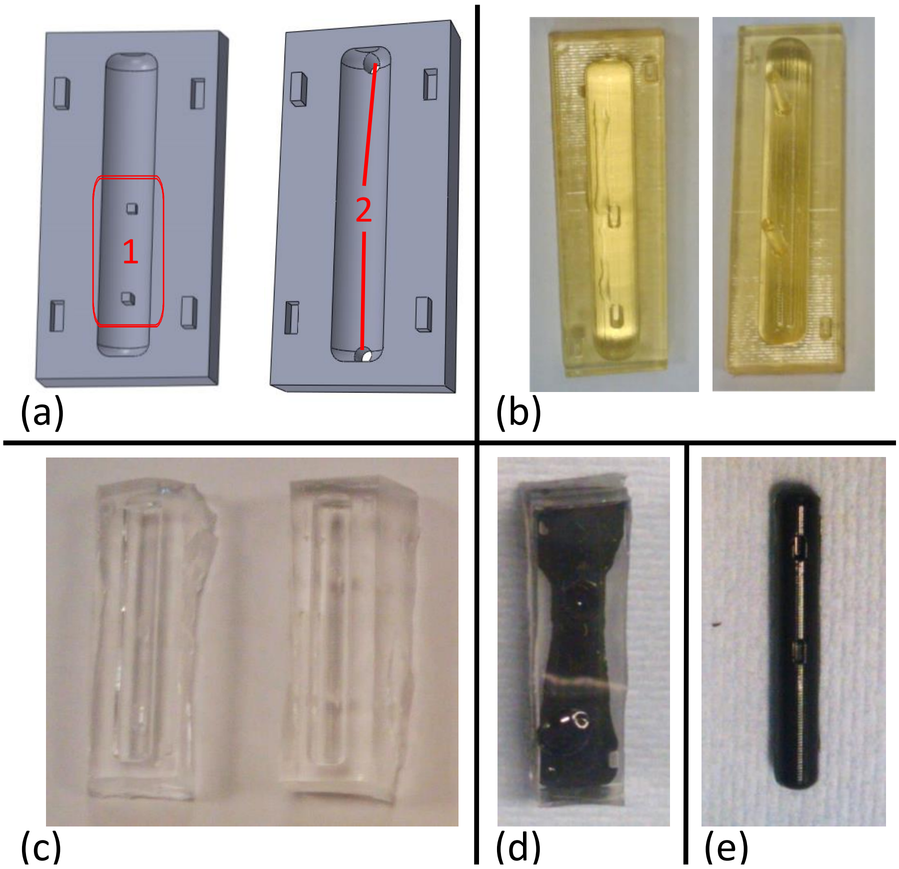

Figure 3.20 Procedure of mould packaging: (a) 3D models of two pieces of moulds. Two supporting pillars were designed on the bottom part (mark 1) and two injection holes were designed on the top part (mark 2); (b) two plastic moulds made by 3D printer for PDMS moulds; (c) two parts of PDMS moulds for sensor device packaging; (d) The epoxy was injected into the closed mould; (e) epoxy packaged sensor device.

Packaging was undertaken using a mould (including two parts, top part and bottom part) to achieve a uniform, smooth and total encapsulation. A typical procedure for mould packaging is shown in Figure 3.20. As epoxy adheres to plastic, the epoxy packaging mould cannot be printed directly based on 3D printing technology. Polydimethylsiloxane (PDMS) does not stick to epoxy and was suitable to use as the packaging mould. To fabricate the PDMS mould, a reverse-mould was required and made by 3D printer. Figure 3.20 (b) and (c) show the plastic reverse-mould and PDMS packaging mould. Considering the sensor device was not a perfect column shape, two short pillars were designed on the bottom part to support the sensor in the centre of the mould (mark 1, in Figure 3.20a). At the top part of the mould, two holes were designed for injection of epoxy and air exhaust (mark 2, in Figure 3.20a). The packaged sensor device had a uniform shape and smooth surface. However, this method was relatively complex and the position of sensor device in the mould was hard to control. Imprecise position resulted in variable thickness of encapsulation of the device.

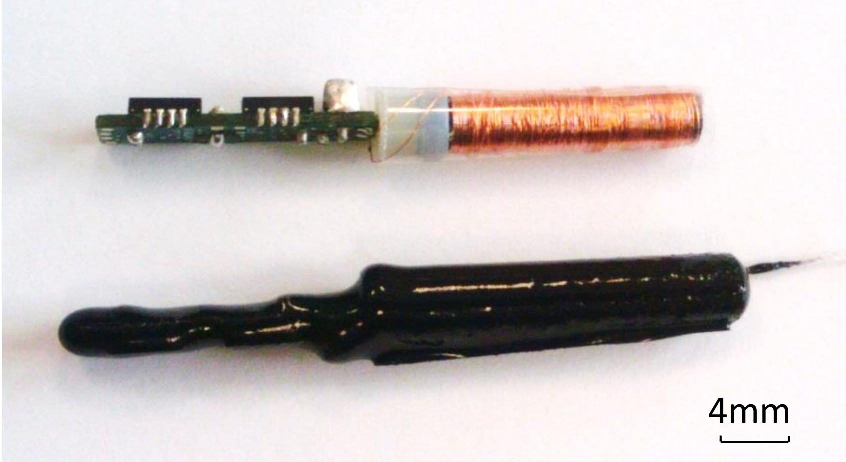

Figure 3.21 Unpackaged device (top) and packaged device using dipping method (bottom). The black epoxy (PX804C) was used to encapsulate the sensor device to protect the electronic circuit from water.

In contrast, the dip packaging method was simpler and easier to perform. It was carried out by immersing the sensor device in an appropriately prepared epoxy mixture (thoroughly mixing at the manufacture’s ratio as described in datasheet), then hung up on a shelf and cured in the air. Considering the effect of gravity, single dip packaging would result in a thin coating layer. By applying epoxy several times, the epoxy layer was relatively uniform and thicker than single packaging. Specifically after initial dipping, the epoxy mixture was applied from the top of the hanging device after 10min, 30min, and 60mins successively, and the epoxy flowed down the whole device under gravity. After several tests, the sensor devices were fully packaged by this protocol as shown in Figure 3.21. Although, these two methods can both achieve encapsulation, the dipping method was chosen because it was much easier and quicker and the epoxy layer was relatively uniform.

Furthermore, the bench test showed that some sensor devices suffered wireless performance drop after packaging. This was because of the deformation of the homemade tube antenna during fabrication and packaging, which resulted in the antenna parameters altering and resonant frequency drift. Therefore, a glass tube was designed and fixed over the antenna as shown in Figure 3.22. A quick cured epoxy (Araldite fast epoxy) was used to glue the glass tube to the sensor device and also enhance the strength of the connection between main board and antenna.

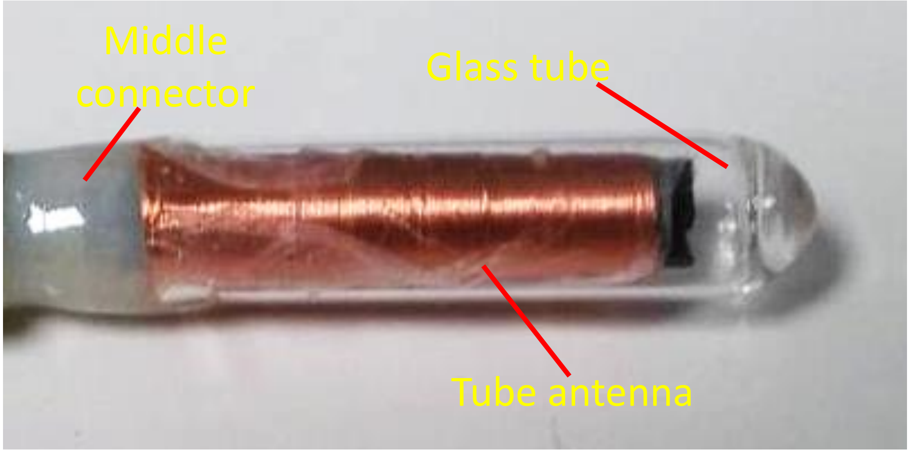

Figure 3.22 A glass tube was designed to protect the homemade tube antenna on the sensor device. The diameter was about 4mm, slightly bigger than the antenna.

Once the sensor device was packaged, it was fully tested on and found to work well in a long-term in-water test over more than 30 days. More details will be introduced in section3.5.4.

3.2.3.2 Encapsulation for animal tests

Considering the final application of the sensor device is in the human uterus, safety is paramount and animal tests are necessary before any trial on humans. The epoxy encapsulation was adequate for bench testing; however, it was not suitable for animal tests due to its limited bio-compatibility. For the animal test, the reaction between the implantable sensor device and its intended implantation site had to be considered and any potential toxic component of the sensor device cannot contact the intra-uterine tissues directly. The conventional strategy is packaging the implantable devices by medical grade material. As a medical device, some regulations need to be considered including Medicines & Healthcare Products Regulatory Agency (MHRA) in UK, Member State Competent Authorities in EU and Food and Drug Administration (FDA) in USA. Medical Device Directive (MDD) 93/42/EEC is a series of directives about the safety and marketing of medical devices and describes the essential requirements for the CE mark which is needed for medical device sales in the EU.

There are international standards that consider the details of different aspects. ISO14971 specifies a process to identify the hazards associated with medical device to estimate and evaluate the associated risks, control these risks and monitor the effectiveness of the controls. ISO10993 pertains to surface devices, external communicating devices and implantable devices to serve as a framework for selecting tests to evaluate biological responses for human safety. Before use, implantable devices require sterilization.

ISO11137 and ISO11135 identify methods to achieve the specified requirements for sterility with radiation and ETO (Ethylene Oxide) sterilisation respectively. Considering our sensor device includes electronic components, high temperature or radiation cannot be used. The ETO sterilisation is deemed as the most suitable method for our final application.

Uterine fluid contains cells, proteins, urea, and electrolytes which may block the sensors and deactivate them due to biofouling, raising the problem of the biocompatibility [101-103]. Because of interference from surface active species, sensor failure can be due to surface blocking, electrical failure or enzyme interaction, and it is also a problem for electrochemical sensors. However, for testing of the prototype incorporating the temperature sensor, biofouling is less of an issue. Therefore, a three-layer epoxy packaging method was used for the animal test as shown in Figure 3.23.

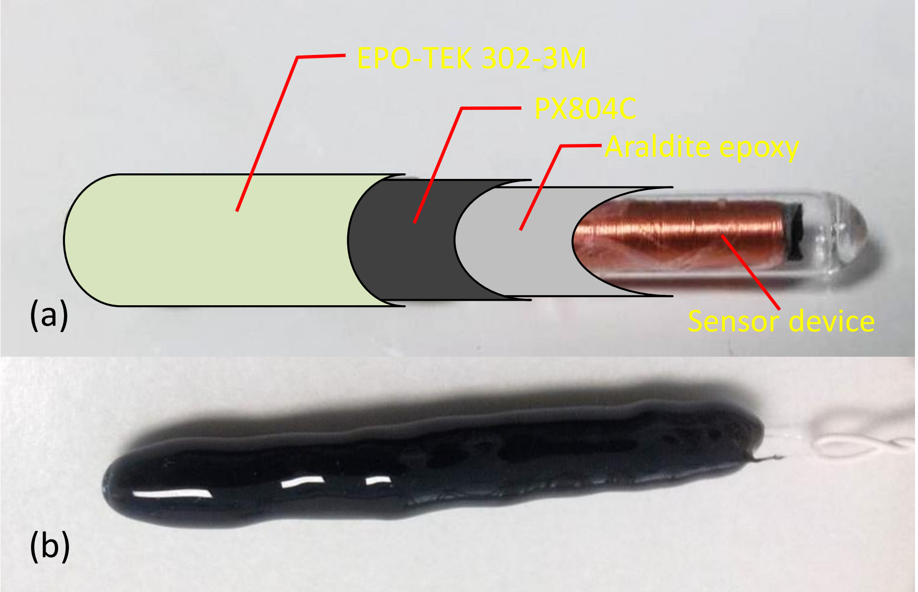

Figure 3.23 Three-layer epoxy encapsulation of the sensor device for animal test and a packaged sensor device: (a) diagram of three-layer epoxy packaging, including a fast cured epoxy layer for device assembly (grey), a second epoxy layer with very good water resistance (black) and an outer epoxy layer which has good bio-compatibility and meets USP Class VI as a medical grade material (light green); (b) a packaged sensor device which was used for animal test.

The sensor device was packaged by three different materials successively; more details about these three layers can be found in Table 3.6. Firstly, a fast cured epoxy was used for sensor device assembly, such as gluing the glass tube on the antenna and bonding the main board and antenna to the middle connector. This epoxy layer enhanced the strength of sensor device, especially the joint of the middle connector. Secondly, the same epoxy as used for the bench tests was used to form the second layer. This has very good chemical and water resistance and electrical insulation. The outermost layer is packaged with a medical grade epoxy, EPO-TEK 302-3M, which meets USP Class VI as a medical grade material for a good bio-compatibility. This three-layer epoxy encapsulation ensured the sensor device is bio-compatible, waterproof, safe and strong enough for the long-term *in-vivo* animal test.

Table 3.6 Details and comparison of three different epoxy layer for sensor device encapsulation.

	Layer 1	**Layer 2**	**Layer 3**
Material	Araldite fast epoxy	PX804C	EPO-TEK 302-3M
Advantage	Fast cured, powerful adhesion	Good chemical and water resistance, high electrical insulation, non-toxic	Meet USP Class VI bio-compatible, low water absorption, high electrical insulation
Aim	Device assembly, increasing strength	Batter waterproofness	Bio-compatible
Cure schedule (minimum) RT: room temperature	20-30 mins (RT)	24 hours (RT) 2 hours (60°C)	24 hours (23°C) 3 hours (65°C)
Colour	Pale yellow	Black	Clear and colourless
Water absorption rate *	Not intended for constant immersion	0.3% (after 30days @ 20°C)	0.095% (after 24hours @23°C)
Volume resistivity	-	11^{10} Ohm-cm	1 x 10^{13} Ohm-cm

*: %absorption = 100 * (B – A)/A. (A: Mass of oven-dry sample in air; B: Mass of surface saturated sample after a certain time immersing in water).

Before any animal test, sterilisation was carried out. Sterilisation with ETO is difficult for an initial animal trial as it requires dedicated equipment which we don’t have in lab and the operator has to be well trained, so that an alternative sterilisation method was used, including 70% ethanol treatment and UV light exposure. Sterilisation was undertaken in a biosafety cabinet (category II). There were four steps to this recipe as shown in Figure 3.24. The packaged sensor devices were thoroughly immersed and sterilised in ethanol for 20mins and then dried off in air for around half hour. Once the device was dry, it was sealed in an aseptic bag. Lastly, the sealed device was exposed to UV light for 10mins on the top side and then turned over for another 10mins exposure.

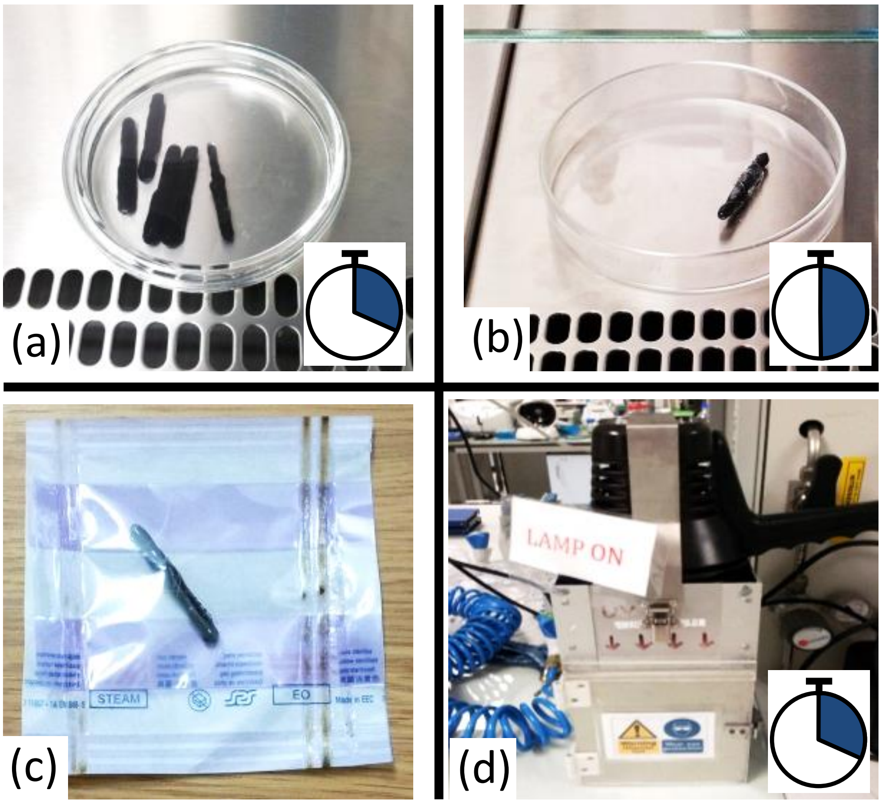

Figure 3.24 sterilisation recipe for animal test: (a) the packaged sensor devices was sterilised in 70% ethanol for 20min; (b) the sterilised sensor device was dried in air for around half hour; (c) it was sealed in an aseptic bag; (d) the sealed device was exposed to UV light 20mins (10mins for each side).

After the encapsulation and sterilisation, the sensor devices performed well in animal tests as introduced in the chapter 5.

3.2.4 Summary of implantable sensor device development

The wireless and batteryless implantable sensor device is the pivotal component in our multi-parameter *in-vivo* sensing platform. After intended application analysis and design considerations, four versions of sensor device were developed. The latest one (SDV4) improved on size and power consumption, and had excellent temperature sensing performance. Two different sensor device prototypes were proposed, including T-type and stick-type sensor devices. The prototypes were comparable in size to widely used IUDs. The T-SD was similar to the IUDs but the arms restrain the antenna size. Compared with T-SD, the **stick-type** was much robust and more reliable during testing. Different encapsulation methods were developed for bench test, animal test and further human trial. Overall, the well developed and packaged sensor device was suitable for the animal test.

3.3 Design of wearable receiver

As shown in Figure 3.2, a wearable receiver operates between the implantable sensor device and PC server. It delivers energy, data communication, and provides a user-friendly interface. During development, the requirements of the receiver were considered as shown in Figure 3.25.

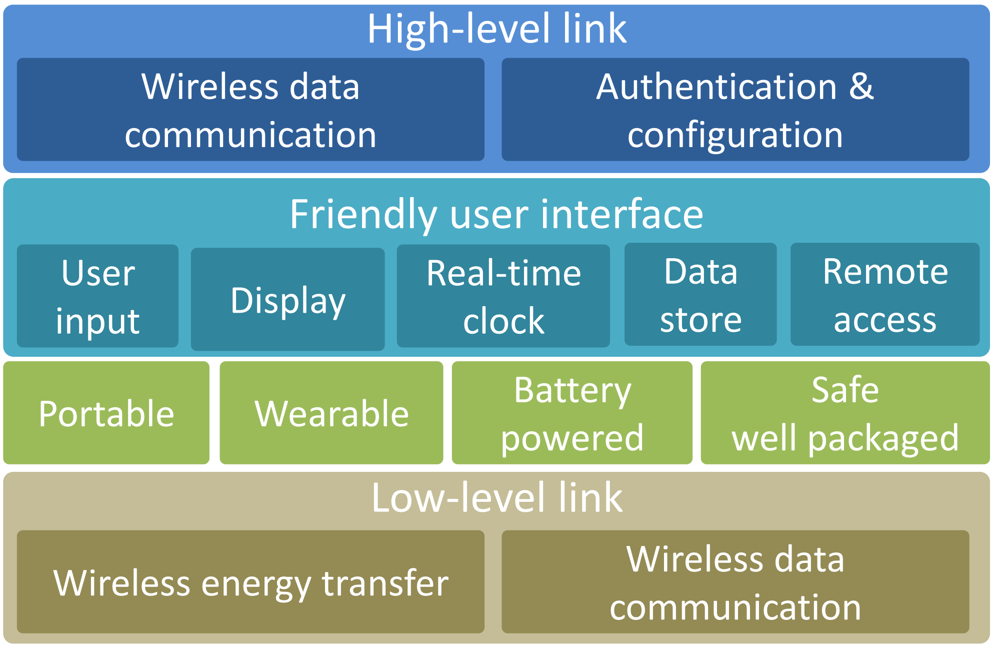

Figure 3.25 development requirements of the wearable receiver. The receiver will deliver high-level and low-level communication as shown in Figure 3.2. Moreover, a user-friendly interface will enhance the user experience. As a wearable device, the receiver should be portable, battery powered and well packaged for daily use.

The receiver needs to support the low-level link to the implantable sensor device. Specifically, the receiver is required to deliver energy to the implantable sensor device via an electromagnetic field, with data upload through the same wireless link back to the receiver. Once the internal information is sensed, the data needs to be available for upload to the server synchronously or asynchronously. The high-level link between the PC server and receiver needs to support wireless communication, authentication and remote configuration. To enhance the user experience, an intuitive user interface is required. This might include interactive operation by the user and a data display screen. A real-time clock, local data storage and remote accessing are necessary for data management and sharing. While achieving these functionalities, the receiver needs to be portable and wearable as the intention is for continuous measurement over many days. A re-chargeable battery is the optimal power supply for a minimized receiver. The electronic circuits need to be and well packaged to ensure the receiver is safe to use, and available to daily living.

3.3.1 Electronic circuit design of the wearable receiver

To meet the development requirements outlined above, and based on experience from typical microsystem design as discussed in section 3.1 (including system structure and core technologies employment), a multi-function receiver is proposed, and its structure is shown in Figure 3.26.

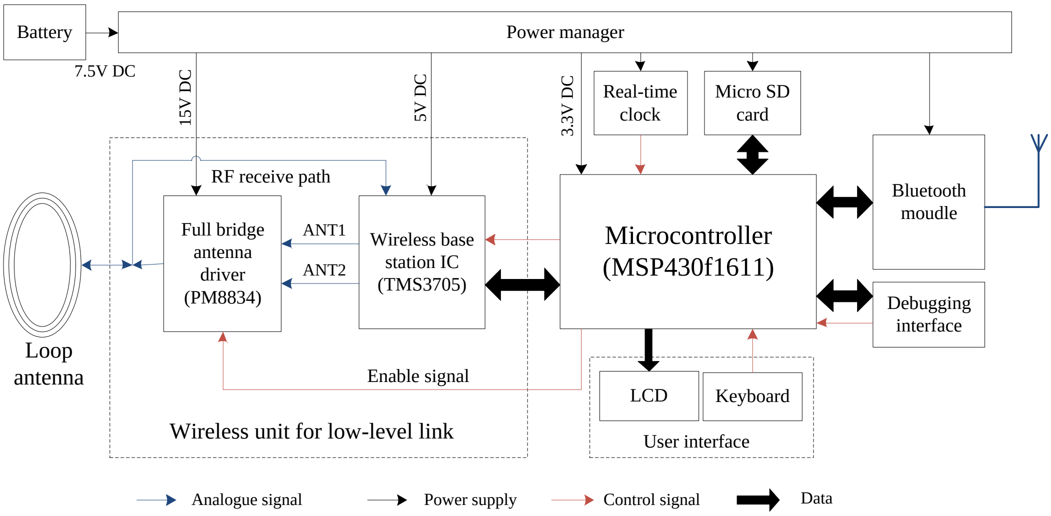

Figure 3.26 Overview of the receiver structure. The microcontroller is the core component to link and control different peripherals. A low-level wireless unit was developed for wireless energy transfer and data communication with the implantable sensor device. A user interface was designed including a keyboard input and a LCD for data display. A Bluetooth module was used for the high-level communication with upper servers or smart terminals. A real-time clock and micro SD card interface achieved local data storage. A full function power manager converted power supply from a re-chargeable battery to match the different voltage requirement of the peripherals. The signal flows are marked using different colours.

Considering of good programmability, flexibility and scalability, a mixed signal microcontroller (MSP430 series from Texas Instruments Inc.) was employed to link and control different peripherals. A wireless unit was developed to support wireless energy transfer and low-level data communication as discussed in section 3.1.2 and 3.1.3. This wireless unit was paired to the sensor devices at a matched resonant frequency (134.2 KHz) and communication protocol. In parallel, a Bluetooth module was designed for the data communication, authentication and remote configuration via the high-level link. The LCD and keyboard created a user-friendly interface which was used for information display, parameter setting, and task launch. A real-time clock and micro SD card supported real-time synchronous and non-volatile memory to ensure robust local data storage. A full functional power manager was developed for the multiple power supply output from the re-chargeable battery to different peripherals. By controlling the power supply switch (on or off), optimised power consumption and increased battery lift-time were achieved. The combination of these components met the requirements of the intended wearable receiver.

3.3.1.1 Design of receiver version 1 (RV1)

Once the main structure of the receiver was built, a first prototype was developed. Receiver version 1 (RV1) was used to verify the electronic circuit design and initial embedded programming. Two separate boards were developed including an RF development board for the development of the wireless unit and a main function board for the other functional units, as shown in Figure 3.27.

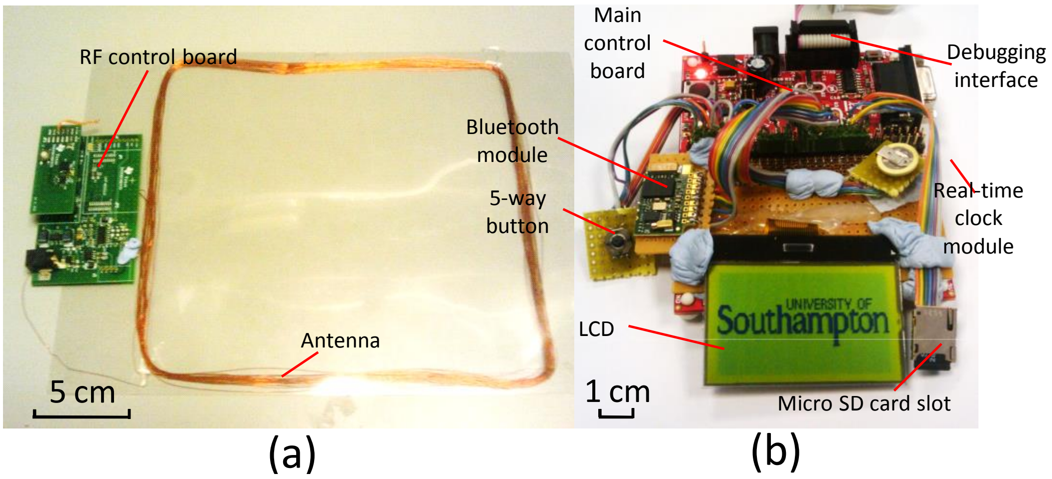

Figure 3.27 First version of receiver (RV1): (a) a wireless unit development board included a RF control board and a loop antenna. In this figure, the antenna is 20cm by 20cm and sealed in a transparent laminating paper; (b) main function board with abundant peripherals, including the main microcontroller board, debugging interface, real-time clock, micro SD card slot, a 128X64 dot matrix LCD, a 5-way button (up, down, left, right and centre), and Bluetooth module.

The wireless unit development board included a RF control board modified from an evaluation board based on TMS3705 (Texas Instruments Inc.) and a homemade loop antenna. The development board included the basic circuits for wireless energy transfer and wireless communication and was used for embedded programming, circuit optimisation, wireless performance evaluation and long-term testing. In parallel, the main function board was used for the circuit development of other peripherals, embedded programming, functional unit debugging and system integration evaluation. It included an evaluation board for the microcontroller and several homemade peripheral circuits. The main control board had an on-board debugging interface for programming and debugging. A well-designed extension interface can be connected with external homemade sub circuit boards. The real-time clock unit was designed based on MCP79410 (Microchip Technology Inc.), an I^2C low-power real-time clock enabling accurate clock/calendar. An external button battery was added for the battery backup. The internal 1Kbits EEPROM and 64bytes SRAM can be used for non-volatile configuration storage. The embedded software was developed to support file system access, meaning the data could be recorded in a normal .txt file and accessed directly rather than using customised software. A LCD was used for information display. The 128X64 dot matrix was sufficient to display configurations and options. After embedded software programming, the university logo was displayed when the receiver booted up. A 5-way button including up, down, left, right and centre click provided a powerful and easy user input method and the receiver was easily configured through this button and the LCD.

Several Bluetooth modules are available on the market, these can be used to shorten the development cycle and eliminate the high frequency analogue circuit design which would increase the complexity of system development. Therefore the receiver was designed based on a Bluetooth module, and the focus was on embedded software development for the module control and the communication software for the PC server and smart terminals. The latest Bluetooth protocol is version 4.0 which supports higher speed and lower power consumption, however as the majority of Bluetooth modules are still supported by Bluetooth V2.0, and this version was deemed adequate for our intended application with better compatibility to existing devices.

Although RV1 had two separate development boards, which were large and functional units were fixed by soldering cables and Blue Tack, it was helpful for circuit verification, system development and performance evaluation. Once this work was finished, system integration was undertaken to merge the functional boards together for optimised PCB layout and device size. RV1 relied on multiple external power sources so that an integrated power supply was required in the second version receiver (RV2).

3.3.1.2 Design of receiver version 2 (RV2)

Receiver integration and optimisation presented several challenges. A wearable receiver should be as small as practical to the user. Secondly, the challenges were from the PCB design and layout. The receiver contained several functional units, some of which were analogue circuits, while others were digital. The interference between analogue and digital circuits results in significant performance drop. This meant that optimised layout in a limited board was necessary in order to develop a high performing receiver. Finally, the receiver must be robust enough to undergo bench and animal testing.

To improve performance and minimise the size, a two-board three-layer stacked receiver was designed and developed as shown in Figure 3.28. The LCD was placed on the top layer. The functional units discussed above were loaded onto the middle board (main function board, MFB). The power supply circuits including voltage regulators and switch were built onto the bottom board (power supply board, PSB). Wires or pins were used to connect the two boards. The PSB was isolated from the MFB to optimise the electrical performance and minimise the interference from the power conversion circuit. This stacked structure made full use of space, and made RV2 was much smaller than earlier RV1.

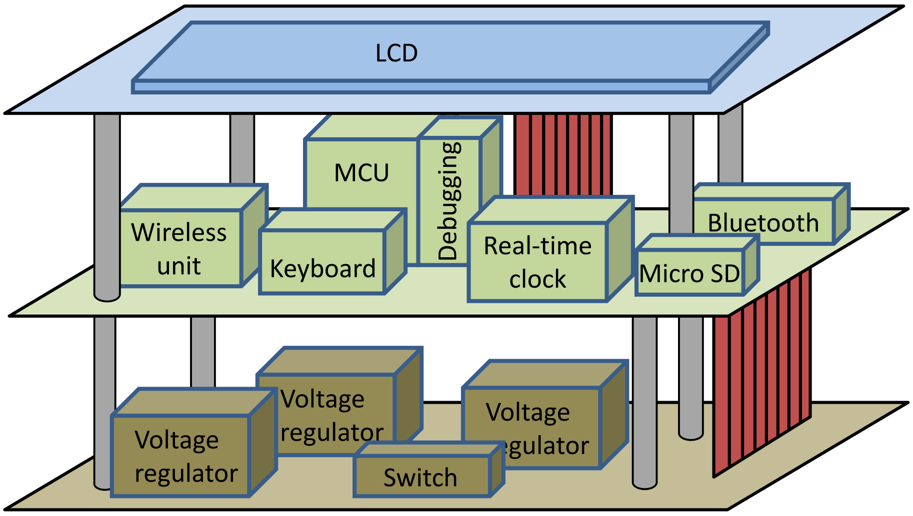

Figure 3.28 Two-board three-layer stacked structure of the second version receiver (RV2). The LCD was placed at top of the receiver. The main functional units were on the middle board (MFB) and the power supply circuit was isolated on the bottom board (PSB). This design used the three-dimension space effectively and limited interference from the power conversion circuit.

Development of main function board (MFB)

Similar to the sensor device, MFB was designed as a four-layer board and divided into different blocks for layout. The PCB layout of MFB can be seen in Figure 3.29a. As mentioned, two more interlayers for power supply and grounding, and the inclusion of numerous via holes can effectively increase the grounding area and optimise heat dispersion. The analogue circuits were separated from the digital circuits and designed in different blocks. For example, mark 1 in the Figure 3.29 is the wireless unit block (mark 1) and it was separately grounded from the digital circuits block (mark 2). Mark 3 is the Bluetooth circuit at the bottom right corner and it isolated separately from the other blocks. This well-designed layout miniaturised the possible interference between the different circuits, particularly the analogue and digital circuits, and as a result improved the signal quality. The RV2 was 60mm X 35mm which was much smaller than RV1. The schematic diagram and PCB design of MFB of RV2 can be seen in appendix A (5-7). A fabricated board is shown in Figure 3.29.

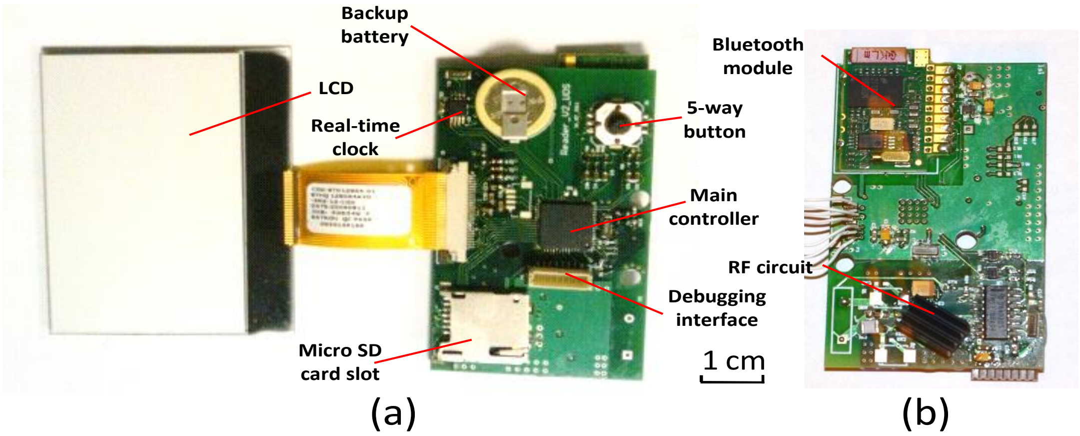

Figure 3.29 A fabricated MFB of RV2: (a) top view of the MFB. We can see the circuits on the topside including main controller, LCD, 5-way button (up, down, left, right, and centre), Micro SD card slot, real-time clock and serial debugging interface; (b) bottom view of the MFB. The Bluetooth module and RF circuit are on the bottom.

Development of power supply board (PSB)

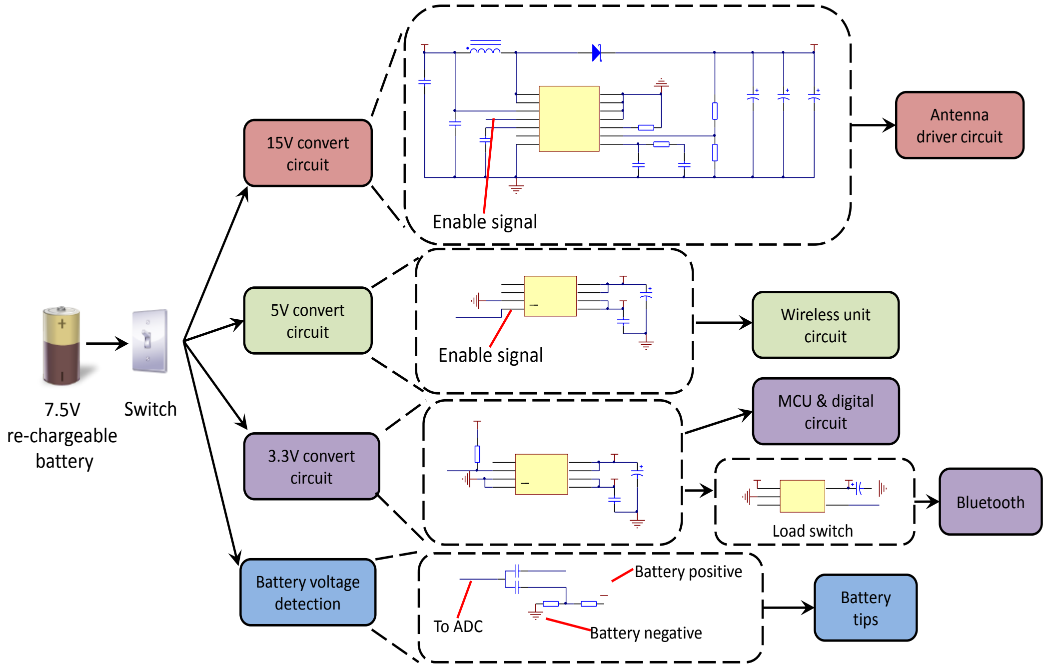

Figure 3.30 The structure of PSB and schematic diagram for core circuits. Three voltage converters with different voltages were designed for the different functional units. The battery information was monitored by a battery voltage detection circuit for battery tips and recharge reminder. Enable signals and load switch were used to control the power supply and optimise power management and power consumption.

As the receiver is portable, it required a PSB designed to support a battery powered supply. In consideration of the power requirements for wireless energy transfer and data communication, the receiver required adequate power ability to drive the primary coil antenna. As size was an issue, the design of a high power output, high efficiency and good performance power supply was a main challenge for the intended PSB. Three different voltages were needed for the receiver's functional units, including 15V for the antenna driver circuit, 5V for the wireless unit circuit and 3.3V for the main digital circuit. The PSB design with flexible power control for the RV2 is shown in Figure 3.30.

A lithium re-chargeable battery (manufactured by Enix Energies, 7.5V, 2.2AH, 70mmX37.5mmX19mm) was selected for the power source with a good balance between size and capacity. Downstream of a switch, three different voltage converter units were designed separately. A large current voltage boost converter circuit based on TPS61175 (Texas Instruments Inc.) was designed for high current output of the antenna driver circuit. This boost converter was designed and evaluated in the development and simulation software (SwitcherPro, Version 3.12.5.0, from Texas Instruments Inc.) before PCB fabrication. The simulation result of the voltage conversion efficiency is shown in Figure 3.31a. The output current can deliver 1.2A at 15V, and its efficiency was more than 90% when the output current was between 300mA and 1A. This was sufficient for the RF circuit, and this power supply unit worked well in the hardware tests. As the digital circuit required a relatively low voltage and limited current, a low-dropout voltage regulator was adequate. TPS76533 (Texas Instruments Inc.) and TPS76550 (Texas Instruments Inc.) were chosen for the 3.3V and 5V, due to their ultra-low quiescent current (35µA) and simple circuit. Based on the enabling signals, a flexible power controller was developed to control the power supply for various functional units, such as antenna driver circuit, wireless unit and Bluetooth unit. The idle units can be powered off to save unnecessary power consumption and achieve better power management. The schematic diagram and PCB design of the PSB of RV2 can be seen in appendix A (8, 9). A fabricated PSB is shown in Figure 3.31. The large grounding area optimised the heat distribution, and delivered better analogue signal characteristics.

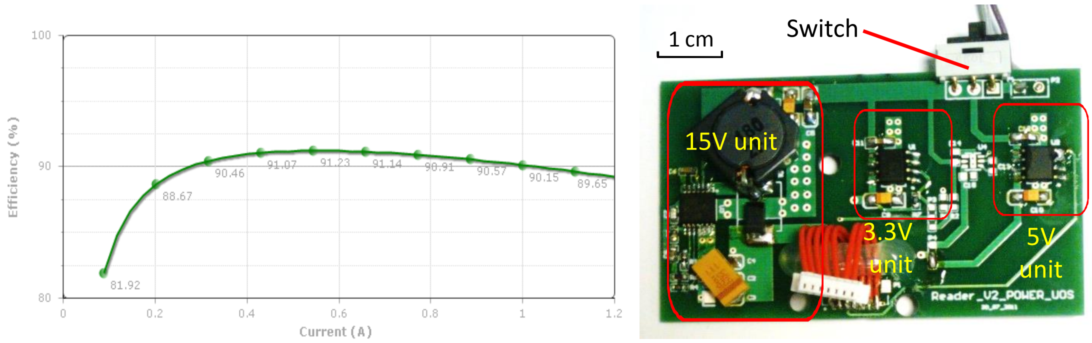

(a) (b)

Figure 3.31 Simulation result of voltage conversion efficiency and a fabricated PSB of RV2: (a) efficiency curve of 15V converter circuit; (b) top view of PSB which has three voltage conversion units, 15V, 3.3V and 5V from a lithium battery.

The voltage outputs of these three converter circuits were measured and proved as accurate and very stable; their ripple was reliably smaller than 0.08% of the output. Therefore, they were deemed adequate to power the MFB of RV2. The results of the power supply output evaluation are shown in Table 3.7.

Table 3.7 Performance evaluation of the power supply board.

Voltage converter for		**15V**	**5V**	**3.3V**
No load	**Vout(V)**	14.780	4.997	3.300
	Ripple (V_{p-p}, mV)	11.60	2.40	2.80
With load	**Vout(V)**	14.775	4.993	3.296
	Ripple (V_{p-p}, mV)	11.80	3.44	3.68
The output voltage and power ripple were considered at both no-load and with-load conditions. The output voltage was measured by a precision multimeter (Agilent U1252A) and the ripple was measured using an analogue oscilloscope (Philips PM3335). V_{p-p}: Voltage of Peak to Peak.				

This PSB was designed to be the same size as the MFB, this enabled assembly using three assembly holes and insertion of spacers. The assembled receiver is shown in Figure 3.32.

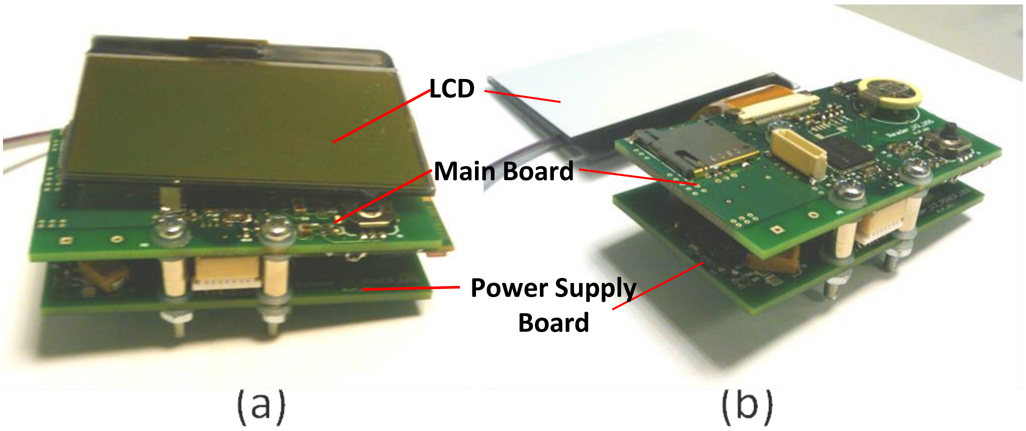

Figure 3.32 Assembled RV2 includes a MFB, a PSB and a LCD: (a) side view of receiver; (b) left side view of receiver

3.3.2 Assembly of the wearable receiver

After circuit design and functional testing, two different protective cases were proposed for the RV2 to fabricate different wearable receiver prototypes, including all-function receiver and miniaturised receiver. The all-function receiver prototype enabled all functional units and peripherals to be accessed by the user. By using the LCD and 5-way button, a user interface was provided enabling the user to configure the receiver directly. This included configuring Bluetooth, changing the receiver setting and modifying the working procedure. The receiver can be operated as a stand-alone unit and does not require the interaction with a server. Details are shown in Figure 3.33.

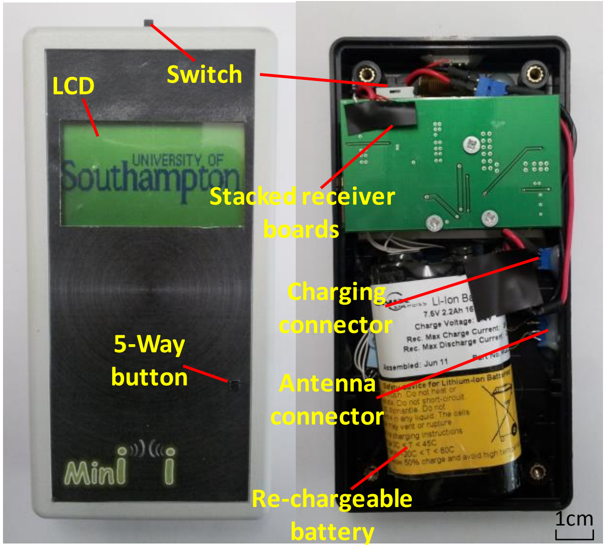

(a) (b)

Figure 3.33 Demonstration of all-function receiver: (a) front view of packaged receiver; (b) inside view of packaged receiver. Main units are marked in the pictures.

Although the all-function receiver was flexible and powerful to use, it was large (130mmX65mmX26mm) and could be improved. Additionally, the available options for the user may be more than needed. Therefore, a smaller case was proposed resulting in a smaller and simpler system to the user. The system enables a user to access and control the receiver through a server or smart terminal, such as a cell phone. Therefore, the LCD and 5-way button were removed and Bluetooth was automatically enabled after power on. The user can connect with the receiver without the need for any interaction with the receiver after switch on. This case was printed using a portable 3D printer (UP! mini). The assembled receiver was much smaller than previous version, 65mmX40mmX21mm. The empty case and assembled receiver are shown in Figure 3.34.

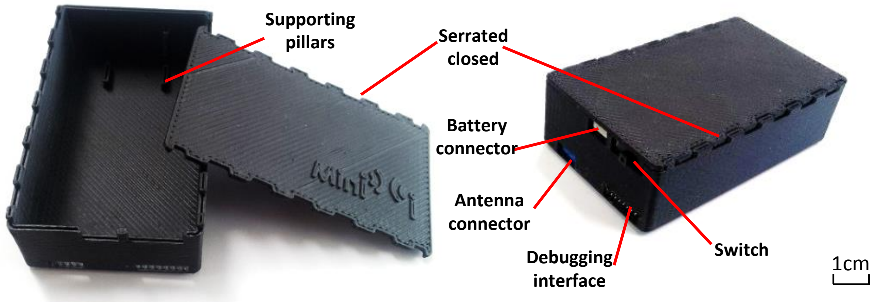

(a) (b)

Figure 3.34 Empty case and assembled receiver: (a) empty case for miniaturised receiver including a case body and lid. Pillars were incorporated into the case to support the PCB board and a serrated edge was designed to close case lid; (b) assembled receiver. The key connectors are marked in the picture.

Considering the intended application and necessary animal testing, some different antenna prototypes were developed and a multi-antenna receiver system was proposed. Different antennas for the receiver were designed and developed as shown in Figure 3.35. For example, a soft loop antenna was sealed in a laminating paper making it wearable for embedding into a piece of clothing. A rigid antenna was made on a plastic frame making it suitable for fixed position application. A much smaller antenna (13.5cm x 4.5cm) was incorporated into a disposable sanitary towel for wearing discretely in underwear. Although the performance of this antenna was not as good as the bigger one, it had a better position relative to the sensor device and a shorter working distance requirement. An elastic antenna was also designed to be worn around the waist. Considering a user's comfort and normal activity, a single fixed size antenna would not be suitable for all users. So the antenna coil was designed and embedded on an elastic band which can fit a range of waist sizes, and contend with distortion associated with normal activity, such as breathing and moving. Based on the elastic antenna, a belt antenna was designed. The coil was embedded in the elastic band and closed by a multi-pin connector. A row of hooks were incorporated to enable adjustment of the belt size. It was used more like a belt and very easy to wear. More details about these antenna testing will be introduced in chapter 5.

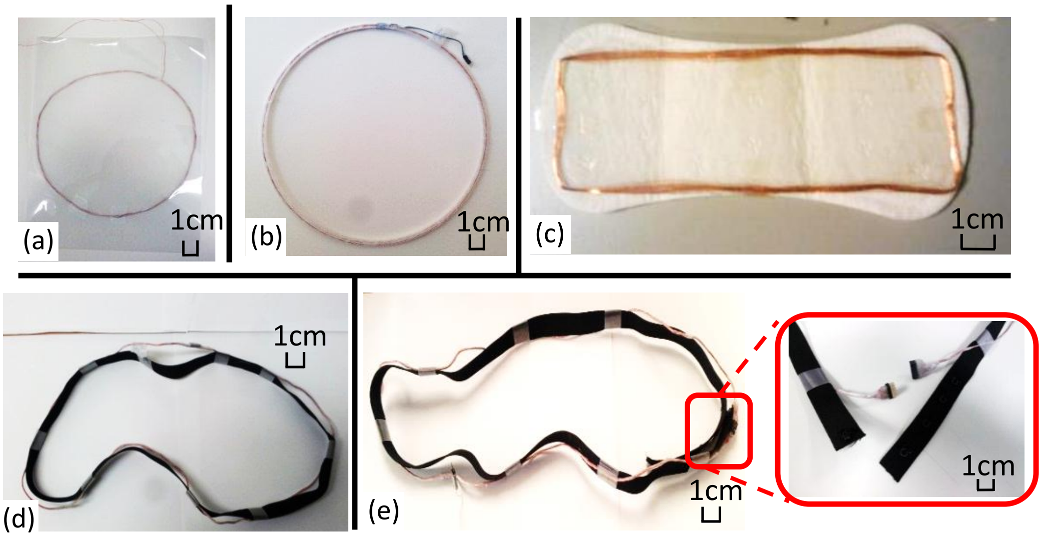

Figure 3.35 Designs of antenna prototypes: (a) antenna was sealed in a laminating paper and was able to be embedded into cloth; (b) a rigid antenna was made on a plastic frame; (c) antenna was embedded in a disposable sanitary towel; (d) elastic antenna which had the coil embedded on an elastic band; (e) belt antenna includes a coil embedded in an elastic band with a multi-pin connector and a row of hooks designed to make the belt adjustable.

For applications where the position and orientation between the sensor device and receiver varies, i.e. for the following animal testing on rabbit (will be introduced in section 5.2), the receiver antenna cannot fit on the rabbit, a multi-antenna receiver system was proposed based on the miniaturised receiver and rigid antennas. For this test, the receiver and antenna had to be fixed to the rabbit cage rather than on the rabbit.

This multi-antenna receiver system was designed based on multiple Bluetooth links for different receivers as a star network. A PC, which worked as a server, was at the centre of this network and can access different receivers individually. It is possible that the implantable sensor device was charged by more than one receiver, and subsequently the data was collected from the receiver through the optimally positioned antenna. This multi-antenna receiver system was developed based on miniaturised receiver and did not need any hardware upgrade; the software running on the server achieved an effective working procedure which will be discussed in the next section. A typical prototype underwent lab testing is shown in Figure 3.36.

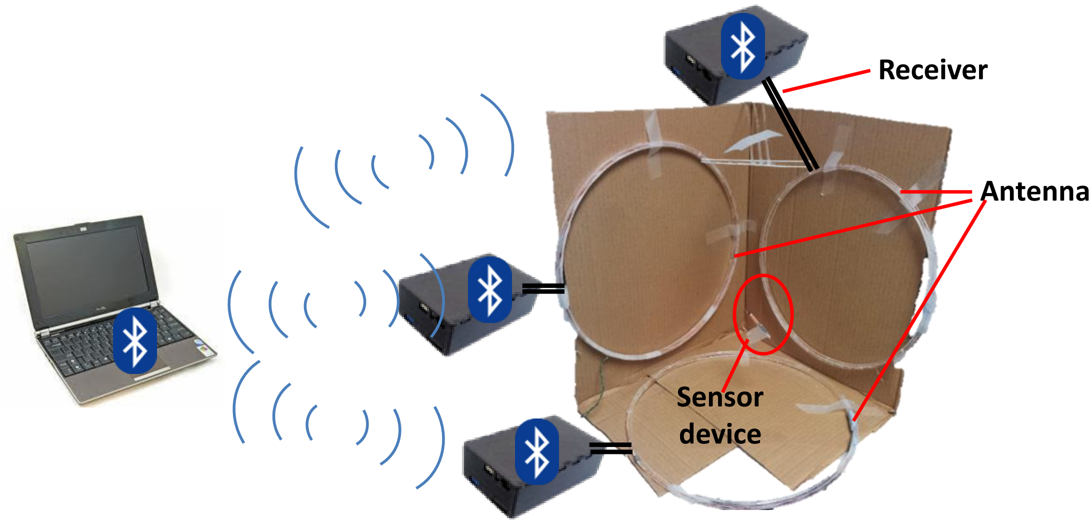

Figure 3.36 A multi-antenna receiver system was tested in the lab. Three small receivers and three rigid antennas were used for 3D coverage. The range of available positions and orientation of the sensor device (marked by yellow circle) was improved using this conformation. The control and coordination of the three separate receivers were achieved by designing software on a PC via individual Bluetooth links; this will be discussed in section 3.4.2.

3.3.3 Summary of wearable receiver development

The wearable receiver is the core portable device in the system and it works as the medium between user and sensor device. Design was constrained by the limitation and requirements from size and power consumption, and also multiple functionalities. After the development of two different versions, the **latest receiver (RV2)** is as small as a cell phone and in lab tests delivered long-term real-time monitoring. A two-board three-layer stacked structure and carefully designed multi-layer PCB layout resulted in a receiver with little interference and high signal performance. A user friendly interface was designed to provide an optimal user experience.

3.4 Design of remote real-time monitoring software

The blueprint of the intended system shown in Figure 3.2 relies on a software module that supports long-term real-time *in-vivo* sensing and monitoring. Following on from the work on the sensor device and wearable receiver, the monitoring software was developed not only to enable remote monitoring but also for system development and debugging.

3.4.1 Monitoring software running on PC for the wearable receiver

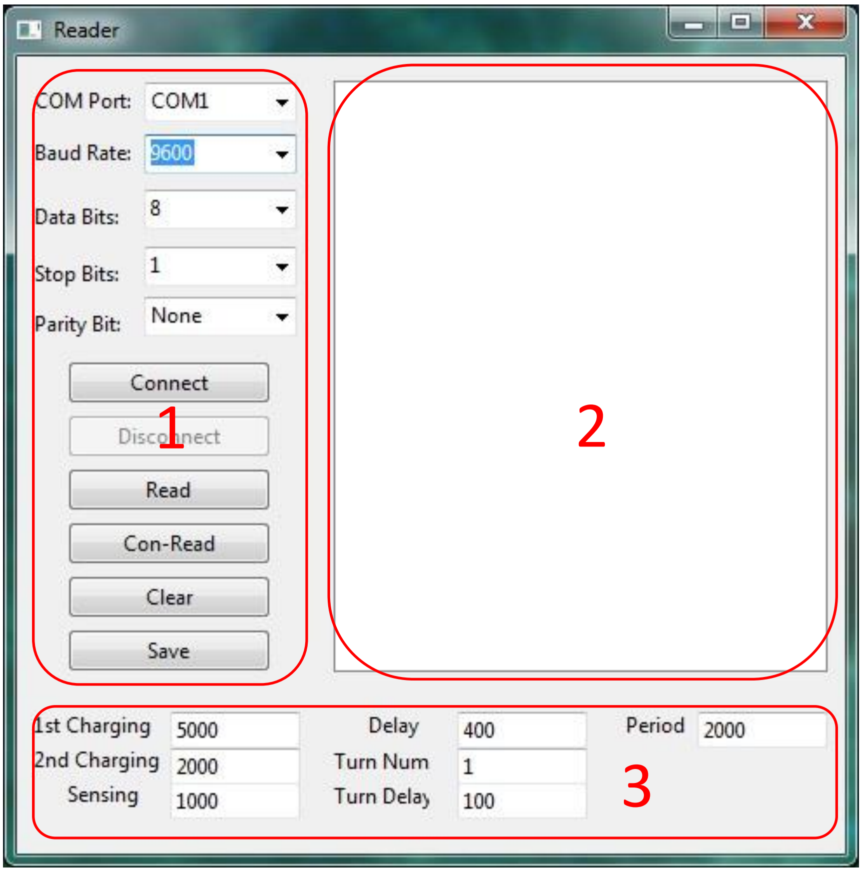

COM Port: COM1
Baud Rate: 9600
Data Bits: 8
Stop Bits: 1
Parity Bit: None

1st Charging 5000
2nd Charging 2000
Sensing 1000
Delay 400
Turn Num 1
Turn Delay 100
Period 2000

Figure 3.37 Snapshot of PC server software: (1) shows connection setting and operation options of the receiver; (2) is the data real-time display frame; (3) identifies the working procedure setting bar.

This PC software was developed based on Java, operating on a Windows operating system, to connect with the wearable receiver for configuration and data communication remotely. It also provided a user interface for real-time display of information. As well as data collection it undertook data storage and post-processing of data. This software enabled the system to perform long-term real-time *in-vivo* sensing. Although the current research work focused on data collection and system debugging, the data processing was undertaken in different software (Matlab, a widely used numerical computing software developed by

MathWorks). Data processing and fast diagnosis can be easily developed and embedded into the software in the future. A snapshot of software graphic user interface (GUI) is shown in Figure 3.37.

There are three working sections as marked in Figure 3.37, including 1) receiver connection setting and operation options, 2) data display frame and 3) the working parameters setting bar. A receiver connection setting was used for the basic settings of the communication link between the server and receiver. Irrespective of whether the physical connection is a wired link (UART (Universal Asynchronous Receiver/Transmitter) cable, USB (Universal Serial Bus) cable) or wireless link, such as Bluetooth, the connections can be all considered as a virtual serial port to software. Therefore, this significantly decreased the complexity of software design and made it easy to configure the connection to the receiver. This software supported both single sampling mode and continuous sampling mode. Obviously, single sampling worked just once after triggering of the “Read” button. “Con-Read” was triggered to enable continuous sampling at pre-set time intervals (as chosen by the operator). Primary processed data, extracted information and debugging information were displayed in the data display frame and stored in text files. The user can gather information easily for data monitoring and system debugging, and further data processing and investigation for further diagnosis based on a database can be undertaken.

The “working procedure setting” bar enabled configuration of the working procedures. The working procedures were the order of tasks that the sensor device undertook, such as a task list including tasks sequence and period. An optimal working procedure results in faster response, lower power consumption, better signal quality and working efficiency. It was crucial to our intended wireless and batteryless sensing device and we undertook research into optimised working procedure based on this powerful software.

Specifically, a procedure was developed to transfer energy efficiently, limit the crosstalk noise between energy transfer and data transmission due to the shared link and shorten the sampling cycle. The flow charts of two optimised working procedures for single sampling and continuous sampling modes are shown in Figure 3.38. Multi-step charging was adopted for the sensor device rather than single charging, as it ensures sufficient energy for each working step and less overall charging time than single charging. A timer was set to start the sampling cycle as a pre-set interval automatically for the continuous sampling mode. More details can be found in Figure 3.38.

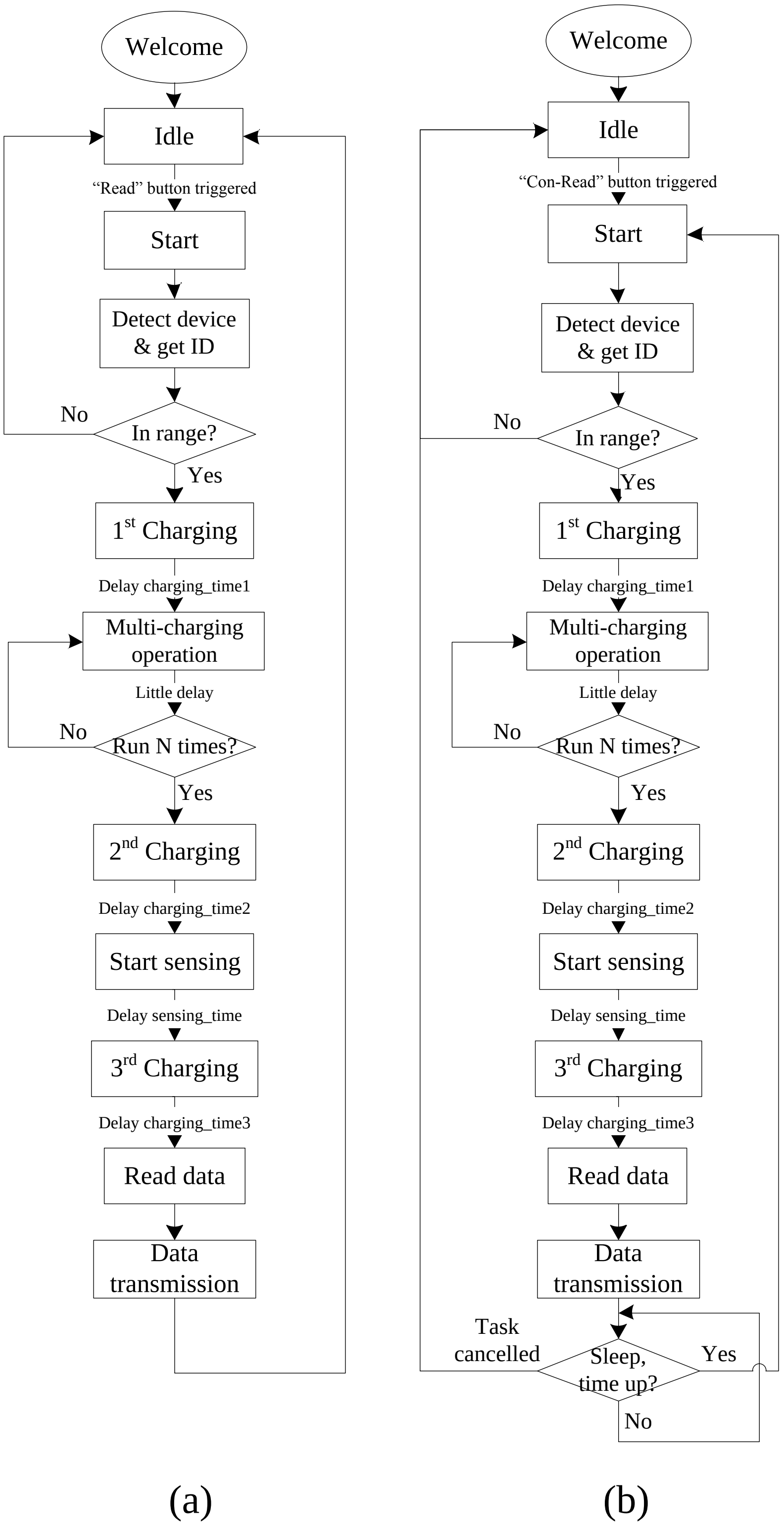

Figure 3.38 Flow charts of working procedures for single sampling and continuous sampling: (a) procedure of single sampling. Firstly, the system enters the idle mode after receiver power up. When the "Read" button was triggered, a sampling cycle was started as follows. The first charging and multi-charging operations ensured the sensor device reserve enough energy for its booting procedure. Second and third charging are used to transfer enough energy to sensor device for ADC working and wireless data transmission respectively. After data transmission, system entered idle mode and waiting for the next sampling cycle; (b) procedure of continuous sampling. The procedure for continuous sampling was quite similar to a single sampling cycle and the difference was the sampling cycle would run automatically in a pre-set time interval. After data transmission, the system entered sleep mode and a timer was counting down to indicate the next sampling cycle. If the "Cancel" button was triggered, the system would return back to the idle mode.

This software provided an accessible interface for system development and long-term real-time *in-vivo* monitoring, and the well-designed parameter setting options enabled optimisation for the working procedures. The time of each sensing cycle was dependent on the charging time of the different charging phases, the charging time was adjusted according to the working distance between sensor device and receiver antenna. Generally, a complete sensing cycle needs around 8s for implanted sensor device charging, sensing and data uploading.

3.4.2 Monitoring software running on a PC for the multi-antenna receiver system

As discussed in section 3.3.2, a multi-antenna receiver system was necessary and developed for applications with varying position and orientation between the sensor device and receiver, such as the situation when the receiver antenna cannot be fixed on the monitored object (e.g. a rabbit confined within a fixed area or lone cage). Similar to the pre-mentioned PC software, a snapshot of the software for multi-antenna receiver system is shown in Figure 3.39.

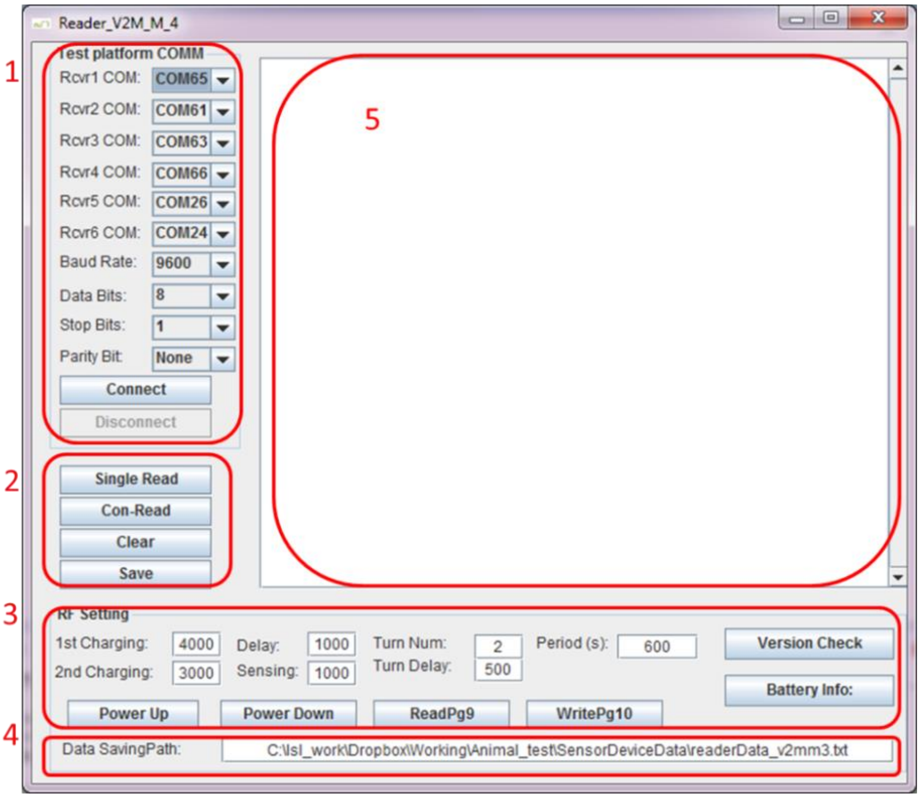
Reader_V2M_M_4

Test platform COMM
Rcvr1 COM: COM65
Rcvr2 COM: COM61
Rcvr3 COM: COM63
Rcvr4 COM: COM66
Rcvr5 COM: COM26
Rcvr6 COM: COM24
Baud Rate: 9600
Data Bits: 8
Stop Bits: 1
Parity Bit: None

RF Setting
1st Charging: 4000
2nd Charging: 3000
Delay: 1000
Sensing: 1000
Turn Num: 2
Turn Delay: 500
Period (s): 600

Data SavingPath: C:\lsl_work\Dropbox\Working\Animal_test\SensorDeviceData\readerData_v2mm3.txt

Figure 3.39 Snapshot of multi-antenna system software: (1) receiver connection setting; (2) receiver operation options; (3) working procedure setting bar; (4) data saving setting; (5) data real-time display frame.

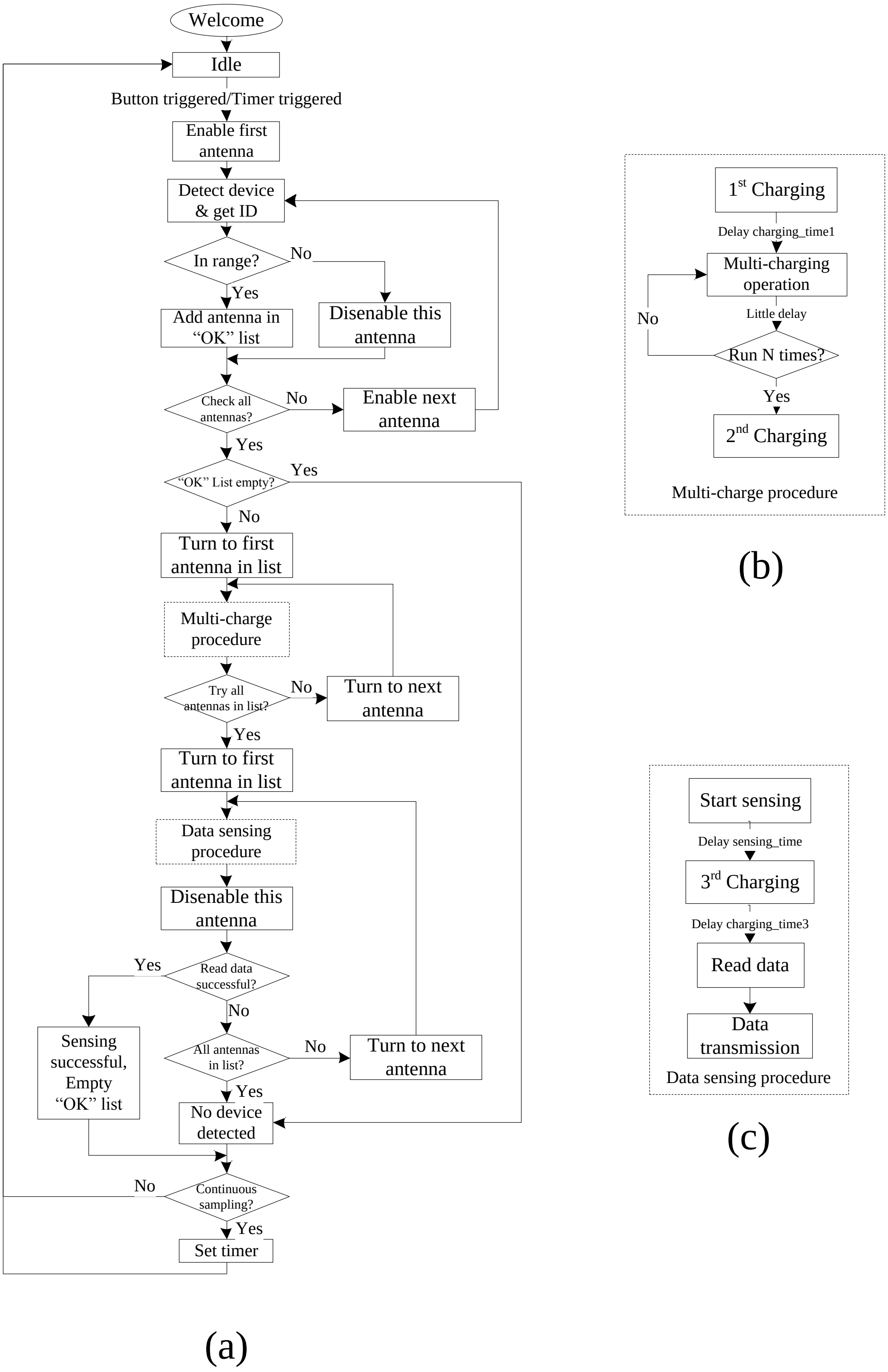

Figure 3.40 Flow charts of working procedures for multi-antenna receiver system: (a) working procedure of multi-antenna receiver system. After system power up, the system enter idle mode and waits for an event trigger, such as button and timer for continuous sampling. Once triggered, a sampling cycle is started. Firstly, antennas are enabled one by one to detect the sensor device, if the device is in range of that antenna, then this antenna is added in the "OK" list (a list of available antennas). After cycling through all antennas, the charging phase of all available antennas is entered in the "OK" list. The charging by all available antennas (one by one) enabled sufficient energy to be delivered to the device, even when the position and orientation were not good. The available antennas read the data successively after the charging phase. Once the data has been retrieved successfully, this sampling cycle is finished. If all available antennas do not get any correct data, then a failed message is sent back to the software; (b) flow charts of multi-charge procedure; (c) flow charts of data sensing procedure.

Figure 3.39 illustrates the similarity of this software to the software introduced in section 3.4.1, and the GUI design was also similar. However some aspects are different. It has capacity for six serial ports connections, and the receivers can be enabled or disabled very easily. To enable flexible debugging, some buttons were added to the working procedure setting bar. By using these debugging buttons, instructions can be sent to the receiver for debugging purposes. For example, “Version Check” and “Battery Info” can read out the version of the receiver and its battery voltage. “Power up” enabled the wireless units on the receiver. A saving path option improved data management. For control of the multi-antenna, the working procedure was also was improved. A flow chart of the specially designed working procedure is shown in Figure 3.40.

Compared to the single receiver system, the challenge for the multi-antenna receiver system was how to coordinate the different antennas and sampling quickly and efficiently, irrespective of the position and orientation of the sensor device.

Once the sample cycle was triggered, three phases would be carried out. The first phase was sensor device detection. All antennas were enabled individually to detect whether the sensor device was in range or not. The antenna which detected the sensor device was added to an “OK” list, resulting in a list of all available antennas for sampling. The second phase was the charging phase; all available antennas charged the sensor device which enabled the sensor device to harvest energy from any available direction. The final phase was sensing, when the sensor device harvested sufficient energy and this sampling cycle was finished after which data was read from the antenna in the optimal position. This multi-antenna receiver system supported single sampling and continuous sampling which used a timer to trigger the sampling cycles. The duration of each sensing cycle time of the multi-antenna receiver system was not only dependent on the total charging time of each antenna, but also the number of available antennas. The charging time of each antenna was adjusted according to the working distance between the sensor device and receiver antenna. Overall, a sensing cycle needs around 20s for a single reading from multi-antenna receiver system (acquired via two available antennas, generally).

The multi-antenna receiver system and its customised software reduced the dependence on the position and orientation between the sensor device and receiver making it suitable for the device testing on rabbit, a free moving animal confined to a lone cage.

3.4.3 Monitoring software running on Android smart terminal

To optimise information sharing and enable the system to be interfaced with more portable applications, mobile devices were also supported. Based on an open source embedded operation system, Android [104], a cell phone monitoring software was developed. This software provided similar functions to the PC monitoring software and enabled the development of a portable real-time *in-vivo* sensing platform. Some snapshots are shown in Figure 3.41.

```
02: 25.55, 2011-10-03   11:50:51
02: 25.60, 2011-10-03   11:51:08
02: 25.61, 2011-10-03   11:52:08
```

select a device to connect
Paired Devices
Reader_1
00:18:B2:01:7A:42
SL8E10
5C:AC:4C:F8:5D:74

Work Parameter Setting
1st Charging Time: 3000
Charging Turns: 2
Turns Delay: 300
2nd Charging Time: 2000
Delay after charging: 100
3rd Charging Time: 1000
Sensing Period: 60000

Figure 3.41 Snapshots of monitoring software on a smart phone. The snapshots were captured from a HTC G1 phone during a temperature continuous measurement and the phone in the picture is just a demo picture: (a) real-time temperature display; (b) menu, including 'connect a device', 'make discoverable' for Bluetooth setting, and 'setting' for working procedure setting; (c) connection of a receiver, list the available receivers and one receiver was found; (d) working parameter setting which was similar to the PC software.

3.4.4 Friendly GUI design of a hand-held all-function receiver

As discussed in the wearable receiver design section (section 3.3.2), a user-friendly interface was developed for the all-function receiver. A 5-way button and 128×64 dot matrix LCD were employed for user input and information output. By embedded programming, a well-designed tree-structure menu was achieved to enable receiver configuration and operation. The general structure and some snapshots of this menu are shown in Figure 3.42.

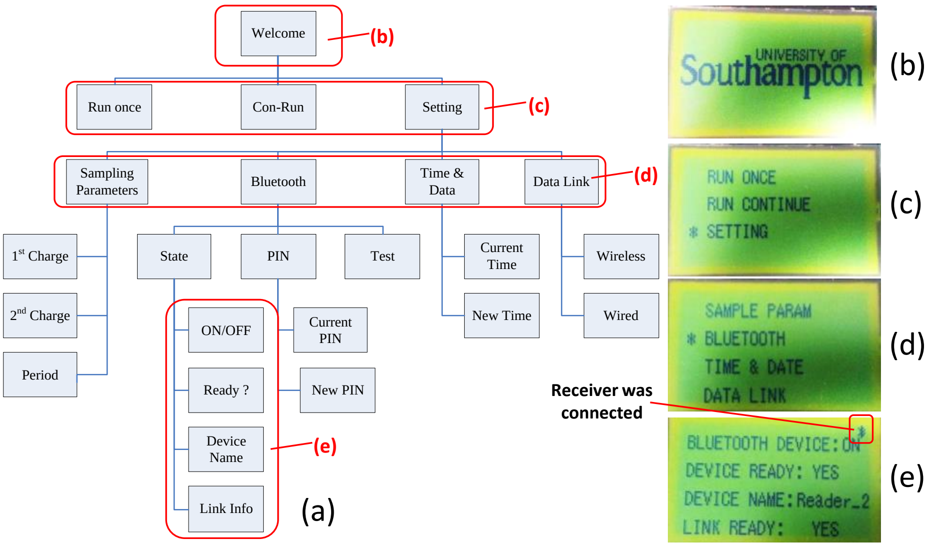

Figure 3.42 Tree structure of full-function receiver GUI and four snapshots of main menu pages: (a) tree structure of full-function receiver GUI showing different menu pages for receiver configuration and operation; (b) welcome page after receiver power on; (c) first level menu and setting selected; (d) second level menu and Bluetooth setting selected; (e) Bluetooth state page. A Bluetooth logo appeared on the top right corner after connecting with a receiver.

3.4.5 Summary of monitoring software development

In parallel with the development of an implantable sensor device and wearable receiver, different software versions were developed for remote real-time monitoring. They included two Java based software designed for the single and multi-antenna receiver systems, Android monitoring software for smart phones and an embedded software GUI which was running on the full function receiver. A friendly user interface not only enabled user access remotely and easily, but was also used for system development and debugging. Furthermore, the optimised working procedure achieved better wireless performance, faster sampling cycle and relatively longer working distance. All software versions were designed with good scalability to enable the developer to readily add more functions.

3.5 Further tests for system performance evaluation

In parallel with system development, prototypes underwent testing on the bench. In addition to the tests discussed in the previous sections, some additional evaluation was undertaken to determine system performance and prove the system was adequate for our intended application.

3.5.1 Power consumption and energy transfer capacity evaluation

Considering our intended implantable sensor device doesn't have any battery and the energy is from wireless energy transfer, quality of sensor device is very sensitive to the power consumption. Its power consumption may affect the maximum working distance and the duration of a measurement cycle. Too much power consumption will extend sensor device charging time and even make it unusable. Therefore, it is necessary to analyse the power consumption of the sensor device. Because sensor device works in different mode during each measurement cycle and different modes have different energy requirement, this experiment was undertaken by analysing power consumption at different modes.

Generally, there are 5 basic modes of sensor device, including active mode, standby mode, low power consumption mode (LPM), ADC working mode and wireless data transmission (Tx) mode. After power on, the sensor device enters active mode to fully boot up. Once finish the initialization, sensor device enters standby mode if there is no task need to do and the power consumption drop from active mode. Low power mode (LPM) is designed to ensure the sensor device utilised minimal power consumption and sensor device disables all unnecessary units to save energy in this mode. To capture the intra-uterine environment data, ADC working mode and Tx mode are required. ADC working mode means sensor device's ADC unit is working to measurement the intended parameters, such as temperature. When the data is ready, sensor device will enter Tx mode to upload the latest data to receiver. The optimal way to keep the power consumption at the lowest level is to leave the device in the LPM as long as possible.

In this experiment, a sampling resistor was connected with the sensor device (SDV2) in series with the power supply cable. The current passing through the sampling resistor was the same as the sensor device consumed, so we can evaluate the device power consumption by monitoring the current in the resistor. Two custom designed embedded programs were developed to put the sensor device in different modes in sequence while an oscilloscope recorded the waveform of the voltage on the sampling resistor as shown in Figure 3.43. The calculated consumption of each item is shown in Figure 3.44.

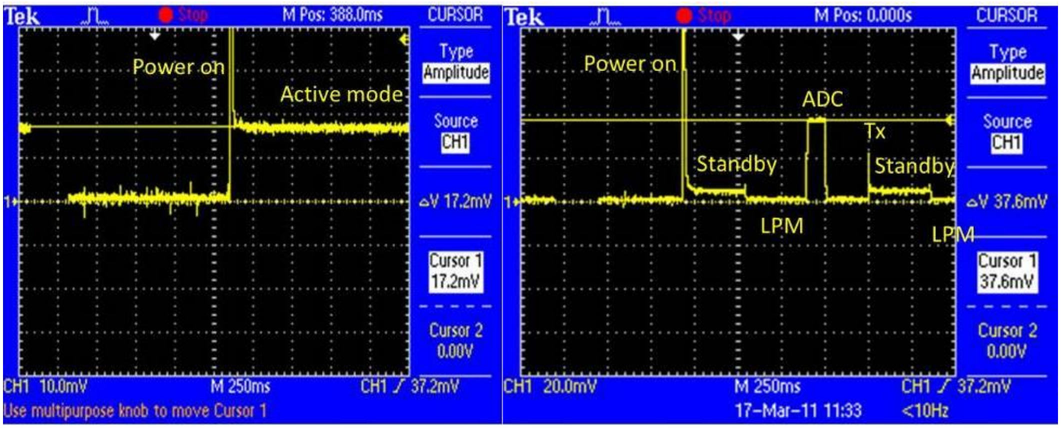

(a) (b)

Figure 3.43 Waveform of sensor device power consumption evaluation: (a) a booting procedure to the active mode. It illustrates the minimum power requirement of the sensor device before entering the standby mode or low power mode. (b) power consumption waveform for a typical working procedure, including power on, standby, ADC working, wireless data transmission and low power mode.

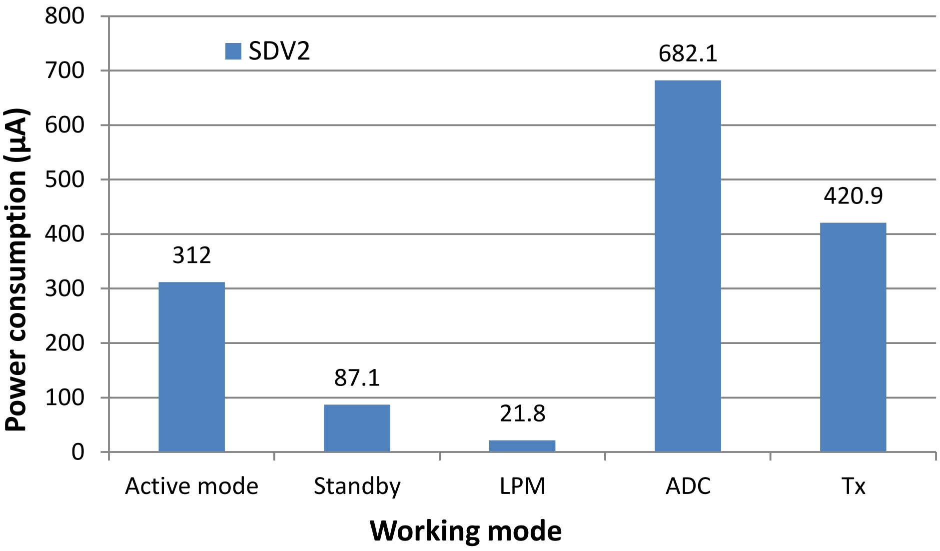

Figure 3.44 Power consumption for different working modes of the sensor device, including active mode, standby mode, low power consumption mode (LPM), ADC working and wireless data transmission (Tx).

From the calculated power consumption, the ADC working and RF data transmission had the highest energy requirements, while the low power mode needed the least energy. Therefore, to save energy and increase the working distance, it is necessary to decrease the ADC and RF unit working time and allow the device to stay in low power mode as long as possible. Based on the above analysis, an optimised working procedure of the sensor device was developed as shown in Figure 3.45.

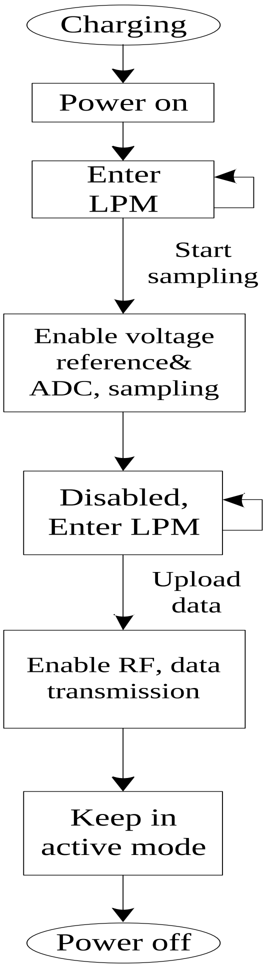

Figure 3.45 Flow chart of typical sensor device sampling cycle. At the beginning of each sampling cycle, the sensor device charges wirelessly and the voltage of the capacitor increases. Once the voltage is high enough to power up the sensor, the device enters LPM immediately to save energy while waiting for instructions. When the sensor device receives sampling instruction, it enables voltage reference, ADC and necessary units for sensing and starts sampling. After the ADC works, sensor device enters LPM immediately and waits for data upload instruction. After data transmission, sensor device kept in active mode until energy is all consumed and powered off.

Once we have the knowledge of sensor device power consumption, we can understand the relation between wireless energy transfer capacity and sensor device maximum working distance. As a capacitor was used to store energy, the energy harvest procedure can be analysed as a capacitor charging, equivalent wireless charging current is a good indicator for the evaluation of wireless energy transfer capacity. Treating the capacitor as charging at a constant current (equivalent charging current), gives the equations below. Recording the voltage waveform of the energy storage capacitor gives the equivalent charging current.

$$Q = U \cdot C = I_{eq} \cdot t \qquad (3.5\text{-}1)$$

$$I_{eq} = (U \cdot C) / t \qquad (3.5\text{-}2)$$

where Q is the electrical charge stored in the capacitor, U is the voltage applied to the capacitor, C is capacitance of capacitor (100uF), I_{eq} is the equivalent charging current and t is charging time.

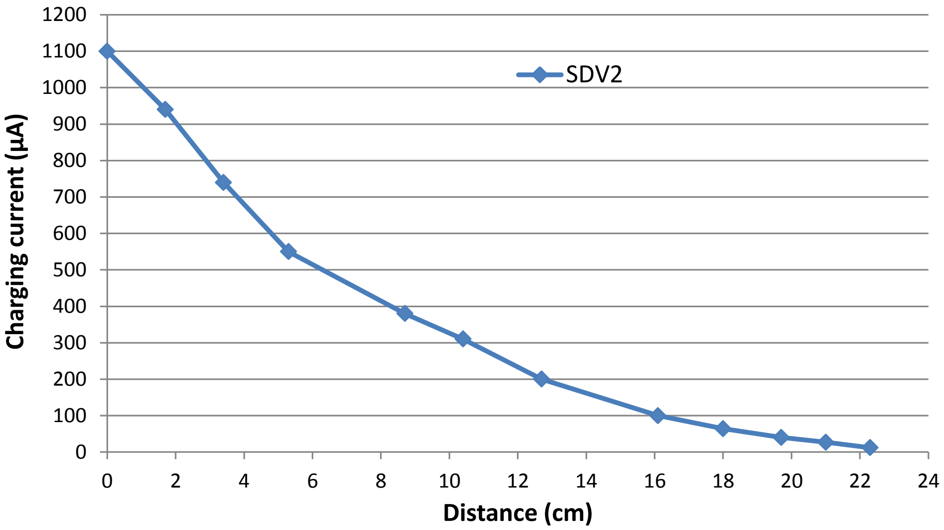

Figure 3.46 Experimental equivalent charging current of sensor device at different distance.

This experiment was undertaken based on sensor device V2 and a 20cmX20cm receiver antenna. From the experimental equivalent charging current results, we observed that the current decreases sharply when the working distance increases. Considering the minimal power consumption of sensor device at LPM is around 22µA, this can also be seen as the minimal charging current for sensor device sampling. If a charging current is smaller than this line, the sensor device would not get enough energy to run a sampling cycle. In this experiment, the sensor device working distance is around 21cm.

3.5.2 Electromagnetic field evaluation of the wearable receiver

Electromagnetic radiation exists in all kinds of electronic systems, especially in wireless communication systems. In our final application, the sensor device will be power by a wireless link from the receiver and also data transmission will be achieved on the same link. Considering the influence of wireless signals, the electromagnetic field of the receiver was evaluated. In this experiment, the wireless signals influence on human tissue was also discussed for the system safety in intra-uterine application.

Because the magnetic field (H-field) and electric field (E-field) strength decrease rapidly with increasing distance, we focus on the near field region around the antenna, a distance range from 0 to 52mm. The test bench set up is shown in Figure 3.47.

]

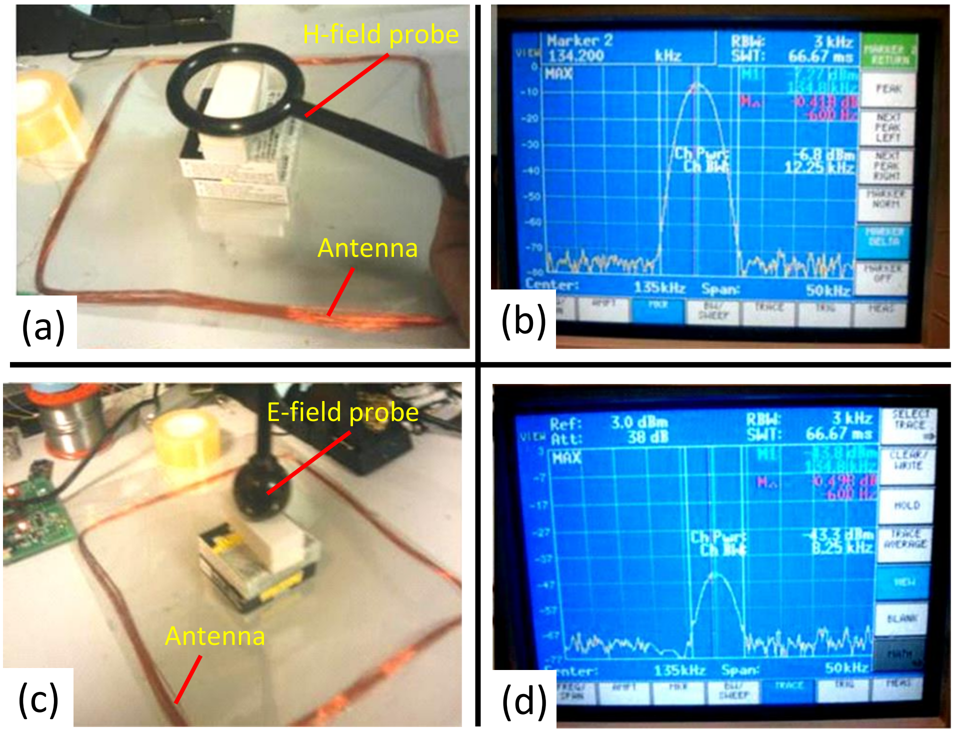

Figure 3.47 Photo and signal from the spectrum analyser: (a) H-field probe was used to measure H-field; (b) A sample waveform from H-field probe;(c) E-field probe was used to measure E-field; (d) A sample waveform from E-field probe

Probe Set HZ-11 is a professional suite from Rohde&Schwarz for E and H near-field measurements. It comprises 3 passive H-field probes (electrically shielded loops with diameters of 1cm, 3cm, and 6cm) and 2 passive E-field probes (one rod and one spherical probe). The H-field probes have the directionality of loop antennas. Their sensitivity is proportional to their diameter. The E-field probes are designed for omnidirectional signal reception over a wide frequency range. The spherical probe has a higher sensitivity than the rod probe. We used the 6cm loop H-field probe and spherical E-field probe in this test.

Based on electromagnetic theory, we used a two-loop antennas model. For simplified calculations, consider the situation in the central part of the magnetic field. The receiver antenna is the primary coil and the H-field loop probe is the secondary coil, as shown in Figure 3.48.

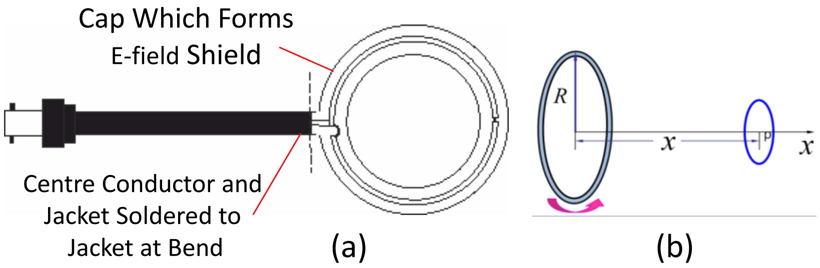

Figure 3.48 Internal structure of loop H-field probe (a) and two-loop antenna model (b).

As a consequence of the current in the primary coil, an H-field is produced, and the secondary coil has an induction current when it enters this H-field. According to electromagnetic field theory, a larger current makes a stronger magnetic field, and results in a bigger induction current in the secondary coil. Using a Spectrum Analyser and H-field Probe, the received power can be recorded and the voltage and current can be calculated using the formulas below.

$$P_{dBm} = 10\log\frac{P_{mW}}{1mW} \qquad (3.5\text{-}3)$$

$$P_{mW} = \frac{U^2}{R_0} = I^2 R_0 (R_0 = 50\Omega) \qquad (3.5\text{-}4)$$

where PdBm is receiving power in dBm, PmW is receiving power in milli-watt and R_0 is the resistance of the H-field probe, 50 Ohm. The loop antenna H-field strength can be calculated using the formula:

$$H = \frac{N \cdot IR^2}{2(X^2 + R^2)^{\frac{3}{2}}} \qquad (3.5\text{-}5)$$

where N is the turn number of the H-field probe, I is the current of H-field probe, X is the distance between the test point and antenna, and R is the radius of H-field probe. The calculated results can be found in Table 3.8. Based on the results of the H-field strength, a decrease in the H-field is seen with increasing distance. However, the change is not significant, and it is probably because the loop probe is much smaller than the receiver antenna and the test distance is not far relative to the antenna size.

Table 3.8 Calculated results about magnetic field strength

Distance (mm)	Receiving power (dBm)	power (µW)	voltage (mV)	voltage (dBmV)	current (µA)	current (dBµA)	Magnetic field strength (A/m)
0	-4.09	389.942	139.632	42.900	2792.640	68.920	0.047
11	-4.31	370.681	136.140	42.680	2722.795	68.700	0.045
22	-4.78	332.660	128.969	42.210	2579.378	68.230	0.043
37	-5.85	260.016	114.021	41.140	2280.421	67.160	0.038
52	-7.27	187.499	96.824	39.720	1936.489	65.740	0.032

Similar to H-field measurements, the E-field parameters can be calculated based on a spherical capacitor model using the receiving power from Spectrum Analyser. The internal structure of the spherical E-field probe and spherical capacitor model are shown in Figure 3.49.

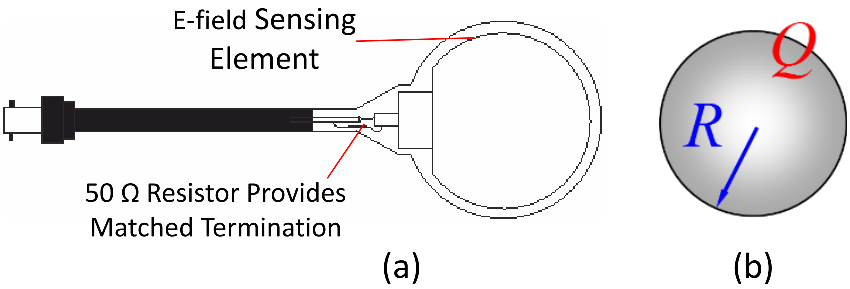

Figure 3.49 Internal structure of spherical E-field probe (a) and spherical capacitor model (b)

The E-field can be regarded as a charged spherical capacitor and the E-field of a homogeneous charged sphere can be calculated using the formula below.

$$E = \frac{Q}{4\pi\varepsilon_0 \cdot r^2} \qquad (3.5\text{-}6)$$

where E is E-field strength, Q is the electric charge, ε_0 is the dielectric constant of free space and r is the radius of sphere. Q is:

$$Q = U \cdot C \qquad (3.5\text{-}7)$$

where U is the potential difference and C is the capacitance.

The capacitance of spherical capacitor is given by:

$$C = 4\pi\varepsilon_0 \cdot r \qquad (3.5\text{-}8)$$

where r is the radius of spherical capacitor. The calculated results are shown in Table 3.9.

Table 3.9 Calculated results about electric field strength

Distance (mm)	Receiving power (dBm)	Receiving power (μW)	voltage (mV)	voltage (dBmV)	current (μA)	current (dBμA)	Electric field strength (V/m)
0	-38.8	0.132	2.567	8.190	51.347	34.210	0.143
11	-40.1	0.098	2.210	6.890	44.209	32.910	0.123
22	-41.4	0.072	1.903	5.590	38.064	31.610	0.106
37	-43	0.050	1.583	3.990	31.660	30.010	0.088
52	-43.8	0.042	1.444	3.190	28.875	29.210	0.080

Based on the calculated results, a decrease in E-field strength is observed. Also the specific absorption rate (SAR) can be calculated. SAR is a measure of the rate at which energy is absorbed by the body when exposed to a RF electromagnetic field [105]. It is defined as the power absorbed per mass of tissue and has units of watts per kilogram (W/kg).

It can be calculated from the electric field within the tissue as:

$$SAR = \int_{sample} \frac{\sigma(r)\left|E(r)\right|^2}{\rho(r)} dr \qquad (3.5\text{-}9)$$

where σ is conductivity of the tissue (S/m), ρ is mass density of the tissue (kg/m^3) and E is electric field strength (V/m). The typical values of conductivity and weight density of human tissues are shown in Table 3.10. SAR can be also considered at a point as [106].

$$SAR = \frac{\sigma\left|E\right|^2}{\rho} \qquad (3.5\text{-}10)$$

Table 3.10 The physical properties of some human tissues, including relative permittivity, conductivity and weight density [90, 107-109]

Tissues	Conductivity (s/m)	Weight density (kg/m^3)
Fat	0.024769	916
Stomach	0.548849	1126
Heart	0.26852	1059
Muscle	0.42782	1059
Liver	0.136344	1151
Cerebellum	0.169251	1035.5
Kidney	0.216068	1147
Bone	0.021771	1500
Small intestine	0.681966	1153
Prostate	0.475941	1151
Skin	0.002848	1125
Lung	0.300042	563
Uterus	0.5	1052
Estimates of SAR are based on the results from earlier work and some published data on different human tissue properties as shown in Table 3.10 [90]		

The calculated SAR for the human uterus at different distances is shown in Table 3.11. The peak advised SAR under current USA standards is below 1.6W/kg, and the European Union standard is below 2W/kg [106]. Compared with the results calculated in above experiments, the calculated SAR in the system is much lower than the standards for either Europe or USA.

Table 3.11 Calculated results of the SAR for the human uterus for electromagnetic field.

Distance(mm)	SAR(W/kg)
0	9.67E-06
11	7.17E-06
22	5.31E-06
37	3.68E-06
52	3.06E-06

3.5.3 Testing signal transmission

Experiments mentioned in previous sections demonstrated good system performance in air, however, the blocking phenomenon from the other media, such as water and tissue have to be considered according to our intended application. In order to evaluate the performance of wireless energy transfer and communication in real conditions where the sensor device may be surrounded by tissue and liquid, a serial blocking test was undertaken in lab.

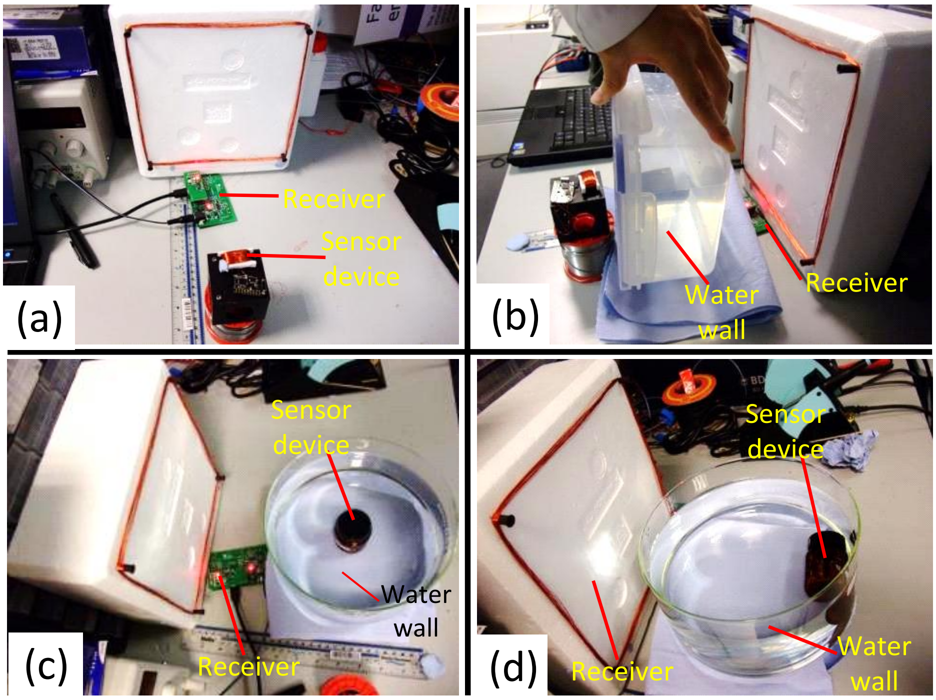

Figure 3.50 Blocking test for a sensor device with a 2.2cm X 0.6cm X 1cm antenna and a receiver with 20cm X 20cm antenna. The blocking was evaluated by comparing the best working distance in and out of the water. The sensor device was unpackaged and it was put into a little bottle to protect it from water: (a) test in air for the best working distance without any blocking; (b) test using water wall; (c) test in the centre of water bath; (d) test at the far end of water bath.

To visually evaluate the impact on wireless performance from the media around the sensor device, the best sensor device working distances were compared between in air and in specific media. Figure 3.50 shows some of the details of these experiments. As the density of human tissue is similar to water, we used water as the blocking media. Firstly the best working distance in air was marked and then different shaped water walls were put between the sensor device and receiver. The maximum sensor device working distance was almost constant with and without water well, so there was no obvious blocking phenomenon in this test. Furthermore, to mimic the intended body implantation, a packaged sensor device was wrapped by chicken meat and then repeated the block test. Similarly, there was no obvious change in the maximum working distance between in air and wrapped by tissue. Subsequently, the system worked well in the tests on pigs and rabbits without obvious deterioration which will be introduced in chapter 5.

The resonant frequency of our system is 132.4 KHz, which is much lower than conventional wireless communication system. Low resonant frequency is predicted to generate good propagation characteristics through various media, and good noise immunity from existing wireless communication systems. Based on these testing, we do not anticipate any limitations to the system wireless performance due to blocking of signal by tissue when the sensor device is deployed in the uterus.

3.5.4 Long-term in-water test

After sensor device encapsulation, a long-term test in water is required to evaluate the waterproofness of the sensor device. Considering the water permeation will result in sensor device circuit shortage and then system failure, the continuous measurement will be terminated, therefore, a continuously temperature recoding test is designed and the lifetime of the tested system is directly related to sensor device waterproofness.

A sensor device which was packaged by Epoxy (PX804C, single layer packaging) was immersed in a water bath and set to continuously record temperature. After more than 1 month (27/11/2012-29/12/2012), the temperature data was still available and valid (daily temperature variations are shown in Figure 3.51), this means the tested sensor device worked well after more than 1 month immersion in water and the waterproofness of packaged sensor device can be predicted as good enough for more than 1 month in water environment.

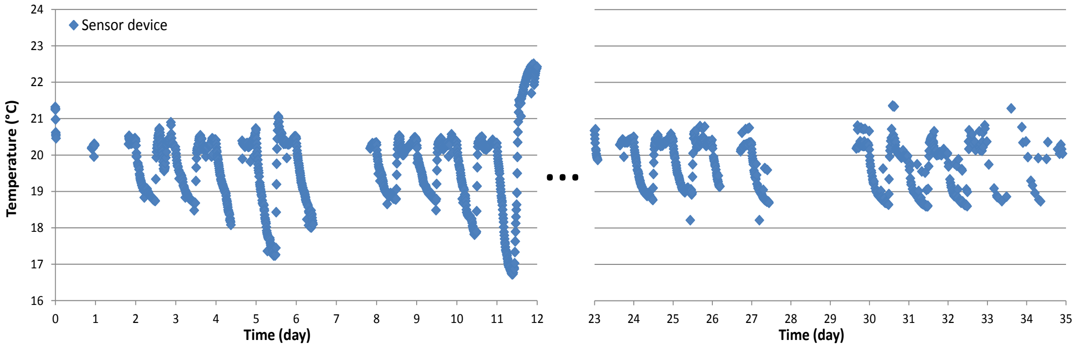

Figure 3.51 Temperature variation during long-term testing in water. The gap in the temperature reading was due to the recording system being interrupted during a power down. The packaged sensor device was immersed in water for the duration of the test.

For animal testing and eventual human testing, a three-layer encapsulation solution was proposed with improved waterproofness than the single layer packaging for the bench test as it has thicker insulation layer. Therefore, the encapsulation methods we developed are adequate for the next phase of development, testing and intended application.

3.5.5 Summary of system performance evaluation

For improved evaluation of the prototype sensing platform, some additional evaluations were undertaken. The power consumption test provided the power consumption data for the sensor device for different tasks. The electromagnetic radiation was investigated and the calculated SAR of the prototype was much lower than the standards for either Europe or USA. No obvious blocking phenomena were observed in the blocking test and sensor device worked reliably for more than 1 month in a long-term in-water test. The specification of the latest system prototype is shown in Table 3.12.

Table 3.12 Specifications of the system prototype.

Sensor device size	Φ4.35±0.06 X 34.25±0.98 mm
Sensor device weight	1.10±0.006 g (unpackaged) 1.90±0.24 g (3-layer epoxy packaged)
Receiver size	65X40X21 mm
Receiver weight	37.25±0.68 g
Working frequency	134.2 KHz
Working range(best)	23 cm
Sensor device power consumption	21.8 μA (LPM) 312 μA (Active) 682.1 μA (ADC working)
Blocking by water	No obvious attenuation
Blocking by meat	No obvious attenuation
Working in water	>30 days

Chapter 4

Design of implantable biosensors

Implantable biosensors are at the centre of the intended sensing platform for intra-uterine environment monitoring including temperature, dissolved oxygen concentration (DOC) and pH. The implantable biosensors are required to be as small as practical and optimised for use on an implantable device. Specifically, the sensors need to be constructed to work reliably within the uterus. This requires considerations of safety, device reliability and energy usage. The sensors will need to be produced in line with current regulation guidelines on implantable medical devices.

In this chapter, implantable biosensors for temperature, DOC and pH are discussed separately and the development details of each biosensor are introduced.

4.1 Design of the implantable temperature sensor

4.1.1 Methods for human body temperature measurement

Different types of thermometers are used in routine clinical body temperature measurements. They can be divided broadly into two types: non-electrical and electrical thermometers [110].

Non-electrical thermometers have been used for many decades, and the most common one is the mercury-in-glass thermometer. The liquid crystal thermometer is another conventional temperature indicator. Temperature sensitive liquid crystals are packaged in a plastic strip and their colour changes with temperature. Mercury-in-glass thermometer and liquid crystal thermometer are simple, cheap and easy to use; however, their resolution is limited to around 0.1°C, with a slow response. The mercury-in-glass thermometer has been banned for medical use in many countries since 2012 due to the toxicity of mercury. Infrared thermometers are based on the measurement of the infrared thermal radiation of objects where the radiant power is converted to an electronic signal and then temperature reading. This kind thermometer has a fast response and is a non-contact temperature measurement. They are designed as handheld devices and are relatively large due to their complex electronic components. Batteries are required for the infrared detector and electronic circuit.

Similar to the infrared thermometer, there are some technologies are under development for temperature measurement [110]. For example, based on electromagnetic radiation detection, microwave radiometry can be used to measure temperature. Magnetic resonance thermometry has also been developed for temperature measurement relying on the temperature dependent physical parameters which affect the magnetic resonance signal. Ultrasound penetrates objects and the absorption correlates with the object temperature. The measurement of the speed and frequency spectrum of back-reflected ultrasound provides an estimation of the temperature of the object. Similarly, back-reflected near infrared light can also be used for temperature measurement because light absorption is highly correlated to object temperature. Overall, these technologies don’t need contact with the object and can provide more accurate readings than the mercury-in-glass thermometer. However, these devices required complex electronic circuit and have relatively high power consumption rates.

A range of electrical thermometers have been developed for temperature measurement, these include thermocouples, platinum resistance thermometers (PRTs) and thermistors [110, 111]. A thermocouple comprises two different metallic conductors. Predictable electric potentials are produced at the junction of these two conductors at different temperatures. Thermocouples function over a wide temperature range making them suitable for industrial measurement and control of temperature. However, a limitation of thermocouples is the size. Reduction of a thermocouple to a size suitable for implantation application would be difficult. They are also limited to an accuracy of 1°C. PRTs report temperature through correlation of the resistance of a platinum element with temperature. PRTs are more accurate with better repeatability than a thermocouple, but the temperature sensitive element is usually fragile and requires complex fabrication. Moreover, the sensitivity of PRTs is limited compared with other thermometers.

Thermistors are widely used for temperature measurement and have the advantage of small size and high precision. Thermistors can be classified into two types: positive temperature coefficient (PTC) and negative temperature coefficient (NTC) thermistors, depending on the temperature coefficient of resistance. PTC thermistors are employed as sensors to protect against overheating because their resistance rises suddenly at a predetermined critical temperature. An NTC thermistor is suitable for our intended application, because they are highly sensitive, very small and easy to embed into microsystems. Although they have a non-linear response to temperature in their wide measurement range, they can be approximated to linear when used within a small temperature range and after calibration, good accuracy of temperature readings can be achieved. A thermistor (MA100, General Electric Co.) has been used to monitor the intra-vaginal temperature [76, 77]. The thermistor was fixed into a tampon-like enclosure, and wired to a processor unit placed outside the body. Communication between the sensor and computer was via a Bluetooth link. This device achieved continuous, *in-vivo* measurement of female intra-vaginal temperature.

4.1.2 Development of the temperature sensor

After consideration of the environment where sensor is going to be used, and the comparison of different approaches for temperature sensing, a thermistor was considered suitable for our application. However, the development of an implantable temperature sensor doesn’t have to only consider size and power consumption of sensor, but also the size and power consumption of electric circuit and complexity of the construction.

4.1.2.1 **Discrete digital output temperature sensor**

To accelerate the development of the sensor device and debugging of the basic platform, a TSic506F (Innovative Sensor Technology) was used on the first sensor device (SDV1) as shown in Figure 3.12. TSic506F is a rapid response, low-cost temperature sensor IC with a digital output. The digital output gives easy access to temperature readings with fewer requirements for the hardware. It is a three-pin in-line packaged component with dimensions of 5mmX5mmX5mm. The power consumption is typically 45µA and it can be easily built into a device. Although this sensor was very helpful at the beginning of the sensor device development, calibration was hard to achieve due to built-in circuitry and the resolution of 0.1°C and accuracy of ±0.1°C were inadequate for the final application.

4.1.2.2 **MCU built-in temperature sensor**

Due to the size and accuracy limitation of the Tic506F, the built-in temperature sensor of MCU (MSP430F2013, Texas Instruments Inc.) was also considered, which decreases the sensor device size. The most significant advantage of this type of sensor is the size. The sensor and the circuit are already embedded in the MCU, and the MCU internal voltage reference and ADC can be used for the built-in temperature power supply and conversion without increasing the sensor device size. The sensor device version 2 (SDV2) and version 3 (SDV3) were all developed with this sensor.

The technical specification of the built-in temperature sensor is in the datasheet [112]. A formula showing the relation between the analogue output and temperature variation for the MCU sensor is.

$$V_{sensor} = TC_{sensor} \cdot T[^{\circ}C] + V_{sensor}(T_A = 0^{\circ}C)[mV] \qquad (4.1\text{-}1)$$

where V_{sensor} is the voltage reading of the built-in sensor, TC_{sensor} is sensor temperature coefficient, T [℃] is the temperature in °C and V_{sensor} (TA=0˚C) is the sensor output at 0˚C. After transformation, the temperature can be calculated as:

$$T[^{\circ}C] = (V_{sensor} - V_{sensor}[T_A = 0^{\circ}C]) / TC_{sensor} \qquad (4.1\text{-}2)$$

$$T[^{\circ}C] = V_{sensor} / TC_{sensor} - V_{sensor}[T_A = 0^{\circ}C] / TC_{sensor} \qquad (4.1\text{-}3)$$

Empirical values of TC_{sensor} and V_{sensor} at different temperatures are shown in Table 4.1. The resolution of the built-in temperature sensor is about 0.018 ℃ (The sensor temperature coefficient is 1.32mV/K, built-in voltage reference is 1.2V and ADC is 16-bit). The values are found to vary with the sensor temperature coefficient and offset of output voltage, which results in individual differences among different individual sensors. Therefore, calibration of each sensor is necessary.

Table 4.1 Built-in temperature sensor properties, including the temperature coefficient, sensor offset voltage and sensor output voltage [112].

Parameter	**Test conditions**	**VCC**	**Values**			**Unit**
			Minimum	**Typical**	**Maximum**	
TC_{sensor}, **sensor temperature coefficient**	-	-	1.18	1.32	1.46	mV/K
$V_{offset,sensor}$, **Sensor offset voltage**	-	-	-100		100	mV
V_{sensor}, **sensor output voltage**	T_A=85°C	3V	435	475	515	mV
	T_A=25°C	3V	355	395	435	
	T_A=0°C	3V	320	360	400	

A temperature calibration system was constructed at the National Oceanography Centre (NOC), University of Southampton. The system is a temperature controlled instrument for temperature sensor calibration and performance evaluation. The SDV3 was calibrated and tested using this system (after encapsulation). The system setup can be seen in Figure 4.1.

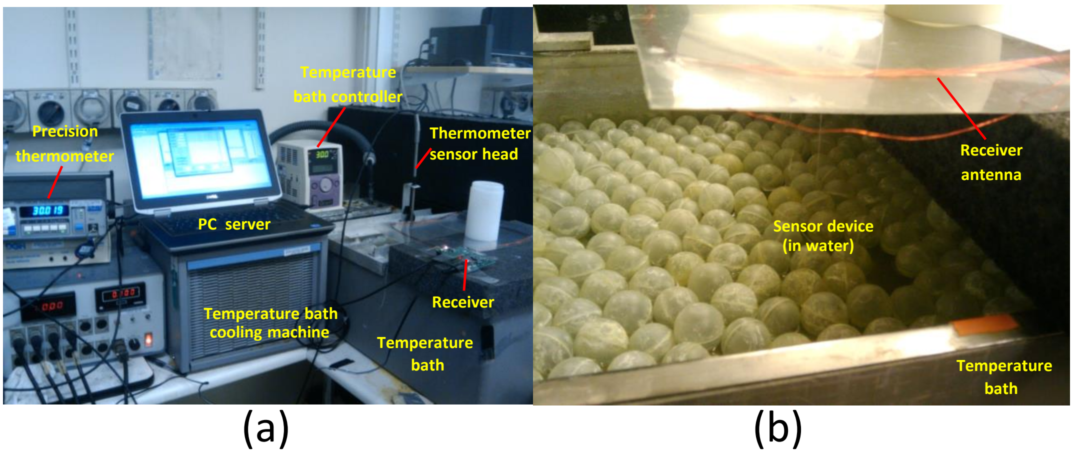

Figure 4.1 The setup for temperature sensor calibration system in NOC: (a) instrument connections. The sensor device is immersed in a temperature controlled bath which is connected to a temperature controller and a cooling machine. The temperature bath controller has an internal temperature sensor and a heater to heat up the water in the bath. By controlling the heater and cooling machine, the temperature controller maintains a stable temperature. The receiver is wired to a PC server for data logging. A precision thermometer is mounted close to the sensor device as a reference reading; (b) setup of the receiver and sensor device. The sensor device is immersed in the water and the antenna of the receiver is set toward to the sensor device.

The temperature calibration system included a water bath in which the water temperature was controlled by a temperature controller and cooling machine. The temperature bath contains water covered by a layer of plastic balls to decrease water evaporation. The temperature bath controller keeps the water temperature stable by switching on a heating bar and cooling machine using the feedback from the bath thermometer. The sensor device was immersed in the water and a receiver was positioned on top of the water bath. The antenna was fixed on a foam sheet aligned toward the sensor device. Due to the distance between the sensor device and bath controller thermometer, a precision thermometer was used to provide a more accurate reference reading and this sensor head was placed in the water bath as close as possible to the target. A PC server recorded the sensor device reading and reference reading simultaneously. This experiment was based on a receiver with a 20cm X 20cm antenna and the packaged sensor device V3 as shown in Figure 3.21. The temperature bath was set to change the temperature every hour from 30°C to 45°C at a constant step of 1°C. The temperature variation measured by the thermometer is shown in Figure 4.2.

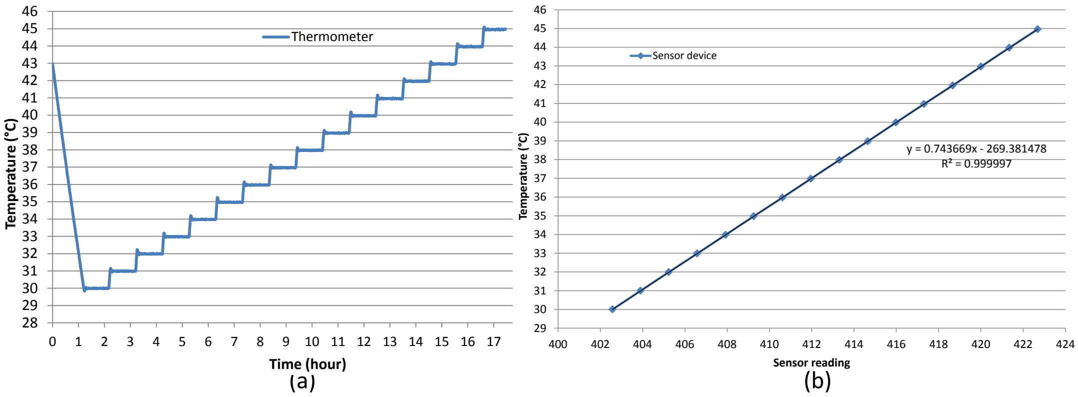

Figure 4.2 Built-in temperature sensor calibration: (a) temperature calibration procedure and the temperature variation captured by a precision thermometer. The temperature was changed every hour from 30°C to 45°C at a constant step of 1°C; (b) Response curve of sensor device with reference reading from a precision thermometer. A good linear response is illustrated.

The temperature bath required some time to reach a stable state so the temperature readings were taken after 30 mins when the temperature changed were used for calibration. A good linear response is seen, as shown in Figure 4.2b. The trend line equation used to demonstrates a correlation coefficient of 0.9999.

$$y = 0.7437x - 269.38 \qquad (4.1\text{-}4)$$

Based on the formula (1.1) and the trend line above, we have:

$$\begin{cases} 1/TC_{sensor} = 0.7437 \\ V_{sensor}[T_A = 0^\circ C]/TC_{sensor} = 269.38 \end{cases} \qquad (4.1\text{-}5)$$

and transformed as:

$$\begin{cases} TC_{sensor} = 1.3446 \\ V_{sensor}[T_A = 0^\circ C] = 362.2159 \end{cases} \qquad (4.1\text{-}6)$$

According to the acceptable range of these two parameters from the datasheet in Table 4.1, the result is in the normal range of values. Therefore, the calibrated built-in temperature sensor operates according to:

$$T[^\circ C] = (V_{sensor} - 362.2159)/1.3446 \qquad (4.1\text{-}7)$$

Based on this updated formula, we carried out a test to compare the readings from the calibrated sensor device and the precision thermometer. The temperature bath was set to change the temperature every hour from 30°C to 46°C at a constant step of 1°C. Seventeen hours is a testing cycle which temperature increases from 30°C to 46°C and a testing of two and half cycles is shown in Figure 4.3, the red line is the reference reading from the precision thermometer, and the blue line is the sensor device readings. Clearly there is close alignment between the precision thermometer and the test sensor device.

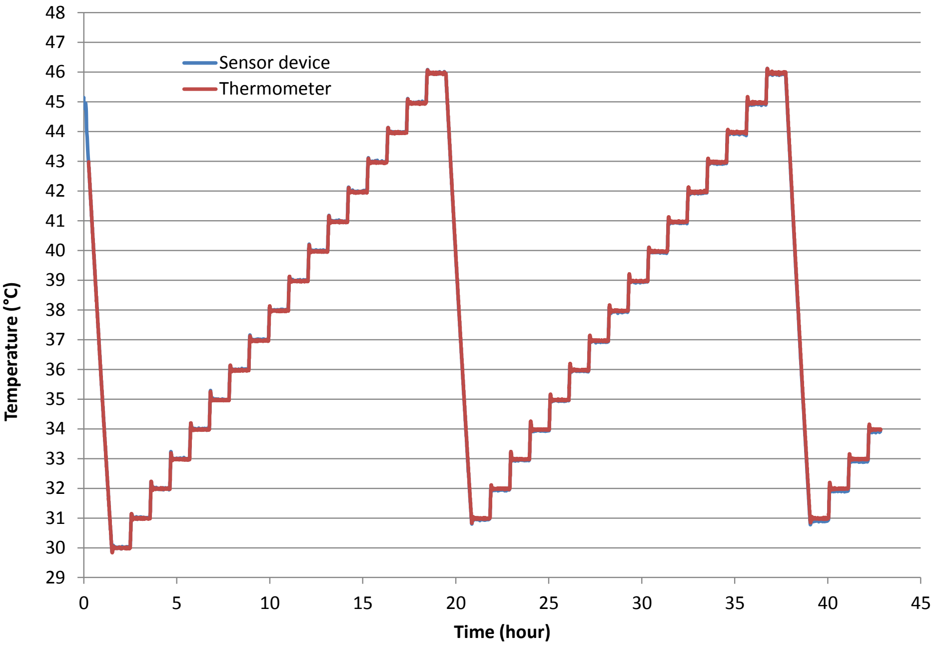

Figure 4.3 The comparison between the temperature readings from precision thermometer and sensor device. Red line is the readings from precision thermometer and blue line is from a sensor device.

However, a difference can be found for later time points from Figure 4.3. The error in the temperature readings of the built-in temperature sensor compared with the precision thermometer is shown in Figure 4.4. The mean difference in the first cycle was 0.012°C, which then decreased to -0.024°C and -0.066 in following cycles.

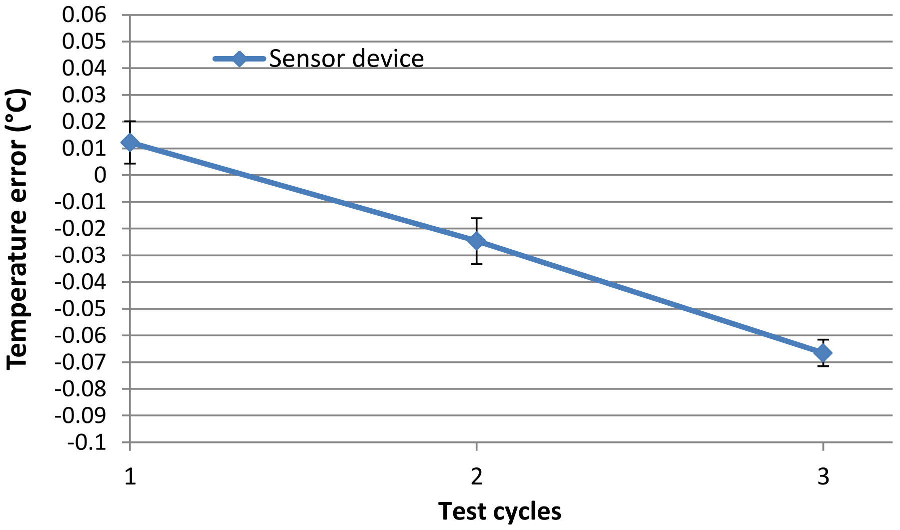

Figure 4.4 The error in the temperature readings of the built-in temperature sensor compared with the precision thermometer.

This test revealed a long-term drift in the built-in temperature sensor which could be attributed to the built-in sensor fabrication and internal circuit stability, such as the built-in voltage reference, built-in constant current source and resistors. As we cannot manipulate the built-in components, or carry out optimisation, it is impossible to eliminate this drift from the hardware for this thermistor.

The built-in temperature sensor used in SDV3 is designed for general applications and has a large working range with a limited temperature coefficient. A large working range is redundant in the context of normal variations in human body temperature. Therefore the temperature coefficient needs to be improved for better resolution. However it is hard to improve the sensor’s working range and coefficient, as the circuits are embedded in the chip and cannot be altered. The MCU package also influences the response time, and the stability of the temperature sensor. Furthermore, the power consumption of the built-in temperature sensor measurement was about 910µA; 190µA from built-in voltage reference and 720µA from ADC. Insufficient energy results in incorrect temperature readings. An external low-power voltage reference can decrease the energy requirement and improve temperature sensing. Based on these results, a new temperature sensor was developed, based on an external thermistor.

4.1.2.3 External thermistor with external electric circuit

NTC thermistors are widely used due to their small size, high sensitivity and good long-term stability. A discrete thermistor, 100K6A1B (BetaTHERM Sensors), was selected for use in the SDV4. The dimensions of the sensor head is 2.4mmX2.4mm, making it compatible with a final sensor device which is 4mm wide, as shown in Figure 3.16. To improve long-term stability, REF1112 was employed due to its low temperature coefficient, 10ppm/°C typically. REF1112 is a stable two-terminal shunt voltage reference with a minimum operating current of 1µA. The low operating current results in low power consumption of the sensor device, and although the actual working current was bigger than 1µA, at about 5µA, it was a big improvement on the previous version (190µA).

100K6A1B was tested using in the same calibration system as described previously. The thermistor was connected to a sensor device, and connected to a PC through a USB cable. The device under test and experimental setup are shown in Figure 4.5. The thermistor was fixed onto the precision thermometer sensor head to minimise possible differences due to the relative positions of the sensors.

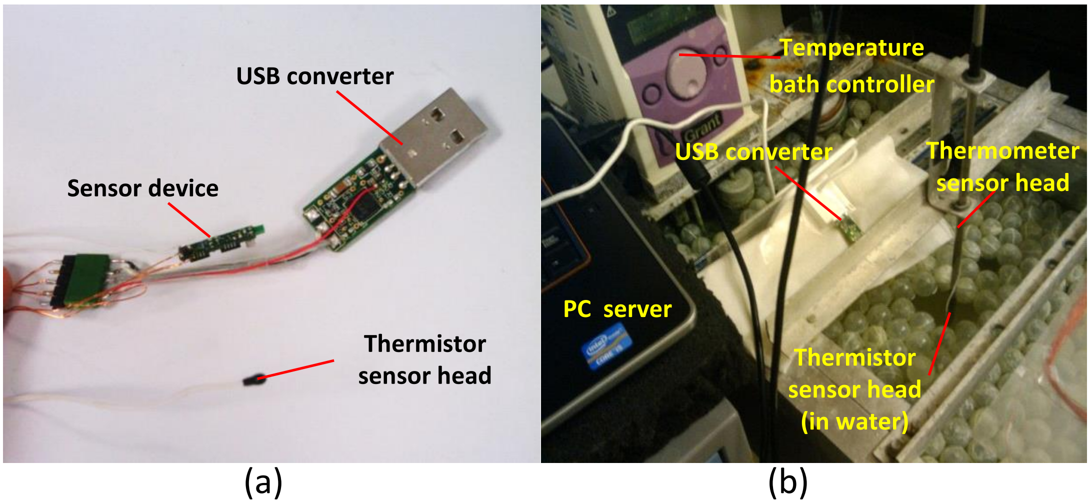

Figure 4.5 Thermistor tested device and experiment setup: (a) a sensor device with a thermistor is wired to a USB converter to achieve the data transmission to the PC server; (b) the testing system is setup on the temperature bath which provides a programmable temperature environment. The thermistor sensor head is mounted on the precision thermometer sensor head.

In line with the potential measurement temperature range of device, the temperature bath was set to change the temperature every hour from 35°C to 40°C at a constant step of 0.2°C. The temperature readings were collected at 30mins after setting the temperature. The result of external thermistor calibration is shown in Figure 4.6.

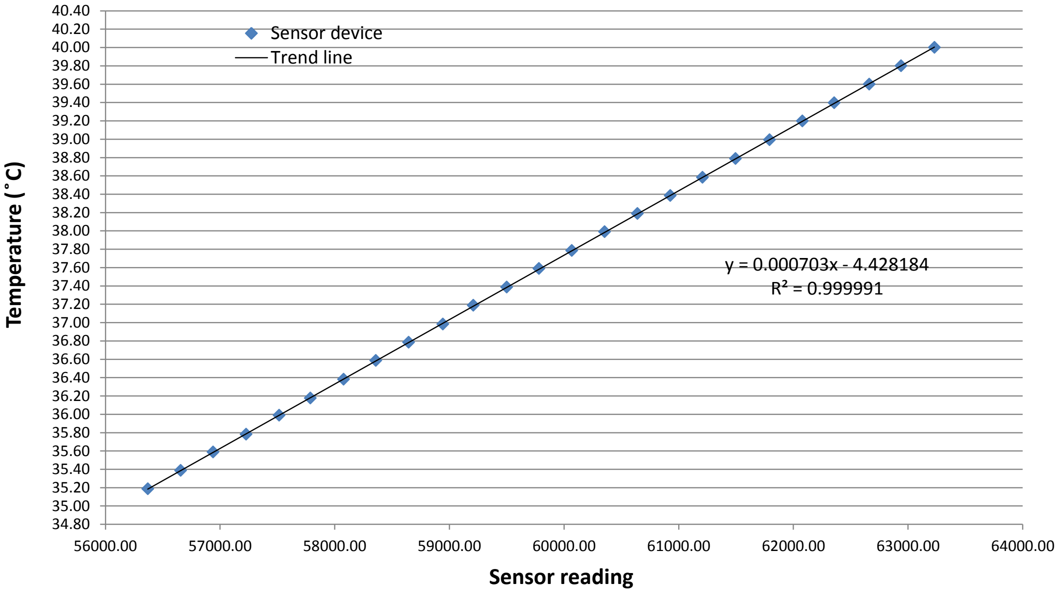

Figure 4.6 Calibration data for the external thermistor. Temperature variation was captured by a precision thermometer and thermistor. The temperature changed every hour from 35°C to 40°C at a constant step of 0.2°C. A good linear response is illustrated.

Although the thermistor has a non-linear temperature response in the full measurement range of more than 100°C, the thermistor response can be regarded as a linear output over a small temperature range, such as from 35°C to 40°C. Calibrated by using the readings from a precision thermometer, the employed thermistor response trend line shows a linear relationship in Figure 4.6, and the resolution is about 0.0007°C. After calibration, a long-term testing was undertaken for the thermistor stability evaluation; the testing result is shown in Figure 4.7.

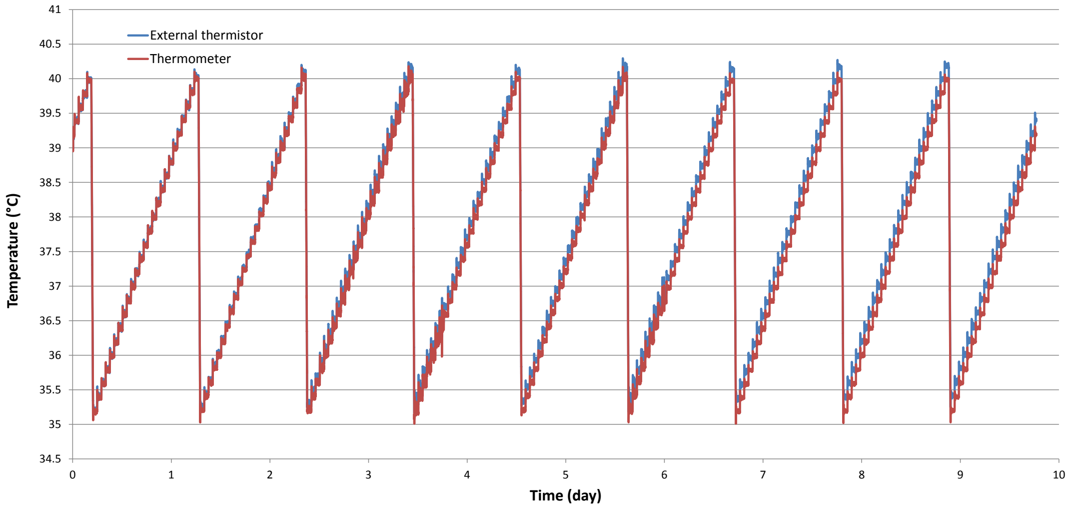

Figure 4.7 Temperature charts based on the reading from thermometer and sensor device in a long-term test. The temperature changed every hour from 35°C to 40°C at a constant step of 0.2°C.

The error in the temperature readings from the thermistor compared with the precision thermometer is shown in Figure 4.8. The mean difference over the first cycle is 0.00039°C, smaller than the built-in temperature sensor. Drift appeared in the following cycles. The average drift is about 0.0265°C per cycle.

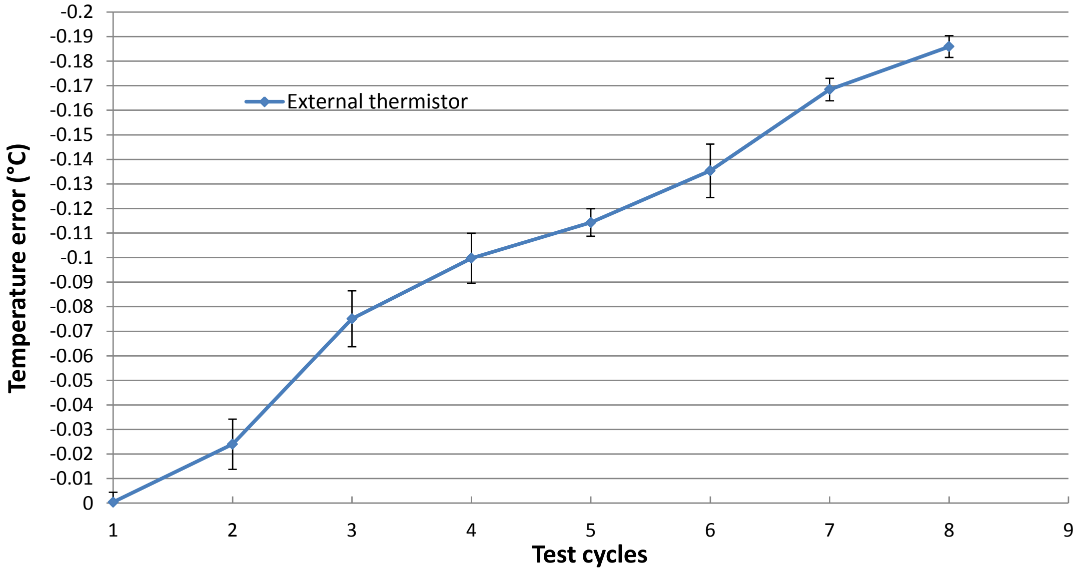

Figure 4.8 The error in the temperature readings of the external thermistor compared with the precision thermometer.

This long-term drift might be attributed to water permeation into the thermistor sensor head. Long-term drift may also be due to drift in the circuit components, such as the resistor in series. The thermistor sensor head needs to be repackaged using better materials with low water absorption coefficient, and a high precision resistor with low temperature coefficient should be used to improve the stability. Using this approach, long-term drift might be minimized.

As discussed in section 3.2.3, three-layer encapsulation achieved good bio-compatibility, but also better waterproofness due to thicker insulation layer than single-layer encapsulation. After encapsulation, the packaged thermistor was calibrated and tested *in-vivo*. Because the previous calibration system was not available, another similar calibration system was set up in the lab as shown in Figure 4.9.

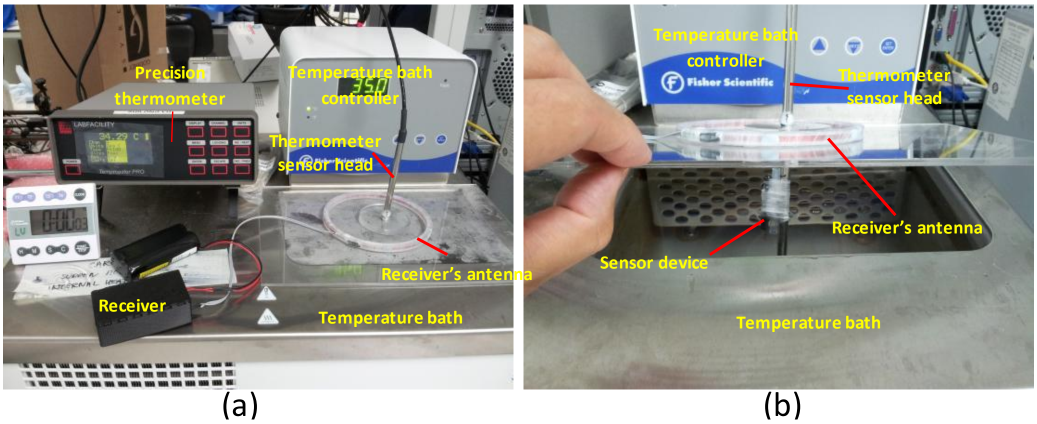

Figure 4.9 The temperature sensor calibration system set up in lab: (a) bench setup of the calibration system. It included a temperature bath which was already integrated the heating and cooling components. The temperature bath controller has an internal temperature sensor and maintains a stable temperature by controlling heating and cooling. A plastic lid covered the water bath to decrease evaporation. A precision thermometer is used to provide an accurate reference temperature reading and the sensor head was mounted on the lid at a fixed position and depth; (b) the sensor device was fixed on the thermometer sensor head and immersed in water. The receiver was set on the top of water bath and its antenna was toward to the sensor device. A PC logged data during the test through Bluetooth connection.

To evaluate the performance of the sensor device with thermistor, a 2-week test was undertaken on the calibration system as shown in Figure 4.9. Before testing, the sensor device was calibrated and then worked continuously immersed for 2weeks. Temperature measurement tests were carried out before and after the test to evaluate the performance during this long-term test; details are given in section 5.2. Calibration and temperature measurement tests were focused on the temperature range from 36°C to 40°C and the result is shown in Figure 4.10.

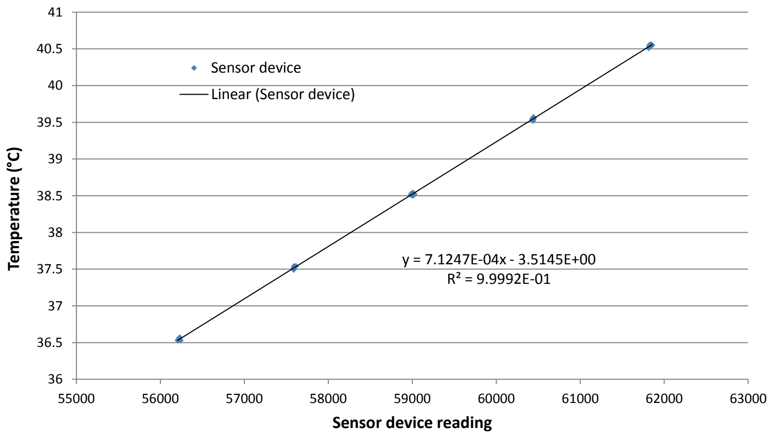

Figure 4.10 Calibration of packaged sensor device. Temperature calibration procedure and the temperature variation were captured by precision thermometer and sensor device. The temperature was configured to change every hour from 36°C to 40°C at a constant step of 1°C. A good linear response is illustrated.

After calibration, temperature measurement tests were undertaken before and after the 2 weeks immersion test. The temperature variations of two tests are shown in Figure 4.11, with temperature errors shown in Figure 4.12.

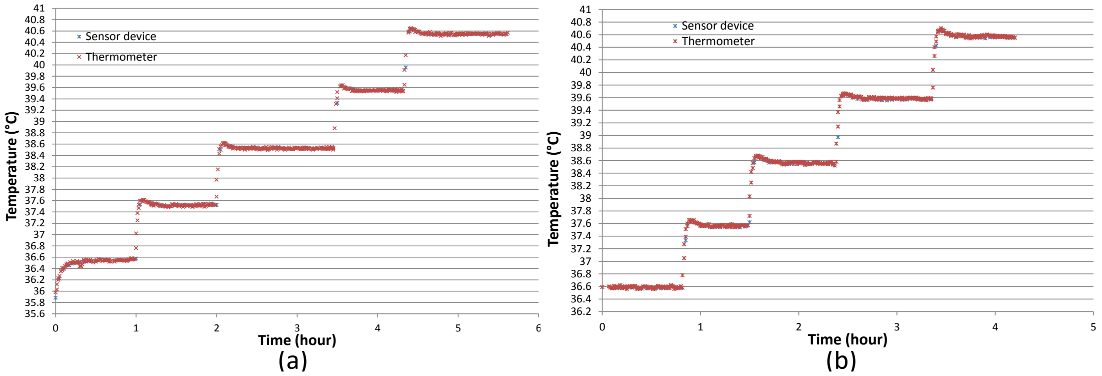

(a) (b)

Figure 4.11 Performance of the sensor device before (a) and after (b) 2weeks continuous measurement. Temperature was configured to change every hour from 36°C to 40°C at a constant step of 1°C. The temperature readings from both sensor device and precision thermometer were recorded.

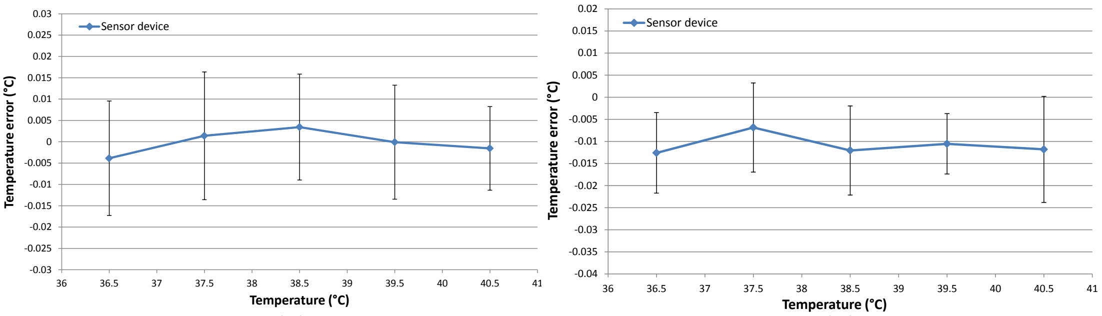

(a) (b)

Figure 4.12 The error of sensor device temperature readings before (a) and after (b) 2 weeks continuous measurement. The temperature readings were captured when the readings were stable. The accuracy of sensor device can reach ±0.03°C during whole test. After 2 weeks test, a drift of 0.01°C was observed.

During this long-term test, the accuracy of the sensor device was ±0.03°C for the entire test, with a drift of 0.01°C observed after 2 weeks continuous *in-vivo* work. This drift might be caused by component aging and stability. Compared with the performance of the unpackaged thermistor, an improvement was seen in the stability of the thermistor after encapsulation. Another temperature test was carried out to evaluate sensor device performance during continuously changing temperature conditions, as shown in Figure 4.13.

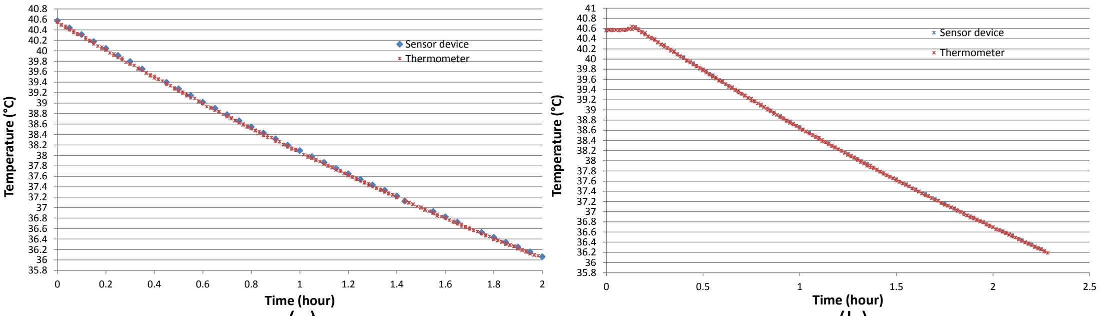

(a) (b)

Figure 4.13 Results of temperature measurement tests before (a) and after (b) 2 weeks continuous work. The temperature bath heater was switched off after the water reached the highest temperature point and the temperature dropped from 40.5°C to 36°C.

As these tests shown, the sensor has good alignment with the precision thermometer readings. The differences between sensor device and thermometer were no more than 0.03°C. Overall, the sensor device is deemed to be adequate for use in our intended intra-uterine application.

4.1.3 Summary of implantable temperature sensor development

Different types of thermometers have been considered and three different temperature sensors developed. A discrete digital output temperature sensor (TSic506F) was used during the early stages of device development; this provided a temperature reading for device debugging and testing. Considering the advantage of size and space requirements, a built-in temperature sensor was employed for temperature sensing. However, the limitations of the sensor stability and power consumption made it unsuitable for our intended sensor device. Moreover, it was impossible to carry out optimisation on the hardware, because the sensor and electric circuits were all embedded in the MCU. A **NTC thermistor** was chosen based on its stability and accuracy. In consideration of size and power consumption, the packaged sensor device with embedded thermistor can reach an accuracy of ±0.03°C for 2 weeks continuously work, making it suitable for testing *in-vivo*, and eventual human testing.

4.2 Design of a miniaturised implantable DO sensor

4.2.1 Technologies for DOC measurement

Clinically, it is difficult to obtain information of the intra-uterine dissolved oxygen concentration (DOC). Measurements can be undertaken by sampling of uterine fluid, amniotic fluid, fetal blood samples or directly using wired sensors incorporated into needles [2, 3, 5, 6, 113, 114]. Obviously, these snapshot technologies are complicated to implement and fraught with a variety of pitfalls, due to the different conditions between collection strategies and measurements, and delays in analysis. The devices use cables, are of limited use and can only be used for a short period. An optimal solution is a miniaturised DO sensor embedded within an implantable sensor device.

Conventionally, there are two different technologies that can be used to measure DOC including optical sensors and electrochemical sensors [115].

Briefly, optical sensors utilize luminescence in order to determine DOC of bulk solution. The typical optical sensor consists of a light generator, sensing element, luminescent layer and diffusion layer as shown in Figure 4.14.

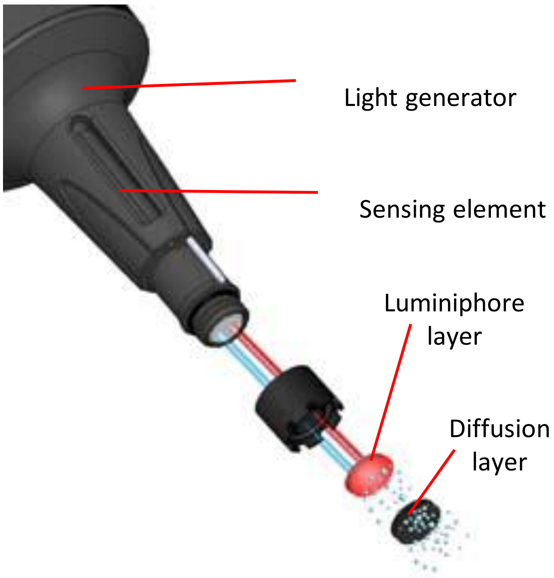

Figure 4.14 exploded view of the structure of typical optical sensor for dissolved oxygen sensing. This kind of sensor utilizes optical luminescence to determine DOC and includes a light generator, sensing element, luminophore layer and diffusion layer [79].

The light generator emits light of an appropriative wavelength, causing the luminophore layer to luminesce, or turn red. The luminophore layer has fluorescence properties such as the luminescence intensity and lifetime that change with ambient oxygen concentration. The dissolved oxygen in the vicinity of the sensor continually diffuses through the diffusion layer to the luminophore layer, and the DOC is determined from the intensity and lifetime of the luminescence using a photodiode (light detector).

As the oxygen is not consumed by this kind of sensor, the sensor won’t affect the DOC of bulk solution. Optical sensors are relatively stable with good accuracy. A typical optical sensor as manufactured by YSI has an accuracy of ±0.1mg/L (about ±3.1μM) with a response time of approximately 25 seconds [79]. However, due to the requirements of a light generator and sensing element, it is difficult to minimize optical sensors and reduce their power consumption. The luminophore layer also requires a certain time (dozens of seconds) to respond to the oxygen change. Moreover, the luminophore film needs to be replaced periodically due to fluorescence attenuation by photo-bleaching. Therefore, an optical DO sensor is not suitable for our intended application.

In contrast, an electrochemical DO sensor is based on electrochemical reduction of O_2 at a negatively polarized electrode. This can be built using micro electrodes which can be easily fabricated onto silicon substrates with micro-fabrication technologies. The most common electrochemical DO sensor is the Clark-type DO sensor first proposed in 1956 by Leland Clark [116]. A typical Clark-type DO sensor from YSI achieves an accuracy of ±0.2mg/L (about ±6.2 μm) with a response time of 8 seconds [117]. The advantages of an electrochemical DO sensor in terms of size and power consumption make it suitable for a microsystem. A technique to structure a miniature Clark-type DO sensor within a membrane-separated container has been reported [118]. The authors used channels to separate and connect the different electrodes in order to reduce crosstalk between the electrodes. This device has a fast response time of 6.8s (90%), good linearity (0.995, correlation coefficient) and a relatively long lifetime (around 60h). Another micro-fabrication dissolved oxygen sensor was proposed by Wang [119] in which platinum thin film electrodes were fabricated on silicon substrates using standard photolithographic techniques, and a solid state proton conductive matrix (PCM) coating was achieved by drop-casting. The PCM is an attractive method to replace the liquid electrolyte filled compartment between the membrane and the electrode for device robustness and lifetime. The authors presented a single device capable of long-term stability, reliability, hysteresis, linearity and sensitivity, but the differences between individual sensors remains a significant issue. In conclusion, the **electrochemical DO sensor** is most appropriate for measurement in the uterus.

4.2.2 Principles underlying an implantable DO sensor

Electrochemical DO sensors usually utilize two or three electrodes, including a working electrode, reference electrode and counter electrode (optional). The working electrode is made from an inert metal, such as platinum or gold, and the electrochemical reactions of interest occur on its surface. The reference electrode is a nonpolarizable electrode, and has a stable and well-known electrode potential. For example, a widely used reference electrode for electrochemical experiments is Ag/AgCl electrode and its electrode potential is around 0.222V (vs. SHE, standard hydrogen electrode) at room temperature, although this is dependent on the temperature and solution composition. A diagram of a two electrode electrochemical DO sensor is illustrated in Figure 4.15a.

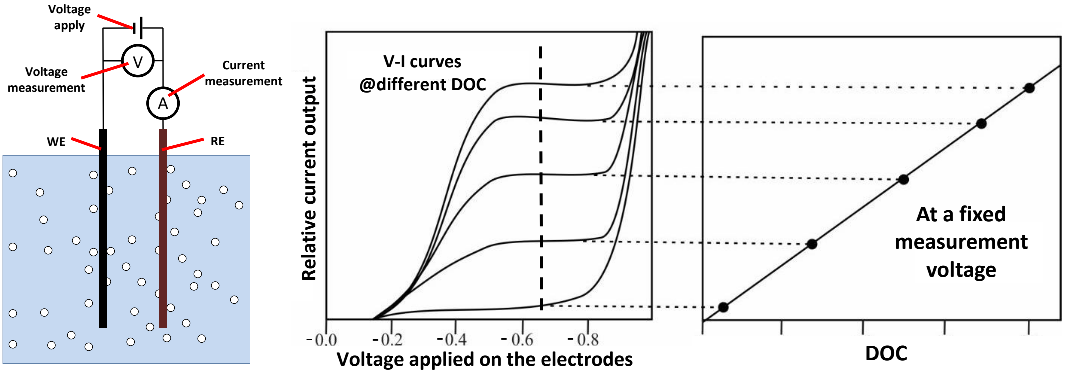

(a) (b) (c)

Figure 4.15 Illustration of the working principle of an electrochemical DO sensor [120, 121]: (a) diagram of a typical two-electrode electrochemical DO sensor. The black electrode is the working electrode and the dark red one the reference electrode; (b) V-I chart of oxygen reduction at the working electrode surface. A varied saturated current was observed at different DOC; (c) the current at a fixed measurement voltage can be used to obtain DOC of the bulk solution.

The electrochemical DO sensor is immersed in an electrolyte. When a negative voltage is applied to the working electrode against the reference electrode, dissolved oxygen in the electrolyte is consumed according to the following chemical reactions.

$$O_2 + 4e^- + 2H_2O \rightleftarrows 4OH^- \qquad (4.2\text{-}1)$$

$$O_2 + 2e^- + 2H_2O \rightleftarrows H_2O_2 + 2OH^- \qquad (4.2\text{-}2)$$

$$H_2O_2 + 2e^- \rightleftarrows 2OH^- \qquad (4.2\text{-}3)$$

This produces an electrical current through the working electrode which can be measured through the use of an electronic circuit. According to the surface diffusion conditions, and electrode material the oxygen can be consumed directly (4.2-1), or with hydrogen peroxide as an intermediate as in (4.2-2) followed by (4.2-3) [122]. The oxygen reduction current contributes to the current measured from the working electrode. If the negative voltage applied to the working electrode increases, the current increases at the beginning and then saturates. This value is limited by the diffusion of oxygen to the working electrode surface. When the negative voltage is further increased, the current through the electrode increases rapidly due to reduction of water to hydrogen. The voltage-current (V-I) chart of the oxygen reduction at the working electrode surface is shown in Figure 4.15b. The saturated current varies with DOC. Although the saturated current is not directly proportional to ambient DOC, it is determined by the diffusion conditions and the equivalent partial pressure of dissolved oxygen (oxygen tension), which is dependent on the DOC of the bulk solution. Therefore, after calibration, the saturated current can be used to measure DOC. When using Ag/AgCl as the reference electrode, the measurement voltage is usually selected at between -0.5V and -0.8V, and the optimal value is determined from the V-I chart of cyclic voltammetry [120, 121].

From the V-I chart, two important voltages can be determined, including the rest voltage and measurement voltage. The rest voltage is the voltage applied to the electrodes without any oxygen reduction, leading to zero current. The measurement voltage is the optimal voltage to measure the oxygen reduction current. By applying these two voltages, a step waveform for the voltage is used for the DOC measurement. The current response to this step voltage is shown in Figure 4.16.

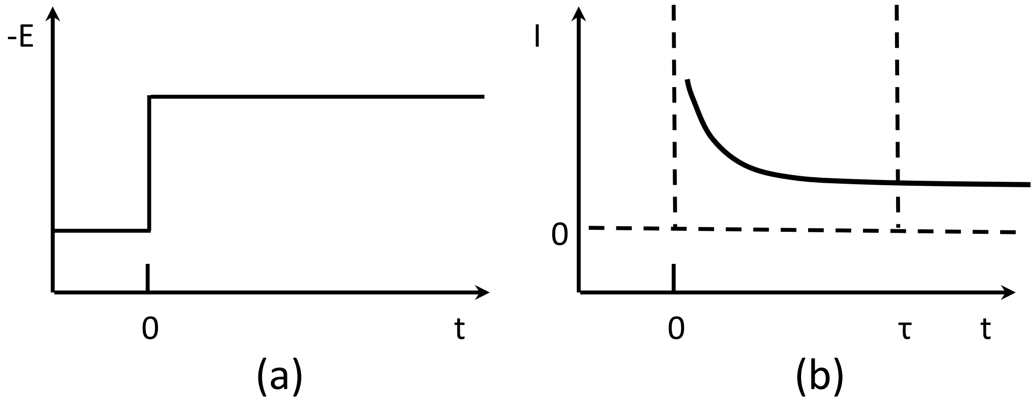

Figure 4.16 Current response to a step measurement voltage waveform: (a) step waveform of voltage applied on the two electrodes; (b) current-time curve observed in response to the step voltage. The current trends to a stable value which is limited by the dissolved oxygen diffusion process to the working electrode.

When the measurement voltage is applied to the working electrode, the dissolved oxygen around the electrode is consumed. A current spike occurs at the beginning because the reaction is fast, but this current decreases rapidly due to oxygen consumption. At the same time, an oxygen concentration gradient is formed around the electrode. This oxygen concentration gradient causes oxygen molecules to diffuse to the working electrode from the bulk. The oxygen reduction current decreases to a stable value which is limited by oxygen diffusion. This stable current is proportional to the diffusion rate which is dependent on the DOC of the bulk solution, and it is conventionally used to measure the DOC.

The reference electrode is consumed and polarized to a certain extent, while the current through the reference electrode increases, the electrode will change. The instability of the reference electrode may result in sensor failure. Therefore, a counter electrode is employed to bypass the current of the reference electrode for improved stability of the reference electrode when the current is large. A high resistance feedback circuit allows the potential of the working electrode to be measured against the reference electrode.

Bare electrochemical DO sensors have some drawbacks attributable to direct contact with the sample solution. The complex composition of the sample solution may lead to other chemical reactions which contribute to the current through the electrodes. Some by-products can deteriorate the electrode surface and result in sensor failure. Bare sensors are more affected by flow. Therefore, a membrane covered electrochemical DO sensor is used, and the most widely used membrane covered sensor is the Clark-type DO sensor [116, 118, 119, 123-125]. A typical 2-electrode Clark-type DO sensor is shown in Figure 4.17.

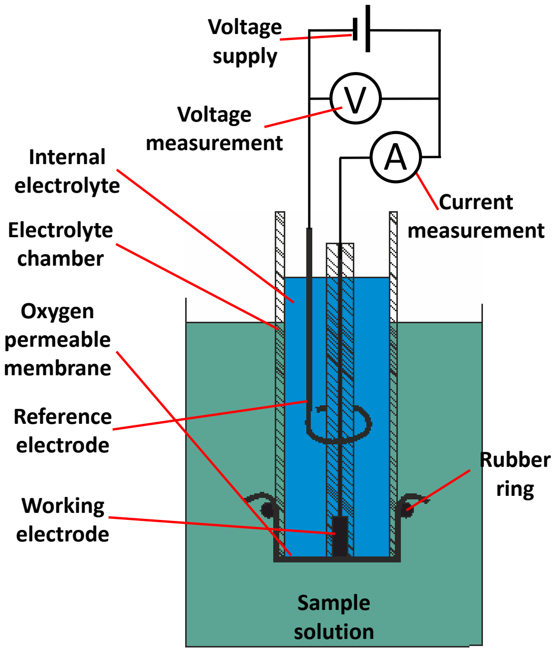

Figure 4.17 Schematic of a typical 2-electrode Clark-type DO sensor, including working electrode, reference electrode, OPM (Oxygen Permeable Membrane), internal electrolyte. The working electrode and reference electrode are immersed in the electrolyte and separated from the sample liquid by an OPM. When it works, a voltage is applied between the working and reference electrodes and the current is measured.

This system has a working electrode, reference electrode and optional counter electrode. The electrodes are immersed in an electrolyte and separated from the sample liquid by an oxygen permeable membrane (OPM). The working electrode is positioned close to the OPM to reduce the oxygen diffusion time. 3M KCl is a common electrolyte widely used for Clark-type sensor employing an Ag/AgCl reference electrode. This membrane covered sensor delivers a well-characterised and stable internal environment for the electrode and reduces interference from electrolysis to improve the sensor performance. During a measurement cycle, an oxygen concentration gradient is formed across the OPM with oxygen diffusion controlled by the OPM properties. As the oxygen reduction current is depends on oxygen diffusion, the diffusion conditions are critical to sensor performance and stability. Any changes in diffusion conditions result in uncontrolled measurement errors and sensor drift. Diffusion conditions are dependent on the sensor structure and dimensions and are sensitive to the ambient flow of the sample liquid. Using basic diffusion models, an evaluation of the sensor properties can be established providing a reference for the sensor design.

4.2.2.1 Diffusion modelling

To simplify the simulation, we consider that mass transport occurs only by diffusion, with electrode area (A) small enough and solution volume (V) large enough to achieve a stable oxygen concentration in the bulk solution that is not affected by electrochemical reactions. As the intended electrode area is small, at less than $0.01mm^2$, it is easy to achieve this condition.

Planar diffusion is one dimensional diffusion, as shown in Figure 4.18. The diffusion is only in the x direction, and the oxygen concentration is the same at the same distance to the electrode. An infinite planar electrode or a planar electrode with vertical boundary is the typical planar diffusion conditions.

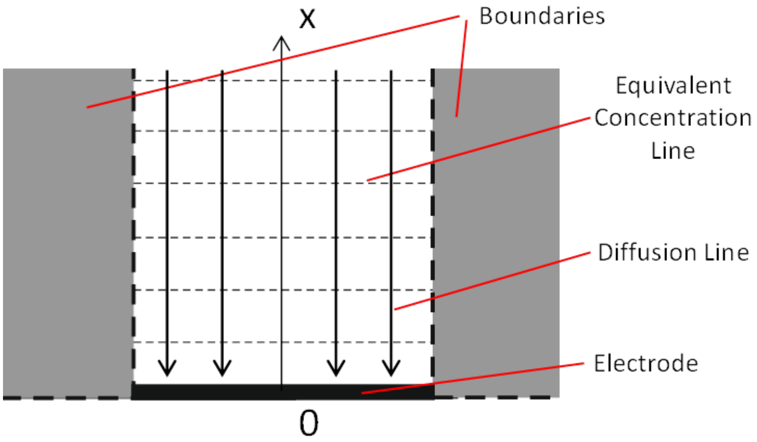

Figure 4.18 Diffusional geometry at a planar electrode. This is typical one dimensional diffusion, and liquid has same concentration at same distance to the electrode.

The concentration change of solution caused by diffusion can be predicted by Fick's second law as below:

$$C(x,t) = C^{*} erf\left(\frac{x}{2\sqrt{Dt}}\right) \qquad (4.2\text{-}4)$$

where $C(x,t)$ is the oxygen concentration in the x direction at time t, C^{*} is the oxygen concentration of the bulk solution, x is distance to the electrode and D is the diffusion coefficient. The erf( ) is the error function identified:

$$erf(x) = \frac{2}{\sqrt{x}} \int_{0}^{x} e^{-t^{2}} dt \qquad (4.2\text{-}5)$$

The time-dependent concentration profile around the electrode is shown in Figure 4.19.

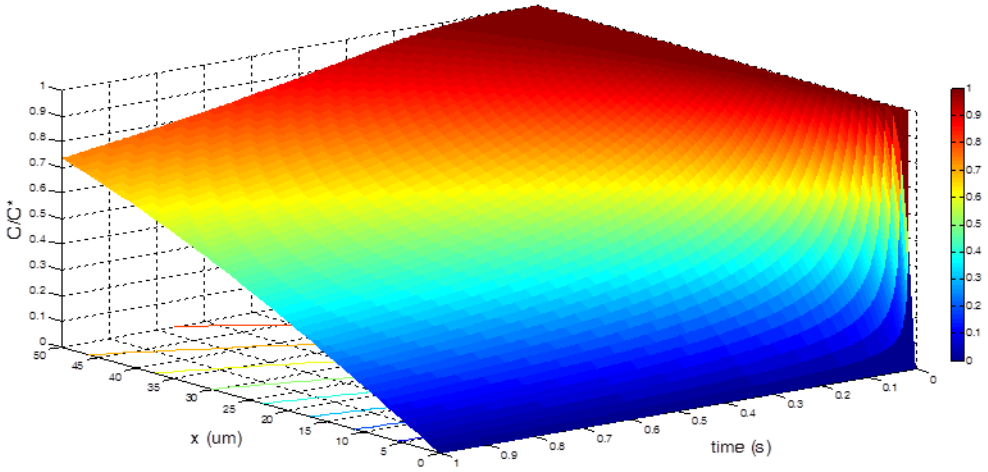

Figure 4.19 Time-dependent concentration profiles after the voltage is applied. Diffusion coefficient D is 1×10^{-5} cm^{2}/s.

The diffusion current is proportional to the oxygen flux at the electrode surface and is given by the Cottrell equation [120]:

$$I(t) = nFAC^* \sqrt{\frac{D}{\pi t}} \qquad (4.2\text{-}6)$$

where n is the number of electrons transferred per molecule, F is the Faraday constant and A is the electrode area, C^* is the oxygen concentration of bulk solution, D is the diffusion coefficient and t is time. The diffusion current is proportional to $1/\sqrt{t}$ due to the consumption of oxygen near the electrode surface, and the current is very close to zero when time is very long.

For DO sensor miniaturisation, microelectrodes are needed with a at least one dimension on the micrometres scale [126]. Different diffusional geometry is found for different types of microelectrodes, and three conventional models include spherical or hemispherical, disk and band microelectrodes. Although these microelectrodes have different shapes and different behaviour, there are some common features in the diffusion current. Based on Fick’s second law, the diffusion currents can be determined from:

$$I(t) = nFAC^* \sqrt{\frac{D}{\pi t}} + I_{ss} \qquad (4.2\text{-}7)$$

At short times, when the diffusion-layer thickness is smaller than the critical dimension of microelectrode, the current at the microelectrode follows the Cottrell equation (4.2-6). Over longer time, the diffusion-layer increases to become larger than the microelectrode critical dimension and the diffusion current approaches a steady state or a quasi-steady state given by the second term in 4.2-7. The steady state currents of these differently shaped microelectrodes are given by the equations shown in Figure 4.20.

	Sphere	**Disk**	**Band**
Diffusional geometry	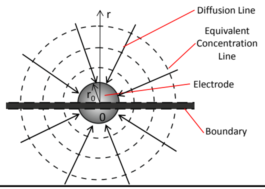	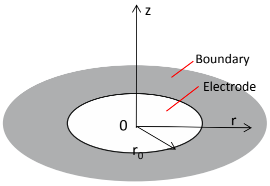	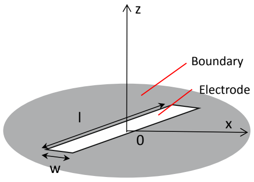
steady-state current	$I_{ss} = \frac{nFAC^*D}{r_0}$	$I_{ss} = \frac{4nFADC^*}{\pi r_0} = 4nFDC^* r_0$	$I_{ss} = \frac{2\pi nFADC^*}{w\ln(64Dt/w^2)}$

Figure 4.20 Equations for steady state current for microelectrodes of different geometries [120].

Compared with the sphere and disk microelectrodes, the band microelectrode can be configured with a relatively larger electrode area, with one critical dimension meeting the microelectrode requirements. Specifically, its critical dimension, width *w*, should be very small, but the length *l* can be much larger. The larger geometric area of a microelectrode leads to sizable currents and improved signal quality. For example, the area of a disk microelectrode with 5μm radius is about $7.9 \times 10^{-7} cm^2$, and a 5μmX100μm band microelectrode has a geometric area about 6.4 times the disk microelectrode.

After comparison of different electrode geometries, we selected a **band microelectrode** because of the size and bigger geometric areas at similar critical dimension. Furthermore, to further increase the reduction current with similar diffusion conditions, an array of band microelectrodes can be used in certain circumstances; more details will be presented in section 4.2.3.

4.2.2.2 The stability of reference electrode

The reference electrode (RE) is one of the most crucial components and its stability determines the long-term stability and lifetime of the DO sensor. A number of REs have been widely used, including the Calomel electrode, standard hydrogen electrode and Ag/AgCl. Because the calomel electrode requires a large amount of mercury and the standard hydrogen electrode is difficult to embed into microsystems, they are not suitable for an implantable DO sensor. In contrast, the **Ag/AgCl electrode** is the optimal RE due to its relatively simple structure, stability and easy to use in microsystems.

However, the lifetime of a miniaturised Ag/AgCl RE is limited, and deterioration of the Ag/AgCl RE may be attributed to contamination by the electrolyte solution, damage by mechanical stress, light, non-negligible solubility of AgCl in solutions with high Cl^- concentration and consumption of the thin silver film by chloridization [127, 128]. Specifically, the solubility of AgCl in 100mM KCl at 25°C is 0.0029mmol/l but it increases more than 700 times to 2.22mmol/l in 3M KCl [129]. This was considered to be caused by the formation of silver complex ions ($AgCl_x^{-(x-1)}$, x =2, 3 or 4) and this complex ion diffuses into the solution bulk [130]. The solubility of AgCl in KCl solutions at different concentration and the fading of AgCl RE in 3M KCl solution are shown in Figure 4.21.

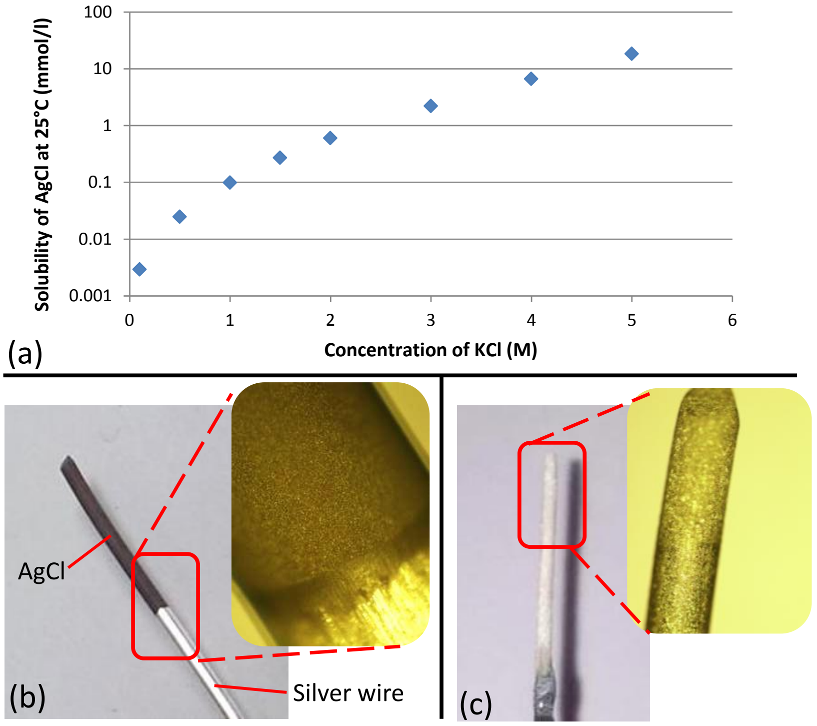

Figure 4.21 The solubility of AgCl in KCl solution and the fading of AgCl RE in 3M KCl solution: (a) the solubility of AgCl exponential increases for high concentration KCl solution [129]; (b) A layer of AgCl was coated on one end of a silver wire; (c) After 2 days in 3M KCl solution, the AgCl layer faded and there was no AgCl left.

Previous work has been undertaken to improve of Ag/AgCl RE, including using a complex structure, protective membranes and ionic liquid maintaining chloride concentration. Some researchers have proposed and developed a micro-patterned layer-by-layer polyelectrolyte junction [131]. The polyelectrolyte junction was formed in the microchannel connecting a nano porous Pt electrode and the sample solution, and had layer-by-layer structure of oppositely charged polyelectrolytes. Ag/AgCl RE have been developed with a coating of Nafion or polyurethane on its entire surface to avoid dissolution of AgCl into the biological environment [132]. Gel-like electrolyte based on agar [133, 134] and alginate [42] sol have been used to maintain the concentration of necessary ions and reduce electrochemical crosstalk.

Although the layer-by-layer polyelectrolyte junction and the membrane effectively block the mass transport of ions, the complex structure and difficult fabrication do not make it for an easily miniaturised biosensor. An available strategy is to increase the amount of AgCl on the RE. A much bigger RE compared with the WE is required and a thick AgCl layer (several μm) is necessary to stabilize of the Ag/AgCl RE. A closed chamber filled with gel-like electrolyte provides a safe and stable environment for the Ag/AgCl RE, and it is suitable for micro-fabrication of a miniaturised biosensor. Alginate sol is an optimal material for forming a gel-like electrolyte because it does not require high temperature for gelating. Considering the non-negligible solubility of AgCl in solutions with high Cl^-

concentration, an effective solution is to use a relatively low concentration solution, such as 150mM KCl to provide good stability without any extra treatment.

It was found that an Ag/AgCl RE has better stability and less dissolution into bulk solution after it was baked at 60°C in an oven for at least 2 days. This electrode was stable even in a solution with a high Cl^- concentration. This may be associated with dehydration after baking which makes the AgCl layer of the RE more solid, although it needs few days for rehydration before reaching a stable state ready for use.

4.2.2.3 **OPM fabrication and characterization**

Motivation of OPM fabrication and characterization

Different materials can be used for OPM with different permeability of oxygen including PDMS [42, 135], Teflon [136] and RTV (Room Temperature Vulcanizing) silicon [137]. A thin PDMS film was chosen as the optimal material for the OPM due to its ease of moulding and fabrication. Considering the residual solvent present in PDMS (Hexane and Toluene) after moulding, and the potential risk from the solvent, a solvent-free PDMS membrane was considered.

SILASTIC MDX4-4210 Biomedical Grade Elastomer is a widely used medical grade PDMS (MG-PDMS), it doesn’t contain any peroxides, peroxide by-products, chlorophenyl, and has no organic plasticizers, phthalates or latex additives. It meets high quality standards for medical applications, including the testing requirements described in ISO 10993-1 for “limited” (≤24 hours) and “prolonged” (≤30 days) contact duration, and testing requirements of United States Pharmacopeia (USP) Class VI and European Pharmacopoeia (EP) silicone elastomers [138]. It is really good for fast prototyping, moulding, encapsulation of electronic components of biomedical devices and fabrication of medical device components, such as cochlear prosthesis[139] and drug matrix for controlled release drug delivery systems [140].

PDMS membranes are usually fabricated by spinning uncured PDMS on the target surface directly, or spin-coating on a substrate and then lifted off before or after bonding. The thickness of the PDMS membrane depends on its physical properties (e.g. viscosity) and spin speed and time. Compared with normal PDMS, MG-PDMS has different properties and as shown in Table 4.2 [138, 141].

Table 4.2 Physical properties comparison between MG-PDMS (MDX4-4210) and normal PDMS (184 Silicon Elastomer).

		184 Silicone Elastomer	**BioMedical Grade Elastomer**
		DOW CORNING	DOW CORNING
Composition		2-part	2-part
Mix ratio		10:1	10:1
Viscosity (Mixed)	Pa.s	3.5	60, initial 110, after 2hours
Elongation	%	120	470
Colour		Transparent	Translucent
Relative density (Cured)		1.04	1.11
Durometer hardness	Shore A	44	30
Tensile strength	Mpa	7.1	5.0
	psi	1025	730
Dielectric strength	volts/mil	475	575
Volume resistivity	Ohm.cm	$2.9\text{X}10^{14}$	$2\text{X}10^{15}$
Surface resistivity	Ohm		$>7\text{x}10^{16}$
Dielectric constant (100Hz)		2.72	3.01
Dielectric constant (100KHz)		2.68	3.00
Dissipation factor (100Hz)		$2.57\text{x}10^{-3}$	$9\text{x}10^{-4}$
Dissipation factor (100KHz)		$1.33\text{x}10^{-3}$	$10\text{x}10^{-4}$
Pot life-time	hour	1.4	
Curing time		48h @25°C 35mins @100°C 20mins @125°C 10mins @150°C	24h @23°C 5h @40°C 2h @55°C 30mins @75°C 15mins @100°C
Tissue culture			No cytopathic effect (CPE)
Oxygen diffusion coefficient	cm^2/s	$5.2\text{X}10^{-6} \sim 3.4\text{X}10^{-5}$	

Because of the different properties of MG-PDMS, our knowledge and experience in handing normal PDMS cannot be applied directly. Furthermore, there is less research and information is available for the diffusion of oxygen through the MG-PDMS membrane. Therefore, the MG-PDMS membrane was investigated after fabrication at different spin speed and time, and the experimental value of oxygen diffusion coefficient determined.

Thickness characterization of MG-PDMS OPM at different fabrication setting

The MG-PDMS membrane was fabricated by spinning the material on glass slide which can be used by lift-off after bonding. The fabrication procedure is as follows: 1) glass slides were cleaned in Acetone for 5 mins and wiped to remove dirt and then rinsed by IPA and methanol successively; 2) glass slides were treated with Duxcoat to make the surface hydrophobic; 3) thoroughly mixed the MG-PDMS elastomer and curing agent in a 10:1 ratio by weight, and put the solution into a vacuum for approximately 40 mins de-gassing; 4) the uncured PDMS solution was spin-coated onto the treated glass slides; 5) the spin-coated membrane samples were cured at 80°C in an oven for at least half hour.

To evaluate the surface condition of the PDMS membrane spin-coated on the glass slide, surface profiling was carried out by surface profiler (TENCOR P-11). A 13X5 grid (65 measurement points) at 5mm distance was measured as shown in Figure 4.22, covering the area of the whole membrane.

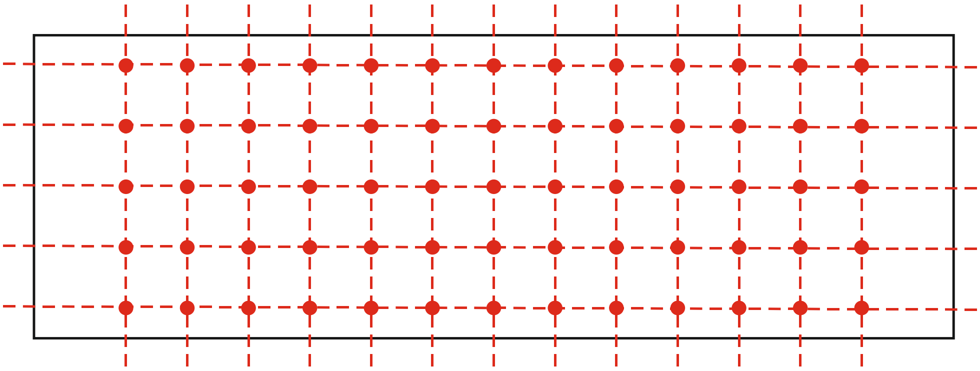

Figure 4.22 Grids for MG-PDMS membrane surface profiling on a 75mmX25mm glass slide. There are 65 thickness measurement points (13X5 red dots) at 5 mm distance covering almost whole membrane sample. From surface profiling, the thickness distribution of MG-PDMS membrane spin-coated on glass slide can be evaluated.

From the surface profiling, the MG-PDMS membrane thickness distribution was estimated as shown in Figure 4.23. The contour figure shows the centre of the membrane was thickest, about 20μm thicker than the edge, and was not suitable. However further than 25mm from the centre, the membrane was flat and the thickness difference was no more than 1μm along the width direction. The membrane further than 25mm was therefore deemed to be adequate for MG-OPM fabrication.

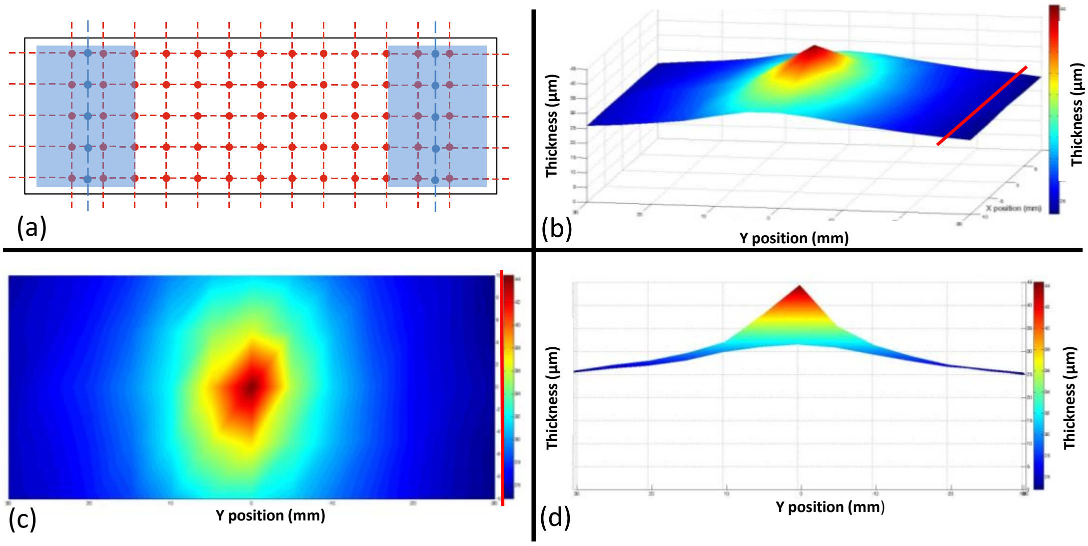

Figure 4.23 Diagram of MG-PDMS membrane surface profiling: (a) diagram of MG-PDMS membrane surface profiling grids (red dots) on a 75mmX25mm glass slide. Blue squares show the area which is flat enough for membrane use and thickness evaluation. Blue dots show the measurement points for thickness evaluation; (b) thickness distribution of MG-PDMS membrane on glass slide; (c) top view of surface profiling; (d) side view of surface profiling. Read line in (b) and (c) show the membrane thickness measurement line.

A number of MG-PDMS membranes were fabricated at different spin speeds (from 1000 RPM to 5000 RPM) and different duration (from 60s to 600s). The thickness was investigated and plotted in Figure 4.24. The relation between the membrane thickness and spin speed and duration provides information for MG-PDMS membrane fabrication.

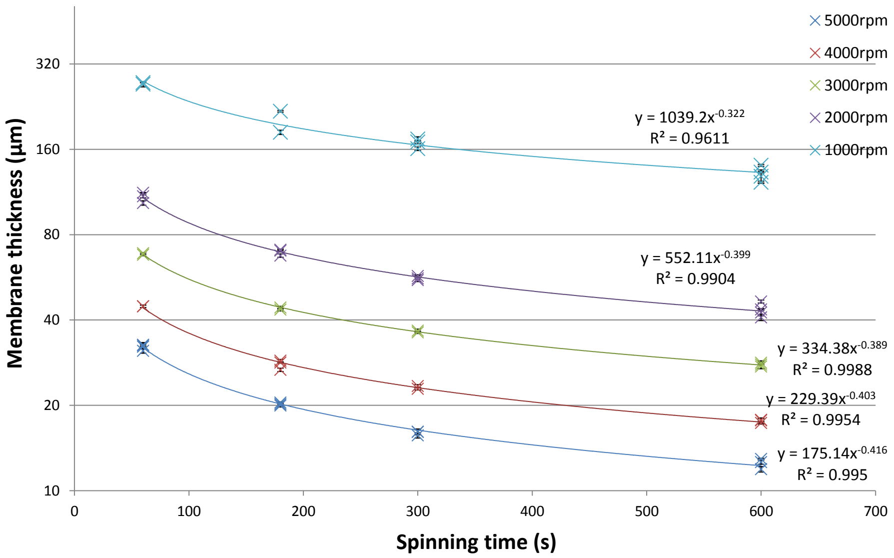

Figure 4.24 Diagram of MG-PDMS membrane thickness at different spin speeds and duration. Similar trend lines of membrane thickness at different spin speeds are seen. The trend has a power function of the type $y=a\cdot X^b$, where x is the spin time, y is the thickness of membrane, a and b are the experimentally derived constants.

Characterization of the oxygen permeability of the MG-PDMS OPM

To characterise the permeability of the MG-PDMS membrane to oxygen, the diffusion coefficient was determined using electrochemical method. A disk ultra-micro electrode (UME) was prepared. The diffusion-controlled steady state currents has two components including Faradaic current and capacitive current. The currents of UMEs with and without OPM can be estimated from the following equations [120]:

$$I_{total-bare} = I_{F-bare} + I_{C1} = 4nFD_{PBS}C_1^* r_0 + I_{C1} \qquad (4.2\text{-}8)$$

$$I_{total-OPM} = I_{F-OPM} + I_{C2} = 4nFD_{OPM}C_2^* r_0 + I_{C2} \qquad (4.2\text{-}9)$$

where I is the current, n is the number of electrons transferred per molecule, F is Faraday constant, D is the oxygen diffusion coefficient of OPM, C* is the DOC of bulk solution and r_0 is the radius of UME. The current is a linear response with DOC and the ratio of oxygen diffusion coefficient can be estimated from:

$$\frac{Slope(current - DOC)_{without-OPM}}{Slope(current - DOC)_{with-OPM}} = \frac{4nFD_{PBS}r_0}{4nFD_{OPM}r_0} = \frac{D_{PBS}}{D_{OPM}} \qquad (4.2\text{-}10)$$

From this equation, we see that the area of the UME does not affect the experiment result. The current from the oxygen reduction was determined from the V-I curves recorded from experiments with and without OPM, as shown in Figure 4.25. The temperature was stable at room temperature (20.55±0.2°C). In this figure, a clear no-current zone and oxygen reduction zone were observed. Considering the Ag/AgCl electrode potential and electrode potential for oxygen reduction, the steady state current for oxygen reduction was measured at -0.55V. In addition the DOC of the bulk solution was measured by a commercial DO probe (YSI ODO probe) and the current-DOC curves of UMEs with and without OPM were obtained.

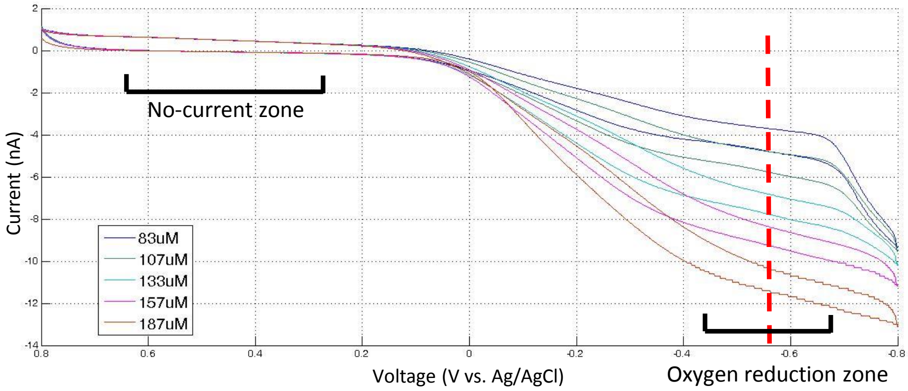

Figure 4.25 V-I curves obtained from CVs for different DOC shown in different colours. A clear no-current zone and oxygen reduction zone can be observed, and different current responses of oxygen reduction zone were found for different DOC. The red line shows the steady state current measurement at -0.55V vs. the Ag/AgCl electrode potential.

An experimental system was with an electrochemical cell is shown in Figure 4.26. Different DOC of the bulk solution was prepared by bubbling N_2, and the V-I curves of UMEs investigated with cyclic voltammetry (CV).

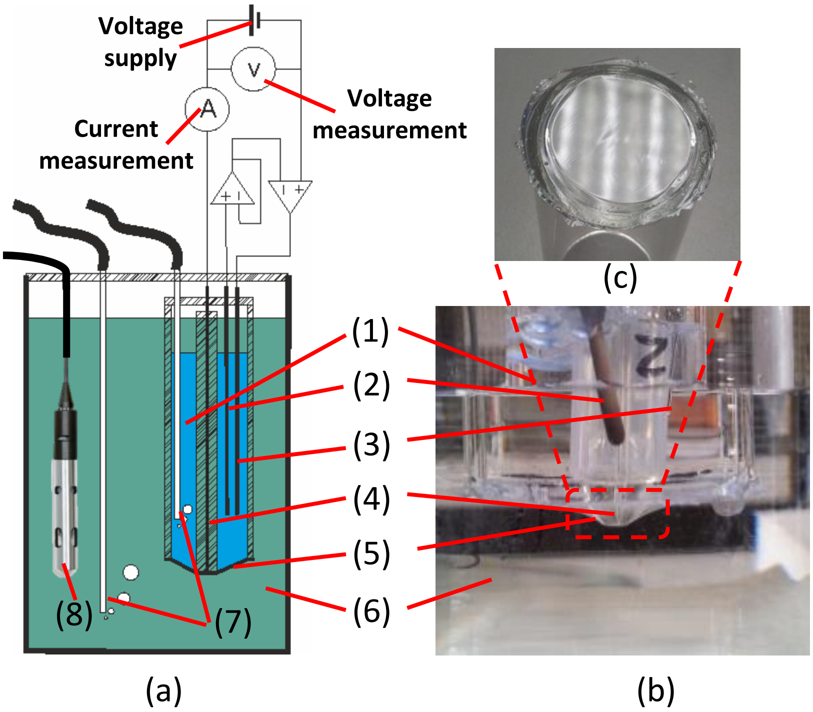

Figure 4.26 Diagram of the experiment setup for recording CV from the UME with an OPM: (a) schematic view of system setup; (b) picture of detailed system setup; (c) free-standing MG-PDMS membrane (about 50µm thick) bonded onto one end of glass tube 25mm diameter. The experiment system had an electrochemical cell including UME working electrode (4), Ag/AgCl reference electrode (2) and Pt counter electrode (3) immersed in the internal electrolyte (1, 1xPBS). An MG-PDMS membrane (5) separated electrodes from the sample solution (6). The UME surface was fixed to the OPM as close as possible and N2 was bubbled continuously to eliminate the extra current contributed from the DO in the internal electrolyte. A commercial DO probe (8, YSI ODO probe) recorded real-time DOC of bulk solution simultaneously. N2 bubbling (7) provided different DOC in bulk solution.

For the V-I curves of UME without OPM, another experiment was undertaken as shown in Figure 4.27. Based on equation (4.2-10), the DO diffusion coefficient of MG-PDMS membrane was estimated using the slopes of the trend lines. Considering that the DO diffusion coefficient in PBS is about $1.94\times10^{-9}m^2/s$ [142], then the diffusion coefficient of DO in MG-PDMS was calculated to be $(1.05\pm0.25)\times10^{-9}m^2/s$ (more experimental data can be seen in appendix B-1). The diffusion coefficient of DO in normal PDMS was reported to be between $5.2\times10^{-10}m^2/s$ and $3.4\times10^{-9}m^2/s$ [143, 144], therefore the oxygen permeability of MG-PDMS is similar to normal PDMS. The errors in the experimental diffusion coefficient estimate may come from the difference in the samples and the nonideal experiment setup.

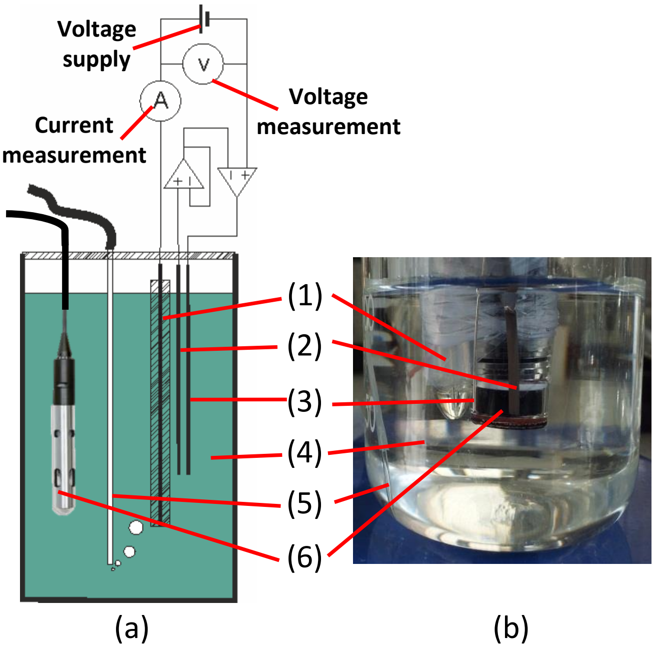

Figure 4.27 Diagram of an experimental setup for CV of UME without OPM: (a) schematic view of system; (b) detailed system setup. UME working electrode (1), Ag/AgCl reference electrode (2) and Pt counter electrode (3) were immersed in the sample solution (4). A commercial DO probe (6) was used to record real-time DOC of bulk solution and N2 bubbling (5) provided different DOC.

4.2.3 Design of implantable DO sensor

The implantable DO sensor was designed and developed as shown in Figure 4.28. The micro DO sensor had a similar structure to the Clark-type DO sensor but is much smaller.

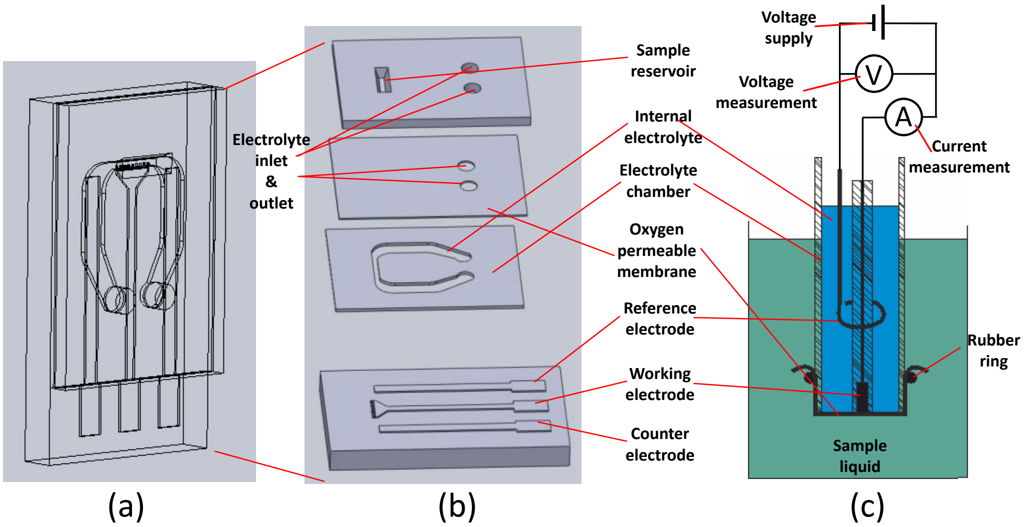

Figure 4.28 Schematic of the implantable DO sensor compared with a typical Clark-type DO sensor: (a) perspective view of DO sensor; (b) exploded view of DO sensor including microelectrodes fabricated on the glass substrate, electrolyte chamber layer, OPM and sample container; (c) schematic of typical Clark-type DO sensor.

The DO sensor was designed as a multi-layer structure, including microelectrodes (on the glass substrate), oxygen permeable membrane (OPM) and sample solution reservoir layer. Three electrodes were patterned on the glass substrate including an array of working electrodes (WE), reference electrode (RE) and an optional counter electrode (CE). An electrolyte chamber layer was designed on top of the microelectrodes, providing a relatively stable internal electrolyte environment. This layer also worked as an insulating layer to cover unexposed metal between electrodes and soldering pads. The electrolyte chamber was enclosed by the OPM. A sample reservoir layer was bonded to the OPM and the sensing area of the DO sensor was defined by the open window of the sample reservoir layer on top of the working electrode. Sample solution contacts the OPM directly and oxygen molecules diffuse through the OPM to the sensor electrodes. Inlet and outlet were added through the OPM and reservoir layer for electrolyte injection. A cross section view of the DO sensor is shown in Figure 4.29.

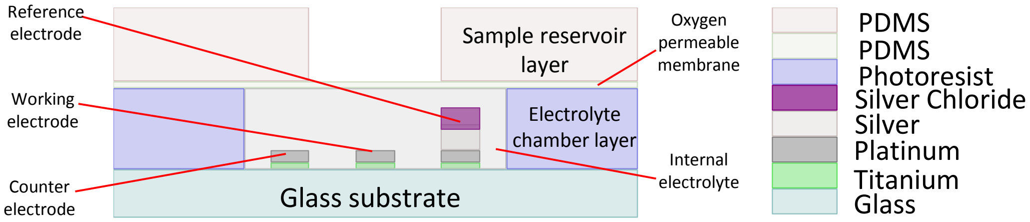

Figure 4.29 Cross section schematic of DO sensor. Different colours identify different materials.

To pattern the microelectrode and electrolyte chamber layer, two masks were designed as shown in Figure 4.30.

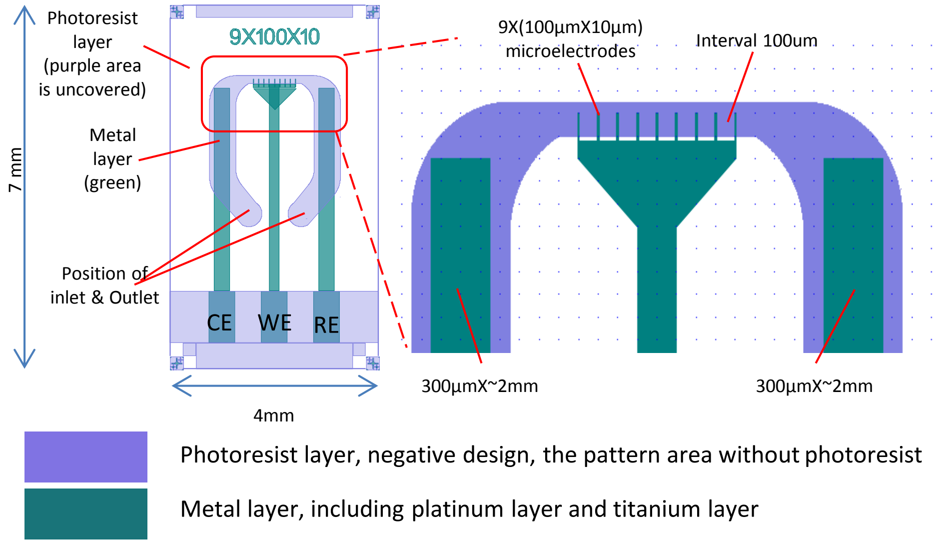

Figure 4.30 Masks for fabrication of microelectrodes and electrolyte chamber layer. Green mask shows metal layer. The platinum (on a layer of titanium) electrodes are as shown in green. Another mask was designed to pattern the photoresist layer forming the electrolyte chamber (purple); the purple area shows where there is no photoresist.

Microelectrodes were designed with solder pads on a 7mmX4mmX0.7mm glass substrate. An array of platinum band microelectrodes was used as the WE. Nine 100µm by 10µm band microelectrodes are shown in Figure 4.30 with a spacing of 100µm. Two larger electrodes (300µmX2mm) were positioned beside the WE. One was used for RE and the other an optional CE for a 3-electrode configuration. These electrodes were accessed with a photoresist cover. The photoresist layer constructed a chamber for electrolyte storage and all electrodes were fabricated to be within this chamber. This layer also electrically insulated the tracks. The inlet and outlet for electrolyte injection were at two ends of the chamber.

Different configurations of WE were designed as shown in Figure 4.31. Different designs of WE had different geometric areas, diffusion conditions and reduction currents which resulted in different sensor performance.

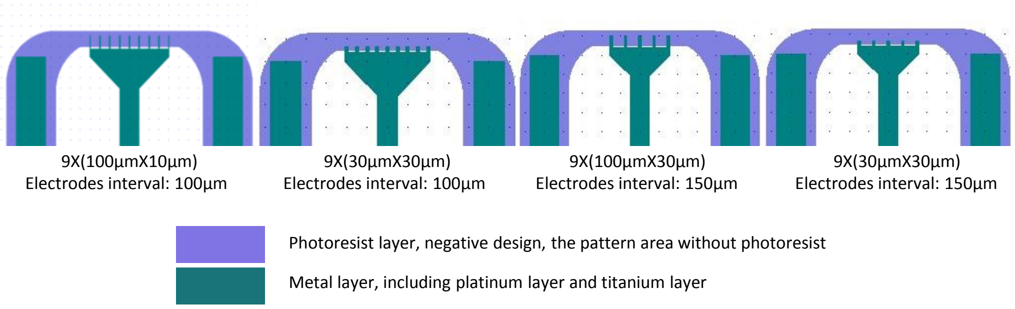

Figure 4.31 Sensor designs incorporating different patterns and different WE dimensions.

A Ag/AgCl reference electrode was used for the DO sensor. A silver layer was electrochemically deposited on the platinum layer, which was chlorinated to provide a AgCl coating on the RE. A gel-lie electrolyte (alginate gel soaked in 150mM KCl solution) was injected into the internal electrolyte chamber. This gel contains abundant chloride ions and is capable of maintaining a stable Ag/AgCl electrode potential, enhancing RE stability. The thin PDMS film was used for the OPM.

As discussed in section 4.2.2, the conventional method of measuring DOC is by applying a measurement voltage onto the DO sensor, and then measuring a stable current, which is proportional to the oxygen diffusion rate and the DOC of the bulk solution. The current response of a microelectrode to a step voltage is shown in Figure 4.32. The oxygen reduction current requires a period of time to reach steady-state. The intended final application of the device demands strict limitations on energy, and long measurement times implies a large energy demand. In order to minimise the energy requirement for the DOC measurement, the current at 100ms after applied voltage was used. Although the oxygen reduction current doesn’t reach steady-state after 100ms, the slope of current decreasing reflects the activity of oxygen reduction at a certain extent and is proportional to the DOC around the working electrode. Therefore, after calibration, this parameter is potentially to be used for DOC measurement. Furthermore, this measurement after a short time gives a larger current than the steady-state current, and should result in a better signal to noise ratio.

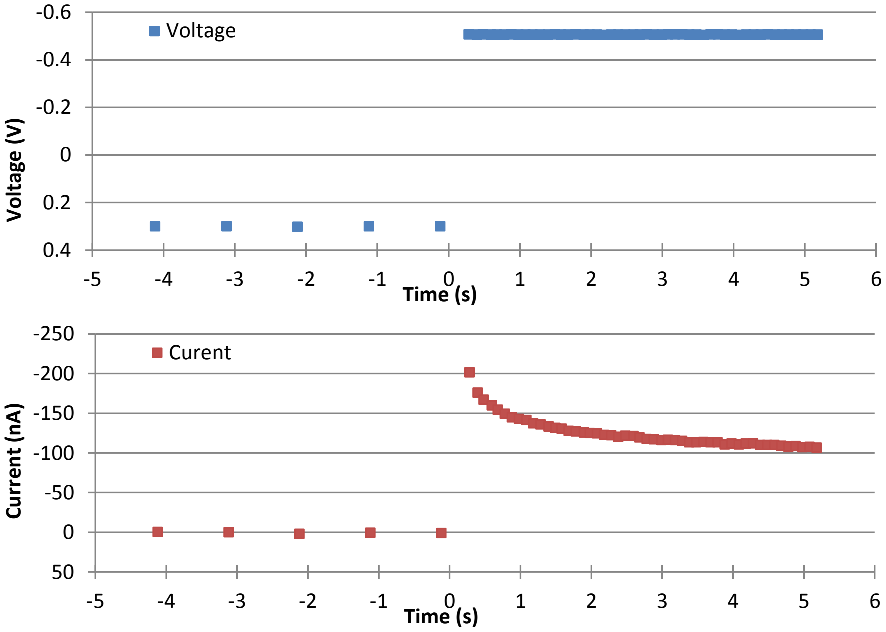

Figure 4.32 Current response of a microelectrode to a step voltage. Before time 0, the voltage on the DO sensor was the resting voltage which gives no current. At time 0, the voltage was changed to the measurement voltage and the oxygen reduction current increased immediately, this then reduced to a stable value which was limited by the oxygen diffusion process to the working electrode. The sampling rate before time 0 was 1sample/s, and subsequently increased to 10samples/s after time 0.

4.2.4 Fabrication of implantable DO sensor

A seven step process was used to fabricate the implantable DO sensor and the fabrication was undertaken in the cleanroom and CHB (Centre for Hybrid Biodevices) laboratory of Southampton University. Specifically, the fabrication of microelectrodes and SU8 layer for the DO sensor and pH sensor were manufactured by Katie Chamberlain[1] and the fabrication of TMMF layer was manufactured by Shimul Saha[1] (1: Centre of Hybrid Biodevices, Faculty of Physical Sciences and Engineering, University of Southampton, UK).

1. Fabrication of microelectrodes.

A wafer of sensor chips with patterned microelectrode array was fabricated using photolithography. A titanium layer was coated onto a glass wafer to form an adhesion layer and platinum was sputtered onto the titanium layer. A positive mask and photoresist were used to pattern the microelectrodes. More details are shown in Figure 4.33.

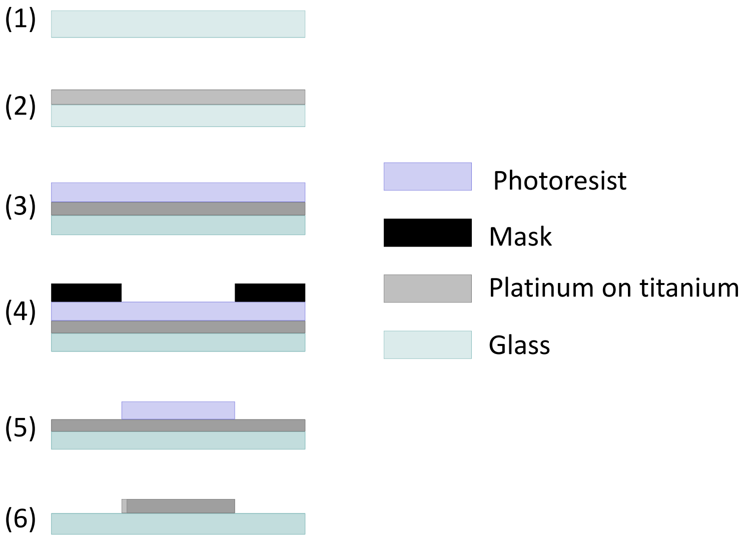

Figure 4.33 Fabrication procedure for the microelectrodes: (1) 0.7mm thick cleaned glass wafer was used as substrate; (2) 25nm titanium was sputtered on the glass substrate and then 300nm platinum was sputtered on to the titanium layer; (3) photoresist (S1813) was spin coated over the platinum layer; (4) Photoresist was patterned through a mask and developed; (5) Ion Beam (machine Oxford Instrument IonFab) was used to etch the metal with Argon beam (all the metal not coated with S1813 was removed) (6) Photoresist was removed by fuming nitric cleaning.

2. Fabrication of electrolyte chamber layer.

An electrolyte chamber layer was overlaid onto the sensor chip wafer and the wafer was cut into chips. This was made with SU8 (SU8-3025) giving a 25μm thick layer. The fabrication procedure is outlined below:

(1) Ti Prime is applied onto the sensor chip as an adhesion layer by spin coating at 3000rpm for 30s and then baking at 120°C for 2mins.

(2) SU8 is spin coated at 3000rpm for 30s and then soft bake at 95°C for 10mins.

(3) SU8 layer is patterned through an electrolyte chamber layer mask. After exposure, wafer is baked at 65°C for 1min and at 95°C for 3mins.

(4) SU8 is developed by using EC solvent for 2mins 30seconds and then rinse by IPA.

(5) Thorough nitrogen dry and hard bake at 150°C with a slow oven ramp up (20°C per minute), and slow oven ramp down.

(6) Wafer is scribed into chips.

Due to the difficulty of forming thick layers from SU8, a dry firm photoresist, TMMF (TMMF-S2055) with a thickness of 55μm was used to form a multi-layer giving a well thicker than 200μm. The fabrication procedure is below:

(1) Put the wafer in an oven at 211°C for 2mins.

(2) Laminate the TMMF at a temperature of 80°C.

(3) Repeat to laminate 4 layers of TMMF.

(4) Soft bake for 15mins at 60°C and wait 30mins until the TMMF surface is no longer sticky.

(5) After exposure through a mask, the wafer is baked at 30°C with a ramp to 90°C over 3mins and then held at 90°C for 12mins, followed by ramp down to room temperature. The wafer is then left at room temperature overnight.

(6) TMMF layer is developed by using EC solvent for about 25mins and then rinse by IPA.

(7) Wafer is scraped into chips.

3. Silver electroplating the reference electrode.

To form the Ag/AgCl reference electrode, a silver layer was plated onto the Pt reference electrode with the system shown in Figure 4.34. The target electrode (cathode) was connected to the negative terminal of power supply through a resistor with a silver wire as the anode. The current was monitored to maintain stable plating current. The silver electroplating solution was from a commercial recipe (Spa Plating UK). The chemical reactions are:

$$\begin{cases} Cathode: Ag^{+}{}_{(aq)} + e^{-} \rightarrow Ag_{(s)} \\ Anode: Ag_{(s)} \rightarrow Ag^{+}{}_{(aq)} + e^{-} \end{cases} \qquad (4.2\text{-}11)$$

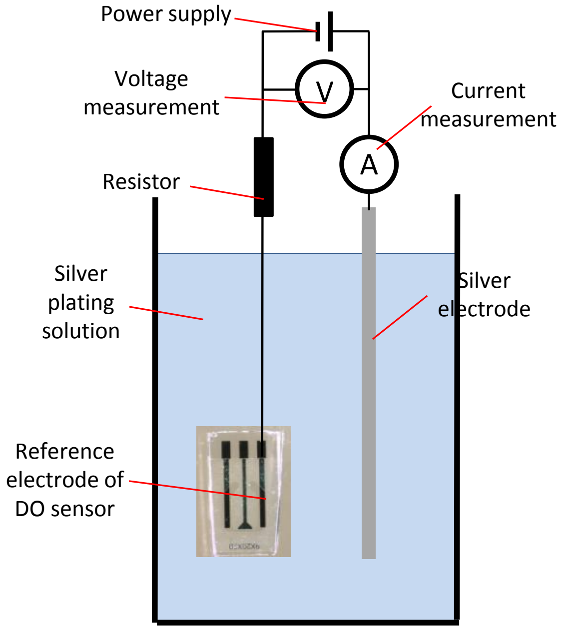

Figure 4.34 Schematic diagram of silver electroplating system setup. The cathode was the target electrode and the anode was a silver wire. A resistor was connected in series and the voltage applied on the electrodes was controlled to maintain a stable plating current.

Around 5µm of silver was coated onto the reference electrode at a current density of 333µA/mm^2 for 5mins.

4. Fabrication of OPM and reservoir layer.

MG-PDMS was spin coated onto the glass substrate using the procedure below:

(1) A glass slide is cleaned by immersion in Acetone for 5mins and wipe with a tissue to remove dirt, then rinse with IPA and methanol.

(2) The glass slide is coated with Duxcoat to make the surface hydrophobic.

(3) MG-PDMS is prepared by thoroughly mixing the base elastomer and curing agent in a 10:1 mix ratio by weight, and then de-gassing in a vacuum chamber for approximately 40mins.

(4) The PDMS mixture was spin coated onto the glass slides at 5000rpm for 5mins, and then baked in an 80°C oven for at least half an hour.

This technique produced a 13µm thick MG-PDMS OPM layer. To fabricate the sample solution reservoir with inlet and outlet, a potting mould was designed and printed using the 3D printer as shown in Figure 4.35.

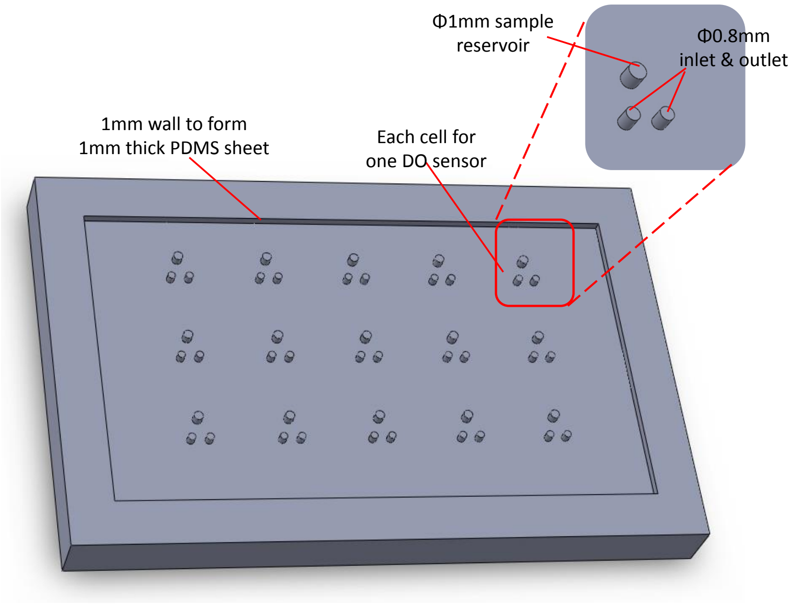

Figure 4.35 Design of potting mould used to fabricate the reservoir layer. A 5X3 cell array was designed with each cell, used for one DO sensor. 1mm wall was built around the mould. MG-PDMS mixture was poured into this mould to give a 1mm thick PDMS sheet. Each cell had 3 pillars, including a φ1mm pillar for the sample reservoir and 2 φ0.8mm pillars for inlet and outlet.

The process was as follows:

(1) Treat the potting mould surface with Duxcoat to make the surface hydrophobic.

(2) Prepare the MG-PDMS as above.

(3) Pour the MG-PDMS mixture into the mould gently and de-gas for approximately 15mins.

(4) Remove extra PDMS by scraping with a glass slide and then bake in an oven overnight at 80°C.

5. Procedures for multi-layer bonding.

Two sets of interfaces need to be bonded together, this including bonding the electrolyte chamber layer and OPM, and bonding the OPM and reservoir layer. Considering the OPM is only 13μm thick, it is very hard to handle. Therefore, the OPM was bonded to the reservoir layer first, and then this was bonded to the sensor chip.

Oxygen plasma treatment was used for PDMS bonding [145]. The reservoir layer was peeled off from the potting mould after curing. The surfaces of the reservoir layer and OPM were treated with oxygen plasma at 50w for 30s and then two surfaces were pushed together and bonded. Next, they were placed on the 80°C hotplate for around half hour under pressure. The holes for inlet and outlet were punched through and the reservoir layer with OPM was cut into single DO sensor chips.

Bonding of PDMS to SU-8 is not possible with plasma methods, heat or solvent-based processes. Bonding of PDMS and SU8 was achieved through a chemical reaction between their interfaces as shown in Figure 4.36[146].

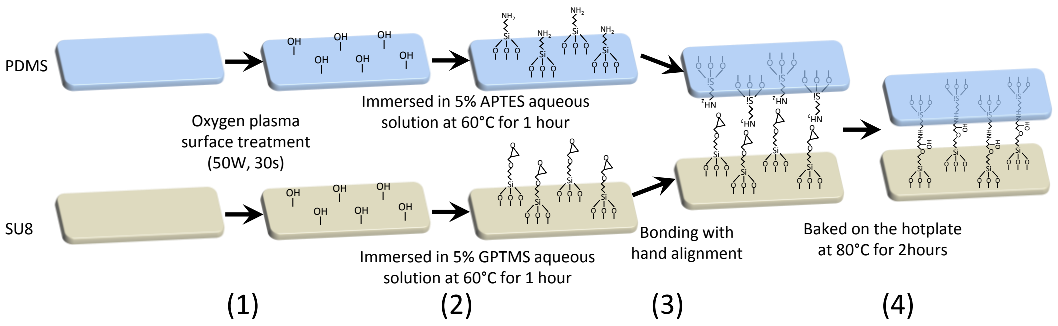

Figure 4.36 Bonding procedure between PDMS and SU8 [146]: (1) Oxygen plasma treated both surfaces of PDMS and SU8 at 50W for 30s. Hydroxyl groups were generated on the surfaces; (2) PDMS surface and SU8 surface were immersed in 5% aqueous solution of ATTES and GPTMS respectively, and they were left in 60°C oven for 1hour; (3) Treated surfaces were washed thoroughly with DI water and dried by nitrogen gas. Then two surfaces were brought into contact with hand alignment. Applied a certain pressure to make sure surfaces contact completely; (4) Baked on the hotplate at 80°C under a certain pressure for at least 2hours.

PDMS bonded by treating it to produce chemical groups capable of reacting with epoxy groups on the SU-8 surface. After oxygen plasma treatment, 5% 3-Aminopropyltriethoxysilane (APTES) aqueous solution was used to treat the PDMS surface to attach amino groups, which in turn can form stable chemical bonds with epoxy groups. To enhance the bonding strength, 5% 3-Glycidoxypropylmethyldiethoxysilane (GPTMS) aqueous solution was used to treat the SU8 surface, producing unreacted epoxy groups. This bonding procedure can also be used for bonding between PDMS and TMMF.

6. Formation of reference electrode.

After silver plating and multi-layer bonding, 3M KCl solution was injected into the internal chamber of DO sensor from the inlet and then immersed in a beaker of 3M KCl. The silver layer was coated by AgCl completely after 2 mins at a current density of 33uA/mm^2. After formation of the AgCl layer, the DO sensor was left at 60 °C for about 2days to stabilize the Ag/AgCl.

3% sodium alginate solution was prepared by dissolving 3g sodium alginate in 100ml 150mM KCl. This was injected through the inlet into the internal chamber of the DO sensor. The sensor chip was immersed in 0.05M $CaBr_2$ for 1day to form gel-like calcium alginate electrolyte. After fabrication, the leads of the DO sensor, inlet and outlet were sealed by epoxy and the device stored in 150mM KCl.

An implantable DO sensor (7mmX4mmX2mm) was fabricated as shown in Figure 4.37.

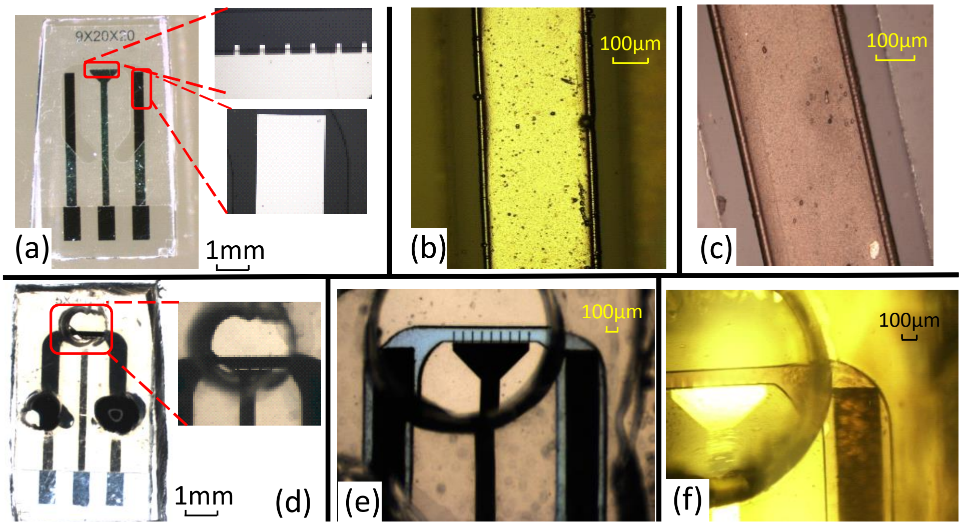

Figure 4.37 Fabrication of DO sensor: (a) Sensor chip with platinum electrodes and electrolyte chamber layer; (b) Silver was electroplated onto the reference electrode; (c) AgCl was generated on top of the silver reference electrode; (d) After multi-layer bonding, the internal chamber was checked for leakage with food dye; (e) Internal electrolyte (3% sodium alginate dissolved in 3M KCl solution) was injected into the internal chamber; (f) Gel-like electrolyte in the internal chamber.

4.2.5 Evaluation of DO sensor

Evaluation of built-in Ag/AgCl RE

The stability of the built-in Ag/AgCl RE was evaluated by measuring the open circuit potential (OCP) against a commercial RE (general purpose glass RE, Sigma-Aldrich). A long-term experiment (>1month) was set up as shown in Figure 4.38.

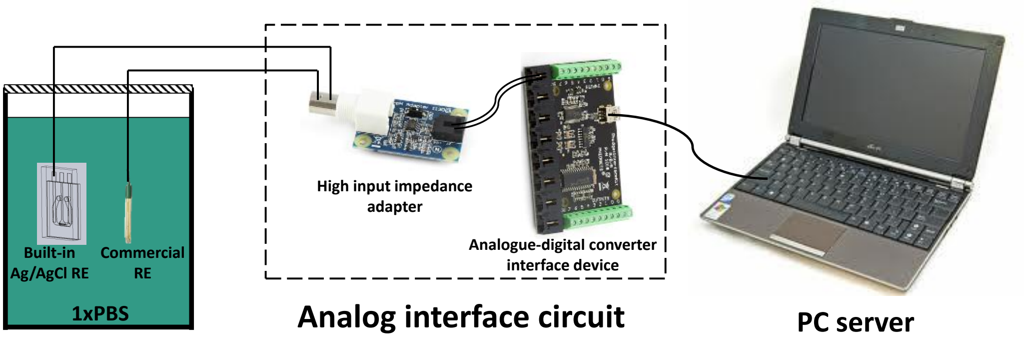

Figure 4.38 Schematic view of the experiment set up for the built-in Ag/AgCl RE evaluation. The miniature Ag/AgCl RE and a commercial RE were immersed in a beaker of 1xPBS solution which was sealed to minimise evaporation. An analogue to digital converter interface device (Phidgets 1018_2 interface kit) was used to measure the OCP of the built-in Ag/AgCl RE against a commercial RE. The device has a high input impedance adapter (Phidgets 1130_0 pH/ORP adapter, 1T ohm). Monitoring software recorded the OCP during this long-term experiment.

In this long-term experiment, the OCP variation of a newly fabricated Ag/AgCl RE was recorded for more than 42days as shown in Figure 4.39.

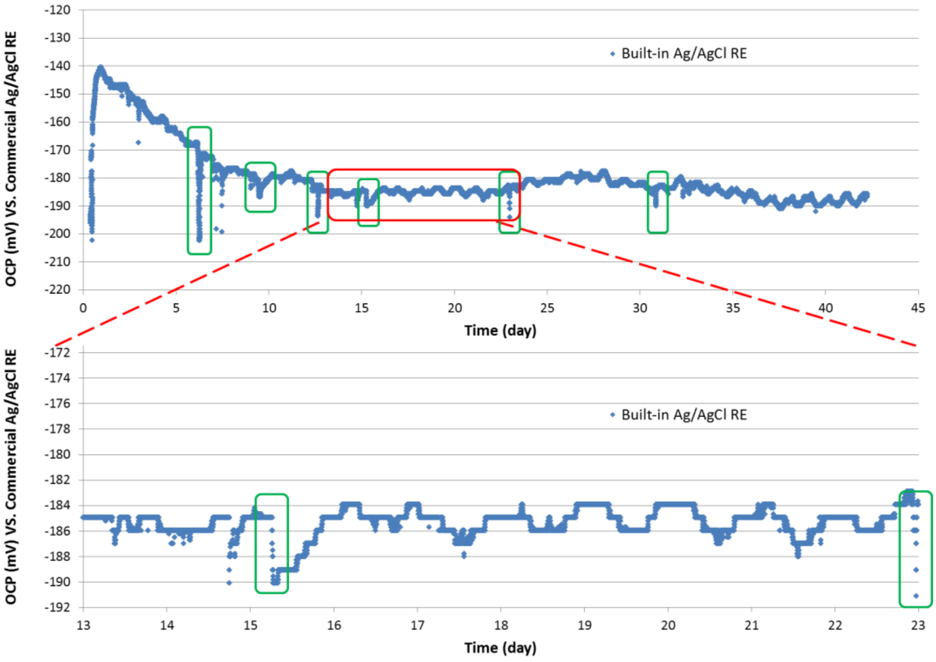

Figure 4.39 The OCP variation of the Ag/AgCl RE recode for more than 42days. The data for 10 days is zoomed in after the stabilization of built-in Ag/AgCl RE (red box). Because of the non-ignorable solution evaporation, sample solution was refilled some times during this experiment, and this may result in OCP steep variation as shown in green box.

For good stability, the miniature RE must have a constant OCP against the commercial RE. From the long-term experiment, the OCP of the Ag/AgCl RE became stable in 7 days. This process of stabilization may be associated with the hydration of AgCl layer. The Ag/AgCl RE was stable OCP, with a variation smaller than 10mV over the following 35 days. A daily variation of a few mV was observed. The Nernst equation shows that the OCP of the Ag/AgCl electrode depends on temperature.

$$E = E^0 - \frac{RT}{F}\ln a_{cl^-} \qquad (4.2\text{-}13)$$

Here E is the potential of the Ag/AgCl electrode, E^0 is the standard electrode potential against standard hydrogen electrode, R is the universal gas constant, T is the absolute temperature, F is the Faraday constant and a is the chemical activity of the Cl^- ions. This shows that small variations were possibly associated with the daily temperature changes. As shown in the V-I chart of oxygen reduction at a working electrode (Figure 4.15), the oxygen reduction current is constant over a certain voltage range around 200mV, therefore a few mV variation in the Ag/AgCl RE is deemed adequate for the DO sensor.

Evaluation of DO sensor

A test bench was developed for the evaluation of DO sensor as shown in Figure 4.40.

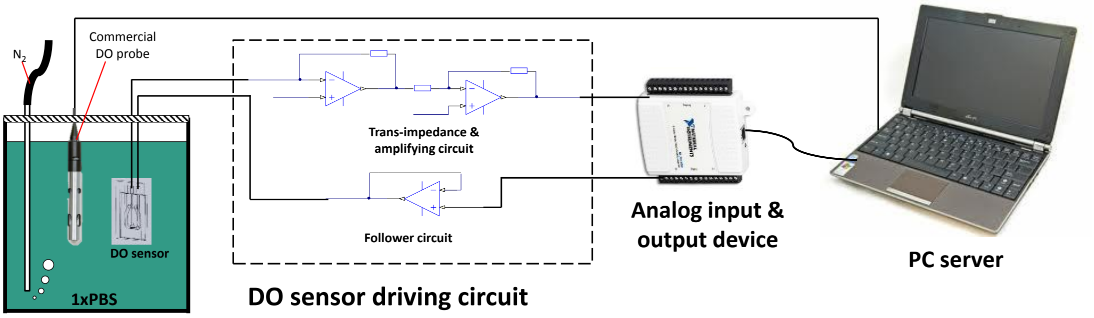

Figure 4.40 Schematic of the test bench for DO sensor evaluation. The DO sensor and a commercial DO probe (YSI ODO probe) were immersed in a beaker of 1xPBS, and N_2 bubbling was employed to change the DOC of the bulk solution. The beaker was closed with Parafilm to maintain a relatively stable test environment. A DO sensor circuit made from an analogue interface drives the DO sensor and measures the oxygen reduction current. Although the DO sensor has an optional counter electrode, a 2-electrode configuration circuit was implemented due to the small currents (nano-amps). The schematic diagram and PCB design are in appendix A (10, 11). An analogue input and output device (NI USB-6251, National Instruments) was used for analogue-digital conversion and uploading data to a PC.

A series of cyclic voltammetry (CV) tests were undertaken to evaluate the electrochemical characteristics of the DO sensor. The V-I profiles of the DO sensor at different DOC solutions are shown in Figure 4.41.

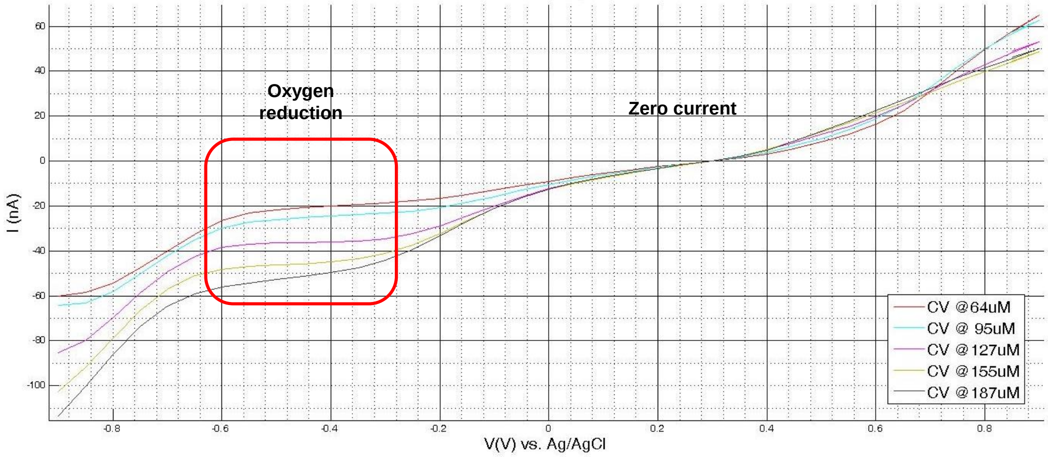

Figure 4.41 V-I relationship for the DO sensor obtained from the CV experiments. The scan was from +0.9V to -0.9V, and the scan rate was 25mV/s. The DOC of bulk solution was changed by bubbling N_2. DOC was also measured with a commercial DO probe (YSI ODO probe).

Different zones are clearly observed in the V-I chart. The zero current zone describes the voltage range over which few electrochemical reactions happen and a nearly zero current achieved. It is the stable state without oxygen consumption. The DO sensor should stay at a rest voltage within this zero current zone when no measurements are taken. When the voltage moves more positive, the current increases because of oxygen generation. Similarly, when the voltage moves negative the current increases due to hydrogen generation.

Based on these V-I profiles, the measurement voltage for oxygen reduction can be determined. In the zero current zone, current was zero at around 0.3V. Therefore, the rest voltage of DO sensor was determined as 0.3V. In the oxygen reduction zone, limited oxygen reduction currents were observed in the zone from -0.4V to -0.6V irrespective of a bit shift of voltage. Therefore, the measurement voltage was selected at -0.55V.

The DO sensor was calibrated on the test bench as shown in Figure 4.40. Three DO sensors with different working electrode arrays (9X20µmX20µm, 5X30µmX30µm, 9X100µmX10µm, respectively) were evaluated; the calibration results are shown in Figure 4.42.

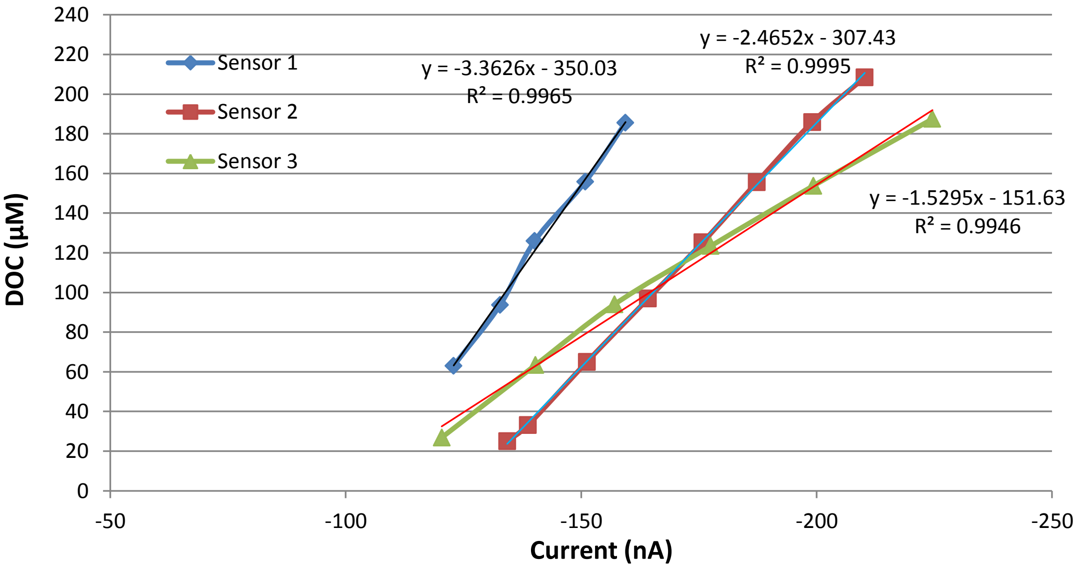

Figure 4.42 Calibration result for 3 DO sensor prototypes. Sensors 1-3 were DO sensors with different working electrodes (9X20µmX20µm, 5X30µmX30µm, 9X100µmX10µm, respectively). The x axis is the reference DOC readings from commercial probe and the y axis is the oxygen reduction current measured at a measurement voltage of -0.5V vs. Ag/AgCl.

Good linear responses were obtained from these DO sensors. The sensitivity was 3.36µM/nA for the sensor with 9X20µmX20µm working electrode (3600µm^2), 2.47µM/nA for the 5X30µmX30µm DO sensor (4500 µm^2) and 1.53µM/nA for the 9X100µmX10µm DO sensor (9000 µm^2). The current densities of sensors were calculated as 8.27×10^{-5}nA/µM·µm^2, 8.99×10^{-5}nA/µM·µm^2 and 7.26×10^{-5}nA/µM·µm^2 respectively. The current density varied due to the variance of working electrodes area from the fabrication, such as the slight misalignment between microelectrodes layer and electrolyte chamber layer.

Errors in the DOC measurement are shown in Figure 4.43 showing that differences between the DO sensor and the commercial DO probe were in the range of ±7µM. Note that the commercial DO probe (YSI ODO probe) has an accuracy of ±3.12µM. These errors may be caused by the defect and instability of the calibration system. For example, the distance between the sensor chip and reference probe may cause calibration errors. More precise results and better performance may be achieved with more precise calibration system.

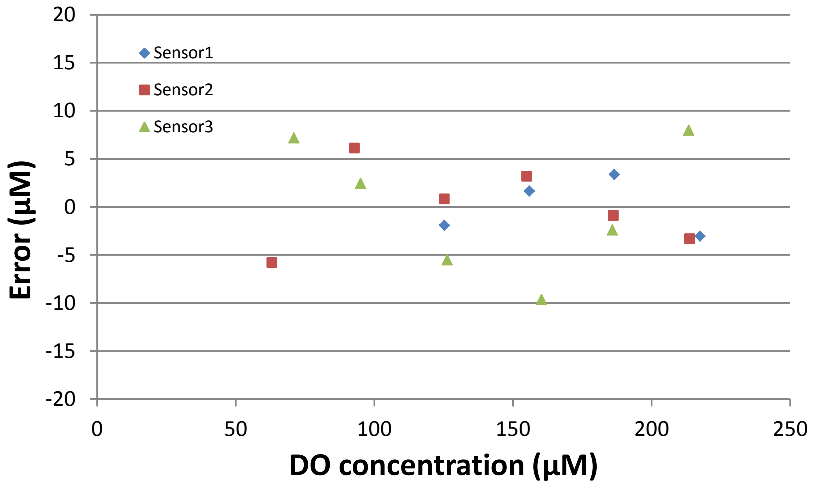

Figure 4.43 Errors in DO sensor measurement determined from a commercial DO probe.

A drift was observed after continuous measurement, although the DO sensor proved to be adequate for bench and short term testing. The results of two calibration cycles for a DO sensor with a 9X100µmX10µm working electrode are shown in Figure 4.44.

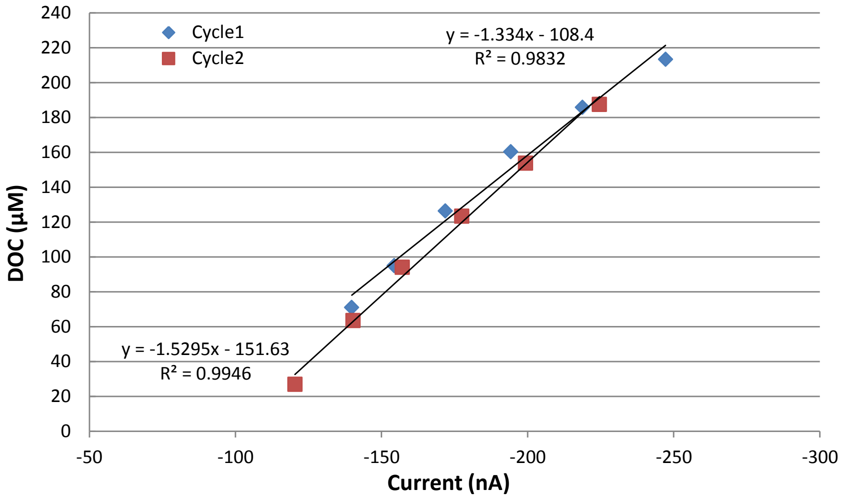

Figure 4.44 Results for DO sensor calibration and recalibration after 1day continuous measurement.

This drift might be due to the change in working electrode surface condition. Platinum electrodes are known to lose activity at a constant potential near the oxygen reduction, and electroplating may occur on the platinum surface, which affects the oxygen measurement [147, 148]. A sequence of potential pulses has been suggested [147, 148] as a strategy to maintain the activity of the platinum electrode and prevent decay in the output signal.

4.2.6 Summary of implantable DOC sensor development

For the intended intra-uterine DOC measurement, a miniaturised electrochemical DO sensor with low power consumption was produced. After discussion of the principles and key technologies of electrochemical DO sensors, a multi-layer DO sensor was designed with an internal chamber for the gel-like electrolyte. The stability of the built-in Ag/AgCl RE and the characteristics of medical grade OPM were also discussed. The DO sensor was fabricated and then tested on the bench using a protocol developed for DO sensor evaluation. Through testing, the electrochemical characteristics of the DO sensor were investigated and the clear reaction zones were observed in the V-I profiles. A good linear relationship between the oxygen reduction current and the DOC of the bulk solution was observed. The measurement error was in the range of ±7μM. However drift was seen after a period continuous measurement.

4.3 Design of miniaturised implantable pH sensor design

4.3.1 Technologies for pH measurement

Simple pH indicators are a set of disposable strips which determine pH based on a halochromic compound. pH indicators are cheap and easy to use. Normally, their resolution is 1pH unit and they are widely used for tests not requiring precision reading. For precise measurements, a pH meter is widely used. The most commonly used pH meters are based on a glass pH electrode. Glass pH electrodes can achieve better resolution (0.01pH) and accuracy (±0.01pH). However, they are poorly suited to implantable sensors, despite their good analytical capabilities [149].

Different kinds of micro-scale pH sensors have been developed, particularly ion-sensitive field effect transistors (ISFET) [136, 150]. A typical ISFET pH sensor is shown in Figure 4.45. Its structure is very similar to the Metal-Oxide -Semiconductor Field Effect Transistor (MOSFET), except the gate metal is a pH sensitive insulating layer. A reference electrode is immersed in the solution and the pH changes the gate voltage.

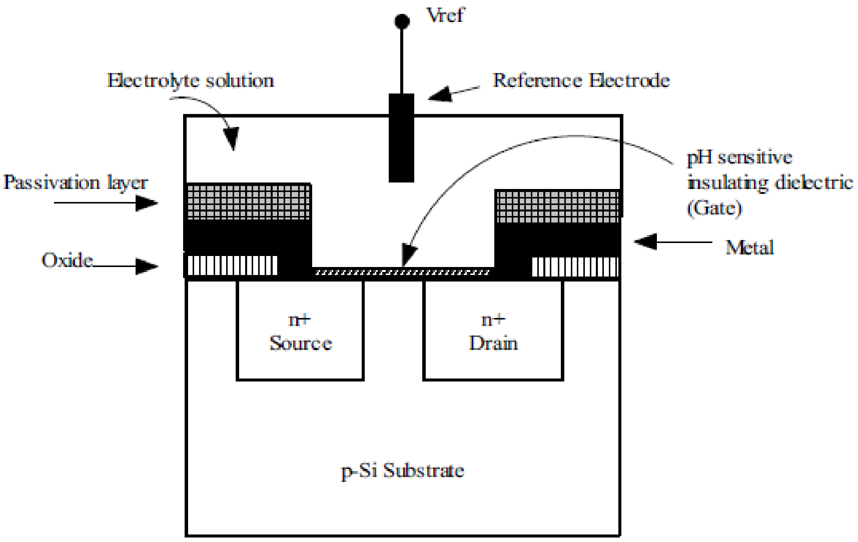

Figure 4.45 Cross-section view of typical schematic of ISFET for pH measurement (taken from [150]).

ISFET pH sensors can have smaller size but with similar accuracy to glass pH electrodes. However, they have a multi-layer structure and require complex macro-fabrication procedures and technologies. They also need complex electrical circuits to drive the ISFET pH sensors. These components and circuits increase the space requirements and power consumption, making this approach unsuitable for an implantable device.

An alternative method to ISFET pH sensors is metal oxide-based pH sensor, which have comparative pH measurement capabilities, a simple structure and can be micro-fabricated [151]. A wide variety of metal oxides have been characterised and iridium oxide (IrO_x) is most commonly used [151-157]. The typical IrO_x pH sensor is made from a thin IrOx film (IROF) evaporated onto a micro electrode. A simple structure enables simple fabrication, the use of a relatively simple processing circuit and small size. After considering the options, an **IrO_x pH sensor** was deemed the most suitable candidate for intended intra-uterine sensing platform.

4.3.2 The principle of IrO_x pH sensor

The mechanisms of the IROF pH sensing are not fully understood yet, although some possible principles have been proposed, based on the pH dependent reduction-oxidation (REDOX) equilibrium at different oxidation states of the iridium oxide [154, 155, 158, 159]. Considering the different forms of IROF, including anhydrous IROF and hydrated IROF, the possible REDOX reactions can be illustrated differently as below.

Anhydrous IROF:

$$\begin{cases} IrO_2 + H^+ + e^- \leftrightarrow IrO\cdot OH \\ or \\ 2IrO_2 + 2H^+ + 2e^- \leftrightarrow Ir_2O_3 + 2H_2O \end{cases} \qquad (4.3\text{-}1)$$

Hydrated IROF:

$$2[IrO_2(OH)_2\cdot 2H_2O]^{2-} + 3H^+ + 2e^- \leftrightarrow [Ir_2O_3(OH)_3\cdot 3H_2O]^{3-} + 3H_2O \qquad (4.3\text{-}2)$$

The pH can be determinate from the molar concentration of H^+, as shown below.

$$pH = -\log(H^+) \qquad (4.3\text{-}3)$$

The Nernst Equation is used to predict the electric potential of an REDOX reaction.

$$E = E^\circ + \frac{2.303RT}{nF}\log a \qquad (4.3\text{-}4)$$

Equation (4.3-3) shows that there is a linear relationship between electrode potential and pH.

$$E = E^\circ + \frac{2.303RT}{nF}\log(H^+) = E^\circ - \frac{2.303RT}{nF}pH \qquad (4.3\text{-}5)$$

The potential of the anhydrous IROF electrode undergoing reaction (4.3-1) can be calculated from (4.3-4) and (4.3-3) at 25 ºC as shown below.

$$E = E^\circ + \frac{2.303RT}{F}\log(H^+) = E^\circ - 59.16(mV)\,pH \qquad (4.3\text{-}6)$$

At a temperature of 25 ºC, the response of anhydrous IROF to pH changes has a slope of about -59mV/pH – a Nernstian response. Similarly, the potential of hydrated IROF electrode under reaction of (4.3-2) as:

$$E = E^\circ - (\frac{3}{2})\frac{2.303RT}{F}\log(H^+) = E^\circ - 88.7(mV)\,pH \qquad (4.3\text{-}7)$$

Due to the mechanism of two electrons transferred per three hydrogen ions as shown in (4.3-2), the hydrated IROF exhibits a super-Nernstian response to pH changes with a slope of approximately -88mV/pH which is larger than the anhydrous IROF. Therefore, a pH sensor based on hydrated IROF has a better sensitivity than the anhydrous IROF sensor.

4.3.3 Current fabrication methods of IROF

A variety of techniques have been used to produce IROF electrodes [160, 161], including sputtering deposition, thermal deposition, sol-gel processes, electrochemical growth and electrodeposition.

IROF can be deposited by reactive sputtering from an iridium metal target, such as iridium wire, in an oxygen environment [156, 162]. This method directly deposits IROF on the target. It is compatible with current fabrication techniques, although it needs specific instrument for the deposition. The IrO_x generated by this method is a dry electrode formed from anhydrous IrO_x. Usually, the hydrolysis of anhydrous IROF is a very slow process, which can take more than 2 months. Therefore, pH sensors based on anhydrous IROF electrodes often exhibit large aging effects which drift over a long period. Furthermore, the potential drift and REDOX interference of IROF made by this sputtering method are related to the sputtering condition, such as oxygen partial pressure, argon pressure, humidity, deposition rate, substrate temperature [156]. In addition, the cost of this method is relatively high because of the use of iridium metal target.

IROF can also be fabricated using thermal deposition technologies. Iridium metal can be directly oxidized in air at 800 ºC after surface wetting in a NaOH solution [163]. Iridium metal can also be oxidized in molten KNO_3 at 420 ºC [164] or in a carbonate melt at 870ºC [160]. Another thermal method is based on the pyrolysis of $IrCl_3$ at 400-500ºC [157]. Thermally generated IROF is also formed by anhydrous IrO_x and is comparable in nature to IROF fabricated by sputter deposition. All these thermal methods require high temperatures for IROF deposition.

A method based on sol-gel dip-coating process was also developed for IROF fabrication [165]. The starting material was iridium chloride and a coating solution was prepared by reacting iridium chloride, ethanol and acetic acid. The iridium oxide coating was formed at a withdrawal rate of 2.0 cm/min and the coated film was heat-treated at 300ºC. IrO_x can be crystallized at temperatures above 450ºC. This method is less expensive because it does not require an iridium target. However, it requires high temperatures to treat the target and anhydrous IROF is generated.

Research into electrochemical growth of IROF [154, 158, 166, 167] has shown that by using this method, IROF can grow on the surface of an iridium metal electrode by cyclic voltammetry in an electrolyte, such as H_2SO_4 and NaOH between the potentials corresponding to H_2 and O_2 evolution. IROF produced by this method is mostly in an amorphous phase and highly hydrated. It commonly exhibits a super-Nernstian response in a range from -60 to -80mV/pH, which is better than the -59mV/pH of anhydrous IROF. However, the sensitivity of IROF made by this method is often unpredictable due to the differences in fabrication conditions, which cause differences in the oxidation state and the extent of hydration. Moreover, it also needs iridium as a deposition target.

Electrodeposition of IROF has been developed based on anodic electrodeposition in a solution containing iridium complexes [168-170], and the generated film is called anodically electrodeposited iridium oxide film (AEIROF). This method enabled IROF to be deposited on a variety of electronically conducting substrates by galvanostatic or potential cycling, such as glassy carbon, Ti, Pt or Pt/Krypton film, which makes it compatible with micro-fabrication technologies and suitable for micro-sensor development. It is a less expensive and simpler procedure; no iridium substrate is required or high temperature equipment. IROF made by this method is also hydrated and gives a super-Nernstian response to pH changes. Although it is relatively complicated to prepare the deposition solution, the electrodeposition method is more suitable for pH sensor fabrication and easy to carry out.

Two recipes of deposition solutions for IROF electrodeposition method are Baur's [168] and Yamanaka's [169, 170]. The first step of Baur's recipe is to prepare an acidic solution of $Ir(OH)_2Cl_4^-$ from either $IrCl_6^{3-}$ or $IrCl_6^{2-}$ by dissolving Na_3IrCl_6 or $Na_2IrCl_6 \cdot 6H_2O$ in 0.1M HCl. Ethanol was added as a reducing agent to ensure complete reduction of $IrCl_6^{2-}$ in HCl. The mixture was heated to boiling point for 3 hours until the reduction was completed. The second step is to form the air-sensitive iridium (III) oxide $Ir_2O_3 \cdot xH_2O$ from $Ir(OH)_2Cl_4^-$ by adding a base, such as NaOH. Because the iridium (III) oxide is unstable in oxygen, a thorough nitrogen purge is necessary before addition of the base. 6M MaOH is used to neutralize the acidic solution of $Ir(OH)_2Cl_4^-$ making the pH of the solution about 12.50. The oxidation of the iridium (Ill) oxide solution can be initiated electrochemically and deposited on the electrode. However, the conditions of the deposition solution prepared by Baur's recipe are difficult to control. As iridium (III) oxide is extremely sensitive to oxygen and a precipitate forms readily after exposure to air. Oxygen leakage into the deposition cell can cause failure of the deposition. Considering this recipe required a strict preparation environment, such as avoiding oxygen during the deposition of IROF, this method was considered to be unsuitable.

In Yamanaka's recipe, the electrodeposition solution is prepared from iridium tetrachloride with the addition of hydrogen peroxide, oxalic acid and potassium carbonate [169, 170]. The iridium oxide can be deposited by electrochemically induced oxidation of an iridium complex. Oxalic acid is added to form the iridium complex in the electrodeposition solution. A possible mechanism in which iridium oxide is formed by anodic oxidation of ligands in the iridium complex is presented below.

$$[Ir(COO)_2(OH)_4]^{2-} = IrO_2 + 2CO_2 + 2H_2O + 2e^- \qquad (4.3\text{-}8)$$

The ligands of the iridium complex in the electrodeposition solution play a crucial role in achieving stable anodic electrodeposition on the electrode, and a high efficiency can be reached at a pH of value of 10. This recipe requires relatively simpler equipment and can be carried out in a conventional laboratory. Therefore, **Yamanaka's recipe** was employed to prepare the electrodeposition solution for IROF pH sensor fabrication.

4.3.4 Electrodeposition solution preparation and AEIROF fabrication

According to Yamanaka's recipe, the electrodeposition solution for AEIROF was prepared as shown in Figure 4.46. The colour change of the solutions were monitored for the assessment of the composition, and a light violet solution was obtained after at least 2 days stabilization similar to the literatures [151, 152, 169].

To simplify the design and accelerate the development, the chips for DO sensor was reused for the pH sensor. The 300µmX2mm platinum electrode was used as the target electrodes for AEIROF deposition. Around 100nm blue-dark AEIROF was obtained at constant current density of 1mA/cm^2 for about 10mins as shown in Figure 4.47.

Procedure	**Colour**	**Image of solution**
(1) Dissolve 0.15g $IrCl_4.H_2O$ in 100ml DI water and magnetic stirred for 30 min.	Black	
(2) 1ml H_2O_2 aqueous solution (30wt.%) is added and the resulting solution is stirred for 10 min.	Dark green	
(3) 0.5g oxalic acid ((COOH)2.2H2O) is added and the solution is stirred for 10 min.	Amber	
(4) Anhydrous K_2CO_3 is added a little at a time to adjust the pH of solution to 10.5	Light amber	
(5) Solution is left standing at room temperature for at least 2 days and then put it in refrigerator.	Light violet	

Figure 4.46 Procedures for preparation of electrodeposition solution, based on Yamanaka’s recipe.

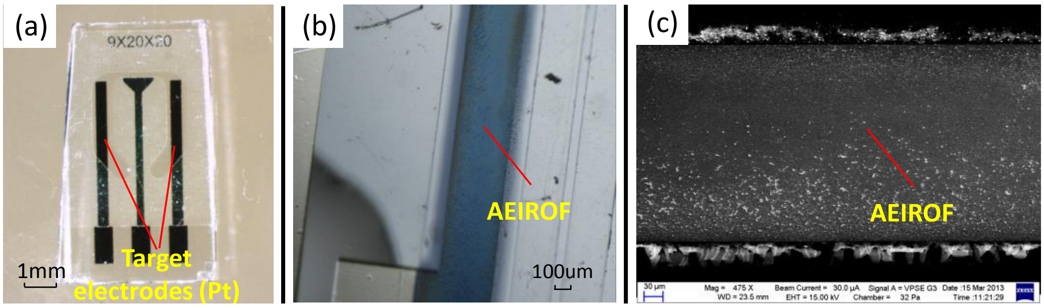

Figure 4.47 Platinum electrodes for AEIROF deposition (a), microscope image (b) and SEM image (c) AEIROF on a platinum electrode.

4.3.5 Evaluation of AEIROF pH sensor

As discussed in section 4.3.2, the electrode potential of the AEIROF electrode has a linear relationship with the pH of ambient solution. The open circuit potential (OCP) (vs. a reference electrode) can be used to measure the AEIROF electrode potential and then determine the solution pH value. An AEIROF pH sensor includes an AEIROF electrode and a reference electrode, such as Ag/AgCl electrode. IROF electrodes fabricated as above were tested in different pH buffers with a Ag/AgCl electrode. The OCP was measured with an analogue board with input impedance higher than 10G Ohm. An auto-testing platform was developed as shown in Figure 4.48.

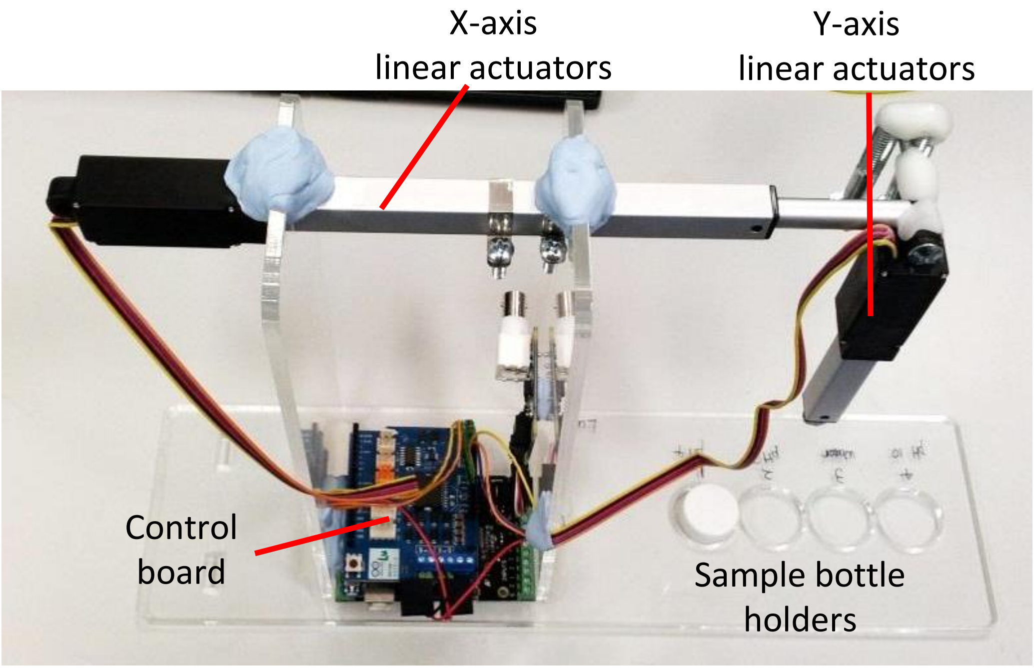

Figure 4.48 Auto-testing platform to test IROF pH sensors. It included two linear actuators to move the probe along X-axis and Y-axis. A control board was connected to PC and software was developed to control the platform to test the pH sensors in different pH buffers. There were four bottle holders including 3 bottles of different pH buffers and 1 bottle of DI water for washing.

The AEIROF pH sensor (an AEIROF electrode and a reference electrode) was fixed on the end of the sensing probe and immersed in standard pH buffers. Each test cycle included several steps in different pH buffers and in each test step the sample OCP was recorded for 5min. Between any 2 testing steps, there was 1 washing step. A typical result of a testing cycle is shown in Figure 4.49.

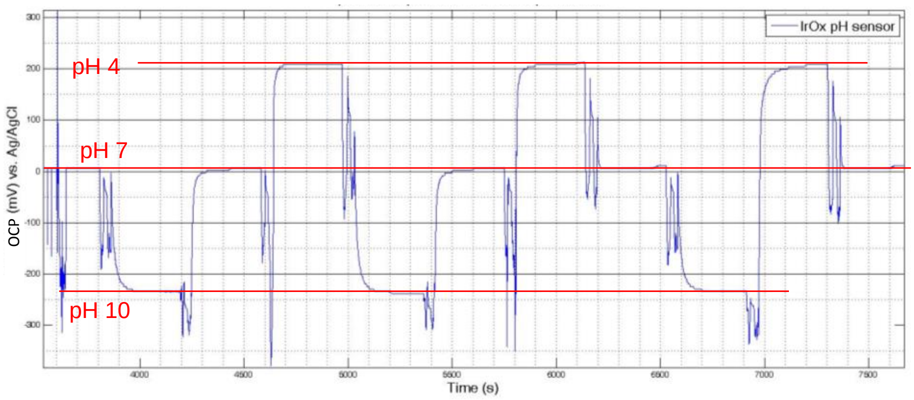

Figure 4.49 A typical result of a testing cycle. The AEIROF pH sensor was immersed in different standard pH buffers and the OCP recorded for 5mins during each test. A wash step was carried out between every two tests.

The AEIROF pH sensor was tested in standard pH 4, 7 and 10 buffers alternately; more than 3 times in each buffer. Figure 4.49 shows that the response time of AEIROF pH sensor is around 50s (time to reach 90% of a stable pH reading). This delay may be due to equilibration of the bulk pH solution into the pores of iridium oxide film. Considering the *in-vivo* environment is relatively stable with intended sampling rate of one per 15min, this response is suitable for our intended application. Five different AEIROF pH sensors were tested after aging in 1xPBS or standard pH7 buffer for at least 5 days. The calibration curves are shown in Figure 4.50. A linear super-Nernstian response can be seen from each sensor with similar slopes of around 76.33±2.58mV/pH.

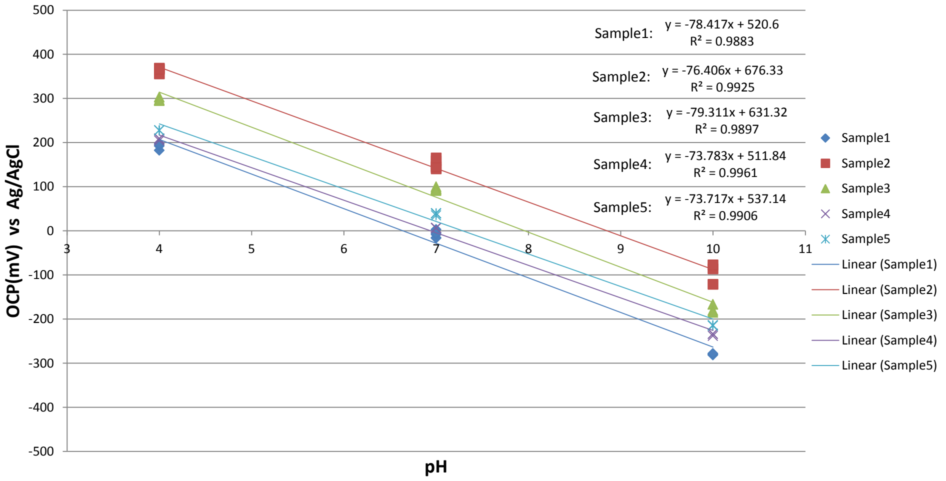

Figure 4.50 Calibration curves for 5 AEIROF pH sensors in different standard pH 4, 7 and 10 buffers. They were tested in each buffer more than 3 times.

The OCP readings of the AEIROF pH sensors and their response are listed in Table 4.3. Sensors 1 to 3 were transferred to different buffers by hand and sensor4 and 5 were tested with the auto-test platform which eliminated the reading error caused by different sensor configurations, testing positions and depths. The deviations of sensor 4 and 5 reading in the same pH buffer were around 0.04pH which is smaller than the samples tested by hand.

Table 4.3 OCP of AEIROF pH sensors in standard pH4, 7 and 10 buffers and the slope of super-Nernstian response.

	OCP (mV) vs. Ag/AgCl				
Sample	**1**	**2**	**3**	**4**	**5**
pH10 (mV)	-280±1.75	-95±23.3	-177.57±9.46	-235.27±2.71	-214.5±0.69
pH7 (mV)	-8.6±7.99	150.46±10.69	95.08±3.31	6.48±0	38.5±2.11
pH4 (mV)	190.5±7.24	363.23±6.94	298.3±4.13	207.43±2.71	227.8±0.00
Slop (mV/pH)	-78.42	-76.41	-79.31	-73.78	-73.72

The drift of ion sensitive pH sensors is common and may depend on the test scenarios, which are related to liquid junction potentials or diffusion potential effects and slow oxidization of AEIROF [120, 154, 171]. The phenomenon usually occurs with solutions containing two different ion concentrations. Due to different diffusion constants, including anionic diffusion being faster than the cations, separations of electrical charges occur at the junction between the sensor and solution. Therefore, a temporary potential is developed which then drifts during the equilibration process. Furthermore, the AEIROF may be slowly oxidized in the bulk solution due to dissolved oxygen, which also results in long-term drift. From the potential drift tests, as shown in Figure 4.51, after 1 hour testing in different pH buffer, the OCP of our AEIROF pH sensor drifted around 15mV over 24 hours and a slow down on the drift can be seen. At the beginning OCP drifted at 5mV/h and then at less than 0.25mV/h. Based on the analysis of a drift at 0.25mV.h, the pH reading drift can be predicted as smaller than 0.07pH per day.

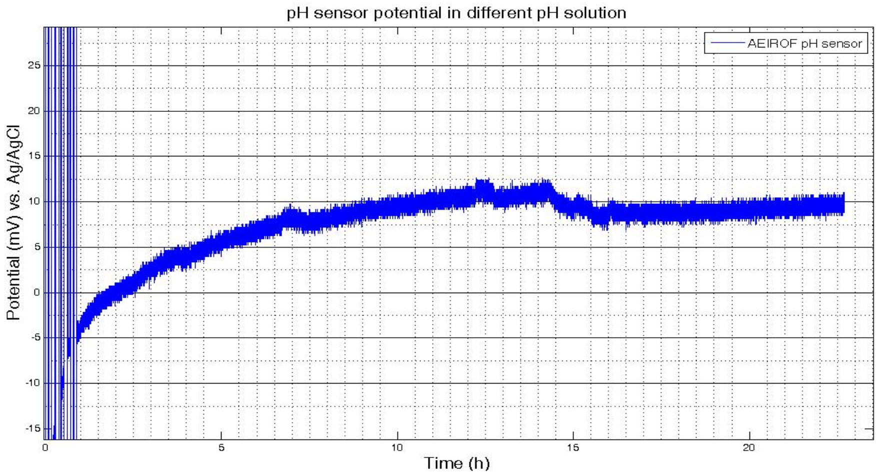

Figure 4.51 Potential drift in standard pH7 buffer for 24 hours. AEIROF pH sensor was tested in different standard pH buffers for 1 hour and then kept in pH 7 buffer to evaluate drift.

4.3.6 Summary of implantable pH sensor development

Different technologies for miniature pH sensor have been reviewed and compared. The IROF pH sensor was chosen due to its small size, wide pH range, high pH sensitivity, fast response time, low potential drift and low sensitivity to other redox pairs interference. From the discussion of different methods used to form IROF electrode, the anodically electrodeposited IROF (AEIROF) based on Yamanaka's recipe was used to fabricate the pH sensor. An auto-testing platform was developed for sensor evaluation and the pH sensor demonstrated a super-Nernstian response with a sensitivity of 76.33±2.58mV/pH. The accuracy can reach 0.04pH, tested with standard pH buffers. This miniaturised AEIROF pH sensor is potentially useful for our intended application.

However, different sensor calibration curves were observed for different samples. The possible reasons for variations in the potential bias and response slope may come from the varied oxidation states and hydration state of AEIROF [154, 158, 167]. It was also found that the pH sensing characteristics are related to the structure and thickness of AEIROF. For example, it has been suggested that thicker AEIROF should give more reproducible pH response [167]. Although some aging procedures have been proposed to improve the pH sensor reproducibility and stability, there is no recognized mature aging method to enable good characteristics of AEIROF pH sensor. For example, it has been suggested that a fresh AEIROF pH sensor should be kept in universal pH7 buffer for at least 2days [152, 172, 173] or with thermal treatment [171]. More work on the sensor stability and reproducibility is required in future.

Chapter 5

Animal tests of prototype system

Considering the intended application scenario is more complicated than the bench testing environment, the prototype proposed in this thesis required *in-vivo* testing prior to a human trial. For example, firstly bench testing environment is relatively simple and constant, but people are different which means a system deployment solution can not suitable to everyone. System deployment, especially receiver’s antenna, has to be designed to fit in different conditions, such as for people with different height and weight. Secondly, bench testing doesn’t need to consider human daily behaviours which may result in system failure, such as human movement, walking, breathing, etc. Thirdly, there is no need to worry about the impact on the testing equipment during bench testing, such as the water bath for temperature sensor test, but in the human internal environment, implanted device may be dangerous to the user and result in tissue damage and infection. Therefore, after the development and bench testing of the system and implantable sensors, a series of animal testing have been undertaken.

Animal testing is the use of non-human animals in experiments for pure research, applied research, drug testing and toxicology tests [174]. The National Academy of Sciences claimed that even sophisticated computers are unable to model interactions between molecules, cells, tissues, organs, organisms, and the environment, making animal research necessary in many areas [175]. A fully implantable sensor device was developed to suit the intended human intra-uterine monitoring application. We opted to test the system in the pig and rabbit. In two series of tests, freshly euthanized pigs were used for prototype system verification and optimisation, and rabbits were employed for *in-vivo* tests. After these tests, the prototype was evaluated and optimised for intended application and a study to capture real-time rabbit intra-uterine temperature was undertaken.

The animal tests were undertaken with the help from our collaborator at the Department of Surgical Research, NPIMR. Especially, for the pig cadaver tests, it includes investigation of implanted sensor device by endoscope imaging, sensor device implantation and retrieval, and all activities deal with pig's body. For the *in-vivo* tests on rabbit, it includes the surgeries for sensor device implantation and retrieval, and histology research after implantation tests.

5.1 Tests on pig cadavers for system verification and optimisation

5.1.1 Introduction of pig tests

The device was implanted in the pig to investigate system verification, optimisation of the wearable receiver and to evaluate the implantation strategy (Figure 5.1). Because the aim of this animal testing is for the proof of concept, verification prototype dimentions, practice of clinical proceudres, and system deployment solution, freshly euthanized pigs were selected rather than live pigs due to the consideration of cost and experiment complexity. All animal tests were undertaken in the line with the ARRIVE (Animal Research: Reporting In Vivo Experiments) guidelines.

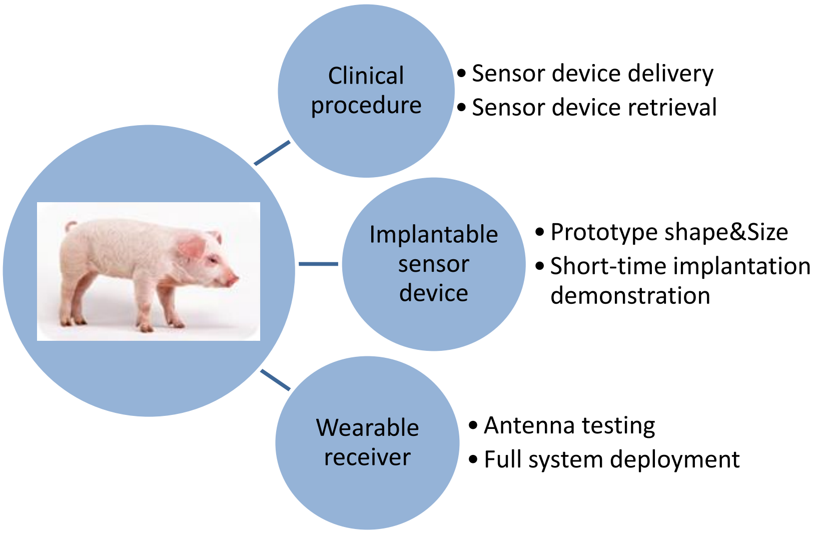

Figure 5.1 Goals of the pig cadaver test, including clinical procedure demonstration, testing of the implantable sensor device and wearable receiver deployment optimisation.

An illustration of the anatomy of the female reproductive system of pig is shown in Figure 5.2. The pig has a long vagina and cervix, while the uterine body, the junction of two long uterine horns is relatively small, especially in the nonparous female pig. Development of multiple foetuses occurs in the uterine horns rather than in the uterine body. Considering the uterine body is quite small and narrow, the intended implantation site was selected to be the end of cervix adjacent to the uterus (as marked by a red box in Figure 5.2).

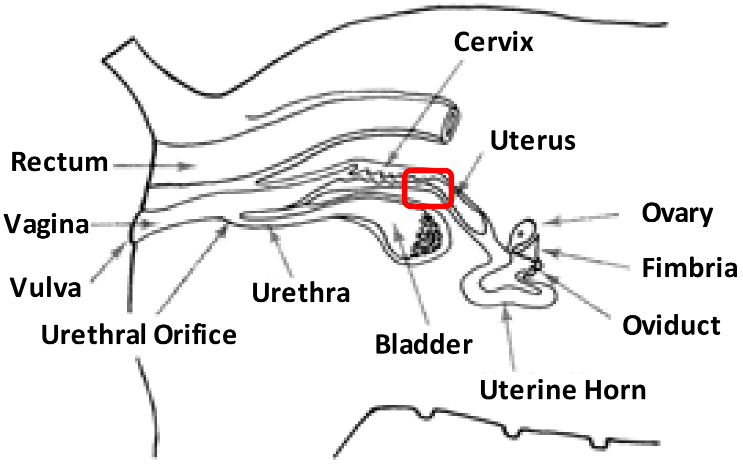

Figure 5.2 Side view of the female reproductive system of pig [176]. The intended sensor device implantation site was the end of cervix and beside the uterine body as marked by a red circle.

5.1.2 Experimental design of device deployment in pig cadavers

Design details of the clinical procedure for sensor device implantation and retrieval

A sensor device insertion set was designed and a clinical procedure was proposed for both the animal tests and the intended human intra-uterine application. For the sensor device insertion and retrieval, a nylon thread was fixed at one end of sensor device (b, Figure 5.3) and an insertion set was designed including an insertion tube and plunger (c, Figure 5.3). A polished polytetrafluoroethylene (PTFE) tube and a Poly(methyl methacrylate) (PMMA) stick were used as the insertion tube and plunger due to their good biocompatibility. The clinical procedure included sensor device implantation and retrieval procedures, which were designed with reference to the insertion and removal instructions of Mirena [177], a widely used contraception intra-uterine device. More details are shown in Figure 5.3.

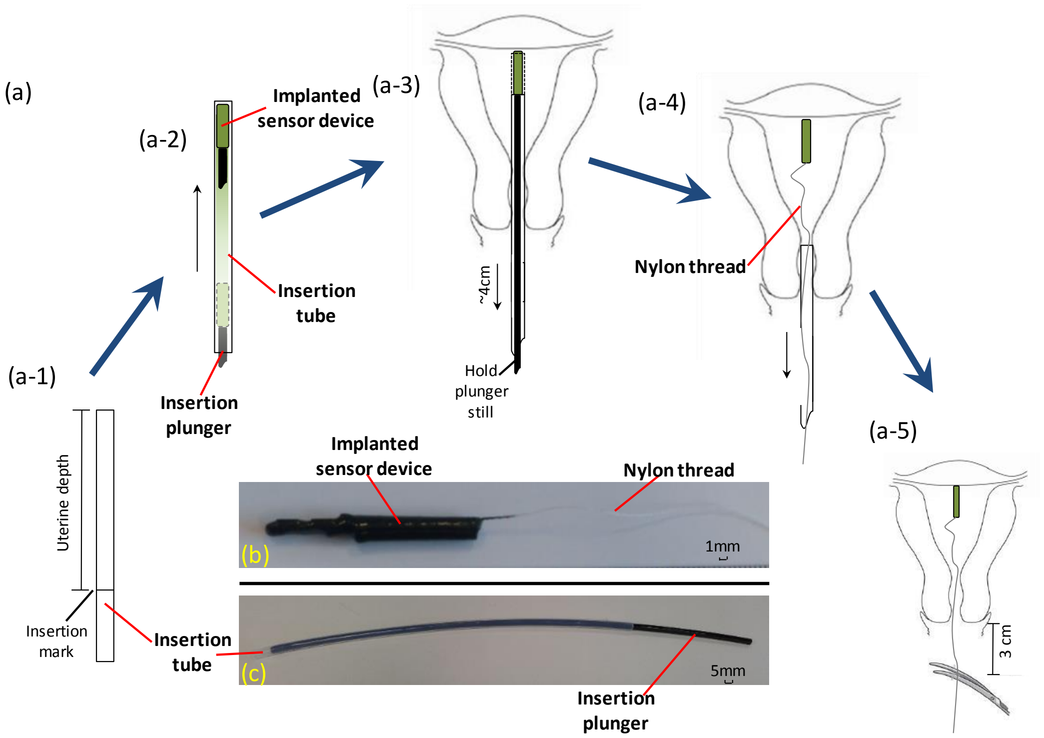

Figure 5.3 Outline of the clinical implantation procedure: (a) flow chart of sensor device insertion procedure, including (a-1) insertion depth determination. The uterine depth is measured and an insertion mark is recorded on the insertion tube; (a-2) sensor device loading. The sensor device is loaded into the insertion tube from the end of handhold part and then it is pushed to the other end by the insertion plunger; (a-3) sensor device delivery. Hold the insertion tube and plunger firmly, advance through the cervical canal into the uterine cavity (it was cervix in pig cadaver tests) until the reference mark on the tube is reached. While holding the insertion plunger steady, pull the insertion tube back about 4cm gently to release sensor device; (a-4) withdrawn of insertion plunger and tube. Firstly, the insertion plunger is taken out carefully from the insertion tube without pulling out the thread. Then, the insertion tube is withdrawn carefully; (a-5) thread cutting. The thread is cut perpendicular to the thread length and leaving about 3cm visible outside the cervix; (b) a nylon thread is fixed at one end of sensor device for sensor device retrieval after a period of implantation. The implanted sensor device is removed by applying gentle traction on the thread with forceps; (c) the insertion set includes an insertion tube and a plunger.

Before implantation, sterilization is necessary to ensure sensor device and insertion set are clear and ready for implantation procedure. In the pig cadaver tests, the insertion depth was determined by endoscope examination and was determined to be 20cm from rostral to the Vagina. Besides, we didn’t cut the thread. Removal of implanted sensor device was achieved by applying gentle traction on the thread with forceps and then pulling back.

Testing the receiver antennas

The performance characteristics of wireless energy transfer and wireless communication are dependent on the position and orientation of the receiver antenna. Proximal to and close to a perpendicular angle to the sensor device antenna results in optimal energy transfer and reliable wireless communication. The design of the receiver antenna is critical to the full system performance. For the *in-vivo* testing, the wearable receiver needs to be fitted to the pig such that it works with the implanted sensor device cooperatively. Design of the system has to consider the pig's normal behaviours and welfare to achieve reliable and secure antenna installation on the pig's body. From the literature [178] and our collabrators' experience on pig rearing, the behaviours and postures of pigs kept in pens include standing, walking, lying, wriggling, climbing on the pen door and possibly rolling over. Five different antennas were developed for the wearable receiver as mentioned in chapter 3 (as shown in Figure 3.35) which were evaluated on pig cadavers as shown in Figure 5.4. The optimal solution of antenna deployment was determined from this evaluation. Similarly, receiver deployment in humans will face many similar challenges to make it compatible with daily living. The information derived from these tests will inform the antenna design for the human trial of the device.

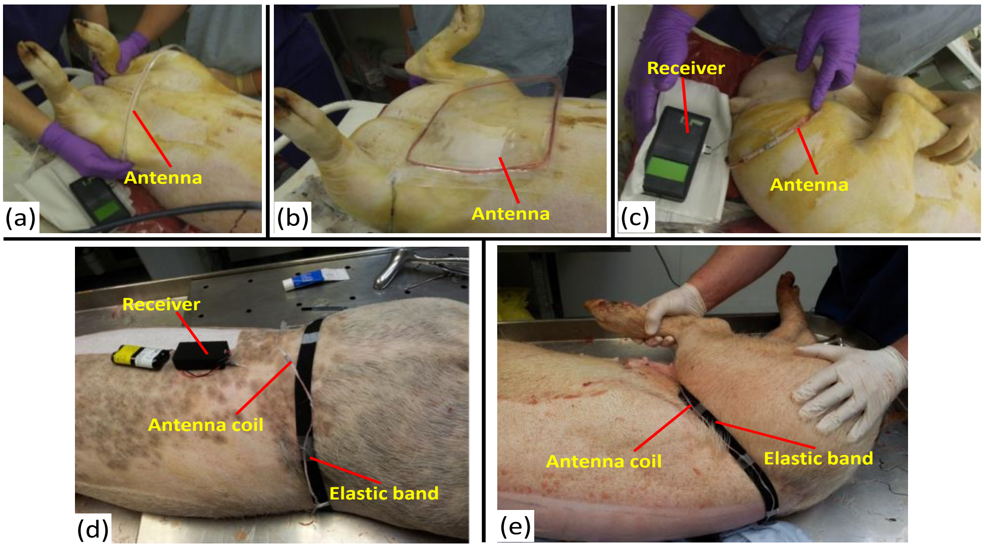

Figure 5.4 A number of antenna designs were tested on pig cadavers: (a) rigid circular antenna; (b) laminated rectangular antenna fitted on the abdomen; (c) flexible antenna fitted on the rump; (d) elastic antenna fitted around the waist; (e) belt antenna was put on around the waist and the rear legs were moved to mimic some of the range of movement associated with walking.

5.1.3 Results and discussion of system testing on pig cadavers

Three batches of pig cadaver tests were undertaken successively in the NPIMR. In all tests, the latest encapsulated sensor device (SDV4) and wearable receiver (RV2) were used. More details are showing in Table 5.1.

Table 5.1 Experiment details of three pig cadaver tests

Pig cadavers test	**1st pig cadaver test**	**2nd pig cadaver test**	**3rd pig cadaver test**
Number of pig cadaver	1	1	1
Duration	1 hour	1 hour	1 hour
Date	01/11/2012	31/01/2013	25/02/2013
Implantation site	At the end of cervix	At the end of cervix	At the end of cervix
Aim	➢ Experience preparation for the initial pig cadaver trial; ➢ Verify the clinical procedures; ➢ To figure out pig reproductive anatomic information and the position of implanted device; ➢ Test various antenna prototypes.	➢ Test elastic antenna; ➢ Verify system deployment; ➢ System functionality testing.	➢ Test belt antenna; ➢ Obtain the information about the impact on system performance from pig normal movement; ➢ Short-term pig cadaver intra-uterine temperature recording.
Results	✓ Successful demonstrated sensor device implantation and collection; ✓ Investigated the implanted sensor device position in uterus; ✓ Tested various antenna prototypes; ✓ Obtained some internal temperature readings.	✓ Successful implanted and collected sensor device; ✓ Tested elastic antenna; ✓ Verify the deployment of receiver, antenna and battery pack; ✓ Obtained some internal temperature readings.	✓ Successful implanted and collected sensor device; ✓ Tested belt antenna; ✓ Verify the system performance with mimic pig normal movement; ✓ Obtained some internal temperature readings.

5.2.3.1 **Trial of using clinical procedure for sensor device implantation and retrieval**

The clinical procedure which is proposed for sensor device implantation and retrieval was applied on fresh euthanized pig cadavers, and the sensor device was easily delivered and withdrawn after a period of implantation at the intended site. As shown in Figure 5.5, a sensor device was implanted at the end of cervix which is 20cm rostral to the vagina opening.

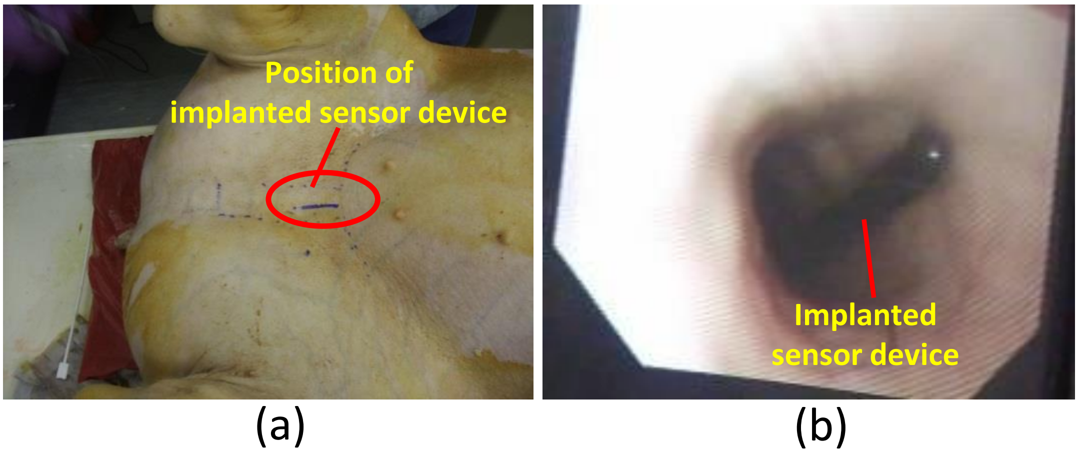

Figure 5.5 A sensor device was implanted at the end of cervix of a pig cadaver by the proposed clinical procedure: (a) implantation position of sensor device in pig cadaver was marked by a red circle; (e) an endoscope image showing the implanted sensor device proximal to the cervical os.

5.2.3.2 Comparison of receiver antennas

The five antenna designs developed for the wearable receiver were tested on pig cadavers successively. They had different shapes and fabrication approaches which resulted in different deployment sites. Their range of deployment sites gave rise to different relative positions and orientations to the impanted sensor device which are critical factors to system wireless performance. Moreover, these antennas would result in different user experiences. An optimal antenna should be proximal to and at right angle to the implanted sensor device. The comparions of these antennas are listed in Table 5.2.

Table 5.2 Results of the comparison of antennas developed for wearable receiver.

Antenna type	Features	Advantages	Disadvantages
Rigid circular antenna	Antenna coil was wound on a rigid frame	Strong, easy to make	Loose fitting Hard to fix
Laminated rectangular antenna	Antenna coil was sealed in a laminating paper	Bendable at a certain extent, easy to fix	Limited orientation, limited wireless performance
Flexible antenna	Antenna coil was packaged by PDMS or Parafilm	Good working orientation, flexible	Hard to fix
Elastic antenna	Antenna coil was fixed on an elastic band	Flexible, easy to use, less influence on normal behaviours	Loose fitting, limited wireless performance
Belt antenna	Antenna coil was fixed on an elastic band and its coil can be broken by using buckle connector. The belt size can be adjusted by a row of hooks	Flexible, used as a normal belt, good fitting	Complex structure

A rigid circular antenna was fabricated by winding antenna coil on a rigid frame. It was easy to make and very strong. It was tested while the pig cadaver was laid down on its back and the antennas was fixed on pig's loin as shown in Figure 5.4a. This antenna was close to the implanted sensor device with the required orientation. However, a gap was unavoidable between the antenna and pig's body. Because the rigid antenna had to be designed wider than the rear legs which were wider than its loin to ensure it can be put on through the rear legs, it was difficult to achieve reliable installation.

A laminated rectangular antenna was made by winding coil on a normal paper and then sealed in a lamination sheet. It was bendable and easy to fix on pig's abdomen as shown in Figure 5.4b. However, it had a reduced wireless performance due to limited orientation of the receiver antennas to the implanted sensor device. Meanwhile, it was hard to make a reliable installation by taping a laminate sheet on pig's abdomen.

A flexible antenna was made by the following steps. Firstly, the antenna coil was wound on a rigid frame. Secondly, the coil was removed from the frame and then packaged in PDMS (or Parafilm). Its relative flexibility resulted in a good fit. As shown in Figure 5.4c, the flexible antenna was tested after fixing on pig's rump. The flexible antenna worked well due to its good orientation and short distance to the implanted sensor device. However, its deployment in a free moving animal would be difficult.

The elastic antenna and belt antenna were designed based on elastic band. After the antenna coil winding, the Parafilm packaged coil was fixed on an elastic band. They were worn on the loin with a predetermined distance and orientation to the implanted sensor device. The elastic band provide a good fit and is likely to be the comfortable and less likely to interfere with normal activities. However, similar to the rigid circular antenna, the coil of elastic antenna had to be designed with a girth longer than the elastic band to ensure it was long enough to go over the pig's rear legs. The longer coil resulted in deformation and loose fitting between the coil and elastic band as shown in Figure 5.4d. It decreased the quality and stability of antenna and system wireless performance. Comparatively, the belt antenna introduced a novel design of coil connector and a row of adjustable hooks which minimized the coil deformation and enabled the belt antenna to fit well on the pig's loin. It was worn like a normal belt as shown in Figure 5.4e. Overall, the belt antenna achieved a short distance and good orientation to the implanted sensor device, meanwhile it is easily to wear, well fitted to pig's body.

From the comparison of different antennas, the belt antenna proved to be the most suitable antenna for the wearable receiver. Its novel design of an antenna coil connector and adjustable hooks made it easy to use as a normal belt and fixed on the pig reliably and securely Moreover, the rear legs of pig were moved forward and backward to mimic its normal behaviours during antenna testing, such as walking. A short period of continuous monitoring was carried out on pig cadaver which showed our current system was able to capture data. Therefore the belt antenna was selected for following live pig tests (if necessary) and human trial.

5.2.3.3 Short period internal temperature measurements on freshly euthanized pig

After the implantation of sensor device, a short period internal temperature monitoring test was carried out using belt antenna. Meanwhile, the two rear legs were moved to mimic normal walking. The internal temperature was measured successfully without obvious influence from the movement of rear legs. The temperature variation is shown in Figure 5.6. In this series of pig cadaver tests, we focused on clinical procedure testing and system functionality testing, more detailed system performance testing results will be introduced in section 5.2 (*in-vivo* tests on rabbit).

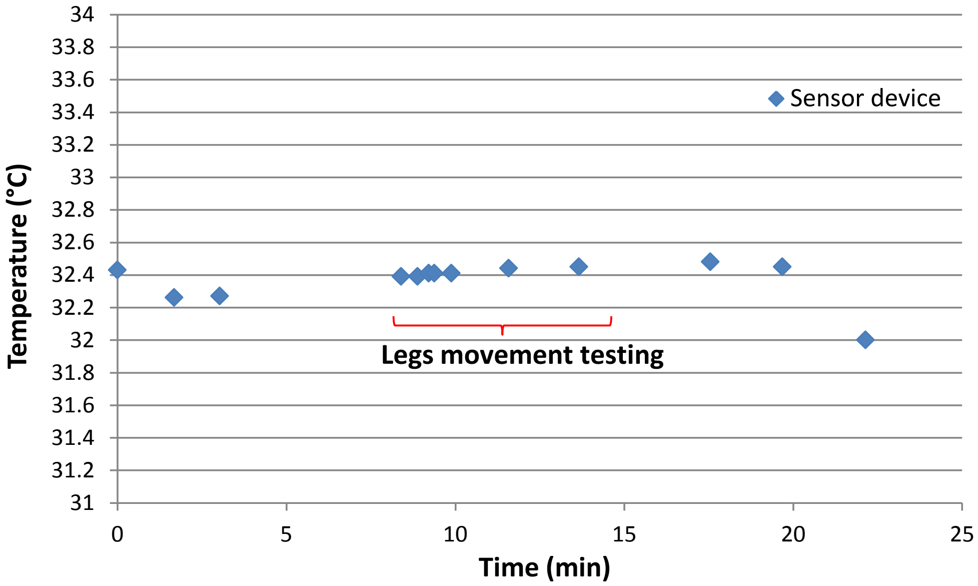

Figure 5.6 A short period internal temperature measurements were carried out on the freshly euthanized pig as it cooled. The reading was not affected by the movement of legs.

The tests of sensor device implantation and retrieval demonstrated that it is easy to use and suitable for sensor device implantation and retrieval on the pig. Meanwhile, valuable experience was obtained on the clinical operation for future human trials and the final intended application.

Considering in near future, live pig test may be required for more system deployment information and system testing before human trial. Based on the experience from the test on pig cadavers, a detailed deployment was proposed for future live pig tests. Compared with pig cadaver, pig normal behaviours had to be more considered for live pig, such as walking, rotating, climbing and sleeping. Therefore, the receiver fixed on the pig need to be packaged in protection casing. A foam jacket based on a design routinely used in animals undergoing postoperative recovery is employed as showin in Figure 5.7. The jacket has protective foam padding covered with a white rigid shell. The jacket has a slot along the midline of the pig suitable for housing the receiver and the antenna will be placed in side the jacket. To minimize the need to handle the animal, additional receiver battery packs will be installed into the slot of the jacket.

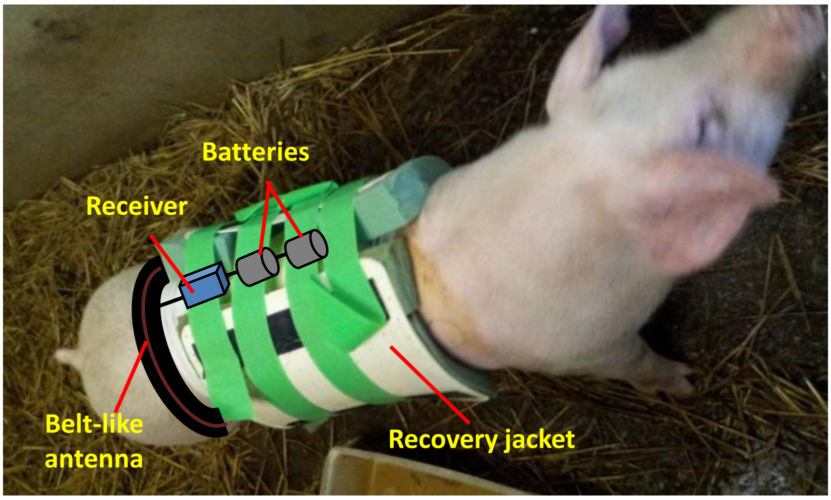

Figure 5.7 Diagram of the deployment of receiver system on a live pig. A foam jacket is used to install and protect devices in the top slot on pig's back, and a belt antenna is put on around the waist.

5.2 *In-vivo* tests on rabbits for prototype system evaluation

5.2.1 Introduction of rabbit tests

As device deployment into the pig uterus could not be achieved in null parous pigs, and parous pigs were not available during the experiment, caged rabbits were used for long-term device testing and assessment of any inflammation reaction to the device. Moreover, a study to capture real-time rabbit intra-uterine temperature was undertaken.

Rabbit tests had to face two challenges from the sensor device implantation and receiver deployment. Firstly, the described clinical procedure for sensor device delivery and retrieval was not suitable to rabbit. Rabbits have a relatively smaller body size and narrower vaginas than pigs, and sensor device and insertion tube were too big to apply on rabbits. An implantation method for rabbit was required. The other issue we had to consider was the deployment of receiver. Unlike the pig tests, while a belt antenna and receiver can be fixed on pig's body using the current design, it is nearly impossible to fit any device or antenna onto rabbit. The rabbit would get rid of the antenna fixed on its body within few minutes. Therefore, the experience gained from pig tests and the current designs for the pig were not able to apply on the rabbit, and an optimal receiver deployment strategy was needed for rabbit tests.

Rabbit core temperature information is always from rectal thermometry or tympanic thermometry, but the intra-uterine temperature was less mentioned and achieved. Clinically, rectal thermometer is the most common method to obtain rabbit core body temperature [179-182]. Recently, infrared thermometer [179] and implantable transponder [179, 183] technologies are becoming common practice. However, these technologies either cannot continuously sense or just achieved hypodermic implantation, so they cannot be used for real-time long-term *in-vivo* intra-uterine temperature monitoring.

Based on the conventional technologies mentioned above, body temperature of rabbit was investigated in many literatures. The average rectal temperature is 39.3±0.928°C measured by a rectal thermometer and normal body temperature range for a healthy rabbit was reported from 38.5°C to 40.0°C [179, 183]. Diurnal variation was also considered as an important character of rabbit body temperature [180, 181, 184]. Generally, rabbit body temperature remains at a high level in the period of 3pm to 3am and after 3am, the temperature fall to another low point at 9am [181]. These temperature recordings were obtained by an applicator of thermistor through the anus and keeping for 2 mins every time. Most literatures were based on similar method which need human interactions and hard to eliminate negative stress from measurement. Meanwhile, sampling rate was very limited, as low as few readings per day. Without sufficient *in-vivo* data, the variation of rabbit core temperature, especially intra-uterine temperature, is still not clear.

5.2.2 Experimental design of *in-vivo* tests in rabbits

The *in-vivo* experiments performed in New Zealand White rabbits were carried out under a project license approved under the home office (UK) Animals (Scientific Procedures) Act 1986. The animals were housed individually for the duration of the experiment and were provided with food (standard rabbit chow) and water ad libitum. They were maintained under controlled temperature (21°C), humidity and a light dark cycle which was controlled by two time switches of the room lights. More details of lighting schedule are shown in Figure 5.8.

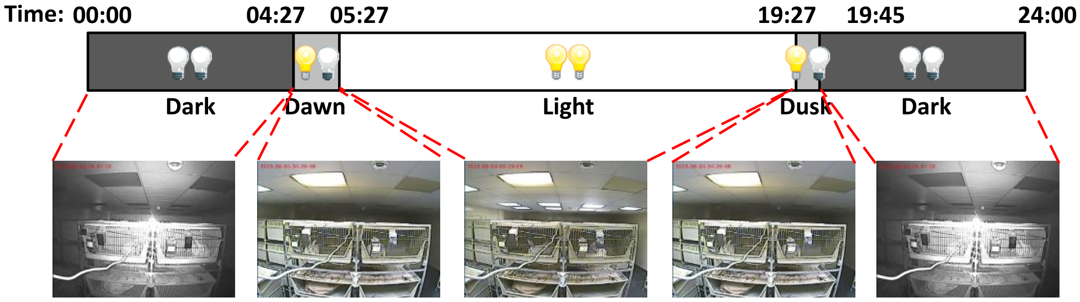

Figure 5.8 Time switches controlled lights in rabbit room and light intensity changing over 24 hours. There were two time switches for the light control of front half and back half of rabbit room. Two bulbs indicator in this figure mean two separated light control of rabbit room (front, back). Yellow bulb indicates lights on and white bulb indicates lights off. The grey level of the ring out of each clock means light intensity. Some images are showing the real scenes under different light intensity.

Based on rabbit anatomic acknowledge, rabbit uterine body and uterine horn were both suitable for implantation test. Considering the small size of rabbit and clinical procedure used on pig for sensor device implantation cannot use to rabbit, implantation by surgery was considered as an alternative for sensor device delivery. Animals were anaesthetised using Hypnorm (Janssen) intra muscularly followed by Diazepam (Hameln Pharma) IV. A small incision was made in the skin covering the abdomen, and the underlying muscle was blunt-dissected to expose the uterine horn. An incision was made into the horn and the sterilised device was implanted and tethered using a single resorbable suture made through the inner lining of the horn. The muscle was apposed and sutured using resorbable sutures, then the overlying skin was sutured. Animals were placed in a heated chamber and monitored until awake. Animals received post-surgery analgesia of Carprofen (Pfizer) subcutaneously and were scored on the animal welfare score for the duration of the experiment.

Three batches of tests were undertaken on five rabbits. In the first test, sensor device was implanted in the uterine horn of rabbit No.1 for one week. Meanwhile, rabbit behaviours were also investigated in this test which will be introduced in section 5.2.2.2. In the second test, two sensor devices were implanted in the uterine body of rabbits No.2 and No.3 for one week simultaneously. Rabbits No.4 and No.5 were used for the third test. Sensor devices were implanted in the uterine horn for two weeks.

A camera system was setup to capture rabbit images for rabbit behaviours research and rabbit activities recording during the tests. It included a CCTV camera and special software running on PC for image automatic capturing. Furthermore, because for the rabbit tests, receiver cannot be fixed on rabbit body directly, a multi-antenna receiver system was employed which was introduced in section 3.3.2 and more details will be discussed in section 5.2.2.3.

More details about sensor device implantation, rabbit behaviours research and multi-antenna receiver system design will be introduced in following sections.

5.2.2.1 Procedure of sensor device implantation

Because the sensor device cannot be delivered to the implantation site by using the same procedure for pig, it was specially designed to be implanted by surgery. Before the trials on live rabbits, the dimensions of rabbit uterus were determined and a wax widget, a little bigger than sensor device (45mmX10mm, as shown in Figure 5.9b), was implanted in a rabbit cadaver for size verification. Rabbit uterus is shown in Figure 5.9a, uterine horn was measured as around 55mm long and its out diameter was about 18mm. Although the inner size was difficult to measure, the wax widget was easy to insert into the uterine horn by a small cut as shown in Figure 5.9c. The uterine body looked like about double size of a single uterine horn and it was also suitable for sensor device implantation.

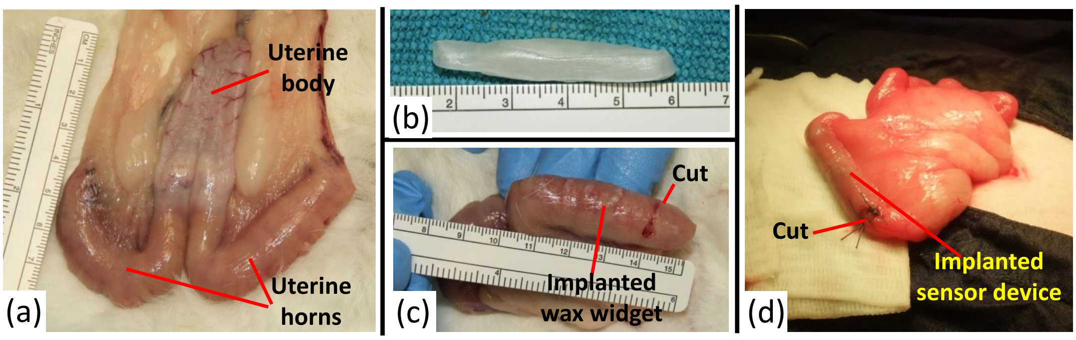

Figure 5.9 Rabbit uterus dimension check and sensor device was implanted by surgery: (a) anatomic structure of rabbit uterus, including two uterine horns and a uterine body; (b) a wax widget which was a little bigger than sensor device was used for size verification; (c) the wax widget was implanted in a uterine horn; (d) a sensor device was implanted in a uterine horn of a live rabbit by surgery.

Once the sensor device was verified and implantation procedure was conformed in rabbit cadavers, sensor devices were implanted in different rabbits by surgery which were operated by our collaborator who hold a proper licence and followed strict clinical procedures. The nylon thread of sensor device was fixed at the suture to maintain a stable position. A figure of implanted sensor device in the rabbit uterine horn is shown in Figure 5.9d.

To investigate the positional information of implanted sensor device, X-ray computed tomography (CT) was employed to detect the position and orientation of sensor device in the uterus. CT images illustrated two sensor devices in live rabbits from different directions are showing in Figure 5.10. The position and orientation of implanted sensor devices were seen different in different rabbits, and the sensor device may move at a certain extent in the implantation site due to rabbit normal movement. Therefore, the receiver deployment had to consider the situation of varied position and orientation of the implanted sensor device.

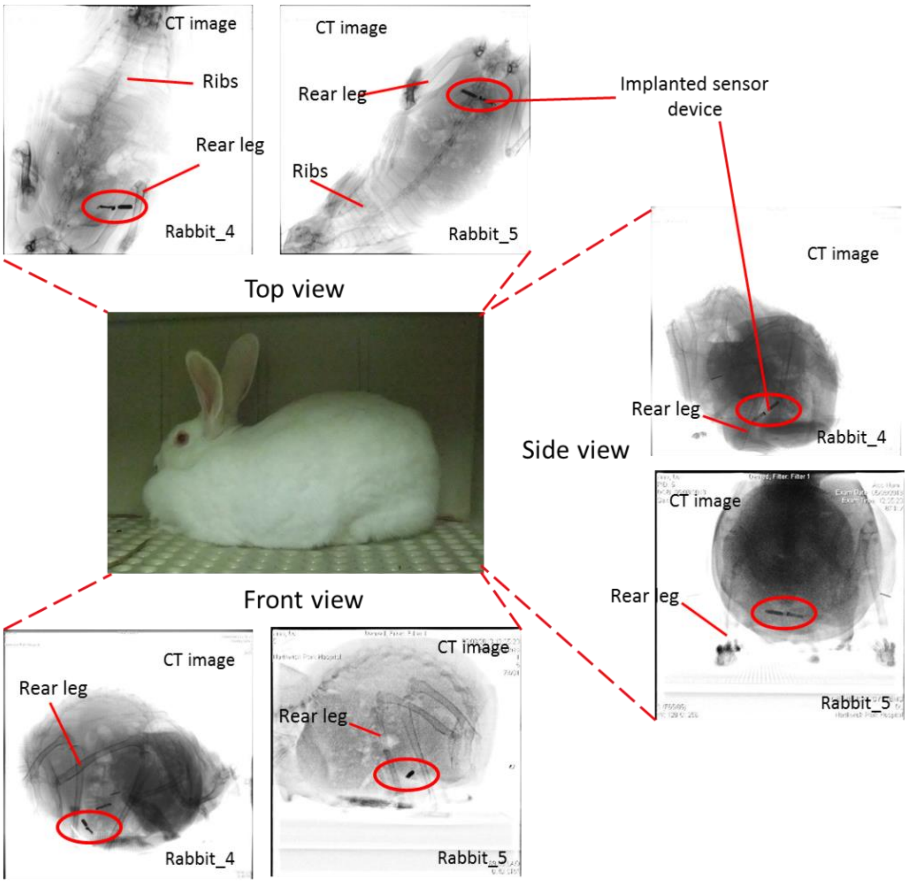

Figure 5.10 CT images for anatomy are showing the position and orientation of the implanted sensor devices in two different live rabbits (Rabbit_4 and Rabbit_5) from different directions. From the CT imaging investigation, position and orientation of the implanted sensor devices were seen different in these two rabbits. The sensor device was marked by red circles.

Moreover, biological reaction came from the sensor device implantation needed to be considered and histology research was undertaken after this series of implantation tests. The inner tissue surface at implantation site and implanted sensor device surface were investigated and histology research report was exported.

5.2.2.2 Establishing rabbit cage behaviour patterns

To achieve optimal receiver system deployment, a study was undertaken on rabbit behaviours. The positional information of rabbits kept in cages can contribute to the optimisation of receiver system design. From the literature, single caged laboratory rabbit was known as spent a large proportion of time inactive (55.7%) and the most common behaviours observed were lying alert and doze (43.2%) [185]. More details about rabbit activities during daytime and nighttime are shown in Figure 5.11.

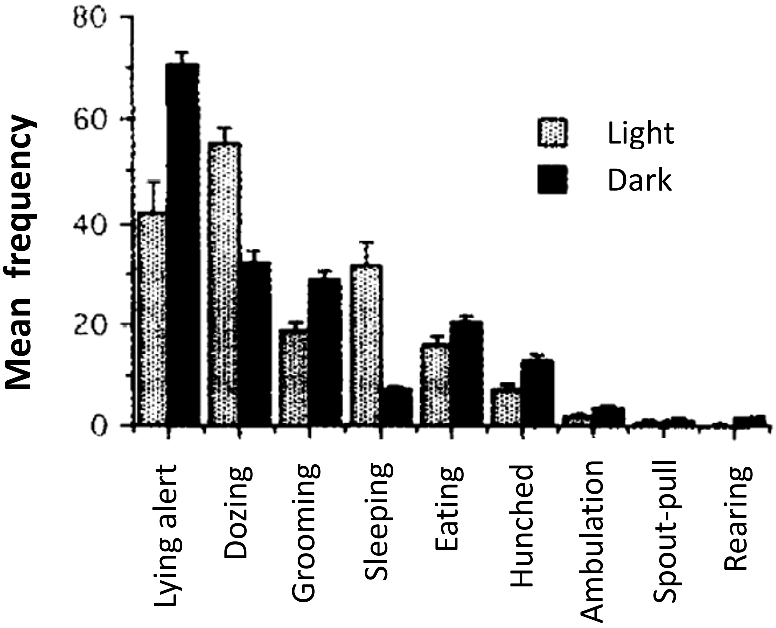

Figure 5.11 Behaviours of caged rabbits with different frequencies during the daytime and nighttime [185].

Furthermore, based on our observations, caged rabbits tend to perform activities at relatively fixed location. For example, the feeding point was at near the front door where the food hopper and water bottle were attached. Rabbit also tends to use relatively fixed places for excretion and rest, although the favourite places of rabbits may different due to individual difference. Therefore, rabbit behaviours research was necessary to identify individual positional information of rabbits to optimise the antenna deployment. A camera system was developed to capture rabbit images and analyse the proportion of rabbit occupancy at different places. The camera system for rabbit behaviours research is shown in Figure 5.12.

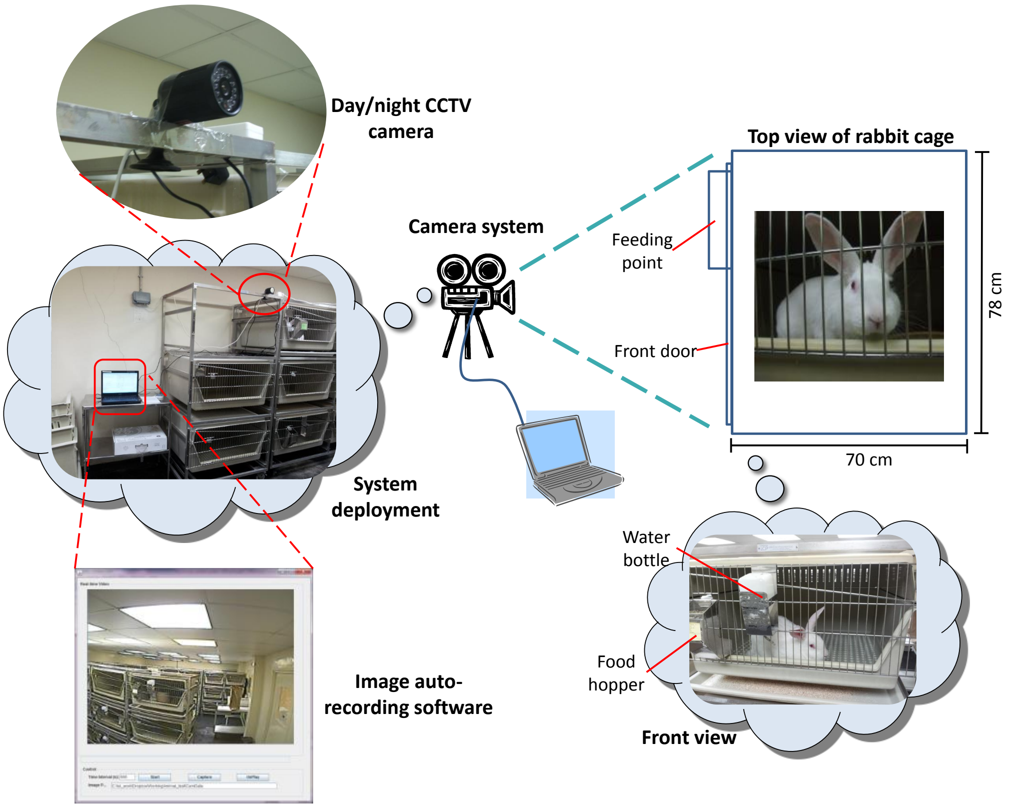

Figure 5.12 Diagram of camera system for rabbit behaviours research. It included a day/night CCTV camera with IR LEDs which was installed toward to the front door of rabbit cage, and a laptop which was running special designed software based on Java for image auto-recording.

To simply the analysis of rabbit occupancy information in cage, rabbit cage was separated into 9 different zones (from zone1 to zone9) as shown in Figure 5.13. The occupancy rates were calculated from the proportion of time the rabbit spent at each zone and this information was obtained from the rabbit images captured by camera system. This study was undertaken from 2 days before test to 1 week after implantation. The occupancy rates are also shown in Figure 5.13.

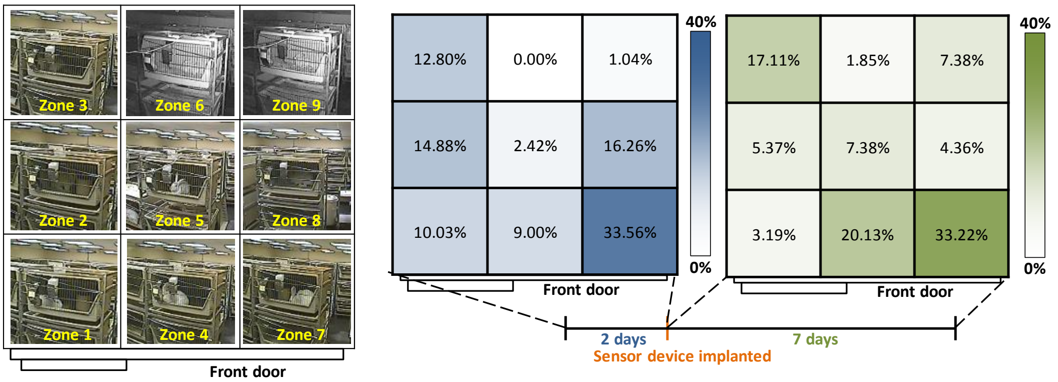

12.80%	0.00%	1.04%
14.88%	2.42%	16.26%
10.03%	9.00%	33.56%

17.11%	1.85%	7.38%
5.37%	7.38%	4.36%
3.19%	20.13%	33.22%

(a) (b)

Figure 5.13 The identification of 9 zones in the rabbit cage and occupancy rate at each zone. The rabbit position was decided by its uterus position: (a) rabbit cage was separated to 9 zones and 9 images were showing rabbit at different zone; (b) occupancy rate at different zones before (blue) and after (green) implantation. Colour density indicates amplitude of occupancy rate. The data came from our first rabbit test.

Based on statistics, the rabbit was observed prefer staying in the front corner of cage, although after implantation a bit difference on occupancy rate distribution was observed. Some zones were confirmed where the rabbit used for specific activities. For example, zone 7 was the rabbit favourite place for rest and far corner (zone 3) was treated as a toilet. Zone 1 and zone 4 were occupied frequently due to the food hopper and water bottle attached on the front door. Furthermore, similar behaviours were observed as pre-mentioned literatures [185]. This rabbit spent most of time inactive for dozing, lying alert and grooming, and less time on rolling, scratching and pawing. Overall, the rabbit favourite places were identified which suggested places the antennas need to cover. It was very useful for the design of receiver system deployment.

5.2.2.3 Design of receiver system deployment

Because the receiver cannot be installed on rabbit directly, the receiver system fixed on the rabbit cage was very important which determined system wireless performance and effective sampling rate. The optimal deployment is using fewer antennas to cover most of rabbit favourite places to achieve reasonable sampling rate.

The number of antennas determined a balance between cage coverage and system cost, such as power consumption, sensing time and receiver system complexity. According to the rabbit size and the receiver output power capability, multiple 30cm diameter rigid antennas were employed and the antennas need to be installed on 3 dimensions to suit varied position and orientation of sensor device implanted in rabbit. Therefore, a six-antenna receiver system was developed to cover rabbit favourite places obtained from rabbit behaviours research, including rest, feeding and toilet area. The details of multi-antenna receiver system design have been introduced in section 3.3.2 and 3.4.2, and the deployment design is shown in Figure 5.14.

Three antennas were installed underneath the rabbit cage to cover rest area (1), feeding point (2) and toilet (3) respectively. Another three antennas were fixed on the side walls at toilet (4), rest area (5) and the further corner (6). These antennas covered almost rabbit living area and were fine adjusted during each test due to individual difference.

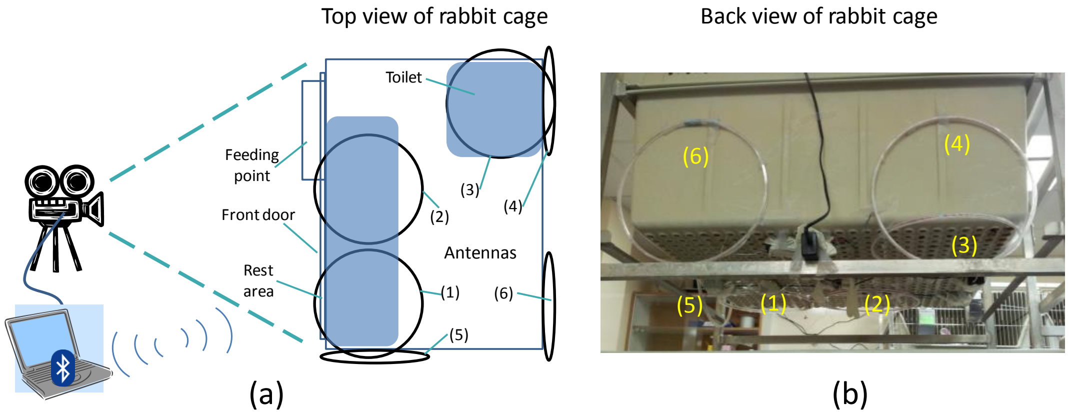

Figure 5.14 Multi-antenna receiver system deployment: (a) diagram of multi-antenna receiver system deployment. Six antennas were installed on the suggested places based on the rabbit behaviours research and a camera was set up face toward the rabbit cage front door for images recording; (b) back view of system deployed rabbit cage and six antennas were marked in the picture.

The interval of multi-antenna receiver system sensing cycles was 3mins and more details of sensing cycle were already introduced in section 3.4.2. But considering rabbit movement and varying orientation of sensor device, the effective sampling rate would be lower than system working frequency. For example, if rabbit moved out of antenna range during sensing cycle or the implanted sensor device was at a poor orientation to the receiver antenna, this sensing cycle might be failed. Therefore, the effective sampling rate is an important indicator to evaluate whole system sampling performance. Considering intra-uterine temperature doesn’t change immediately, an effective sampling rate less than 30mins for the initial implantation test was acceptable.

5.2.3 Results and discussion of *in-vivo* test on rabbit

Three batches of rabbit *in-vivo* tests were undertaken successively and system working performance was evaluated and fresh *in-vivo* data about rabbit intra-uterine temperature were captured. The latest packaged sensor device (SDV4) and multi-antenna receiver system based on latest receiver (RV2) were employed for these tests. More details are showing in Table 5.3.

Table 5.3 Experiment details of three rabbit tests

Rabbit test	**1st rabbit test**	**2nd rabbit test**	**3rd rabbit test**
Number of rabbit	1 (No.1)	2 (No.2,3)	2 (No.4,5)
Valid rabbit	1 (No.1)	1 (No.2)	2 (No.4,5)
Duration	1 week	1 week	2 weeks
Date	04/06/2013-11/06/2013	01/07/2013-08/07/2013	22/07/2013-05/08/2013
Implantation site	Uterine horn	Uterine body	Uterine horn
Receiver system working interval	3 min	3 min	3 min
Image recording rate	1 image/10min	1 image/3min	1 image/3min
Aim	➢ Experience preparation for the initial rabbit trial; ➢ Collect information about rabbit behaviours; ➢ Verify multi-antenna receiver system; ➢ Verify implantation in uterine horn; ➢ Focus on system verification and debugging.	➢ Comparison test on difference rabbit; ➢ Verify a different implantation site, in uterine body; ➢ System evaluation and fresh *in-vivo* data collection	➢ Comparison test for longer implantation, ➢ System evaluation and fresh *in-vivo* data collection.
Results	✓ Successful demonstrated sensor device implantation and collection; ✓ Investigated the implanted sensor device position in the body; ✓ Collected images and analysed rabbit behaviours; ✓ Tested multi-antenna receiver system; ✓ Obtained some rabbit real-time intra-uterine temperature readings.	✓ Implanted in uterine body; ✓ Sensor device No.3 dropped after surgery; ✓ Sensor device No.2 successfully finished the implantation test; ✓ Compared different implantation sites, uterine horn is deemed more suitable for rabbit tests due to its relatively small size; ✓ Obtained some rabbit real-time intra-uterine temperature readings.	✓ Successful demonstrated sensor device implantation and collection; ✓ System worked well; ✓ Two rabbits two-week *in-vivo* data was obtained.

In all tests, sensor device were successfully implanted by surgeries and functionally worked well. However, the sensor device for rabbit No. 3 was dropped out of rabbit body in a few hours after implantation surgery due to the loosing suture. So the rabbit No.3 will be excluded in discussion. Besides, due to unexpectedly power supply cut and computer crash, data loss was happened a few times and data gaps can be seen in data analysis. Data processing and analysis focused on general data trend in whole implantation period and short-time data loss only have minor impact on the result.

5.2.3.1 System performance evaluation

As a wireless real-time long-term monitoring system, system working performance was evaluated from three aspects including error data rate, effective sampling rate and successful reading rate as rabbits were at proper position.

During a wireless and batteryless implantable sensor device working procedure, error data may be caused by the following reasons. Firstly, if the implanted sensor device is at poor position or orientation to the receiver antenna, the efficiency of energy transfer will be reduced and sensor device possibly cannot harvest enough energy during a sensing cycle for sensing. Insufficient energy may cause results unstable voltage reference for the ADC which results in sensing failure. It may also cause communication error due to the insufficient energy for wireless signal transmission. These abnormal working states result in errors on temperature reading. Secondly, error data may happen during wireless data transmission due to environment interference. Overall, error data is common in a wireless and batteryless system. Considering the power consumption and programming complexity, a simple error detection algorithm was employed for wireless data packet checking. However, error data was impossible to completely eliminate. For example, if few bits of wireless data packet are invalid, it is hard to recognize the wrong data. Therefore, after the data collection, error data need to be analysed and filtered out of raw data before further process.

A set of criteria was proposed to identify the possible error data and filter them out from the raw data. Considering the rabbit normal temperature range and intra-uterine temperature fluctuation is limited in a short-time, the data was treated as an error data in the following situations: 1, temperature reading was lower than 35°C (normal temperature range for a healthy rabbit is 38.5°C to 40.0°C [179]); 2, temperature was higher than 41°C; 3, temperature varied more than 0.5°C in 6mins (2 sensing cycles); 4, temperature varied more than 1°C in 30mins (10 sensing cycles). Based on these criteria, identified error data were filtered out and the proportion of error data was calculated. The error data rates for different rabbit tests are presented in each day after implantation in Figure 5.15. Generally, the average error data rates for different rabbit tests were lower than 5%, and daily error data rates were almost lower than 8%. Therefore, the error data was controlled in a reasonable level (lower than 10%) and the filtered data were used for further analysis.

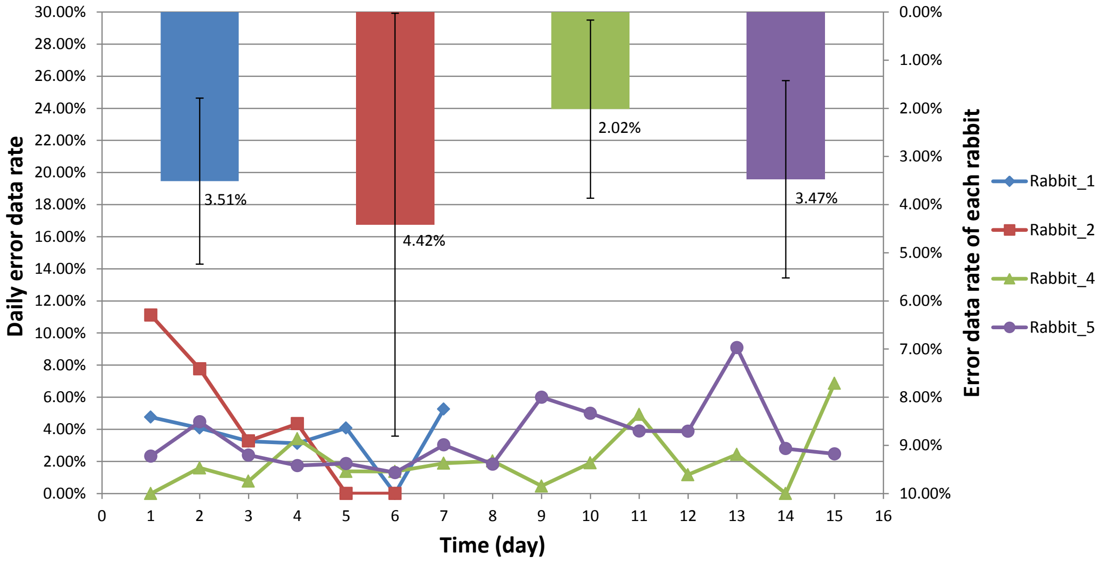

Figure 5.15 Percentage of error data for each rabbit test. Line chart shows daily error data rate after implantation and bar chart shows the average error data rate of each rabbit.

Effective sampling rate is a key indicator for evaluating system working performance under real circumstances. It's always lower than the system working frequency due to rabbit movement and varying position and orientation. Based on the time stamp of successful readings, intervals were calculated between two successful readings. This successful reading interval directly reflects effective sampling rate and daily average intervals are shown in Figure 5.16.

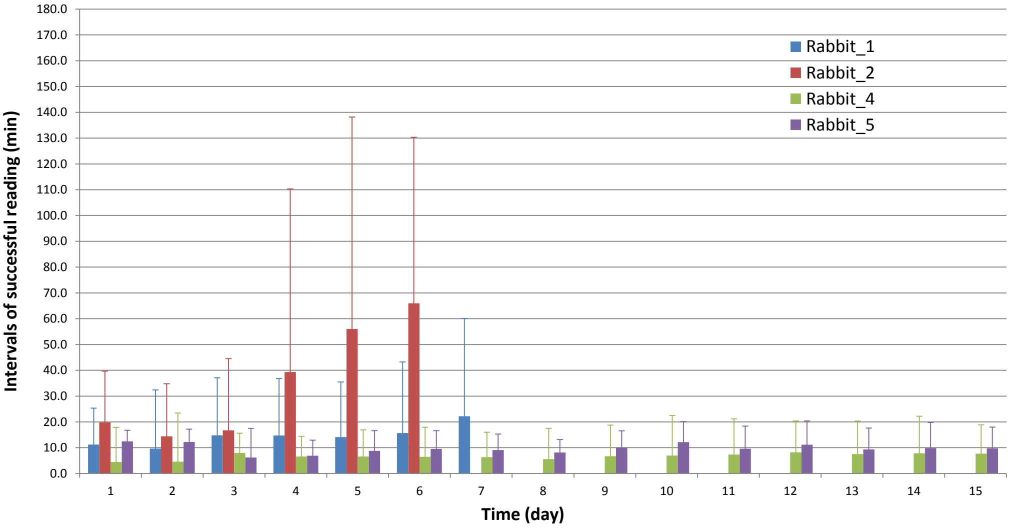

Figure 5.16 Daily average intervals of successful readings were calculated for different rabbit tests.

Because of the antennas deployment optimisation and fine adjustment during these tests, the later tests on rabbits No.4 and No.5 had relatively shorter intervals, both of them tested averagely shorter than 10min. Rabbit No.2 had a worst effective sampling rate and the possible reason was the different implantation site. Because the sensor device was implanted in uterine body of rabbit No.2 where had a relatively higher distance and more parallel angle to the ground plane. Rabbit No.1 had a medium result averagely lower than 20min. The interval differences of rabbit tests were possibly caused by different implantation sites, individual difference on rabbit behaviours and system deployment. Overall, the optimised multi-antenna receiver system was able to achieve continuous measuring at an averagely 10mins effective sampling intervals which was acceptable for rabbit tests.

The conventional method for successful reading rate calculation is calculating the percentage of successful reading data in the all sensing cycles, but it is not considering the rabbit behaviours and not good enough for the rabbit tests analysis. For example, some reading failures came from rabbit movement and postures out of sensing range rather than system error. Therefore, a more accurate method to calculate successful reading rate was considered based on rabbit behaviours information. This rate was calculated by divided successful reading data from valid system sensing cycles. The valid system sensing cycles were decided from the simultaneously captured images and empirically identified whether rabbit was at a detectable position and posture or not. A set of criteria for image analysis was proposed as below.

Considering there were two different image recording rate during rabbit tests, some differences were designed in the criteria. For images recorded at a 3mins interval, the image capturing frequency was same with the receiver system working frequency. For simplification, the number of valid successful sensing cycles equals to how many images showing rabbit was in antenna working range and at a detectable position and orientation. But for the 10mins interval image recording, the image capturing frequency was lower than the receiver system working frequency, so the valid successful sensing cycle number cannot be simply counted by the valid images as above. A set of criteria were designed for predicted valid successful sensing cycles: 1, if an image shows rabbit was in a good position and good orientation, mark it as YES, otherwise NO; 2, predicted valid successful sensing cycle number plus one for a YES image with a previous NO image; 3, predicted valid successful sensing cycle number plus one for a YES image with a next NO image; 4, predicted valid successful sensing cycle number plus three for a YES image with a previous YES image and rabbit had a relatively small movement; 5, predicted valid successful sensing cycle number plus one for a YES image with a previous YES image and rabbit had a big movement. The predicted valid successful sensing cycle number was predicted from image analysis based on these criteria. The accurate successful reading rate for different rabbit tests are shown in Figure 5.17. Generally, it was found greater than 85% except the rabbit No.2 was a slightly smaller than 80% with a possible reason from limited implantation site in uterine body.

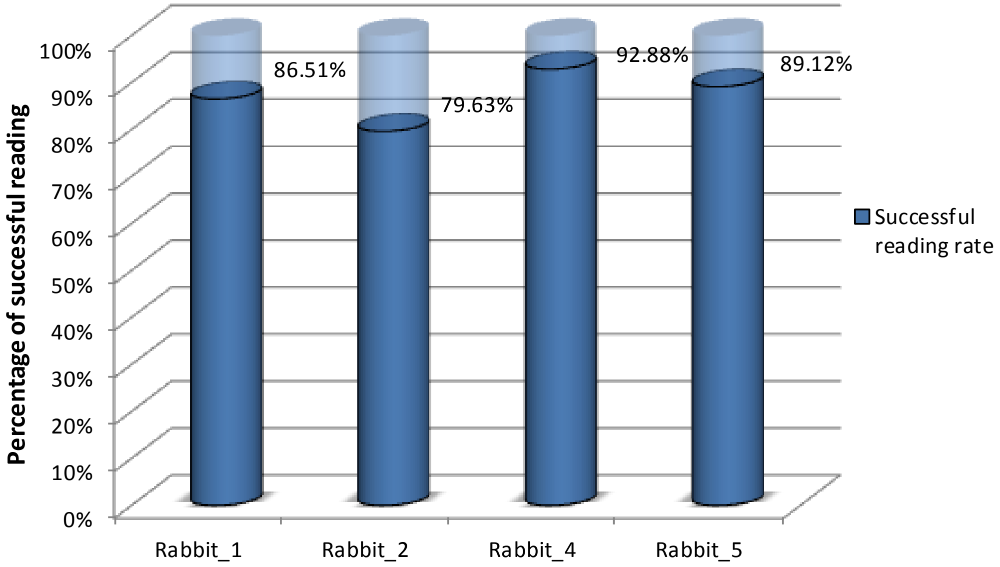

Figure 5.17 Successful reading rates from image analysis for each rabbit test.

Up to 14-day continuous *in-vivo* tests, these three batches rabbit tests showed a good rate of data sampling with an acceptable error data rate lower than 5% and a good successful reading rate when the rabbit was in the sensing area. Our intended *in-vivo* sensing platform was demonstrated and proved to be a monitoring system for rabbit intra-uterine environment.

5.2.3.2 Process and analysis on *in-vivo* data

Rabbit intra-uterine temperature was continuously recorded for up to two weeks in the rabbit tests. The raw data can be seen in appendix B-2. Similar cyclic temperature changing trends can be seen. Rabbit No.2, No.4 and No.5 were sent back from recovery room about 3 hours after surgery, temperature rising was seen in the first day due to postoperative recovery. But rabbit No.1 was in the system after about 6 hours when the surgery finished, the temperature rising was not as clear as others. Moreover, as mentioned in previous section, the data gaps happened in the figures were because of power supply cut and computer crash. Based on these raw data, daily average intra-uterine temperatures were calculated as shown in Figure 5.18.

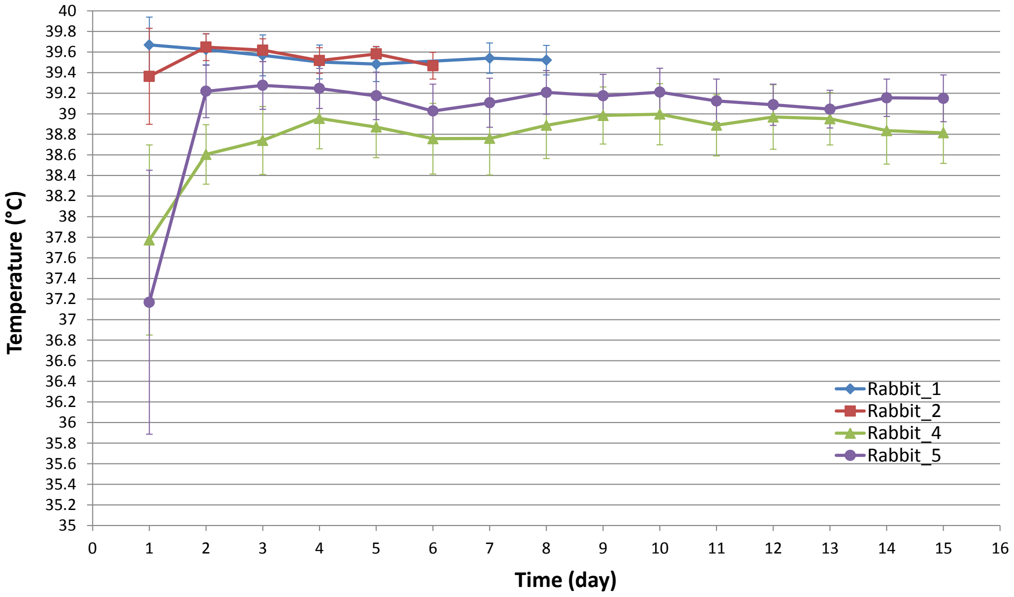

Figure 5.18 Daily average intra-uterine temperatures of four different rabbits. Temperature rising and big temperature variation were observed in the first day after implantation surgery due to postoperative recovery. Stable intra-uterine temperatures were seen with a fluctuation in several days.

The average temperatures in Figure 5.18 are showing general daily temperature variation on different rabbits. The temperature rising and big variation happened at the first day after surgery and then temperature tended to stable state. The daily average temperature varied within 0.5°C after the first day. Individual differences on intra-uterine temperature were also observed the same as reported on rabbit core temperature in literatures [181, 183]. The most temperature difference was around 0.6°C between different rabbit (No.1 and No.5). Furthermore, a cyclic fluctuation close to six days was introduced in literature [181], but it was hard to be confirmed in a limited test duration, although a fluctuation can be seen in several days.

A variation in temperature over each 24-hour period (one complete light:dark cycle) can be observed in the measured temperature data of each animal, however the noise in the data means that there is inadequate data to determine the rabbit diurnal temperature variation for each 24-hour period to be accurately measured. *In-vivo* data from different days of measurement were overlapped over 24 hours as shown in Figure 5.19 (raw data are given in appendix B-2) to determine whether the intra-uterine temperature variation alters in a 24-hour (hence diurnal) pattern. Grey level of bands indicates different light intensities, indicating the phase of the light:dark cycle.

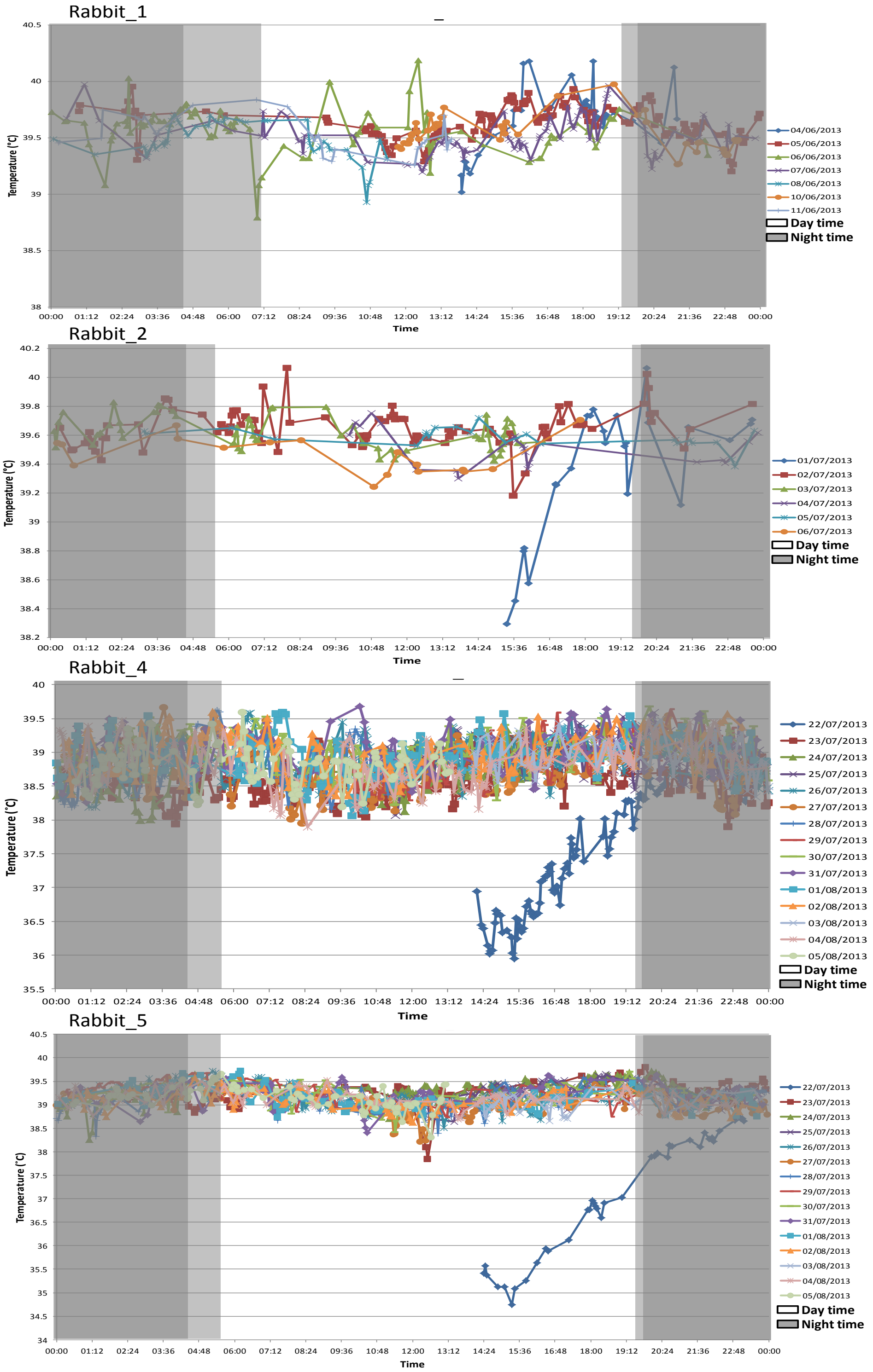

Figure 5.19 Overlapped intra-uterine temperatures of 4 rabbits over 24 hours. Similar inferring of circadian rhythm associated temperature variation trends were seen from all monitored rabbits. Different grey level bands indicate different light intensities. Dark grey bands mean all lights off and white areas indicate all lights on. Light grey bands show the time half lights on and half lights off. Inferring temperature variation can be seen around light changing period.

Because of the data limitation of rabbits No.1 and No.2, more data analysis on intra-uterine daily rhyme was undertaken on rabbits No.4 and No.5. Treated as a cyclic signal, FFT was used to analyse frequency domain characteristics of rabbit intra-uterine temperature. FFT is acronym of Fast Fourier Transform, a widely used algorithm to convert time domain signal to frequency domain components. It is widely applied on many applications in engineering, science, and mathematics. Because the common FFT was proposed for uniform sampling signal and our *in-vivo* data had non-uniform sampling intervals, linear interpolation was carried out before applying FFT. The frequency components of rabbit intra-uterine temperature variation are shown in Figure 5.20. Obvious major frequency components were seen at around 2.3X10^{-5} Hz on both two rabbits as marked in Figure 5.20. This frequency means 2 cycles variation per day and it was agreed by the observed daily rhythm from Figure 5.19.

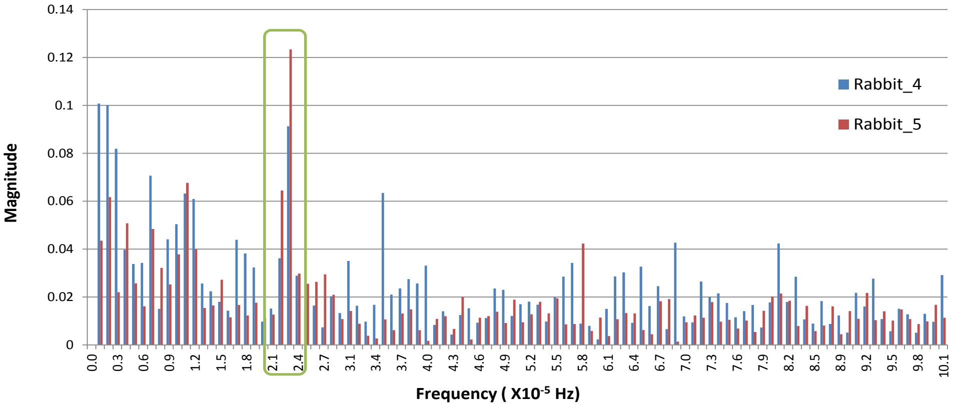

Figure 5.20 Frequency domain analysis for intra-uterine temperature of rabbits No. 4 and 5. Obvious major frequency component was marked by green box at around 2.3X10-5 Hz which was agreed by a two-cycle temperature variation in Figure 5.19.

In the intra-uterine temperature trend line analysis, polynomial fitting was undertaken on daily *in-vivo* data from rabbits No.4 and No.5. Similar polynomial fitted lines on two different rabbits were seen over several days in Figure 5.21. The results of polynomial fitting can be seen in appendix B-3. This diurnal variation trend is similar to that reported in the literature [181] however with a higher resolution due to the greater sampling rate using our methodology. Moreover, these *in-vivo* data were obtained without the likely changes due to measurement induced stress and increased muscle activity that is likely to occur during the reported rectal probe collected temperature measurements.

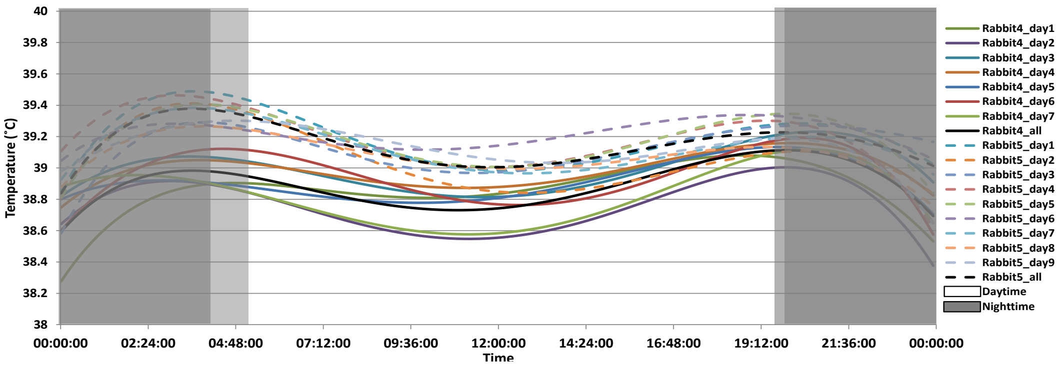

Figure 5.21 Similar polynomial fitted intra-uterine temperature trend lines of rabbits No.4 and No.5 can be seen over several days. Different grey level bands indicate different light intensities. Dark grey bands mean all lights off and white areas indicate all lights on. Light grey bands show the time half lights on and half lights off. The rabbit4_all and rabbit5_all are the polynomial fitted lines of overlapped intra-uterine temperatures of rabbit_4 and rabbit_5.

However, the first two days polynomial fitted trend lines look different, as shown in Figure 5.22. The results of polynomial fitting of the first two days can be seen in appendix B-4. This difference may come from postoperative recovery after implantation surgery. Intra-uterine temperature was changed from a relatively flat state to a clearer daily rhythm. Similar trends were observed during first two days on these two rabbits.

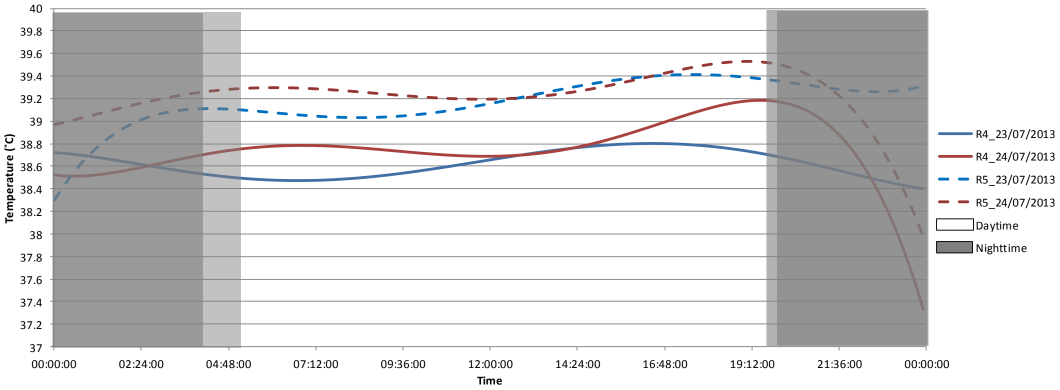

Figure 5.22 Polynomial fitted intra-uterine temperature trend lines of first two days after implantation surgery. Similar trends were observed on two rabbits. Intra-uterine temperature was changed from a relatively flat state to a clearer daily rhythm. Different grey level bands indicate different light intensities. Dark grey bands mean all lights off and white areas indicate all lights on. Light grey bands show the time half lights on and half lights off.

The DC components of polynomial fitted temperature trend lines were calculated and shown in Figure 5.23. It showed general daily intra-uterine temperature variation similar to the daily average temperature. The daily DC components varied around in 0.5°C which described a relatively stable intra-uterine temperature. Moreover, it was also hard to confirm a cyclic fluctuation in limited duration as literature mentioned.

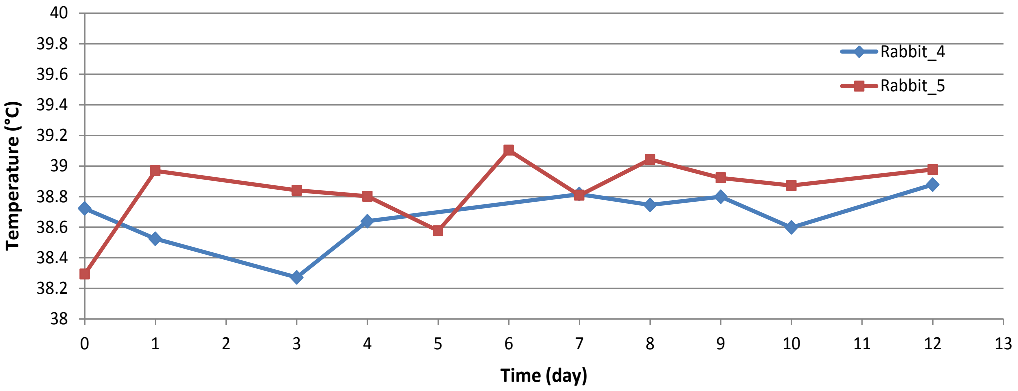

Figure 5.23 The variation of DC components of polynomial fitted intra-uterine temperature trend lines. Relatively stable intra-uterine temperature was observed.

5.2.3.3 Bio-compatibility check and histology research

Although the sensor device was packaged by medical grade material, its bio-compatibility still needed to be checked after a period implantation test in live animals. In this series of rabbit tests, after sensor device retrieval, its surface and the rabbit tissue surface where the sensor device was implanted were checked. There was no obvious change on the sensor device surface after 2 weeks implantation and the tissue touched the sensor device looked similar to the normal tissue which didn’t contact with the sensor device. No obvious infection or inflammation was seen.

Furthermore, gross histological evaluation of the insertion site was undertaken on 3 different rabbits by Professor Paul Sibbons (NPIMR), including rabbits No.2, No.4 and No.5. For each rabbit, two sets of histological sections representing sites along the uterine horn between the proximal end and the distal uterine connection were collected (they were paraffin embedded before cutting). One set of slides was stained with standard haematoxylin and eosin (H&E), and the other one was stained with Picrosirius red plus Miller’s elastin (PicMill). These stains were used to check the structural integrity of the cells and whether they were damaged by the presence of the device. The microscope used was an Olympus BX40 and the capture camera was an Olympus DP70 using the bundled DP software. These samples are shown in Figure 5.24.

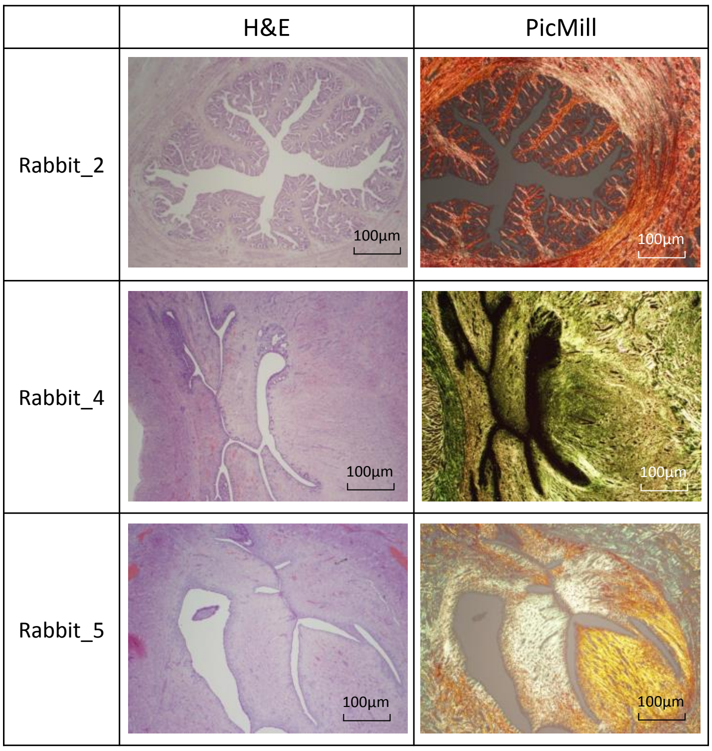

Figure 5.24 Representative photomicrographs of histological sections collected from the place where the sensor device was implanted. Two samples were collected from each rabbit and they were stained with H&E and PicMill, respectively.

All of these sections show normal multiparous rabbit uterine horn. There was specifically no inflammatory response on the luminal aspect of any of these sections, neither was there any luminal damage. In the absence of frank inflammatory infiltrates on analysis of the H&E stained sections no further histological analysis or subtyping of the cell types was undertaken.

From the bio-compatibility check and histology research after the implantation tests, there was no inflammatory response and luminal damage at the implantation site. The encapsulation of sensor device was proved with a good bio-compatibility and good enough for implantation in live rabbit.

5.3 Summary of animal tests on pig cadaver and rabbit

The animal test on pig cadaver verified system design and wearable receiver deployment. The proposed clinical procedure for sensor device implantation and retrieval was demonstrated and confirmed. A robust intra-uterine monitoring system was proved and valuable experience was gained on clinical operation for live pig tests and future trials on human.

From the rabbit tests, real-time long-term intra-uterine temperature monitoring was achieved up to two weeks. This not only demonstrated our *in-vivo* sensing platform in live animals and evaluated system performance, but also obtained novel real-time *in-vivo* data for rabbit intra-uterine environment research (incorporating temperature). The normal rabbit intra-uterine temperature range and inferring circadian rhythm associated variation were discussed.

Chapter 6

Conclusion and future work

6.1 Conclusion

This thesis presented on the relevant background and motivation of intra-uterine environment measurement and reviewed the state of the art human infertility research and some of the challenges facing human reproductive research. A number of technologies and research points have been investigated as shown in appendix C. Specifically, the research points have been well achieved in this thesis are marked by yellow colour, and the other items have been developed for prototype and can be optimised in future work as marked by blue colour. A multi-parameter sensing platform for the intra-uterine environment measurement was proposed and developed and multiple biosensors were fabricated for temperature, DOC and pH sensing as shown in Figure 6.1.

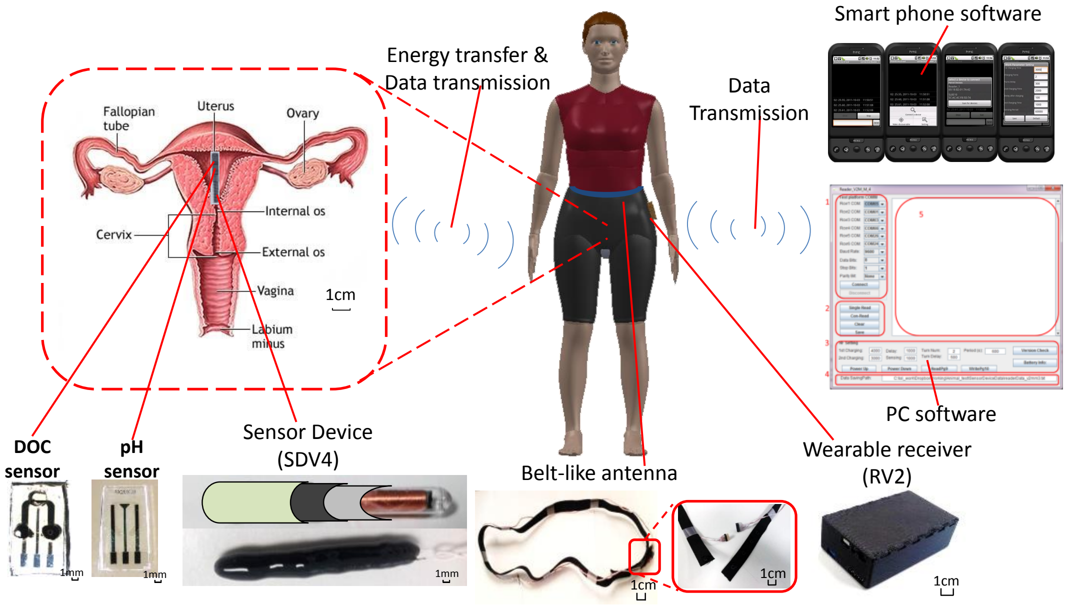

Figure 6.1 Latest prototype of intended multi-parameter *in-vivo* sensing platform.

Development of implantable sensor device, wearable receiver and monitoring software

The wireless and batteryless implantable sensor device is the pivotal component in our intended real-time long-term *in-vivo* sensing platform, it is considered by size and energy requirements. Four versions of sensor devices were developed and the latest one (SDV4) was met the strict size and power consumption limitations and was adequate for use in our intended application. Two different prototypes of sensor device were developed for different application scenarios, including a T-type and stick-type sensor devices. The size of the sensor device is comparable to the Mirena Coil (a widely used commercial contraceptive device). Multi-layer encapsulation resulted in a sensor device adequate for bench testing, *in-vivo* animal tests and an intended human trial. The receiver is the core portable device in the intended system and it works as the relay between the user and sensor device. After the development of two different versions of the receivers, the final receiver (RV2) is adequate for the intended application. Its two-board three-layer stacked structure and carefully designed multi-layer PCB layout resulted in a suitably small receiver with low interference and good signal performance. Multi-platform software versions were developed for remote system configuration and real-time monitoring, and also to enable system debugging. Software included two Java based software versions running on the PC for the single and multi-antenna receiver systems, an Android monitoring software for smart phones and an embedded software GUI running on the receiver. A user friendly interface was designed to deliver optimal user experience.

Development of core technologies

Two core technologies wireless energy transfer and wireless data communication were discussed and developed. Electromagnetic induction technology was employed for wireless energy transfer between the sensor device and receiver. Different antennas were developed for the sensor device and receiver, while balancing the size and antenna’s performance, the tube antenna with ϕ3 mm ferrite core using 0.05mm wire was optimal for the implantable sensor device and a 20cm x 20cm loop antenna was suitable for the receiver. A working distance of 23cm can be achieved. Furthermore, different antennas were developed for different applications. For example, a belt antenna proved to be the most suitable one for the pig tests and intended human trials. Its novel design of an antenna coil connector and adjustable hooks made it easy to apply as a normal belt worn around the waist. A multi-antenna system was developed for applications where the position and orientation between the sensor device and receiver varies, such as the animal tests in the rabbit. LF RFID and Bluetooth were chosen for the wireless communication. The LF RFID provides sufficient data bandwidth to meet the system demand while only requiring very low power consumption. The circuit for wireless energy transfer can also serve as the wireless data communication by acting as a LF RFID link, eliminating the need for more circuits or board space for data communication. Bluetooth has relatively low power consumption requirements and can be easily minimized to fit battery powered portable devices. Its high compatibility makes its development straightforward and able to interact with existing devices. The power consumption of the sensor device and the electromagnetic radiation were investigated, the calculated SAR of our prototype was lower than the recommended medical standards for either Europe or USA.

Development of miniaturised biosensors

Three miniaturised sensors were developed and discussed for the measurement of intra-uterine temperature, DOC and pH. A NTC thermistor was chosen and developed for temperature sensing due to its stability, accuracy, small size, and power consumption. The prototype system was fully tested on the bench and in animal tests. The temperature accuracy is ±0.03°C after calibration and the drift is no more than 0.01°C after two weeks continuous measurement. No obvious blocking phenomena were observed in the blocking test and the sensor device displaying good stability over a >1 month long-term in-water testing. After discussion of the principles and key technologies of an electrochemical DO sensor, a miniaturised electrochemical DO sensor (7mmX4mmX2mm) was developed. A good linear relationship between the oxygen reduction current and the DOC of bulk solution were observed and the measurement error was in a range of ±7μM. The stability of the built-in Ag/AgCl RE and the characteristics of a medical grade OPM were also discussed. A miniaturised IROF pH sensor was developed by using the anodical electrodeposition method based on Yamanaka's recipe for the intended application. An auto-testing platform was developed for AEIROF pH sensor evaluation and our minimized AEIROF pH sensor demonstrated a super-Nernstian response with a sensitivity of 76.33±2.58mV/pH. An accuracy of 0.04pH was achieved through testing in standard pH buffers.

Animal tests on pig cadavers and rabbits

Animal tests were undertaken on pig cadavers and rabbits. The pig cadaver tests verified system design and wearable receiver deployment. The proposed clinical procedure for sensor device implantation and retrieval was demonstrated and confirmed, and valuable experience was obtained for the intended human trials. The rabbit tests delivered real-time (high data capture rate), intra-uterine temperature monitoring over a duration of two weeks from four individual rabbits. This demonstrated our *in-vivo* sensing platform in live animals and evaluated the system performance, in particular by demonstrating reliable data capture at 10mins intervals over a two weeks period. Importantly this novel approach to real-time *in-vivo* data capture has provided new insight into the temperature range in the intra-uterine environment of the rabbit.

Compared with the proposed target specifications in section 2.4.6, the latest system prototype achieved all of the expected properties. More details can be found in Table 6.1.

Table 6.1 Comparison between the target specifications and achievements of the intended multi-parameter *in-vivo* sensing platform for intra-uterine environment monitoring

	Target specifications	**Achievements**
Multi-parameter *in-vivo* sensing platform		
Data link	Should support bidirectional wireless data communication.	Two wireless communication links, the low-level (between the implanted sensor device and wearable receiver) and high-level (between the wearable receiver and the data processing server). wireless communication links
Portability	Sensor device should be fully implantable, receiver should be wearable.	Sensor device is fully implantable and receiver is wearable.
Working distance (between sensor device and receiver)	Depends on application scenarios, generally, should be no less than 10cm.	23 cm (best)
Sensor device		
Size	Size comparable to the commercial IUDs. Should be smaller than 36mm X 32mm	Φ4.35±0.06 X 34.25±0.98 mm
Weight	No clear reference. Should be light enough to stay in uterus	1.10±0.006 g (unpackaged) 1.90±0.24 g (3-layer epoxy packaged)
Shape	No specific requirement but should be similar to the IUDs	Two different shapes, including T-type and stick-type of sensor devices
Power supply	Without power cable and battery	Achieved wireless and batteryless design of implantable sensor device
Power consumption	Should be optimised for batteryless design	21.8 μA (LPM) 312 μA (Active) 682.1 μA (ADC working)
Encapsulation	Need to be well packaged for lab testing, animal tests and human trial. The clinical requirements have to be considered	Three-layer encapsulation solution for good strength, bio-compatibility and waterproofness
Waterproofness	Should be waterproof and can be working in biological liquid environment for its lift time	Successful passed in-water testing more than 30 days
Lifetime	Should be no less than one menstrual cycle (around 1 month)	Successful passed in-water testing more than 30 days
Scalability	Should be programmable and scalable, support connectivity to multiple biosensors and easy to be upgraded	System developed based on programmable microcontrollers and designed rich peripheral interfaces, including ADC input, GPIO, etc.
Wearable receiver		
Size	As a wearable device, receiver should be very portable and its size should not bigger than a cell phone	65X40X21 mm
Weight	Should not be heavier than a cell phone	37.25±0.68 g
Power supply	Powered by rechargeable battery	Powered by a 7.5V re-chargeable lithium battery
Scalability	Should be programmable and scalable, easy to be upgraded	System developed based on programmable microcontrollers and designed rich peripheral interfaces, including LCD, 5-way button, real-time clock, micro SD card, etc.
Biosensors		
Size	Should be compatible to the implantable sensor device	7mmX4mmX2mm
Power consumption	Should be optimised for batteryless design	Low power consumption because of nature of electrochemical biosensors with miniaturised electrodes; Achieved hundreds nA current requirement
Encapsulation	Need to be well packaged for continuously working in biological liquid environment for at least sensor device lifetime.	Fabricated by MG-PDMS; More biosensors integrated encapsulation will be developed in future work

6.2 Recommendation for future work

The current prototype is adequate for bench test and animal test, however, there are some limitations and issues need to be addressed. To achieve the intended human trial and eventual application, some recommendations for the future work are summarized below:

1. The latest sensor device (SDV3) has a minimum diameter of 4mm and is adequate for the bench test and animal test. Because the core chips (MCU and RF chip) are both 4mmX4mm in size, it is hard to reduce the size of sensor device below 4mm using the current approach. However the introduction of ASICs and MEMS technologies would enable the core chips to be designed with smaller outer dimensions enabling the device size to be further reduced.

2. The design of the sensor device antenna has to balance the antenna size with the wireless performance. The current tube antenna has a diameter smaller than 4mm which is adequate for the main board of sensor device. In future, for the further miniaturised sensor device, the antenna may need to be smaller. One possibility is to employ another ferrite core made using a different material. For example, Metglas has a relative permeability of 1×10^6 [186], much higher than the current ferrite core with a relative permeability of 36 [187]. Higher magnetic permeability delivers higher electromagnetic field strength, i.e. the sensor device antenna could be smaller to meet energy transfer requirement.

3. Current encapsulation of the sensor device is adequate for the bench test and animal test. However for the intended human trials, the encapsulation strategy needs to be improved. In future, the packaged sensor device should incorporate a flexible region at a certain point to enable easier delivery into the uterus; the packaging is required to be shatterproof after implantation. Furthermore, the packaging material needs to meet the internationally approved medical grade standard.

4. The designs of the DO sensor and pH sensor have been demonstrated and their basic functions have been evaluated and with good results obtained, however more experiments need to be undertaken to identify their long-term stability, such as long-term drift, repeatability, etc. Once these characters are evaluated, the system integration is required to embed the implantable DO and pH sensor into the proposed implantable sensor device.

5. Biofouling is likely to be a potential issue in effective biosensor function especially in the case of the DO and pH sensors. They may be blocked and deactivated due to surface blocking, electrical failure or enzyme interaction. Several approaches have been developed to limit the degree of biofouling, including the use of relatively inert boron doped diamond electrodes (BDD) [188], surfactant modification [189, 190] and specific membrane coating technology. Although BDD has been demonstrated to perform well in complex biological matrices, it is difficult to characterise and has slower kinetics. BDD is also expensive, less available and not be used widely. Membrane coating is the most widely used strategy and the most generally applicable method to prevent macromolecule access to the sensor surface. The coating material can be chosen from a range of chemicals, such as Nafion, poly Styrene-sulphonate/poly L-lysine (PSS/PL) and fibronectin. Nafion is a perfluorosulfonic acid polymer which is commonly used for coating all types of sensors [136, 191], particularly carbon fibres. Polyion film is expected to provide good gas selectivity by blocking macromolecules, and therefore preventing biofouling, whilst still allowing small molecules to diffuse. PSS/PL is applied as a film; it has been successfully applied to enable nitric oxide sensing. Fibronectin is a protein of the extracellular matrix and has already shown satisfactory characteristics for use in electrochemical sensing strategies [102, 103, 192]. In a previous comparative study, biofouling was induced by immersion into albumin solutions, and the fibronectin coating presented a better performance than others above. Therefore, fibronectin is a possible solution for biofouling protection in the final application.

4. Short period animal tests have been done in this thesis, system functionalities have been verified and system performance has been evaluated. These animal tests provide some proof of concept and demonstrated our intended multi-parameter *in-vivo* sensing platform. However, more animal tests and human trials are necessary before this technology is applied in clinical. Further histological analysis following animal *in-vivo* testing is necessary to evaluate the impact of the sensor device after a certain period of implantation. Live pig testing is a good option which can continuously test our implantable sensor device and wearable receiver, especially belt antenna. Trials on human is essential to prove our concept for human reproduction research and more detailed information may be collected from these valuable experiments, such as the clinical procedures, optimisation on belt antenna for human, etc.

Appendix A: Schematic diagram and printed circuit board (PCB) design

1. Schematic diagram of sensor device version 2:

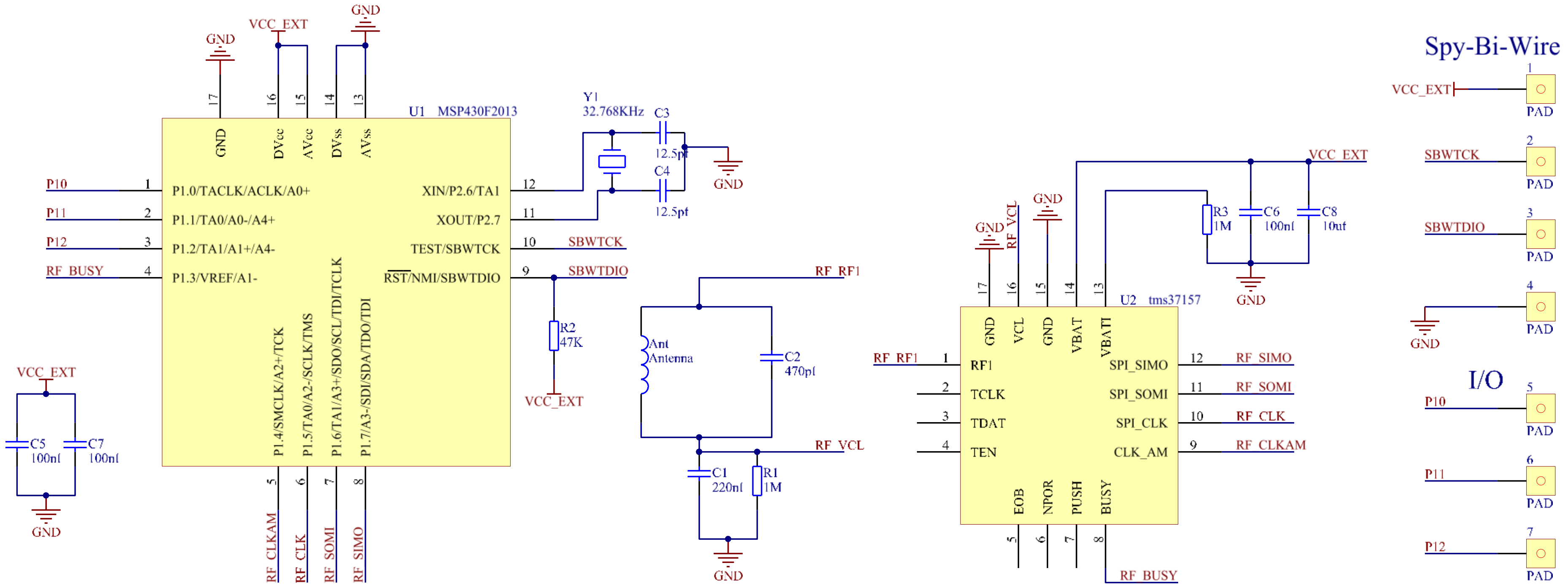

2. PCB design of sensor device version 2:

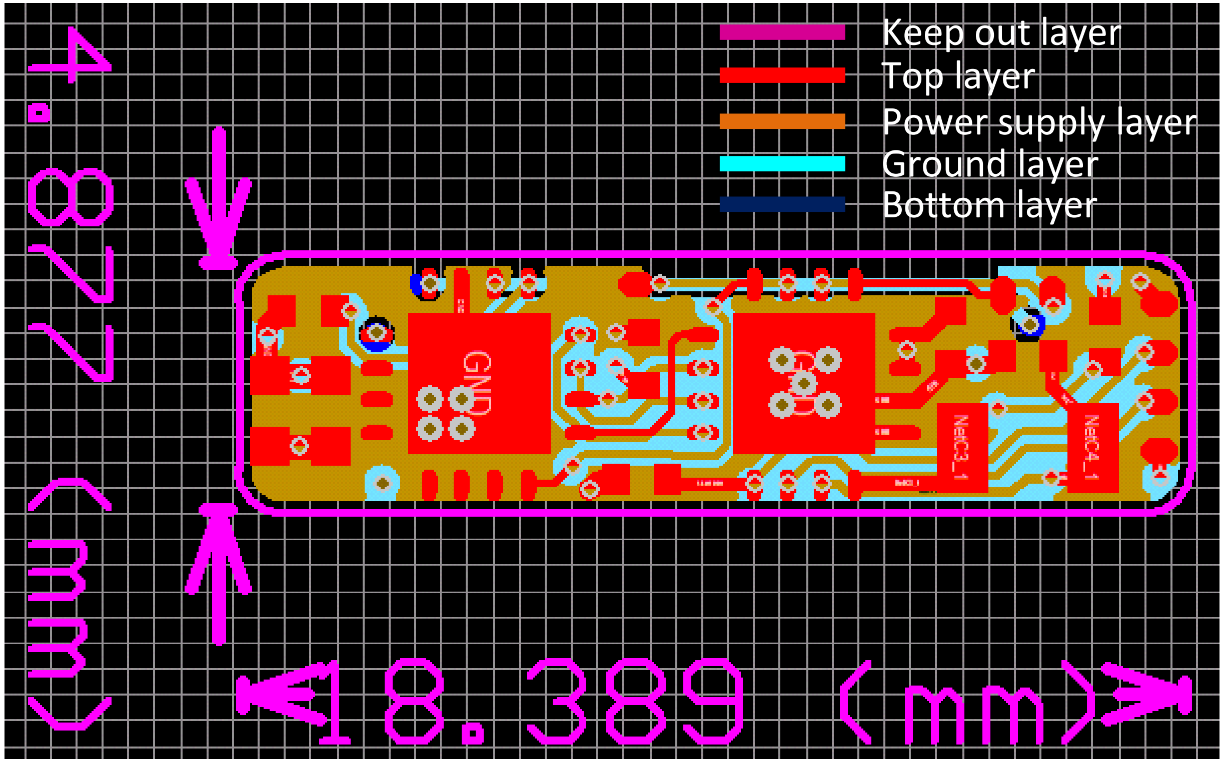

3. Schematic diagram of sensor device version 3:

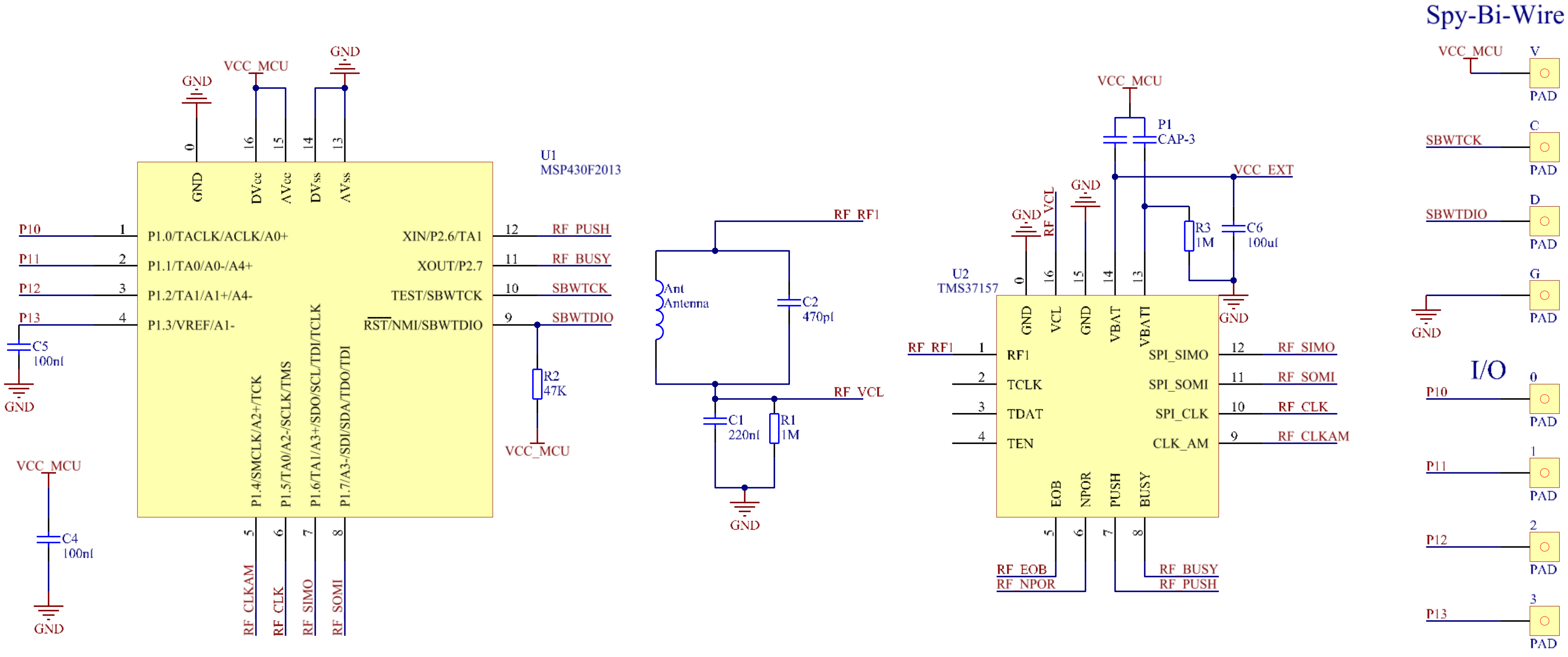

4. PCB design of sensor device version 3:

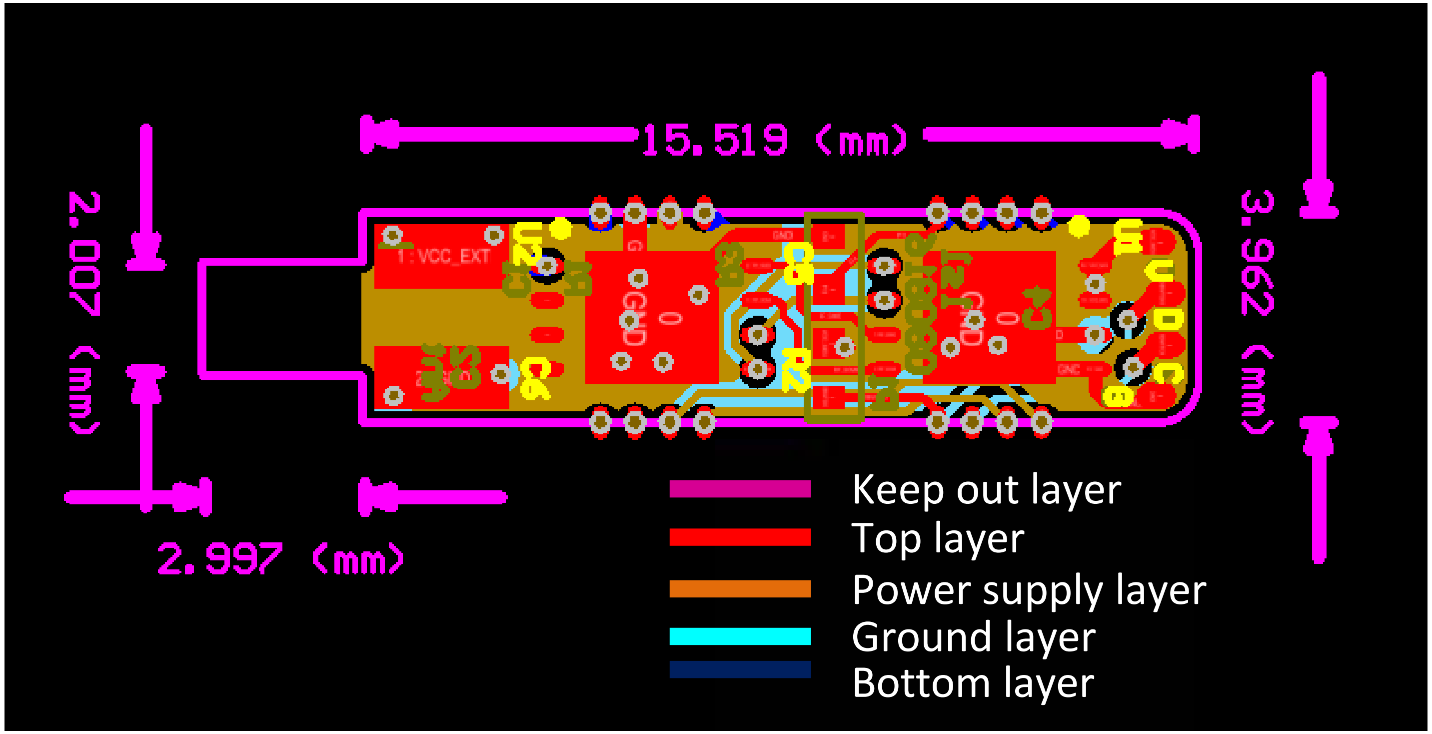

5. Schematic diagram of the main function board of receiver version 2 (Main function circuits):

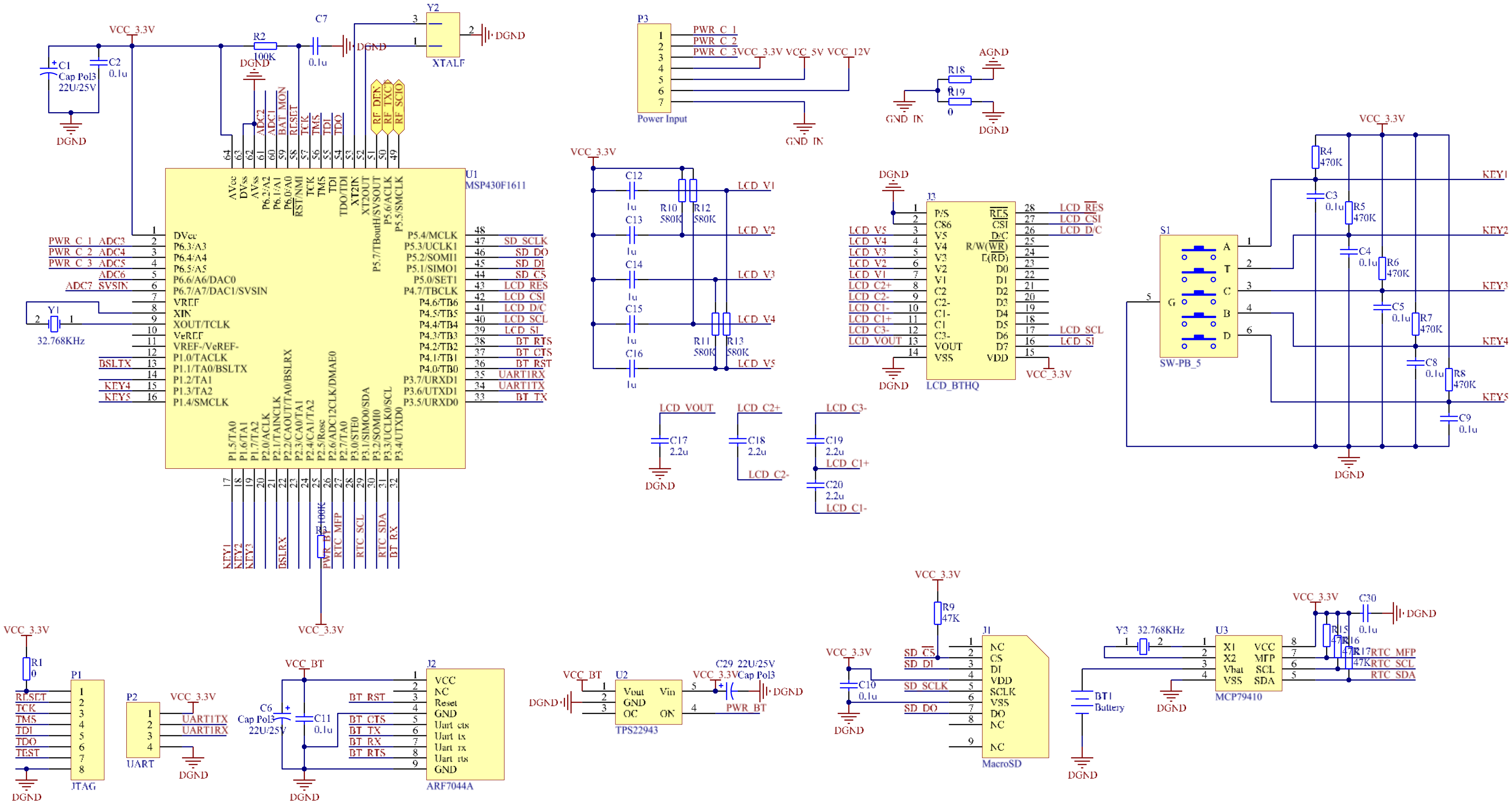

6. Schematic diagram of the main function board of receiver version 2 (RF circuit):

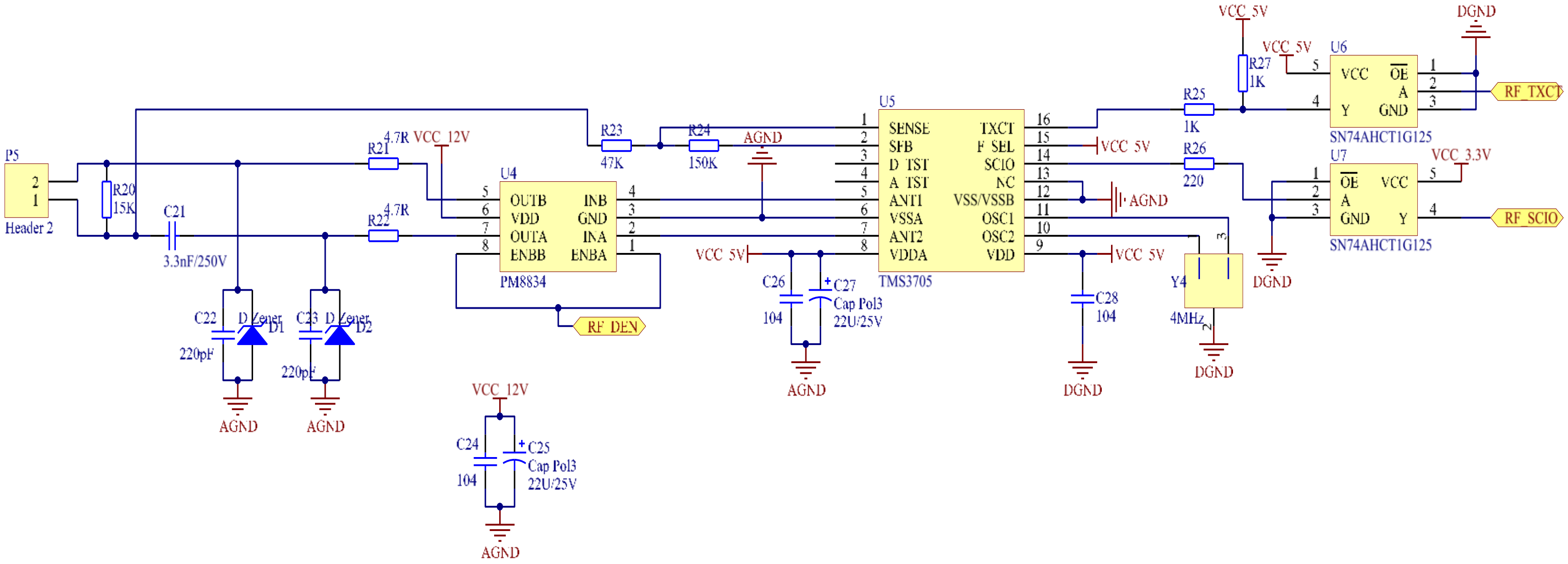

7. PCB design of the main function board of receiver version 2:

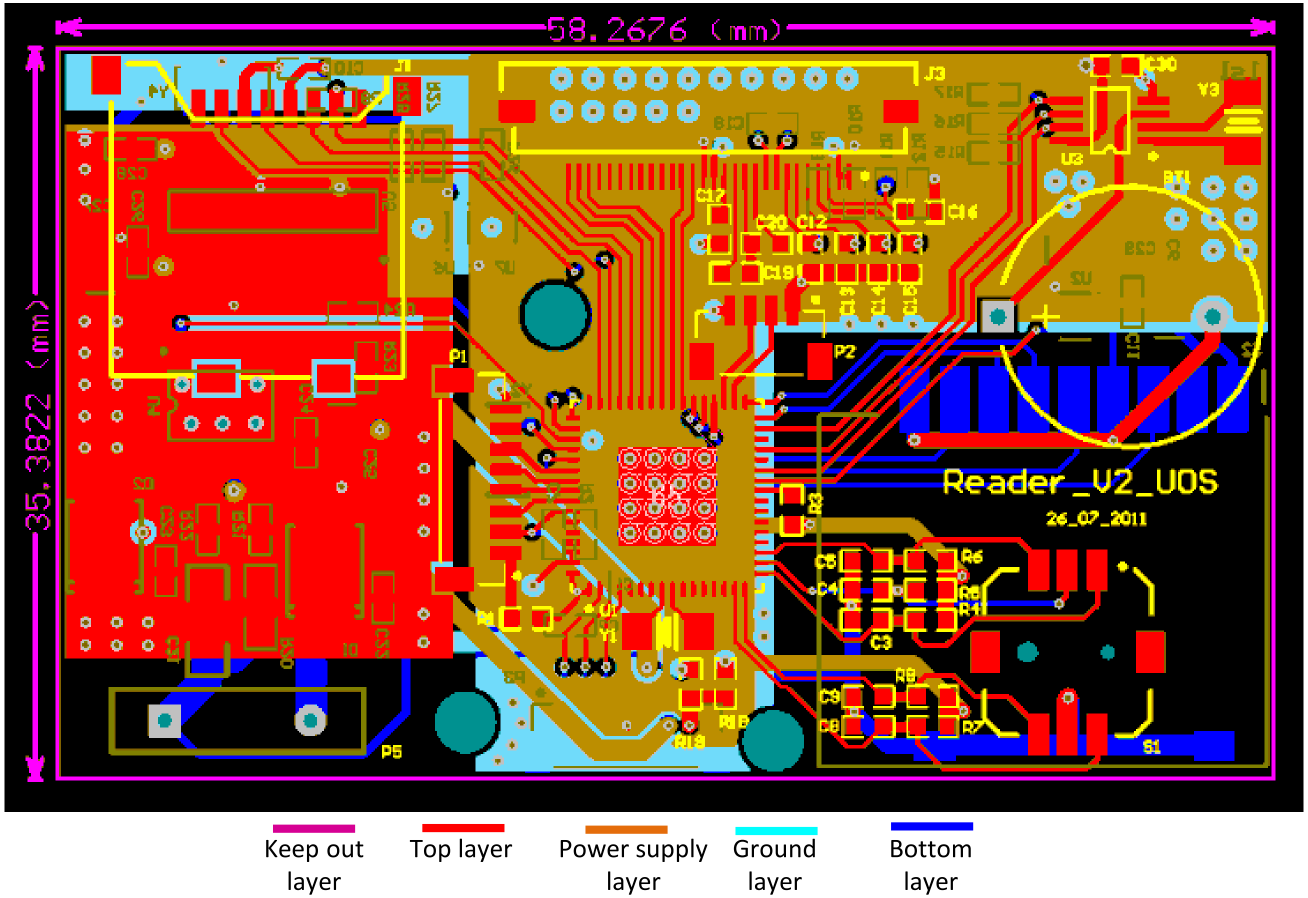

8. Schematic diagram of the power supply board of receiver version 2:

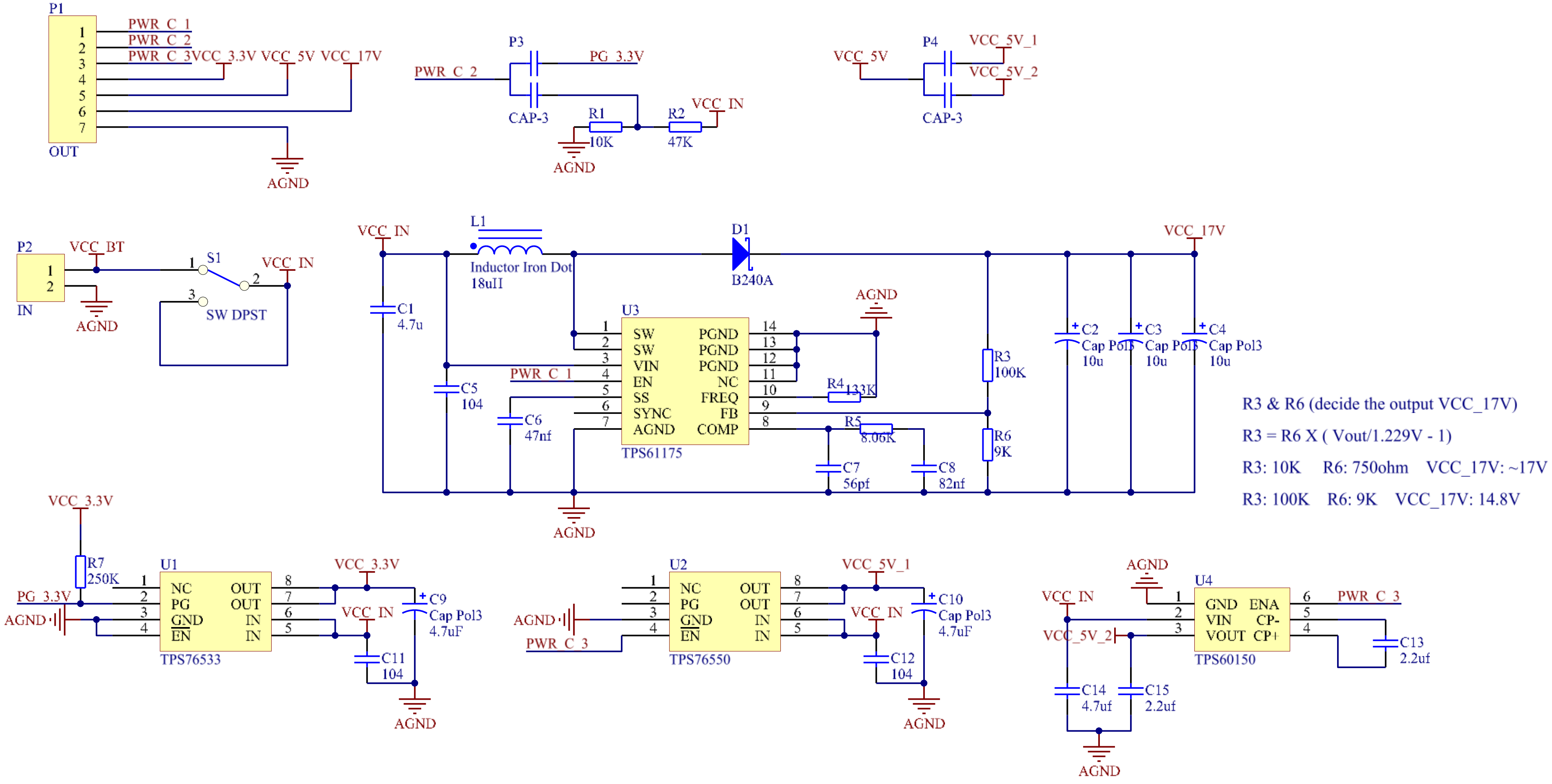

R3 & R6 (decide the output VCC_17V)

R3 = R6 X (Vout/1.229V - 1)

R3: 10K R6: 750ohm VCC_17V: ~17V

R3: 100K R6: 9K VCC_17V: 14.8V

9. PCB design of the power supply board of receiver version 2:

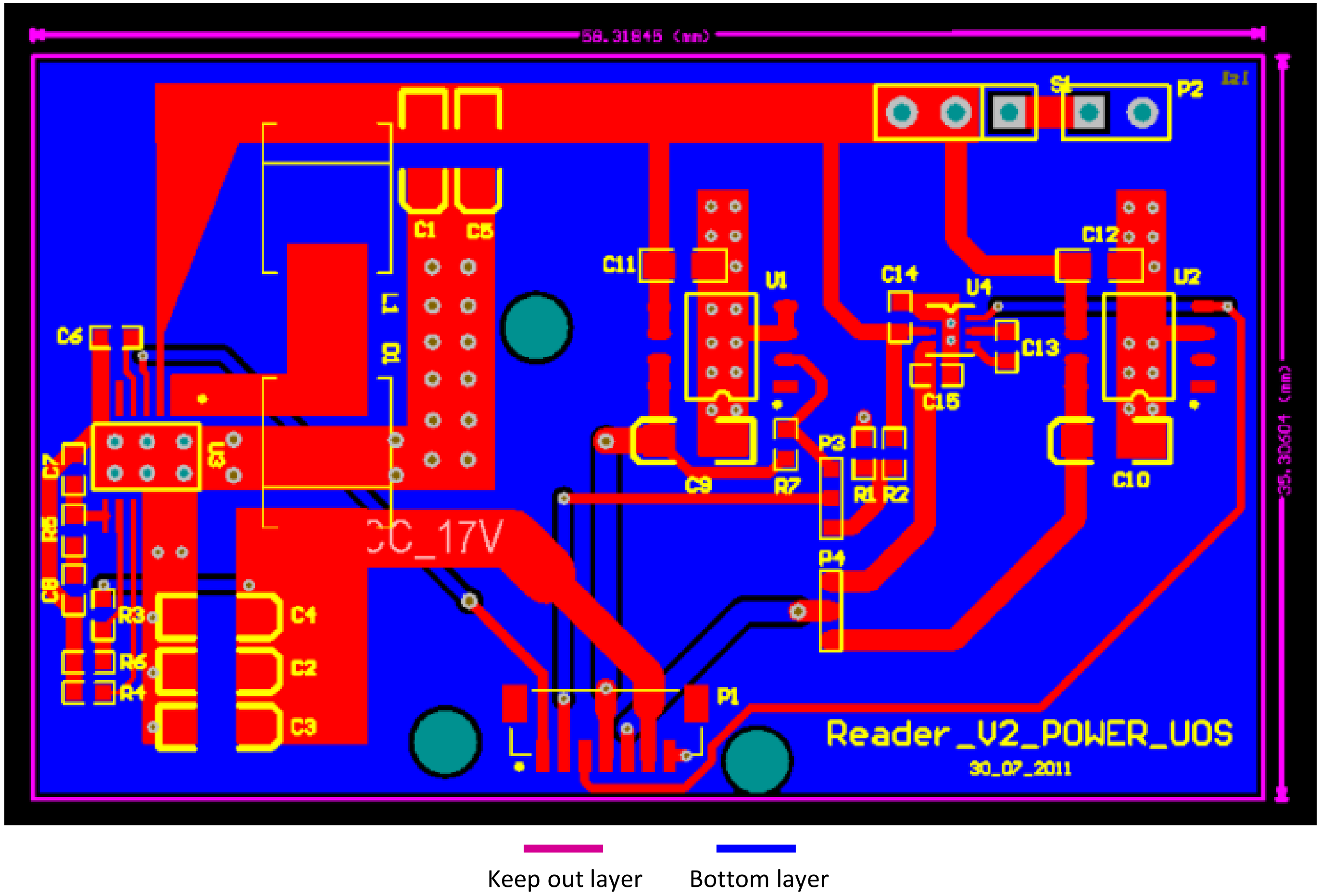

10. Schematic diagram of DO sensor driving board:

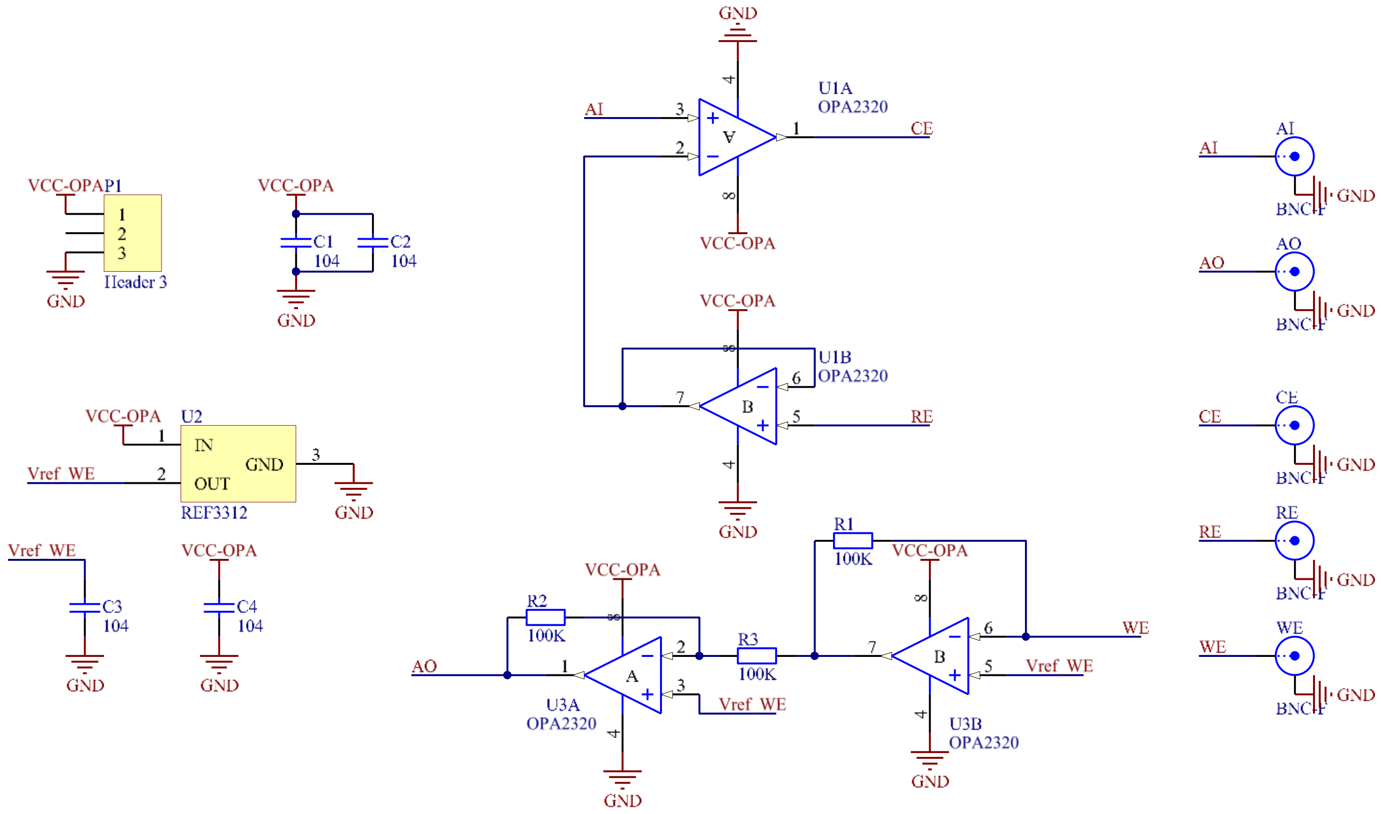

11. PCB design of DO sensor driving board:

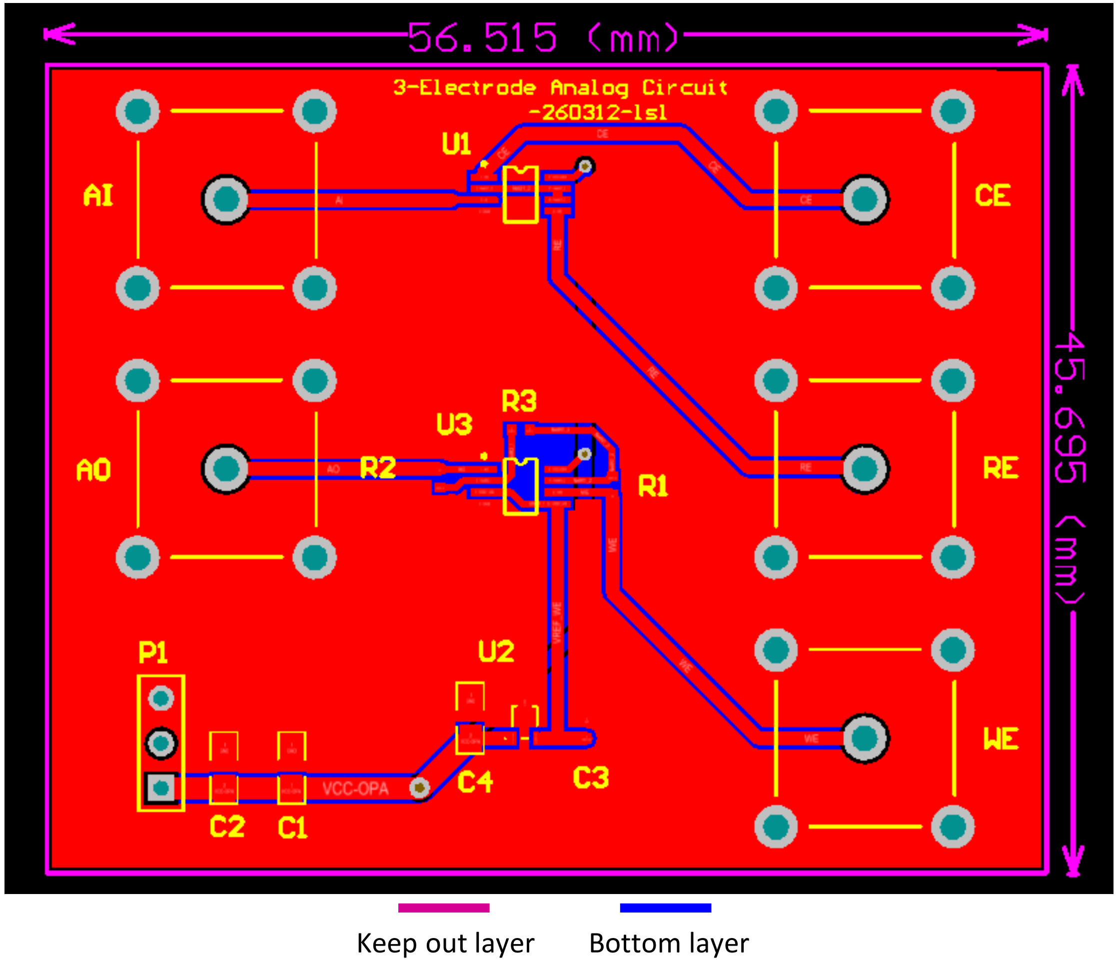

Appendix B: Experimental raw data

1. Results of diffusion coefficient of MG-PDMS and diagrams of relations between oxygen reduction current and DOC of three UMEs.

	Sample 1	**Sample 2**	**Sample 3**
Slope of trendline-with OPM	-3.52E-11	-2.83E-11	-4.42E-11
Slope of trendline-without OPM	-6.80E-11	-6.62E-11	-6.46E-11
Diffusion coefficient in OPM	1.01E-09	8.28E-10	1.33E-09

Sample 1:

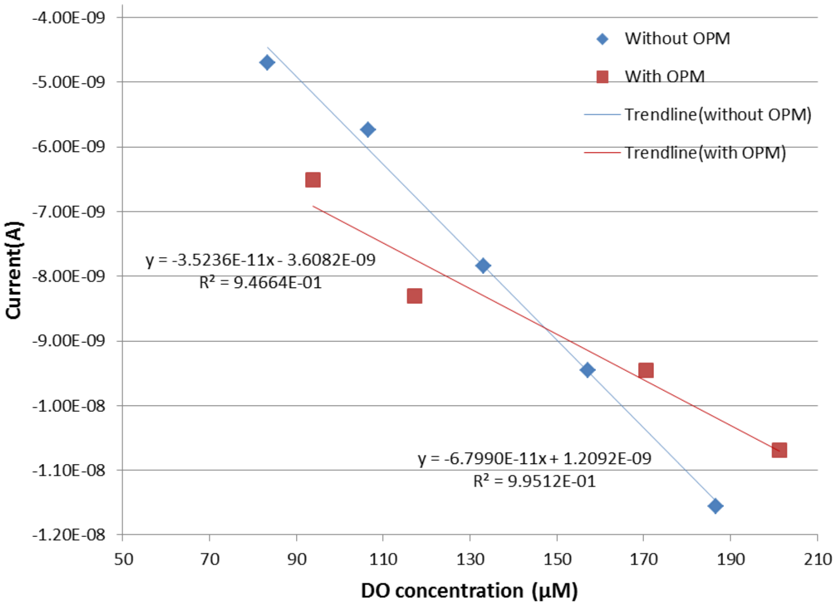

Sample 2:

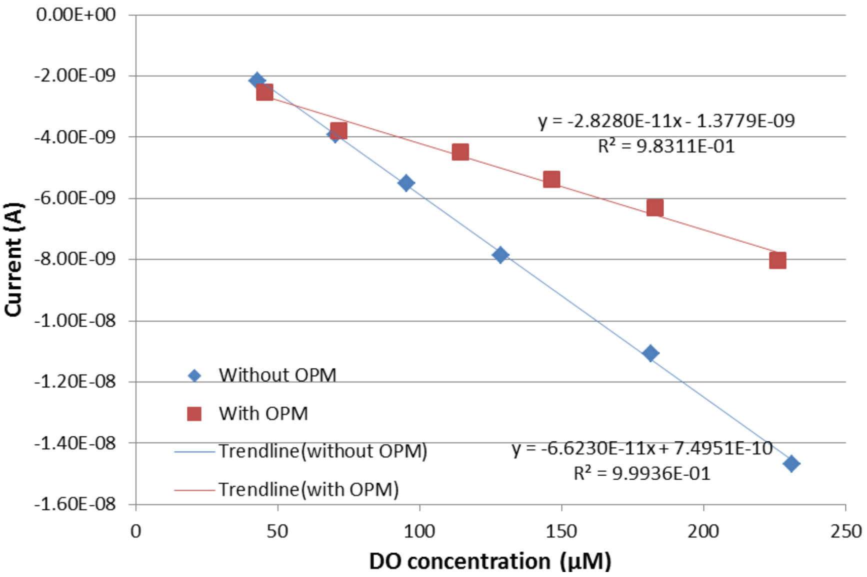
0.00E+00
-2.00E-09
-4.00E-09
-6.00E-09
-8.00E-09
-1.00E-08
-1.20E-08
-1.40E-08
-1.60E-08
Current (A)
0
50
100
150
200
250
DO concentration (μM)
y = -2.8280E-11x - 1.3779E-09
R² = 9.8311E-01
y = -6.6230E-11x + 7.4951E-10
R² = 9.9936E-01
Without OPM
With OPM
Trendline(without OPM)
Trendline(with OPM)

Sample 3:

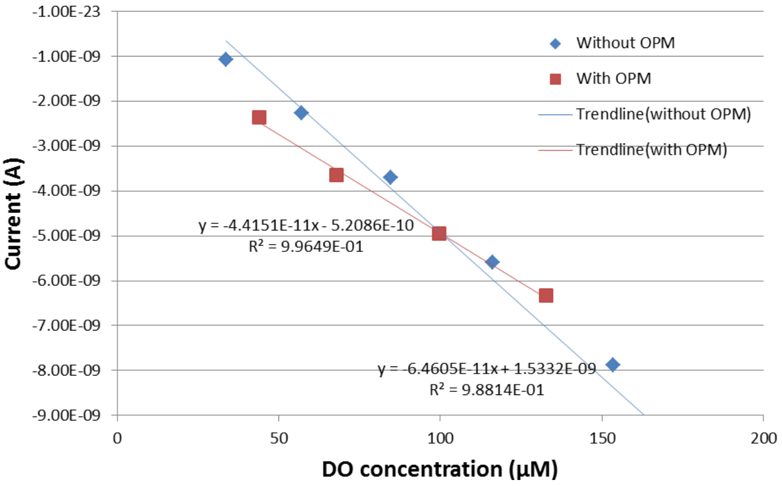
-1.00E-23
-1.00E-09
-2.00E-09
-3.00E-09
-4.00E-09
-5.00E-09
-6.00E-09
-7.00E-09
-8.00E-09
-9.00E-09
Current (A)
0
50
100
150
200
DO concentration (μM)
Without OPM
With OPM
Trendline(without OPM)
Trendline(with OPM)
y = -4.4151E-11x - 5.2086E-10
R² = 9.9649E-01
y = -6.4605E-11x + 1.5332E-09
R² = 9.8814E-01

2. Continuously recorded intra-uterine temperature of four rabbits.

Grey bands indicate nighttime when room lights were off. The temperature rise was observed on the first day after implantation due to postoperative recovery.

Rabbit_1:

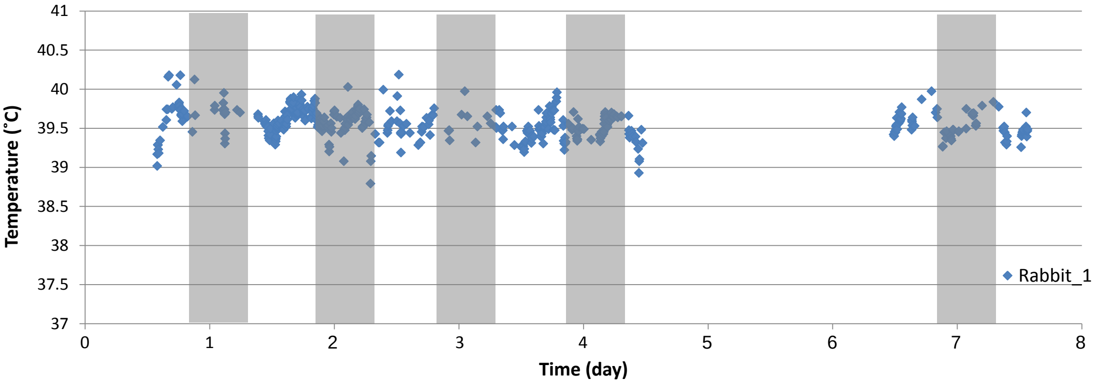

Rabbit_2:

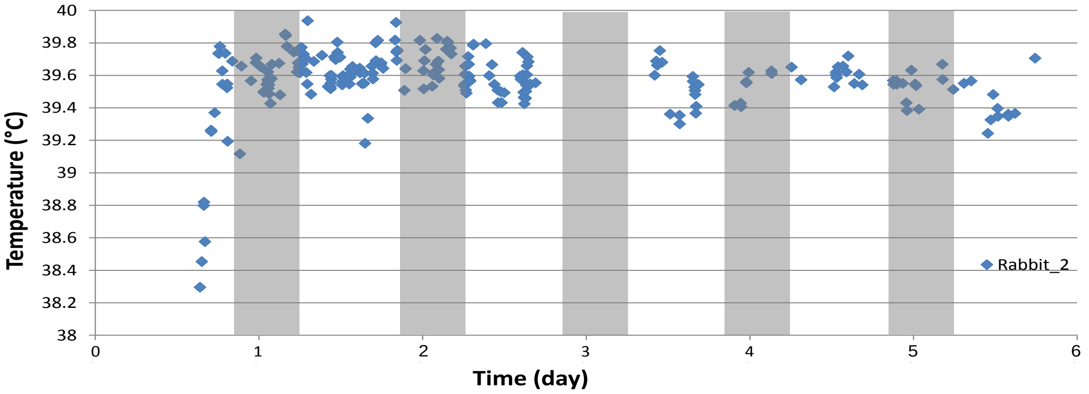

Rabbit_4:

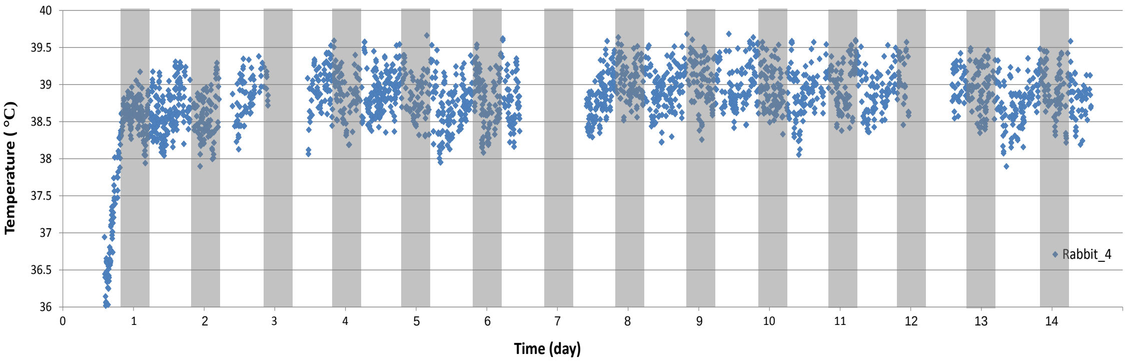

Rabbit_5:

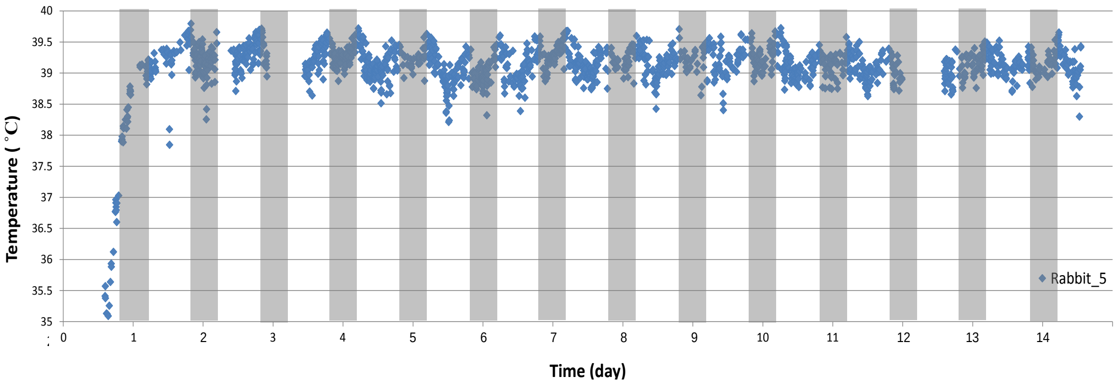

3. Polynomial fitting for intra-uterine temperature of rabbits No. 4 and 5.

Rabbit_4	
Time (day)	**Polynomial fitting equation**
1	$y = 14.34x^5 - 57.74x^4 + 74.455x^3 - 39.3x^2 + 8.4852x + 38.271$
2	$y = 2.3808x^5 - 21.521x^4 + 46.603x^3 - 28.031x^2 + 5.0357x + 36.639$
3	$y = 5.8982x^5 - 5.5966x^4 + 26.943x^3 - 19.416x^2 + 4.0398x + 38.816$
4	$y = 2.1136x^5 - 22.84x^4 + 38.905x^3 - 22.759x^2 + 4.6428x + 38.745$
5	$y = 0.302x^5 - 14.811x^4 + 27.251x^3 - 14.657x^2 + 2.4056x + 38.799$
6	$y = -20.428x^5 + 20.38x^4 + 16.51x^3 - 22.923x^2 + 6.4021x + 38.598$
7	$y = -11.879x^5 + 6.9766x^4 + 15.969x^3 - 13.224x^2 + 1.9015x + 38.878$
Overlapped	$y = 2.3926x^5 - 26.0668x^4 + 43.1402x^3 - 24.0709x^2 + 4.6037x + 38.6042$

Rabbit_5	
Time (day)	**Polynomial fitting equation**
1	$y = 19.414x^5 - 76.122x^4 + 100.09x^3 - 53.563x^2 + 10.348x + 38.841$
2	$y = 14.176x^5 - 62.921x^4 + 88.669x^3 - 49.624x^2 + 9.7167x + 38.802$
3	$y = 29.618x^5 - 96.977x^4 + 113.66x^3 - 56.726x^2 + 11.011x + 38.576$
4	$y = 4.2967x^5 - 38.864x^4 + 63.375x^3 - 35.757x^2 + 6.4315x + 39.103$
5	$y = 6.5456x^5 - 45.865x^4 + 73.689x^3 - 43.321x^2 + 8.9569x + 38.809$
6	$y = 15.989x^5 - 52.893x^4 + 59.488x^3 - 27.043x^2 + 4.461x + 39.043$
7	$y = 6.5767x^5 - 38.102x^4 + 59.555x^3 - 35.137x^2 + 7.1297x + 38.922$
8	$y = 4.6726x^5 - 30.262x^4 + 47.658x^3 - 28.052x^2 + 5.848x + 38.872$
9	$y = -20.503x^5 + 31.684x^4 - 6.1497x^3 - 8.7966x^2 + 3.4058x + 38.977$
Overlapped	$y = 22.224x^5 - 76.112x^4 + 90.804x^3 - 45.057x^2 + 8.3232x + 38.847$

4. Polynomial fitting for intra-uterine temperature of rabbits No. 4 and 5 for the first two days after implantation surgery.

Rabbit_4	
Time (day)	**Polynomial fitting equation**
1	$y = 21.314x^5 - 52.904x^4 + 40.918x^3 - 9.1487x^2 - 0.5043x + 38.722$
2	$y = -80.826x^5 + 162.98x^4 - 109.06x^3 + 26.695x^2 - 1.0743x + 38.524$

Rabbit_5	
Time (day)	**Polynomial fitting equation**
1	$y = 58.921x^5 - 162.21x^4 + 160.61x^3 - 68.919x^2 + 12.625x + 38.294$
2	$y = -50.409x^5 + 92.414x^4 - 50.926x^3 + 6.1382x^2 + 1.7141x + 38.969$

Appendix C: Research points tree of an *in-vivo* sensing platform development

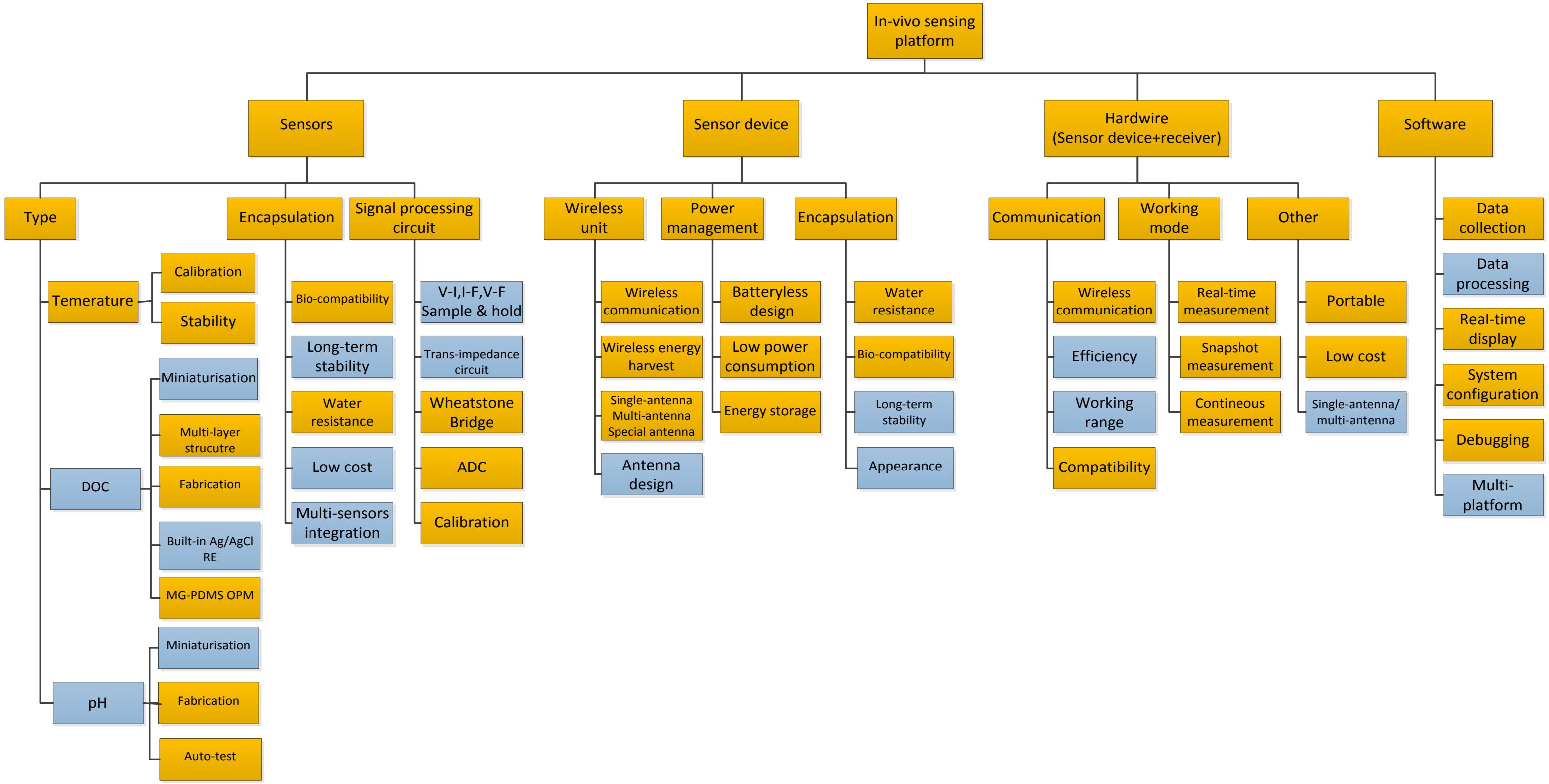

The yellow colour items are the research points have been well achieved in this thesis. The other items have been developed for prototype and can be optimised in future work are marked by blue colour.

References

[1] E. Jauniaux and G. J. Burton, "Pathophysiology of histological changes in early pregnancy loss," *Placenta*, vol. 26, pp. 114-23, Feb-Mar 2005.

[2] E. Jauniaux, *et al.*, "*In-vivo* measurement of intrauterine gases and acid-base values early in human pregnancy," *Human Reproduction*, vol. 14, pp. 2901-4, Nov 1999.

[3] G. A. Yedwab, *et al.*, "The temperature, pH, and partial pressure of oxygen in the cervix and uterus of women and uterus of rats during the cycle," *Fertility and Sterility*, vol. 27, pp. 304-9, Mar 1976.

[4] H. E. Fadel, *et al.*, "Acid-base determinations in amniotic-fluid and blood of normal late pregnancy," *Obstetrics and Gynecology*, vol. 53, pp. 99-104, 1979.

[5] H. E. Johnell and B. A. Nilsson, "Oxygen tension, acid-base status and electrolytes in human amniotic fluid," *Acta Obstet Gynecol Scand*, vol. 50, pp. 183-92, 1971.

[6] H. E. Johnell, *et al.*, "Oxygen tension, carbon dioxide tension and pH in amniotic fluid and maternal arterial blood during induced maternal hyperoxia and hypoxia," *Acta Obstetricia et Gynecologica Scandinavica*, vol. 50, pp. 209-214, 1971.

[7] A. T. Fazleabas and Z. Strakova, "Endometrial function: cell specific changes in the uterine environment," *Molecular and Cellular Endocrinology*, vol. 186, pp. 143-147, 2002.

[8] G. A. Bridges, *et al.*, "Deficiencies in the uterine environment and failure to support embryonic development," *J Anim Sci*, Jan 10 2013.

[9] S. Altmäe, *et al.*, "Guidelines for the design, analysis and interpretation of 'omics' data: focus on human endometrium," *Human Reproduction Update*, 2013.

[10] S. L. Pierce, *et al.*, "In vivo measurement of intrauterine pressure by telemetry: a new approach for studying parturition in mouse models," *Physiol Genomics*, vol. 42, pp. 310-6, Jul 7 2010.

[11] G. Skinner, "Regulated fertility services: a commissioning aid," 2009.

[12] D. L. Healy, *et al.*, "Female infertility: causes and treatment," *The Lancet*, vol. 343, pp. 1539-1544, 1994.

[13] W. Cates, *et al.*, "Worldwide patterns of infertility: is Africa different?," *The Lancet*, vol. 326, pp. 596-598, Sep 14 1985.

[14] J. L. Evers, "Female subfertility," *Lancet*, vol. 360, pp. 151-9, Jul 13 2002.

[15] *Basal body temperature*. Available: http://en.wikipedia.org/wiki/Basal_body_temperature

[16] G. Teklenburg, "Preimplantation embryo-endometrial signalling," Utrecht University, 2010.

[17] Y. Cheong, *et al.*, "Uterine secretomics: a window on the maternal-embryo interface," *Fertil Steril*, vol. 99, pp. 1093-9, Mar 15 2013.

[18] M. Pekker. (2012). *Diagnosing post menopausal bleeding*. Available: http://menopause-aid.blogspot.co.uk/2012/03/diagnosing-post-menopausal-bleeding.html

[19] G. SR., "Modern evaluation of the endometrium," *Obstetrics and Gynecology*, vol. 116, pp. 168-176, 2010.

[20] *Transvaginal ultrasound*. Available: http://nymethodist.adam.com/content.aspx?productId=10&pid=10&gid=000604

[21] D. K. Gardner, *In vitro fertilization : a practical approach*, 3 ed.: Taylor & Francis, 2006.

[22] L. F. Scott, *et al.*, "The relevance and use of mouse embryo bioassays for quality control in an assisted reproductive technology program," *Fertility and Sterility,* vol. 60, pp. 559-568, 1993.

[23] E. A. Sullivan, *et al.*, "International Committee for Monitoring Assisted Reproductive Technologies (ICMART) world report: assisted reproductive technology 2004," *Human Reproduction,* February 26, 2013 2013.

[24] C. o. D. C. a. P. C. U.S. Department of Health and Human Services, "Assisted reproduction technology success rates (2011), national summary and fertility clinic reports," December 2013.

[25] M. Kupka, *et al.*, "Assisted reproductive technology in Europe, 2011: results generated from European registers by ESHRE," presented at the 2014 annual meeting of ESHRE, Munich, 2014.

[26] "Fertility treatment in 2011: trends and figures ", ed: Human Fertilisation Embryology Authority, 2011.

[27] "Fertility facts and figures 2008," ed: Human Fertilisation Embryology Authority, 2008.

[28] "Fertility facts and figures 2007," ed: Human Fertilisation Embryology Authority, 2007.

[29] J. E. Swain, "Optimizing the culture environment in the IVF laboratory: impact of pH and buffer capacity on gamete and embryo quality," *Reprod Biomed Online,* vol. 21, pp. 6-16, Jul 2010.

[30] M. A. Will, *et al.*, "Biological pH buffers in IVF: help or hindrance to success," *J Assist Reprod Genet,* vol. 28, pp. 711-24, Aug 2011.

[31] G. Anifandis, "Temperature variations inside commercial IVF incubators," *J Assist Reprod Genet,* vol. 30, pp. 1587-8, Dec 2013.

[32] M. Fujiwara, *et al.*, "Effect of micro-environment maintenance on embryo culture after in-vitro fertilization: comparison of top-load mini incubator and conventional front-load incubator," *J Assist Reprod Genet,* vol. 24, pp. 5-9, Jan 2007.

[33] T. P. Fleming, *et al.*, "The embryo and its future," *Biology of Reproduction,* vol. 71, pp. 1046-54, Oct 2004.

[34] "Culture tips," in *ORIGIO Medicult Media*, 1.1 ed. Denmark, 2010.

[35] C. H. E. Weimar, *et al.*, "In-vitro model systems for the study of human embryo–endometrium interactions," *Reproductive BioMedicine Online,* vol. 27, pp. 461-476, 2013.

[36] N. Simic and A. Ravlic, "Changes in basal body temperature and simple reaction times during the menstrual cycle," *Arh Hig Rada Toksikol*, vol. 64, pp. 99-106, 2013.

[37] J. Beaudoin and R. Marrocco, "Attentional validity effect across the human menstrual cycle varies with basal temperature changes," *Behav Brain Res*, vol. 158, pp. 23-9, Mar 7 2005.

[38] F. C. Baker, *et al.*, "Sleep and 24 hour body temperatures: a comparison in young men, naturally cycling women and women taking hormonal contraceptives," *The Journal of Physiology,* vol. 530, pp. 565-574, 2001.

[39] F. D. Schouten, *et al.*, "Maternal temperature during labour," *BJOG: An International Journal of Obstetrics and Gynaecology,* vol. 115, pp. 1131-1137, 2008.

[40] P. A. Almeida and V. N. Bolton, "The effect of temperature fluctuations on the cytoskeletal organisation and chromosomal constitution of the human oocyte," *Zygote,* vol. 3, pp. 357-365, 1995.

[41] A. C. Sciscione, *et al.*, "A new device for measuring intrauterine temperature," *American Journal of Obstetrics and Gynecology,* vol. 184, pp. 1431-1434, Jun 2001.

[42] C.-C. Wu, *et al.*, "A Clark-type oxygen chip for in situ estimation of the respiratory activity of adhering cells," *Talanta*, vol. 81, pp. 228-234, 2010.

[43] A. S. Lopes, *et al.*, "Quantification of embryo quality by respirometry," *Theriogenology,* vol. 67, pp. 21-31, 2007.

[44] D. Gomes Sobrinho, *et al.*, "IVF/ICSI outcomes after culture of human embryos at low oxygen tension: a meta-analysis," *Reproductive Biology and Endocrinology,* vol. 9, p. 143, 2011.

[45] S. Sjostedt, *et al.*, "The carbon dioxide tension of the amniotic fluid," *American Journal of Obstetrics and Gynecology,* vol. 81, pp. 1-3, 1961.

[46] G. P. Redding, *et al.*, "Theoretical investigation into the dissolved oxygen levels in follicular fluid of the developing human follicle using mathematical modelling," *Reproduction, Fertility and Development,* vol. 20, pp. 408-417, 2008.

[47] E. Mantikou, *et al.*, "Low oxygen concentrations for embryo culture in assisted reproductive technologies," *Human Reproduction Update,* vol. 19, p. 209, May 1, 2013 2013.

[48] G. Redding, *et al.*, "The effects of IVF aspiration on the temperature, dissolved oxygen levels, and pH of follicular fluid," *Journal of Assisted Reproduction and Genetics,* vol. 23, pp. 37-40, 2006.

[49] I. Järvelä, *et al.*, "The effects of a copper-intrauterine device on the uterine artery blood flow in regularly menstruating women," *Human Reproduction,* vol. 13, pp. 1841-1845, July 1 1998.

[50] M. A. M. de Souza and S. Geber, "Doppler color flow analysis of the uterine arteries before and after intrauterine device insertion," *Journal of Ultrasound in Medicine,* vol. 25, pp. 153-157, February 1 2006.

[51] O. Shen, *et al.*, "Effects of a copper-medicated intrauterine device on ovarian artery, uterine artery, and intrauterine blood flow," *Gynecol Obstet Invest,* vol. 66, pp. 253-6, 2008.

[52] Anecova. Available: http://www.anecova.com/pages/the-device/

[53] C. Blockeel, *et al.*, "An in vivo culture system for human embryos using an encapsulation technology: a pilot study," *Human Reproduction,* vol. 24, pp. 790-796, April 1, 2009 2009.

[54] *DuoFertility-Assisted Natural Conception*. Available: http://www.duofertility.com/

[55] *OvuSense*. Available: http://www.ovusense.com/

[56] G. Zhao, *et al.*, "Design and application of a flexible and implantable sensor for detecting uterine musculature contraction," *Biosens Bioelectron,* vol. 25, pp. 100-4, Sep 15 2009.

[57] A. Glukhovsky, "Wireless capsule endoscopy," *Sensor Review,* vol. 23, pp. 128-133, 2003.

[58] A. Uehara and K. Hoshina, "Capsule Endoscope NORIKA System," *Nippon Hoshasen Gijutsu Gakkai Zasshi,* vol. 58, pp. 985-90, Aug 2003.

[59] E. A. Johannessen, *et al.*, "Biocompatibility of a lab-on-a-pill sensor in artificial gastrointestinal environments," *IEEE Transactions on Biomedical Engineering,* vol. 53, pp. 2333-2340, 2006.

[60] *SmartPill*. Available: http://www.smartpillcorp.com/

[61] "SmartPill operational specifications," ed: SmartPill, 2003.

[62] "Bravo pH monitoring system user guide," ed: Given Imaging, 2009.

[63] H. Cao, *et al.*, "Batteryless implantable dual-sensor capsule for esophageal reflux monitoring," *Gastrointest Endosc,* vol. 77, pp. 649-53, Apr 2013.

[64] C. Hung, *et al.*, "Remote detection of gastroesophageal reflux using an impedance and pH sensing transponder," in *Microwave Symposium Digest (MTT), 2012 IEEE MTT-S International*, 2012, pp. 1-3.

[65] H. Cao, *et al.*, "An implantable, batteryless, and wireless capsule with integrated impedance and pH sensors for gastroesophageal reflux monitoring," *IEEE Transactions on Biomedical Engineering,* vol. 59, pp. 3131-9, Nov 2012.

[66] K. Arshak, *et al.*, "A review of low-power wireless sensor microsystems for biomedical capsule diagnosis," *Microelectronics International,* vol. 21, pp. 8-19, 2004.

[67] X. Lin, "Evaluation of Kahne rumen sensors in fistulated sheep and cattle under contrasting feeding conditions," Master of Science in Agriculture, Massey University, 2009.

[68] U. Kilic, "Use of wireless rumen sensors in ruminant nutrition research," *Asian Journal of Animal Sciences,* vol. 5, pp. 46-55, 2011.

[69] *BMDS, IPTT-300*. Available: http://www.bmds.com/products/transponders/iptt-300

[70] C. Peng, *et al.*, "A wireless and batteryless 10-bit implantable blood pressure sensing microsystem with adaptive RF powering for real-time laboratory mice monitoring," *IEEE Journal of Solid-State Circuits,* vol. 44, pp. 3631-3644, 2009.

[71] P. Cong, *et al.*, "Wireless less-invasive blood pressure sensing microsystem for small laboratory animal in vivo real-time monitoring," in *Tthe Fifth International Conference on Networked Sensing Systems (Inss 2008)*, New York, 2008, pp. 80-86.

[72] S. Esmaelzadeh, *et al.*, "Normal uterine size in women of reproductive age in northern Islamic Republic of Iran," *Eastern Mediterranean health journal,* vol. 10, pp. 437-41, 2004.

[73] *Widely Used Intrauterine Devices Characteristics and Distribution*
Available: http://www.k4health.org/pr/b6/b6used.shtml

[74] R. Puers, "Sensors and sensorsystems for in vivo monitoring," in *SICE-ICASE 2006. International Joint Conference*, 2006, pp. 6-13.

[75] J. Colomer-Farrarons and P. L. Miribel-Català, *A CMOS self-powered front-end architecture for subcutaneous event-detector devices*, 1st ed.: Springer, 2011.

[76] J. J. P. C. Rodrigues, *et al.*, "A new wireless biosensor for intra-vaginal temperature monitoring," *Sensors,* vol. 10, pp. 10314-10327, Nov 2010.

[77] J. J. P. C. Rodrigues, *et al.*, "A novel intra-body sensor for vaginal temperature monitoring," *Sensors,* vol. 9, pp. 2797-2808, Apr 2009.

[78] *OvuSense-Advanced fertility monitor*. Available: http://www.ovusense.com/

[79] "ProODO Handheld Optical Dissolved Oxygen Meter Specifications," ed: YSI-Incorporated, 2008.

[80] "HI8242 Portable pH/ORP Meter Specifications," ed: HANNA INSTRUMETNS.

[81] T. Tong Boon, *et al.*, "Toward a miniature wireless integrated multisensor microsystem for industrial and biomedical applications," *Sensors Journal, IEEE,* vol. 2, pp. 628-635, 2002.

[82] D. Uhlmann, *et al.*, "Paratrend sensor as a novel method for continuous monitoring of hepatic microperfusion," *Transplantation Proceedings,* vol. 34, pp. 3339-3341, 2002.

[83] C. H. Hsu, *et al.*, "One-time-implantable spinal cord stimulation system prototype," *IEEE Transactions on Biomedical Circuits and Systems,* vol. PP, pp. 1-1, 2011.

[84] W. Chua-Chin, *et al.*, "A one-time implantable wireless power bidirectional transmission spinal cord stimulation system," in *2010 International Symposium on VLSI Design Automation and Test (VLSI-DAT)*, 2010, pp. 288-291.

[85] *Wireless energy transfer*. Available: http://en.wikipedia.org/wiki/Wireless_energy_transfer#Electrical_conduction

[86] *Qi*. Available: http://en.wikipedia.org/wiki/Qi_(wireless_power_standard)

[87] *A4WP*. Available: http://www.rezence.com/

[88] M. Sole, *et al.*, "A bio-implantable platform for inductive data and power transfer with integrated battery charging," in *Circuits and Systems (ISCAS), 2011 IEEE International Symposium on*, 2011, pp. 2605-2608.
[89] S. C. Tang, *et al.*, "A wireless batteryless deep-seated implantable ultrasonic pulser-receiver powered by magnetic coupling," *IEEE transactions on ultrasonics, ferroelectrics, and frequency control*, vol. 58, pp. 1211-21, Jun 2011.
[90] W. H. Xin, *et al.*, "Study of a wireless power transmission system for an active capsule endoscope," *International Journal of Medical Robotics and Computer Assisted Surgery*, vol. 6, pp. 113-122, Mar 2010.
[91] "HF antenna design notes, technical application report," ed: Texas Instruments, 2003.
[92] *Wi-Fi*. Available: http://en.wikipedia.org/wiki/Wifi
[93] *Bluetooth*. Available: http://en.wikipedia.org/wiki/Bluetooth
[94] *NFC*. Available: http://en.wikipedia.org/wiki/Near_field_communication
[95] *Radio-frequency identification*. Available: http://en.wikipedia.org/wiki/Radio-frequency_identification
[96] *ZigBee*. Available: http://en.wikipedia.org/wiki/ZigBee
[97] *Comparison of wireless data standards*. Available: http://en.wikipedia.org/wiki/Comparison_of_wireless_data_standards
[98] *XBee Wireless RF modules*. Available: http://www.digi.com/xbee/
[99] *Wireless sensor network*. Available: http://en.wikipedia.org/wiki/Wireless_sensor_network
[100] *3rd generation mobile telecommunications*. Available: http://en.wikipedia.org/wiki/3G
[101] M. Frost and M. E. Meyerhoff, "In vivo chemical sensors: tackling biocompatibility," *Analytical Chemistry*, vol. 78, pp. 7370-7377, Nov 1 2006.
[102] R. Trouillon, *et al.*, "Comparative study of poly(styrene-sulfonate)/poly(L-lysine) and fibronectin as biofouling-preventing layers in dissolved oxygen electrochemical measurements," *Analyst*, vol. 134, pp. 784-93, Apr 2009.
[103] R. Trouillon, *et al.*, "Comparative study of the effect of various electrode membranes on biofouling and electrochemical measurements," *Electrochemistry Communications*, vol. 11, pp. 1409-1413, 2009.
[104] R. Meier, *Professional Android 2 application development*: Wiley Publishing, Inc., 2010.
[105] *Specific absorption rate*. Available: http://en.wikipedia.org/wiki/Specific_absorption_rate
[106] D. Seabury, "An update on SAR standards and the basic requirements for SAR assessment," *Conformity*, 2005.
[107] R. DeLonzor, *et al.*, "The electrical conductivity of in vivo human uterine fibroids," *International Journal of Hyperthermia*, vol. 27, pp. 255-265, 2011.
[108] D. F., *Physical properties of tissue: a comprehensive reference book*: New York: Academic Press, 1990.
[109] M. J. Peters, *et al.*, *In advances in electromagnetic fields in living systems* vol. 4, 2005.
[110] T. Wartzek, *et al.*, "Temperature measurement," *Biomed Tech*, vol. 56, pp. 241-257, 2011.
[111] D. Ibrahim, *Microcontroller-based temperature monitoring and control* Newnes, 2002.
[112] "MSP430F20x1, MSP430F20x2, MSP430F20x3 mixed signal microcontroller (Rev. I) ", ed: Texas Instruments, 2012.
[113] L. C. Tao, "Direct intrauterine sampling: the IUMC endometrial sampler," *Diagn Cytopathol*, vol. 17, pp. 153-9, Aug 1997.
[114] J. R. Etzkorn, *et al.*, "Using micro-patterned sensors and cell self-assembly for measuring the oxygen consumption rate of single cells," *Journal of Micromechanics and Microengineering*, vol. 20, Sep 2010.
[115] "BOD testing technology," ed: YSI-Incorporated, 2010.

[116] L. Clark, "Monitor and control of blood and tissue oxygen tension," *Trans. Am.Soc. Artif. Internal Org.*, vol. 2, pp. 41-46, 1956.

[117] "YSI Pro2030 Dissolved Oxygen/Conductivity," ed: YSI-Incorporated, 2010.

[118] C. C. Wu, *et al.*, "Fabrication of miniature Clark oxygen sensor integrated with microstructure," *Sensors and Actuators B-Chemical,* vol. 110, pp. 342-349, Oct 14 2005.

[119] P. Wang, *et al.*, "Micromachined dissolved oxygen sensor based on solid polymer electrolyte," *Sensors and Actuators B: Chemical,* vol. In Press, Corrected Proof, 2010.

[120] A. J. Bard, *et al.*, *Electrochemical methods : fundamentals and applications*, 2nd ed. New York ; Chichester: Wiley, 2001.

[121] A. Manole, *et al.*, "Membrane covered polarographic oxygen sensor manufacturing. Theoretical considerations," *Analele Stiinţifice ale Universităţii "Al. I. Cuza" Iasi, Tomul II, s. Biofizică, Fizică medicală şi Fizica mediului,* 2006.

[122] D. Pletcher and S. Sotiropoulos, "A study of cathodic oxygen reduction at platinum using microelectrodes," *Journal of Electroanalytical Chemistry,* vol. 356, pp. 109-119, 1993.

[123] M. Wittkampf, *et al.*, "Silicon thin film sensor for measurement of dissolved oxygen," *Sensors and Actuators B: Chemical,* vol. 43, pp. 40-44, 1997.

[124] L. C. Clark, Jr., *et al.*, "Continuous recording of blood oxygen tensions by polarography," *Journal of applied physiology,* vol. 6, pp. 189-93, Sep 1953.

[125] K. M, "Performance characteristics of a planar 'clark-type' oxygen sensor," *Sensors and Actuators,* vol. 9, pp. 249-258, 1986.

[126] A. J. Bard and L. R. Faulkner, *Electrochemical methods : fundamentals and applications*, 2nd ed. New York: Wiley, 2001.

[127] H. Suzuki, *et al.*, "A novel thin-film Ag/AgCl anode structure for microfabricated Clark-type oxygen electrodes," *Sensors and Actuators B: Chemical,* vol. 53, pp. 140-146, 1998.

[128] H. Suzuki, *et al.*, "Problems associated with the thin-film Ag/AgCl reference electrode and a novel structure with improved durability," *Sensors and Actuators B: Chemical,* vol. 46, pp. 104-113, 1998.

[129] J. Fritz, "Thermodynamic properties of chloro-complexes of silver chloride in aqueous solution," *Journal of Solution Chemistry,* vol. 14, pp. 865-879, Dec 1 1985.

[130] S. Ito, *et al.*, "Improvement of the silver/silver chloride reference electrode and its application to pH measurement," *Talanta,* vol. 42, pp. 1685-1690, 1995.

[131] J. Noh, *et al.*, "Nanoporous platinum solid-state reference electrode with layer-by-layer polyelectrolyte junction for pH sensing chip," *Lab on a Chip,* vol. 11, pp. 664-671, 2011.

[132] F. Moussy and D. J. Harrison, "Prevention of the rapid degradation of subcutaneously implanted Ag/AgCl reference electrodes using polymer coatings," *Analytical Chemistry,* vol. 66, pp. 674-679, Mar 1 1994.

[133] I. Y. Huang, *et al.*, "Improvement of integrated Ag/AgCl thin-film electrodes by KCl-gel coating for ISFET applications," *Sensors and Actuators B: Chemical,* vol. 94, pp. 53-64, 2003.

[134] T. Kitade, *et al.*, "Needle-type ultra micro silver/silver chloride reference electrode for use in micro-electrochemistry," *Analytical Sciences,* vol. 21, pp. 907-912, 2005.

[135] F. Mizutani, *et al.*, "Use of a siloxane polymer for the preparation of amperometric sensors: O2 and NO sensors and enzyme sensors," *Sensors and Actuators B: Chemical,* vol. 76, pp. 489-493, 2001.

[136] E. A. Johannessen, *et al.*, "Implementation of multichannel sensors for remote biomedical measurements in a microsystems format," *Biomedical Engineering, IEEE Transactions on,* vol. 51, pp. 525-535, 2004.

[137] C. Li, *et al.*, "Toward real-time continuous brain glucose and oxygen monitoring with a smart catheter," *Biosensors and Bioelectronics,* vol. 25, pp. 173-178, 2009.

[138] "SILASTIC MDX4-4210 biomedical grade elastomer product information," ed: Dow Corning, 2005.

[139] G. E. Loeb, *et al.*, "Design and fabrication of an experimental cochlear prosthesis," *Medical and Biological Engineering and Computing,* vol. 21, pp. 241-254, May 1 1983.

[140] M. Kajihara, *et al.*, "Development of new drug delivery system for protein drugs using silicone (I)," *Journal of Controlled Release,* vol. 66, pp. 49-61, 2000.

[141] "184 silicone elastomer product information," ed: Dow Corning, 2010.

[142] S. A. M. van Stroe-Biezen, *et al.*, "Solubility of oxygen in glucose solutions," *Analytica Chimica Acta,* vol. 280, pp. 217-222, 1993.

[143] T. C. Merkel, *et al.*, "Gas sorption, diffusion, and permeation in poly(dimethylsiloxane)," *Journal of Polymer Science Part B: Polymer Physics,* vol. 38, pp. 415-434, 2000.

[144] I. De Bo, *et al.*, "Investigation of the permeability and selectivity of gases and volatile organic compounds for polydimethylsiloxane membranes," *Journal of Membrane Science,* vol. 215, pp. 303-319, 2003.

[145] D. C. Duffy, *et al.*, "Rapid prototyping of microfluidic systems in poly(dimethylsiloxane)," *Analytical Chemistry,* vol. 70, pp. 4974-4984, Dec 1 1998.

[146] B. Cortese, *et al.*, "Characterisation of an irreversible bonding process for COC–COC and COC–PDMS–COC sandwich structures and application to microvalves," *Sensors and Actuators B: Chemical,* vol. 160, pp. 1473-1480, 2011.

[147] D. Pletcher and S. Sotiropoulos, "Towards a microelectrode sensor for the determination of oxygen in waters," *Analytica Chimica Acta,* vol. 322, pp. 83-90, 1996.

[148] T. E. Tang, *et al.*, "The operation of platinum oxygen sensing microelectrodes," *J Bioeng,* vol. 2, pp. 381-8, 1978.

[149] R. L. Elizabeth Prichard, *Measurement of ph*: Royal Society of Chemistry, 2003.

[150] Y. H. Ghallab, *et al.*, "A novel pH sensor using differential ISFET current mode read-out circuit," in *MEMS, NANO and Smart Systems, 2003. Proceedings. International Conference on*, 2003, pp. 255-258.

[151] S. Carroll and R. P. Baldwin, "Self-calibrating microfabricated iridium oxide pH electrode array for remote monitoring," *Analytical Chemistry,* vol. 82, pp. 878-885, Feb 1 2010.

[152] I. A. Ges, *et al.*, "Differential pH measurements of metabolic cellular activity in nl culture volumes using microfabricated iridium oxide electrodes," *Biosensors and Bioelectronics,* vol. 22, pp. 1303-1310, 2007.

[153] E. Prats-Alfonso, *et al.*, "Iridium oxide pH sensor for biomedical applications. Case urea–urease in real urine samples," *Biosensors and Bioelectronics,* 2012.

[154] W. Olthuis, *et al.*, "pH sensor properties of electrochemically grown iridium oxide," *Sensors and Actuators B: Chemical,* vol. 2, pp. 247-256, 1990.

[155] P. VanHoudt, *et al.*, "Iridium oxide pH microelectrode," *Biotechnology and Bioengineering,* vol. 40, pp. 601-608, 1992.

[156] T. Katsube, *et al.*, "pH-sensitive sputtered iridium oxide films," *Sensors and Actuators,* vol. 2, pp. 399-410, 1981.

[157] K. Kinoshita and M. J. Madou, "Electrochemical measurements on Pt, Ir, and Ti oxides as pH probes," *Journal of the Electrochemical Society,* vol. 131, pp. 1089-1094, May 1 1984.

[158] L. D. Burke, *et al.*, "Preparation of an oxidized iridium electrode and the variation of its potential with pH," *Journal of Electroanalytical Chemistry and Interfacial Electrochemistry,* vol. 163, pp. 117-128, 1984.

[159] A. N. Bezbaruah and T. C. Zhang, "Fabrication of anodically electrodeposited iridium oxide film pH microelectrodes for microenvironmental studies," *Analytical Chemistry,* vol. 74, pp. 5726-33, Nov 15 2002.

[160] S. Yao, *et al.*, "A pH electrode based on melt-oxidized iridium oxide," *Journal of the Electrochemical Society,* vol. 148, pp. H29-H36, Apr 2001.

[161] E. T. Hilliard, "Fabrication and testing of a micro-scalable pH sensor for implanted biomedical use," Master of Science in Mechanical Engineering Thesis, University of Pittsburgh, 2011.

[162] J. D. Klein, *et al.*, "Morphology and charge capacity of sputtered iridium oxide films," *Journal of Vacuum Science & Technology A: Vacuum, Surfaces, and Films,* vol. 7, pp. 3043-3047, 1989.

[163] M. L. Hitchman and S. Ramanathan, "A field-induced poising technique for promoting convergence of standard electrode potential values of thermally oxidized iridium pH sensors," *Talanta,* vol. 39, pp. 137-144, 1992.

[164] J. V. Dobson, *et al.*, "EMF measurements of cells employing metal—metal oxide electrodes in aqueous chloride and sulphate electrolytes at temperatures between 25–250°C," *Electrochimica Acta,* vol. 21, pp. 527-533, 1976.

[165] K. Nishio, *et al.*, "Preparation and properties of electrochromic iridium oxide thin film by sol-gel process," *Thin Solid Films,* vol. 350, pp. 96-100, 1999.

[166] I. Song, *et al.*, "Metal oxide/metal pH sensor: effect of anions on pH measurements," *Corrosion,* vol. 54, pp. 13-19, Jan 1 1998.

[167] M. L. Hitchman and S. Ramanathan, "Evaluation of iridium oxide electrodes formed by potential cycling as pH probes," *Analyst,* vol. 113, pp. 35-39, 1988.

[168] J. E. Baur and T. W. Spaine, "Electrochemical deposition of iridium (IV) oxide from alkaline solutions of iridium(III) oxide," *Journal of Electroanalytical Chemistry,* vol. 443, pp. 208-216, 1998.

[169] K. Yamanaka, "Anodically electrodeposited iridium oxide-films (Aeirof) from alkaline-solutions for electrochromic display devices," *Japanese Journal of Applied Physics Part 1-Regular Papers Short Notes & Review Papers,* vol. 28, pp. 632-637, Apr 1989.

[170] K. Yamanaka, "The electrochemical-behavior of anodically electrodeposited iridium oxide-films and the reliability of transmittance variable cells," *Japanese Journal of Applied Physics Part 1-Regular Papers Short Notes & Review Papers,* vol. 30, pp. 1285-1289, Jun 1991.

[171] W.-D. Huang, *et al.*, "A flexible pH sensor based on the iridium oxide sensing film," *Sensors and Actuators A: Physical,* vol. 169, pp. 1-11, 2011.

[172] S. A. M. Marzouk, "Improved electrodeposited iridium oxide pH sensor fabricated on etched titanium substrates," *Analytical Chemistry,* vol. 75, pp. 1258-1266, 2003.

[173] S. A. M. Marzouk, *et al.*, "Electrodeposited iridium oxide pH electrode for measurement of extracellular myocardial acidosis during acute ischemia," *Analytical Chemistry,* vol. 70, pp. 5054-5061, Dec 1 1998.

[174] *Animal testing*. Available: http://en.wikipedia.org/wiki/Animal_testing

[175] "Science, Medicine, and Animals," ed: National Research Council of the National Academies, 2004.

[176] L. H. Thompson, *Managing Swine Reproduction*: University of Illinois at Urbana-Champaign, College of Agriculture, Cooperative Extension Service, 1981.

[177] "Mirena, highlights of prescribing information," ed: Bayer HealthCare Pharmaceuticals Inc., 2009.

[178] A. W. Olsen, *et al.*, "Behaviour of growing pigs kept in pens with outdoor runs: II. Temperature regulatory behaviour, comfort behaviour and dunging preferences," *Livestock Production Science,* vol. 69, pp. 265-278, 2001.

[179] P. H. Chen and C. E. White, "Comparison of rectal, microchip transponder, and infrared thermometry techniques for obtaining body temperature in the laboratory rabbit," *Journal of the American Association for Laboratory Animal Science,* vol. 45, pp. 57-63, 2006.

[180] J. H. Liu, *et al.*, "Endogenous circadian rhythm of basal pupil size in rabbits," *Investigative Ophthalmology and Visual Science,* vol. 37, pp. 2345-9, October 1 1996.

[181] Y. TSUTSUMI, *et al.*, "Variations in body temperature associated with reproductive state in the female rabbit," *Journal of the Faculty of Agriculture, Hokkaido University,* vol. 5, 1968.

[182] B. Nuesslein-Hildesheim, *et al.*, "Pronounced juvenile circadian core temperature rhythms exist in several strains of rats but not in rabbits," *Journal of Comparative Physiology B,* vol. 165, pp. 13-17, Apr 1 1995.

[183] S. Graf, *et al.*, "Regrouping rabbit does in a familiar or novel pen: Effects on agonistic behaviour, injuries and core body temperature," *Applied Animal Behaviour Science,* vol. 135, pp. 121-127, Nov 30 2011.

[184] G. Degerman and J. E. Kihlstrom, "Cyclic variation in the body temperature of the male rabbit," *Acta Physiologica Scandinavica,* vol. 62, pp. 46-50, 1964.

[185] D. Gunn and D. B. Morton, "Inventory of the behaviour of New Zealand White rabbits in laboratory cages," *Applied Animal Behaviour Science,* vol. 45, pp. 277-292, 1995.

[186] "Metglas Magnetic Alloy 2714A," ed: Metglas, 2011.

[187] "Antenna/RFID kit part No.0199000024.," ed: Fair-Rite products co.

[188] R. Trouillon and D. O’Hare, "Comparison of glassy carbon and boron doped diamond electrodes: Resistance to biofouling," *Electrochimica Acta,* vol. 55, pp. 6586-6595, 2010.

[189] B. Hoyer and N. Jensen, "Stabilization of the voltammetric response of organic analytes with self-passivating electrode reactions: Synergistic effect of surfactants and high buffer strength," *Journal of Electroanalytical Chemistry,* vol. 601, pp. 153-160, 2007.

[190] B. Hoyer and N. Jensen, "Stabilization of the voltammetric serotonin signal by surfactants," *Electrochemistry Communications,* vol. 8, pp. 323-328, 2006.

[191] I. A. Ges, *et al.*, "Thin-film IrOx pH microelectrode for microfluidic-based microsystems," *Biosensors and Bioelectronics,* vol. 21, pp. 248-256, 2005.

[192] E. Pearlstein, *et al.*, "Fibronectin: A review of its structure and biological activity," *Molecular and Cellular Biochemistry,* vol. 29, pp. 103-128, 1980.